The *Chandra* Proposers' Observatory Guide

Contents

III   Appendices   273

A   Contact Information   275

B   Acronym List   277

List of Figures

List of Tables

What's New for Cycle 5?

The *Proposers' Observatory Guide* and proposal related materials have been re-organized for Cycle 5. The chapters on proposal-related software (Chapters 11-13 in Cycle 4) have been removed and replaced by a web based help system and step-by-step proposal threads. These can be accessed via the Proposers Web page. A summary of proposal related material is given in Chapter 11.

Please see the Call for Proposals for a complete list of "What's New" items for Cycle 5.

Part I

Technical Description

Chapter 1

Mission Overview

The *Chandra* X-Ray Observatory (*CXO*), combines an efficient high-resolution ($\leq 1/2$ arcsecond) X-ray telescope with a suite of advanced imaging and spectroscopic instruments. The Observatory was successfully launched by *NASA*'s Space Shuttle Columbia on July 23, 1999, with Col. Eileen Collins commanding. Subsequently an Inertial Upper Stage and *Chandra*'s Internal Propulsion System placed the Observatory in a high elliptical orbit. *Chandra* is the X-Ray component of *NASA*'s four Great Observatories. The other components are the Hubble Space Telescope, the late Compton Gamma-Ray Observatory and the Space Infra-Red Telescope Facility currently scheduled for January 2003 launch.

1.1 Program Organization

The *Chandra* Project is managed by *NASA*'s Marshall Space Flight Center. The Project Scientist is Martin C. Weisskopf. Day-to-day responsibility for *Chandra* science operations lies with the Chandra X-ray Center (*CXC*), Harvey Tananbaum, Director. The *CXC* is located at the Cambridge, Massachusetts facilities of the Smithsonian Astrophysical Observatory (*SAO*) and the Massachusetts Institute of Technology (*MIT*). The *Chandra* Operations Control Center (*OCC*) is also located in Cambridge. The *CXC* uses the *OCC* to operate the Observatory for *NASA*.

1.2 Unique Capabilities

Chandra was designed to provide order-of-magnitude advances over previous X-ray astronomy missions with regards to spatial and spectral resolution. The High Resolution Mirror Assembly (HRMA) produces images with a half-power diameter (HPD) of the point spread function (*PSF*) of < 0.5 arcsec. Both grating systems – the Low Energy

3
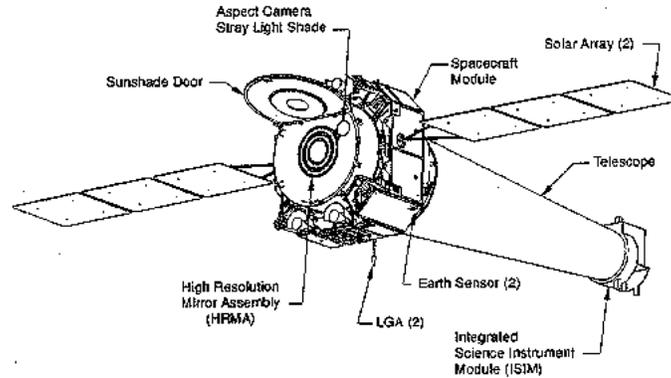
Figure 1.1: The *Chandra* Observatory with certain subsystems labeled. LGA is an acronym for the Low Gain Antenna.

Transmission Grating (LETG) and the High Energy Transmission Grating (HETG) – offer resolving powers well in excess of 500 over much of their bandwidth which, together, cover the range from $\leq$ 0.1 to 10 keV.

1.3   Observatory Overview

An outline drawing of the *Chandra* X-ray Observatory is shown in Figure 1.1. *Chandra* consists of a spacecraft and a telescope/science-instrument payload. The spacecraft provides power; communications, and command, and data management; pointing control and aspect determination. The principal elements of the observatory that will be discussed in this document are:

- The High Resolution Mirror Assembly (HRMA)(Chapter 4)

- The Aspect System (Chapter 5)

- The Focal-plane Science Instruments (SIs):

  - The Advanced CCD Imaging Spectrometer (ACIS)(Chapter 6)
  - The High Resolution Camera (HRC)(Chapter 7)

- The Objective Transmission Gratings:

  - High Energy Transmission Grating (HETG)(Chapter 8)
  - Low Energy Transmission Grating (LETG)(Chapter 9)

These and related elements of the *Chandra* Project are introduced briefly in the remainder of this chapter.

1.4   Pointing Control and Aspect Determination (PCAD)

The PCAD system controls the pointing and dithering of the observatory and provides the data from which both the relative and absolute aspect are determined. Dithering is imposed in order to spread the instantaneous image over many different pixels of the focal plane detector to smooth out pixel-to-pixel variations. The dither pattern is a Lissajous figure (and can be seen quite clearly in the un-aspect corrected data from bright point sources). The amplitude, phase, and velocity depend on which instrument (ACIS or HRC) is in the focal plane.

Key elements of the PCAD system are the set of redundant gyroscopes, momentum wheels, and an aspect system consisting of a four inch optical telescope with (redundant) CCD detector. The aspect camera simultaneously images a fiducial light pattern produced by light emitting diodes placed around the focal-plane instruments along with the flux from up to five bright stars that may be in the aspect camera's field-of-view. An interesting consequence is that the user may request that one of the targets of the aspect camera be at the location of the x-ray target. For bright optical counterparts, this option allows real-time optical monitoring albeit at the price of a reduced-accuracy aspect solution – see Chapter 5 for further details.

1.5   HRMA

The HRMA consists of a nested set of four paraboloid-hyperboloid (Wolter-1) grazing-incidence X-ray mirror pairs, with the largest having a diameter of 1.2 m (twice that of the *Einstein* Observatory). The focal length is 10 m.

The mirror glass was obtained from Schott Glasswerke; grinding and polishing was performed at Hughes Danbury Optical Systems; coating at Optical Coating Laboratory; and the mirror alignment and mounting at Eastman-Kodak Co. The mirrors weigh about 1000kg. Details of the HRMA and its performance are presented in Chapter 4.

The *Chandra* Telescope Scientist is Leon Van Speybroeck, of the Smithsonian Astrophysical Observatory.

1.6   Science Instrument Module (SIM)

The Science Instrument Module consists of the special hardware that provides mechanical and thermal interfaces to the focal-plane scientific instruments (SIs). The most critical functions from an observer's viewpoint are the capability to adjust the telescope focal length and the ability to move the instruments along an axis orthogonal to the optical axis.
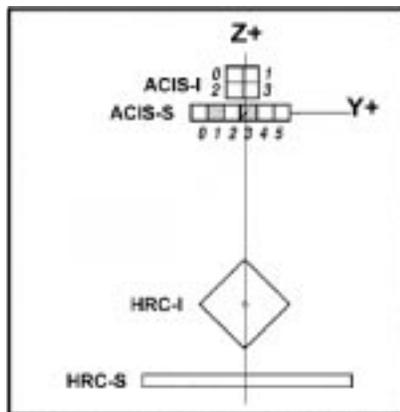
Figure 1.2: Arrangement of the ACIS and the HRC in the focal plane. The view is along the axis of the telescope from the direction of the mirrors. For reference, the two back-illuminated ACIS-S chips are shaded. Numbers indicate positions of chips I0-I3 and S0-S5. SIM motion can be used to place the aimpoint at any point on the vertical solid line.

The SIM houses the two focal instruments - the ACIS and the HRC. Each of these have two principal components - HRC-I and -S and ACIS-I and -S. The focal plane instrument layout is shown in Figure 1.2. The SIM moves in both the X-axis (focus) and the Z-axis (instrument and aimpoint (1.6.1) selection). Note that the Y-Axis parallels the dispersion direction of the gratings.

1.6.1   Aimpoints

Aimpoints are the nominal positions on the detector where the flux from a point source with no commanded offsets is placed. Note there is a slight (20") distinction between the aimpoint and the on-axis position, which for most practical purposes can be ignored. The aimpoints are discussed in detail in the Chapters about each instrument and in Chapter 3.

1.7   Ground System

The ground system consists of the *Chandra* X-ray Center (*CXC*) and the Operations Control Center (*OCC*) in Cambridge, MA, the Engineering Support Center (ESC) at *MSFC*, and various *NASA* communications systems including the Deep Space Network operated for *NASA* by the Jet Propulsion Laboratory. See Section 2.6.2 for details.

1.8 Orbit

The *Chandra* orbit is highly elliptical and varies with time. As of September 2002 the apogee was $\sim 132,000$ km and the perigee was $\sim 16,800$ km. The apogee and perigee are drawing closer to each other and will continue to do so until about 6 years after launch (at a rate of a few thousand km/year) when the trend will reverse. The orbit allows for reasonably high observing efficiency as the satellite spends most of the time well above the radiation belts ($\sim 75\%$) and long continuous observations (~ 160 ksec) are made possible by the orbital period of 63.5h.

1.9 Particle Detector

There is a particle detector mounted near the telescope, called the Electron, Proton, Helium INstrument (EPHIN) (see 2.5). This detector is used to monitor the local charged particle environment as part of the scheme to protect the focal-plane instruments from particle radiation damage. Data taken during an observation are available to the observer.

The Co-Principal Investigators of the EPHIN instrument are Drs. Reinhold Muller-Mellin and Hoarst Kunow of the University of Kiel, Germany.

1.10 ACIS

ACIS is comprised of two CCD arrays, a 4-chip array, ACIS-I; and a 6-chip array, ACIS-S. The CCDs are flat, but the chips in each array are positioned (tilted) to approximate the relevant focal surface: that of the HRMA for ACIS-I and that of the HETG Rowland circle for ACIS-S. ACIS-I was designed for CCD imaging and spectrometry; ACIS-S can be used both for CCD imaging spectrometry and also for high-resolution spectroscopy in conjunction with the HETG grating.

There are two types of CCD chips. ACIS-I is comprised of front-illuminated (FI) CCDs. ACIS-S is comprised of 4 FI and 2 back-illuminated (BI) CCDs, one of which is at the best focus position. The quantum efficiency of the ACIS instrument has recently been discovered to be slowly changing with time, probably as a result of molecular contamination build-up on the optical blocking filter or the CCD chips. The BI CCDs response extends to lower energies than the FI CCDs and the energy resolution is mostly independent of position. The low-energy response of the BI CCDs has been affected by the contaminant build-up. The FI CCD response is more efficient at higher energies but the energy resolution varies with position due to radiation damage caused by protons reflecting through the telescope during radiation-zone passages in the early part of the mission. Details in Chapter 6.

The Principal Investigator is Prof. Gordon Garmire of the Pennsylvania State University.

1.11   HRC

The HRC is comprised of two microchannel plate (MCP) imaging detectors: the HRC-I designed for wide-field imaging; and, HRC-S designed to serve as a readout for the LETG. The HRC-I is placed at right angles to the optical axis, tangent to the focal surface. The HRC-S is made of three flat elements, the outer two of which are tilted to approximate the LETG Rowland circle. The HRC detectors have the highest spatial resolution on *Chandra*, matching the HRMA point spread function most closely. Under certain circumstances, the HRC-S detector also offers the fastest time resolution ($16\mu s$). Details concerning the HRC are in Chapter 7.

The Instrument Principal Investigator is Dr. Stephen Murray of the Smithsonian Astrophysical Observatory.

1.12   HETG

The HETG, when operated with the HRMA and the ACIS-S, forms the High-Energy Transmission Grating Spectrometer (HETGS) for high resolution spectroscopy. The HETGS achieves resolving power ($E/\Delta E$) up to 1000 in the band between 0.4 keV and 10.0 keV. The HETG is comprised of two grating assemblies – the High Energy Grating (HEG) and the Medium Energy Grating (MEG) – on a single structure that can, by command, be placed in the optical path just behind the HRMA. The HEG intercepts X-rays from only the two inner mirror shells and the MEG intercepts X-rays from only the two outer mirror shells. The HEG and MEG dispersion directions are offset by 10 degrees so the two patterns can be easily distinguished. Details are presented in Chapter 8.

The Instrument Principal Investigator for the HETG is Prof. Claude Canizares, of the *MIT* Center for Space Research.

1.13   LETG

The LETG when operated with the HRC-S, forms the Low Energy Transmission Grating Spectrometer (LETGS). The LETGS provides the highest spectral resolution on *Chandra* at low (0.08 - 0.2 keV) energies. The LETG is comprised of a single grating assembly that, on command, can be placed in the optical path behind the HRMA. The LETG grating facets intercept and disperse the flux from all of the HRMA mirror shells. Details are given in Chapter 9.

The LETG was developed at the Laboratory for Space Research in Utrecht, the Netherlands, in collaboration with the Max-Planck-Institut für Extraterrestrische Physik in Garching, Germany. The Instrument Principal Investigator is Dr. Mariano Mendez of the Laboratory for Space Research.

1.14 Effective Area Comparisons

The effective areas of the imaging instruments are shown in Figure 1.3. The ACIS curves allow for the expected degradation of the ACIS eefficiency caused by molecular contamination predicted for the middle of Cycle 5 (2004-05-15). A comparison of the effective areas of the grating spectrometers are shown in Figure 1.4. Note that the data from the HEG and MEG are obtained simultaneously. The comparisons shown here are based on the most recent calibration at the time of issuance of this document and are subject to revision. The proposer is urged to read the detailed material in the appropriate chapters and examine the *CXC* web (see 1.16) site for updates.

1.15 Allocation of observing time

Observing time is awarded through the *NASA* proposal and peer review process. The prospective user must submit a proposal in which the observation is described and justified in terms of the expected results. The proposer must also show that the observation is well suited to *Chandra* and that it is technically feasible. Refer to the *CfP* for more information.

1.16 How to get information and help

The *CXC* WWW page (http://cxc.harvard.edu) provides access to most documents, proposal preparation tools, and proposal submission software. Many documents are also available in printed form by request through the *CXC* HelpDesk or by writing to *Chandra* Directors Office, Mail stop 4, 60 Garden St., Cambridge, MA 02138. The *CXC* web page provides a "HelpDesk" for communicating specific questions and requests concerning all user aspects of *CXO*. An overview of resources available to proposers can be found in Chapter 11.
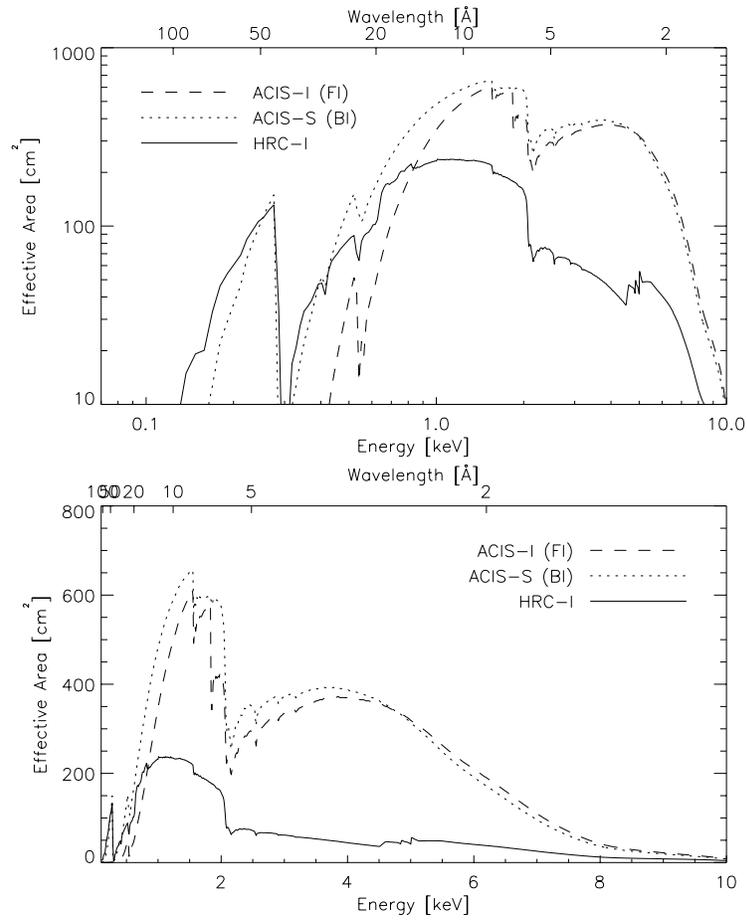
Figure 1.3: Comparison of the on-axis effective areas for observing a point source (integrated over *PSF*) of the HRMA/HRC-I, the HRMA/ACIS(FI), and the HRMA/ACIS(BI) combinations. The ACIS curves show the predicted values for the middle of Cycle (2004-05-15).
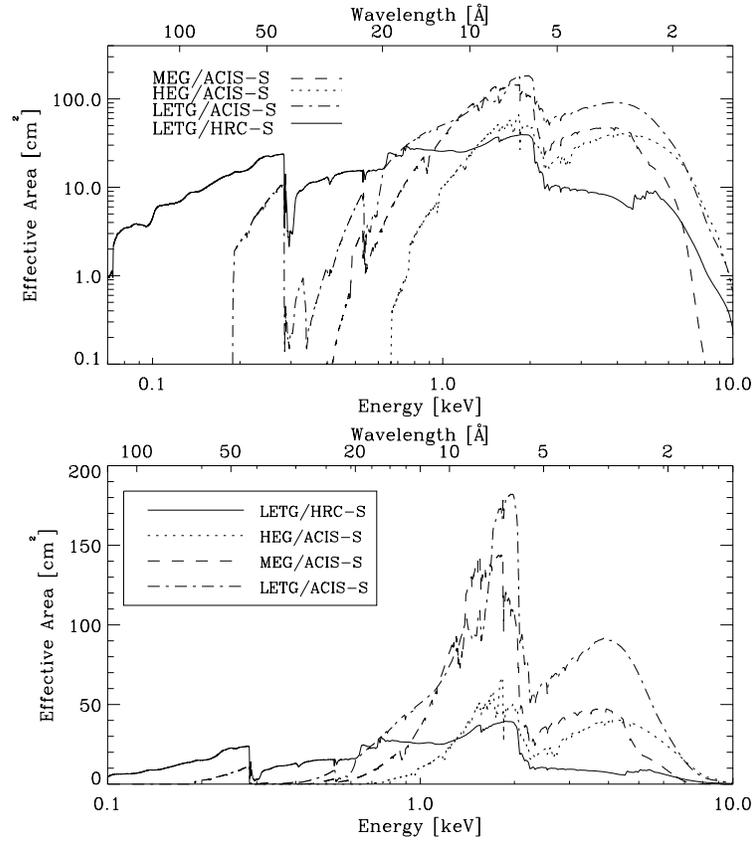
Figure 1.4: Comparison of the first-order effective areas in cm^2 (integrated over the line spread function) of the MEG and HEG and LETG spectrometers. The $(+/-)$ first orders of the diffracted spectrum have been added.

Chapter 2

Spacecraft, Telescope, Operations, & Mission Planning

2.1 Introduction

In this chapter we provide a brief overview of the spacecraft, the telescope system including the Science Instrument Module (SIM), operations, and mission planning.

A number of observatory parameters are given in Table 2.1.

2.2 Spacecraft

An outline drawing of the Observatory was shown in Figure 1.1. The spacecraft equipment panels are mounted to, and supported by, a central cylindrical structure. The rear of the spacecraft attaches to the telescope system.

The spacecraft includes six subsystems:

1. **Structures and Mechanical** Subsystem. This subsystem includes all spacecraft structures, mechanisms (both mechanical and electro-mechanical), and structural interfaces with the Space Shuttle. Mechanisms, such as those required for the sunshade door, are also part of this subsystem.

2. **Thermal Control** Subsystem. Thermal control is primarily passive, using thermal coatings and multi-layer insulation blankets. On-board-computer-controlled electrical heaters augment these passive elements to maintain sensitive items such as the HRMA at nearly constant temperature.

3. **Electrical and Power** Subsystem. This subsystem includes all hardware necessary to generate, condition, and store electrical energy. Power is generated by solar

Table 2.1: Spacecraft Parameters

Chandra "dry" weight (incl. reserve)	4790 kg
Loaded Propellant	969 kg
Electrical Power	3 NiH$_2$ 30 Amp-hr batteries
	Two 3-panel solar arrays
Nominal Operating Power	2034 W (TBR)
Optical bench length	$\sim$ 10 meters
SIM focus adjustment range	$\pm$0.4 inches
SIM focus adjustment accuracy	$\pm$0.0005 inches
SIM Z-position adjustment repeatability	$\pm$0.005 inches
Solid-state recorder capacity	1.8 Gb each of 2
On-board command storage	5400 command words
Nominal command storage period	72 hours
Observatory telemetry data-rate	32 kbps
Telemetry playback downlink rates	1024, 512 and 256 kbps
Nominal ground contact periods	45 to 75 minutes per 8 hours
SI telemetry rate	24 kbps
Telemetry format 1 major frame	= 32.8 seconds
	= 128 minor frames
Clock error	$< 100\mu$s
Clock stability	1:10^9 per day
Clock frequency	1.024 MHz

cells mounted on two solar array wings (three panels each), sized to provide a 15% end-of-life power margin. Electrical power is stored in three, NiH_2, 30-Ampere-hour batteries. Battery sizing requires non-critical components, including science instruments, to be powered down during times when either the earth or the moon (partially or completely) blocks the sun. These eclipses occur infrequently due to the particular nature of the *Chandra* orbit.

4. **Communication, Command, and Data Management** (CCDM) Subsystem. This subsystem includes all the equipment necessary to provide ranging, modulation, and demodulation of radio frequency transmission of commands and data to and from the Deep Space Network *NASA* Communication System. The CCDM includes two low gain antennas, providing omni-directional communications, an on-board computer (OBC), a serial digital data bus for communication with other spacecraft components, the spacecraft clock, and a telemetry formatter which provides several different formats.

5. **Pointing Control and Aspect Determination** (PCAD) Subsystem. This subsystem includes the hardware and control algorithms for attitude determination and for attitude and solar array control. The solar arrays can be rotated about one axis. The PCAD subsystem also includes hardware for safeing the observatory. Specific details of the the PCAD subsystem especially relevant to scientific performance are discussed in Chapter 5.

6. **Integral Propulsion** Subsystem. This subsystem contains thrusters and fuel for control of the orbit and spacecraft orientation. The portion of the system used for orbital adjustment was disabled once the final orbit was achieved for reasons of safety to the observatory. There is enough fuel available to support much more than 10 years of operation.

2.3 Telescope System

The principal elements of the telescope system are the HRMA (Chapter 4), and an optical bench. A schematic is shown in Figure 2.1. The HRMA, comprised of four concentric grazing incidence x-ray telescopes, focuses x-rays on the selected detector located in the Science Instrument Module (2.4).

The telescope system includes:

1. High Resolution Mirror Assembly

2. Optical Bench Assembly

3. Spacecraft Support Structure Assembly
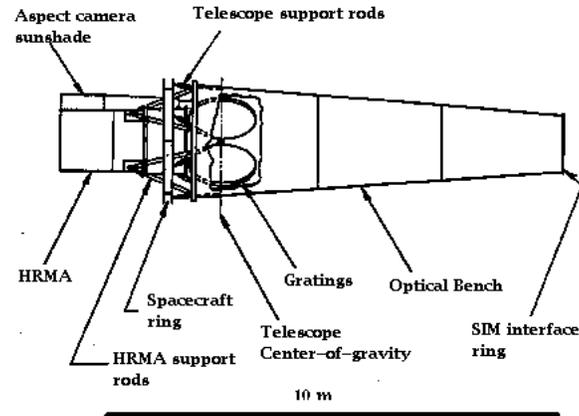
Figure 2.1: Major components of the telescope system.

4. Fiducial Transfer Optical Components

5. Spacecraft to Telescope Support Struts

6. Forward and Aft HRMA Contamination Covers

7. Magnetic Baffle Assembly

8. Stovepipe Baffle

The Optical Bench Assembly is primarily the long composite structure separating the HRMA from the SIM. The Spacecraft Support Structure Assembly includes the ring to which the spacecraft is mounted. The Fiducial Transfer Assembly Optical Components are discussed in Chapter 5. The Spacecraft to Telescope support struts are self explanatory and are shown in Figure 2.1. The forward and aft contamination covers were opened on-orbit and cannot be closed. The forward contamination cover also serves as the sun-shade.

The magnetic baffle assembly was designed to prevent low energy (up to about $\sim$ 100 keV) electrons (reflecting through the x-ray optics) from reaching the focal plane. More details as to these baffles may be found at http://wwwastro.msfc.nasa.gov/xray/spectopics.html.

The stovepipe baffle, located inside the optical bench and at the entrance to the SIM, includes tantalum coated plates to prevent x-rays, other than those passing through the telescope, from reaching the focal plane. There are several such baffles inside the optical bench. Details of the baffles may be found at the WWW address above.

ACIS External Source

Hat Brim

SIM Thermal Skirt

Focused Structure Bench

Stray Light Shield
Assembly

Translation Table

**Isometric view
of SIM viewed
toward -X**

+X   +Z

+Y
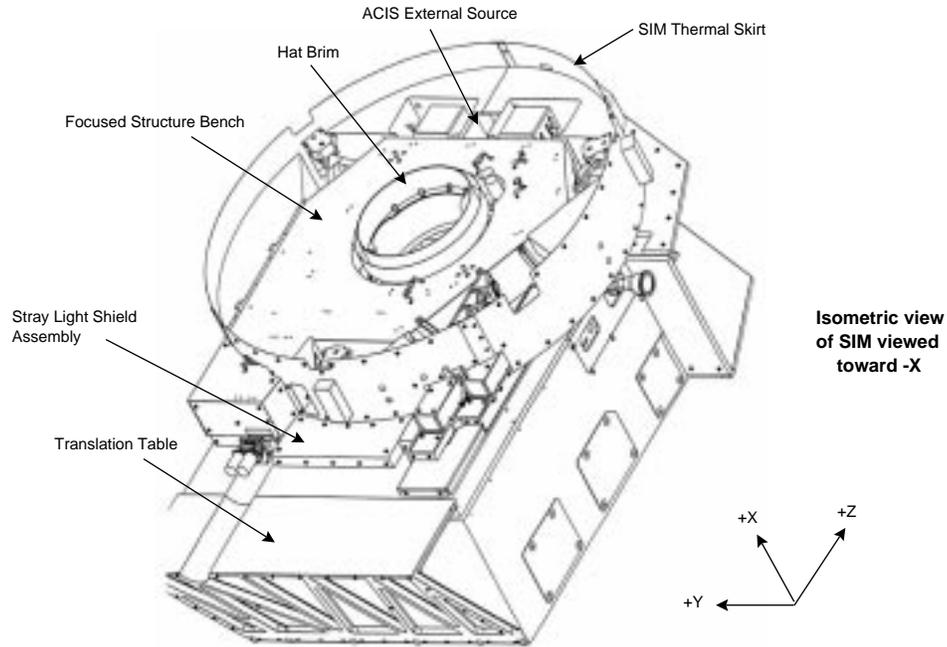
Figure 2.2: A schematic of the Science Instrument Module.

2.4   Science Instrument Module (SIM)

The SIM, shown schematically in Figure 2.2, is a movable bench on which the focal-plane x-ray detectors are mounted. Kinematic mounts (flexures) and thermal isolation are provided between the SIM and the telescope optical bench. A graphite epoxy support structure houses the translation stage on which the instruments are mounted.

2.4.1   SIM Motions

The focal plane instruments are positioned by the SIMZ-axis translation stage with a repeatability to ± 0.005 inches over a translation range of 20 inches. The SIM X-axis motion sets the focus to an accuracy of ± 0.0005 inches over a range of 0.8 inches. The fine-focus adjustment step is 0.00005 inches.

2.5   Electron Proton Helium Instrument (EPHIN)

The local particle radiation environment is monitored by the EPHIN detector. EPHIN consists of an array of 5 silicon detectors with anti-coincidence. The instrument is sensitive to electrons in the energy range 150 keV - 5 MeV, and protons/helium isotopes in the energy range 5 - 49 MeV/nucleon. The field of view is 83 degrees and the instrument is mounted near the HRMA. EPHIN data rates are monitored by the OBC, which activates commands to safe the ACIS and HRC during periods of high radiation such as a solar flare.

The forerunner of the *Chandra*-EPHIN was flown on the SOHO satellite. Information is available at http://ifkki.kernphysik.uni-kiel.de/soho/ephin_e.html

The EPHIN instrument was built by the Institut fur Experimentelle und Angewandte Physik Extraterrestrische Physik at the University of Kiel, Germany. Drs. Reinhold Muller-Mellin and Hoarst Kunow are the Co-Principal Investigators.

2.6   Operations

2.6.1   Launch and On-orbit Verification

Chandra was launched on board the Space Shuttle Columbia from the Kennedy Space Center in Florida on July 23, 1999 at 12:31:00:04 a.m. EDT. The Observatory was deployed from the Space Shuttle a few hours later at 8:45 a.m. EDT. Two burns of the IUS (Inertial Upper Stage) took place an hour after *Chandra* was released. A series of five burns of the Integral Propulsion System (IPS) over the period July 24-Aug 7 took *Chandra* to its final orbit.

Once in final orbit, the Orbital Activation and Checkout (OAC) phase started. During this time, all systems were brought on-line and numerous calibrations were performed. Originally, it was planned to devote approximately 60 days to OAC followed by 30 days of the guaranteed time observations. However, after the contamination covers on the HRMA were opened, and after a few passages through the radiation belts under this condition, the front-illuminated ACIS CCDs showed signs of increased, and spatially-dependent, energy resolution together with increased charge transfer inefficiency (CTI), consistent with radiation damage. Steps were successfully taken to prevent further damage (see Chapter 6). Due to this situation, and because of uncertainties of the long term stability of the FI chips at that time, additional ACIS calibrations were performed and emphasis was placed on observations requiring the use of the FI CCDs. Note that the back-illuminated CCDs were unaffected, and the situation is now stable in that further degradation has been slowed to match pre-launch expectations. See Chapter 6 of this guide for further details. Normal operations started in November 1999.

2.6.2   The Ground System

The *Chandra* "Ground System" is comprised of facilities required to operate the spacecraft, receive and analyze the spacecraft telemetry and provide scientific support to the user community. The ground system includes the following elements:

Deep Space Network (DSN). The DSN is used for communicating commands to the spacecraft and receiving telemetry.

NASA **Communications** (NASCOM). NASCOM provides communications links between the DSN and the OCC and between the OCC and other ground facilities.

Operations and Control Center (*OCC*) is responsible for operating the observatory. This includes activities such as preparing command loads, processing telemetry, attitude determination, monitoring health and safety, etc. *OCC* personnel utilize two major software environments, the Online System (ONLS) and the Offline System (OFLS). The ONLS deals primarily with real-time operations such as receiving telemetry and sending commands through the DSN. The OFLS deals with functions such as mission planning and supporting engineering analysis.

Software Maintenance Facility (SMF). The SMF which maintains the flight software is operated by TRW and is located at their facilities in Redondo Beach, California.

Chandra **Science Center** (*CXC*). The *CXC* is the focal point for service to the scientific community. The *CXC* supports *NASA* in preparing technical material Research Announcements and providing technical assistance for peer reviews. The *CXC* assists prospective observers in developing proposals, generates an observing plan from the proposals that are selected, and carries out certain data processing to supply data products to observers. The *CXC* performs on-orbit calibration and maintains the calibration data-base, produces response functions, etc. The *CXC* is responsible for providing limited assistance to observers, including software, for analyzing data. The *CXC* is also responsible for archiving *Chandra* data.

2.6.3   Commanding

All normal *Chandra* operations are preplanned. The OFLS divides the weekly mission schedule into approximately one day segments and generates spacecraft and instrument commands to be executed that day. Once a day, this command load is uplinked to the spacecraft and stored. Three consecutive daily segments are loaded to assure autonomous operation for 72 hours. Stored command loads can be interrupted if necessary, and updated either because of an emergency or to accommodate Targets of Opportunity. The

interruption process may require up to 24 hours to complete depending on numerous factors including the availability of ground contact. In a true emergency, ground contact can always be scheduled.

2.6.4   Telemetry

The telemetry is formatted into major frames and minor frames - a major frame lasts 32.8 seconds and includes 128 minor frames. Each minor frame contains 1019 bytes of science and engineering data plus a 6 byte header (yes - 1025, not 1024, total bytes!) that includes a 3-byte minor frame counter – the Virtual Channel Data Unit (VCDU) counter – which resets every 49.8 days.

During normal science operations, telemetry data is generated on the Observatory at a rate of 32 kbps, of which 24 kbps are devoted to the "science stream" data from one of the focal plane instruments and the remainder allocated to other systems, including 0.5 kbs to the "next-in-line" instrument. The data is recorded on one of two solid state recorders for subsequent transmission. Each solid state recorder has a capacity of 1.8 Gbits equivalent to 16 hours of operation.

The recorded data are transmitted through one of the low gain antennas to the ground at 1024 kbps, (or 512 kbps, or 256 kbps) during scheduled Deep Space Network contacts every eight hours. Contacts last typically from 45-75 minutes. The ground stations, in turn, transmit the data to JPL which then transmits the data to the *OCC*.

2.6.5   SI Science Data

There are individual telemetry formats for HRC and ACIS data. The 24 kbps data is collected by the CCDM subsystem from each instrument as a sequence of 8-bit serial-digital words through a Remote Command and Telemetry Unit (RCTU). An additional small amount of housekeeping telemetry is always collected from each instrument independent of the selected format.

2.6.6   Event Timing and the Spacecraft Clock

The CCDM subsystem provides prime and redundant 1.024 MHz clocks, and the $(1/1.024\mu s)$ pulses are utilized by the two focal plane instruments for timing. Each instrument has electronics that counts the elapsed time since the beginning of the current telemetry major frame. The time of events recorded on *Chandra* are given in Terrestrial Time (TT) which differs from UTC by about a minute. (See http://tycho.usno.navy.mil/systime.html for a discussion.) The accuracy of the time relationship is 100 microseconds. The spacecraft clock is stable to better than one part in 10^9 per day.

2.7 Mission Planning

2.7.1 The Long-Term Schedule

The *Chandra* scheduling process seeks to maximize the scientific return (the fraction of time on-target) while minimizing any risk to the spacecraft. Once the list of approved target observations for a new cycle has been finalized, these are scheduled by the Science Operations Team (SOT) Mission Planners into weekly bins in a Long Term Schedule (LTS), using Spike scheduling software, originally developed for use with the Hubble Space Telescope and modified for *Chandra*. Observations are scheduled into weekly bins, using approximately 55% of calendar time. This is about 75% of the time available for science scheduling, so *on average* approximately a quarter of the time is left unscheduled in the LTS. A reserve of unconstrained observations are kept in several pool bins. These pool targets are used to fill in weekly short-term schedules.

Once a new LTS is populated at the start of a Cycle, Mission Planners begin the process of weekly scheduling. As the Cycle goes on, the remaining LTS is amended weekly and posted on-line at http://cxc.harvard.edu/longsched.html. Observers should note that the predictive fidelity of the LTS generally decreases farther into the future. The placement of the unconstrained pool targets can change at any time. Each week as the LTS is revised, non-pool targets may also be reassigned for a variety reasons including multi-telescope coordination, and observations may be bumped or not completed because of high radiation or TOOs.

Both the LTS and the STS pages show *CXC* sequence numbers for every observation that are hyper-linked to descriptive target pages. Each target page further contains a link to a plot that displays the roll, pitch, and visibility for the target for the duration of the Cycle. The target page also contains links to images of the appropriate Chandra instrument superposed at the correct roll on 2deg images of the sky available from *NASA* SkyView. Any time an observation is reassigned to a new weekly bin or scheduled precisely within a week in a short-term schedule, a revised set of images is posted.

The LTS takes into account the intrinsic target visibility (based primarily on minimum Sun, Earth and Moon angles; see section Section 3.3.2) as well as additional target constraints approved by the Peer Review. These additional constraints are described in Chapter 3. While constraints can significantly enhance the science return on an observation, proposers should firstly be aware that limitations are imposed on the number of constrained observations that may be accepted at Peer Review (see the *CfP*). Additionally, all constraints effectively translate into time constraints that may affect the number of weekly bins available for scheduling the observation. Weekly schedules are interrupted unpredictably by solar radiation flares or target-of-opportunity (TOO) observations. This inevitably means that the next opportunity to meet all the observing constraints can be significantly delayed if those constraints are stringent.

2.7.2   Selecting Candidates for Short-Term Scheduling

To allow greater flexibility in short-term scheduling, and to optimize the observing efficiency, SOT Mission Planning constructs an observation request (OR) list that is heavily oversubscribed with candidate targets, primarily using pool targets. Before construction of the OR list, all observing parameters must be finalized. Observers will be contacted by an uplink scientist to verify that the observation parameters are correct (and final) before starting the short-term scheduling process. An overview of the process follows.

- uplink scientist contacts the observer

- observer verifies all observing parameters, response required no later than 30 days before LTS date or within 30 days for pool targets [1]

- target is made available for scheduling

- target appears in OR list as a candidate for short-term scheduling

- target is observed in scheduled week, or bumped to a later week

Due to bumping and to the need to oversubscribe candidate target lists, some targets (particularly those with low visibility during the time in question) may be assigned to several OR lists before they are finally observed. Once observing parameters have been finalized, uplink scientists will contact the observer only to inform them if their observation is not carried out as planned in a published short-term schedule.

2.7.3   The Short Term Scheduling Process

SOT Mission Planning assigns priorities in the OR list to emphasize constrained observations. Whenever possible the ORs span a range of angles about the Sun line to prevent excess accumulation of momentum. The OR list is forwarded to the Flight Operations Team (FOT), which constructs the detailed short-term schedule (STS) and command loads for the spacecraft. Along with observing efficiency, thermal, power, momentum, and pointing constraints are all factored in, as well as minimization of maneuver error and optimal guide star acquisition. Several iterations of optimization and safety checks are not uncommon for each weekly schedule before its approval by all teams concerned (FOT and SOT, Mechanisms, Command Management, ACIS, HRC, Pointing Control and Aspect, Flight Director). Once a final schedule is approved, the *CXC* keeps track of unscheduled targets and updates the pool accordingly. The STS is available on-line at http://cxc.harvard.edu/shortsched.html.

The *CXC* currently starts to prepare short-term schedules 3 weeks in advance. Thus at any given time there are 3 weekly schedules in various stages of preparation. Changes

---

[1]requests for changes after this time-frame cannot always be accommodated

in any of these require a rebuild which is very labor intensive. Fast-response TOOs (see section 10.2) are currently the only allowed changes. Even small changes to a schedule typically require 24-48 hour turnaround. During nominal Mission Planning, the final STS is approved and ready for upload by the Wednesday or Thursday before the STS commands begin executing Sunday night or Monday morning (GMT). Hence, given the nominal planning cycle, fast ($<$ 1 week) turn-around TOOs can most efficiently be incorporated into the short term schedule if they are submitted to the *CXC* by mid-week. Such submission/notification will reduce the amount of disruption, allow time to meet constraints and preferences for other targets, and optimize the chances that all the observing requirements for the TOO can be met.

Chapter 3

Offset Pointing, Visibility, and other Constraints

3.1 Introduction

This chapter gathers together several topics pertaining to observation planning, irrespective of focal-plane instrument and grating configuration, to serve as additional guidelines for preparing proposals. Most of these topics are automatically addressed by the observation visualizer software. The intention here is to familiarize the user with these issues.

3.2 Offset Pointing

The offset pointing convention for *Chandra* is that a negative offset of a coordinate moves the image to more positive values of the coordinate and vice-versa. Examples of offset pointings of the ACIS instrument are shown in Figure 3.1. Examples using the HRC are shown in Figure 3.2.

3.3 Visibility

There are a number of factors that limit the precise time when observations can be performed.

3.3.1 Radiation Belt Passages

High particle-radiation levels are encountered as the Observatory approaches perigee. Data acquisition ceases whenever certain particle-radiation thresholds are exceeded. A working number for the altitude at which this takes place is about 60,000 km. Cessation
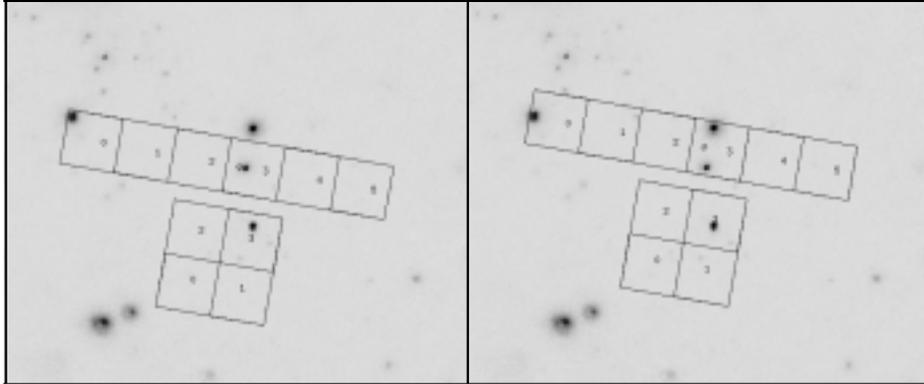
Figure 3.1: Examples of offset pointing with ACIS. North is up and East is to the left. Roll is measured positive, West of North. The roll angle shown is 10°. Left Panel: The target, a bright x-ray source, is offset from the ACIS-S nominal aimpoint with (Y,Z) offset of (-1,0) arcmin. In the Right Panel the offset is (-1,-3). Note the small circle at the location of the ACIS-S aimpoint.

of observations and protection of the instruments in regions of high radiation results in approximately 25% of the 63.5 hour *Chandra* orbit being unusable.

3.3.2   Avoidances

1. Sun avoidance – cannot be overridden – viewing is restricted to angles larger than 47 degrees from the limb of the Sun. This restriction makes about 15% of the sky inaccessible on any given date, but no part of the sky is ever inaccessible for more than 3 months.

2. Moon avoidance – viewing is restricted to angles larger than 6 degrees from the limb of the Moon. This restriction makes less than 1% of the sky inaccessible at any time. This avoidance can be waived, but at the price of a reduced-accuracy aspect solution (see Chapter 5).

3. Bright Earth avoidance – viewing is restricted to angles larger than 20 degrees from the limb of the bright Earth. This restriction makes less than 10% of the sky inaccessible at any time, but there are certain regions which can only be viewed, continuously, for up to about 30 ks. The avoidance can be waived, but at the price of a reduced-accuracy aspect solution (see Chapter 5).

The combination of these avoidances implies that 80 to 85% of the sky is accessible for viewing at any time. The exact value depends on the relative positions of the Sun, Earth,
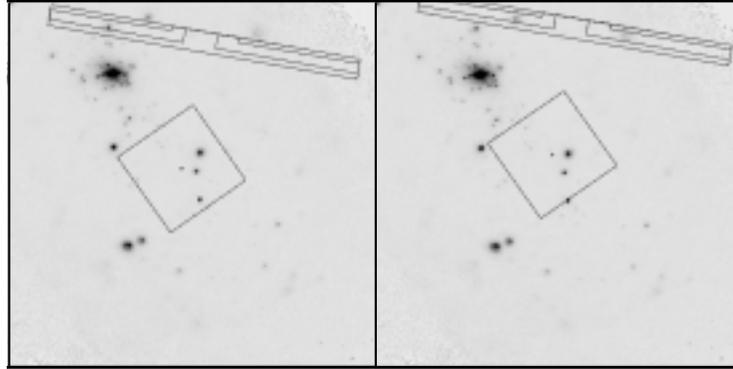
Figure 3.2: Example of offset pointing with HRC. North is up and East is to the left. Roll is measured positive, West of North. The roll angle shown is 10°. Left Panel: The target, the middle source in a group of three aligned N-S, is offset from the HRC-I nominal aimpoint with (Y,Z) offset of (-5,0) arcmin. Right Panel: The offset is (-5,-5). Note the small dot at the location of the HRC-I aimpoint.

and Moon as seen from *Chandra*.

Figure 3.3 illustrates the point that the Earth avoidance region is nearly stationary in equatorial coordinates. This is a consequence of the high orbit and exacerbated by radiation belt passages: For the *Chandra* orbit, the region near RA$\sim 90°$, DEC$\sim -30°$ lies within the earth avoidance zone and continuous observations in this region are limited to < 30 ks duration. This partially blocked region moves several degrees per year, reflecting the evolution of the orbital elements.

3.3.3   Roll Angles

The spacecraft and instruments were designed to take advantage of the Observatory having a hot and a cold side. Thus, the spacecraft is preferentially oriented with the Sun on the $-Z$ side of the $X - Y$ plane, where $+X$ is in the viewing direction, the Y-axis is parallel to the solar panel axes, and $+Z$ is in the direction of the ACIS radiator (see Figure 1.1). In this orientation there is only one "roll angle" (rotation about the viewing- or X-axis - positive West of North) for which the solar panels can be rotated so that they are directly viewing the sun - the nominal roll angle. Small deviations ($\sim$degrees) from the nominal roll angle are allowed which depend on the efficiency of the solar panel and the "beta angle" - the angle between the target and the sun. The roll-angle constraint imposes further visibility restrictions. These can also be evaluated with the *ObsVis* tool (see Chapter 11).
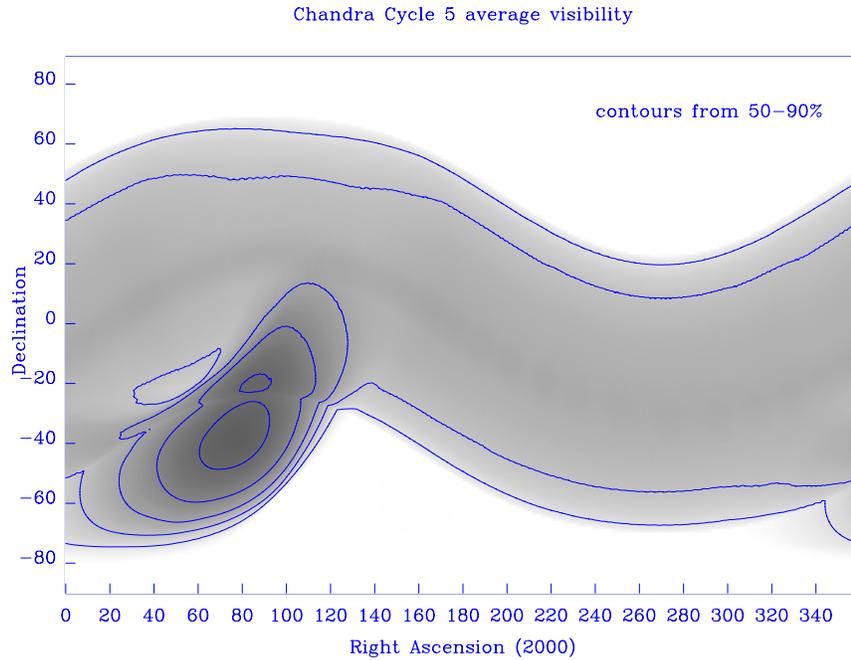
Figure 3.3: The *Chandra* visibility showing contours of fractional visibility averaged over the 12-month interval of Cycle 5. The darker the shade of gray, the lower the visibility.

3.4   Constraints and Considerations

The instrument constraints are discussed in the chapters devoted specifically to the instruments. User-imposed constraints are discussed in the instructions for completing the RPS form. We summarize these here.

3.4.1   Instrument Constraints and Considerations

- The HRC has a brightness limit which limits the flux per microchannel plate pore.

- The HRC has a telemetry limit. Exceeding this limit, amongst other consequences, reduces observing efficiency.

- The HRC has linearity limits. Exceeding these limits voids the effective area calibrations.

- The ACIS has a telemetry limit. Exceeding this limit, amongst other consequences, reduces observing efficiency.

- The ACIS is subject to the effects of pulse pileup. Dealing with this effect requires careful planning of the observation.

- The ACIS has a limit for the total amount of allowed flux in a pixel during an observation. The limit only impacts a small number of potential observations, primarily those of very bright sources that request the dither to be turned off. Please see Section 6.17 for details.

3.4.2 User-Imposed Constraints

Chandra users may need to specify a number of observing constraints particular to their observations. In general, the specification of a user-imposed constraint decreases the efficiency of the observatory and therefore should be well justified in the proposal. Note that only a limited number of constrained observations can be accommodated ($\leq$ 20% of the total). User imposed constraints are summarized here.

Time Constraints:

Time Windows – specific time intervals in which observation must be scheduled. Such constraints are primarily for use in coordinated observing campaigns or for arranging an observation to coincide with some time-critical aspect of the target.

Monitoring Intervals – for observing a target at semi-regular intervals for a specified duration.

Phase Interval – specific phase intervals for observing sources with long, regular periods.

Ordering of observations – specifying that a set of observations be carried out in a particular order (with or without a range in allowed delays between the end of the first observations and the beginning of the second, third, etc.).

Continuity of observation – specifying that an observation may not be interrupted (up to 170 ks).

Group Observation – a target which needs to be observed within a particular time range with other targets in the program.

Roll Constraints: – specifying a particular roll angle and tolerance.

Chapter 4

High Resolution Mirror Assembly (HRMA)

4.1 Description and Physical Configuration

The *Chandra* telescope consists of 4 pairs of concentric thin-walled, grazing-incidence Wolter Type-I mirrors. [X-ray optics are reviewed by B. Aschenbach (1985).] The front mirror of each pair is a paraboloid (P_n) and the back a hyperboloid (H_n). The eight mirrors were fabricated from Zerodur glass, polished, and coated with iridium on a binding layer of chromium.

The High Resolution Mirror Assembly (HRMA), shown schematically in Figure 4.1, contains the nested mirrors, center, forward and aft aperture plates, baffles, inner and outer cylinders, mounts, pre- and post-collimators, fiducial light transfer components, mirror support sleeves, forward and aft contamination covers, flux contamination monitors, and thermal control hardware. The outer mirror pair is number 1, and, progressing inwards, 3, 4, and 6. (The original design had six mirror pairs; numbers 2 and 5 were eliminated.) The pair diameters range from about 0.65 to 1.23 meters. The distance from the center of the Central Aperture Plate (CAP) separating the paraboloid and hyperboloid mirrors to the Gaussian focal point is 10.0548 meters, with each mirror pair varying slightly about this value. (Note that this distance is close to, but not exactly, the focal length.) Some other characteristics are given in Table 4.1 and in section 4.5

Table 4.1: *Chandra* HRMA Characteristics

HRMA	
Optics	Wolter Type-I
Mirror coatings	Iridium
Nominal coating thickness	330 Å
Mirror outer diameters (1, 3, 4, 6)	1.23, 0.99, 0.87, 0.65 m
Mirror lengths (P_n or H_n)	84 cm
Total length (pre-collimator to post-collimator)	276 cm
Unobscured clear aperture	1145 cm^2
HRMA mass	1484 kg
Focal length	10.070 ± 0.003 m
Plate scale	$48.82 \pm 0.02\,\mu\mathrm{m\,arcsec^{-1}}$
PSF FWHM (with detector)	0.5 arcsec
Effective area:	
@ 0.25 keV	800 cm^2
@ 5.0 keV	400 cm^2
@ 8.0 keV	100 cm^2
Ghost-free field of view	30 arcmin dia
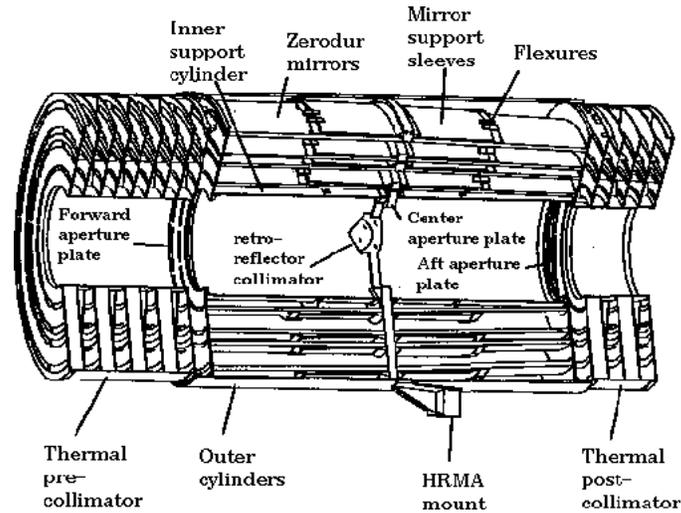
Figure 4.1: The 4 nested HRMA mirror pairs and associated structures.

4.2 Calibration and Performance

4.2.1 Calibration and Model

VanSpeybroeck (1997), Weisskopf (1997), and Zhao et al. (1997), describe the ground calibration of the HRMA and present some preliminary results. During these tests, the mirror assembly was mounted horizontally in a vacuum chamber and irradiated with X-rays from a source located at a distance of approximately 500 meters. The data taken in the XRCF (the X-Ray Calibration Facility at *MSFC*) include the effective areas and image distributions as a function of incident energy and angle. The mirror performance during these tests differs from that expected in space because of gravity distortions and the finite source size and distance; consequently, the calibration data cannot be directly compared to flight observations. The approach taken was to develop a model based upon surface and assembly measurements taken before the X-ray calibration activity. The X-ray calibration data then were used to validate this model and to make minor adjustments in model parameters to achieve satisfactory agreement with the observations. Further minor modifications were made as a result of flight experience.

The HRMA characteristics illustrated in this chapter were generated by a ray-trace program using this model. Note that this chapter typically gives characteristics of the HRMA only; unless otherwise indicated, blurring caused by the detector and the aspect solution is *not* included. These effects are *very* important for on-axis sources, and are included in the instrument chapters (Chapters 6 and 7). See also section 4.4.

4.2.2 HARM Effective Area

The unobscured geometric clear aperture of the HRMA is 1145 cm^2. The obstruction of the HRMA clear aperture by supporting struts is less than 10%. Since reflectivity depends on energy as well as grazing angle, the HRMA throughput varies with X-ray energy.

Figure 4.2 shows the HRMA effective area as a function of X-ray energy, in linear scale, as well as the HRMA/ACIS and HRMA/HRC effective areas. Figure 4.3 shows the same curves with log-log scale.

Figure 4.4 shows the effects of off-axis vignetting on the effective area for various energies; the plotted results are averages over the azimuthal angle.

The above predictions are based upon the mirror model discussed previously and scaled by the HRMA ground calibration data. The agreement between the effective area predicted for the ground calibration using this model and the actual measurement, as well as the scaling function used for the on-orbit prediction, are shown in Figure 4.5.
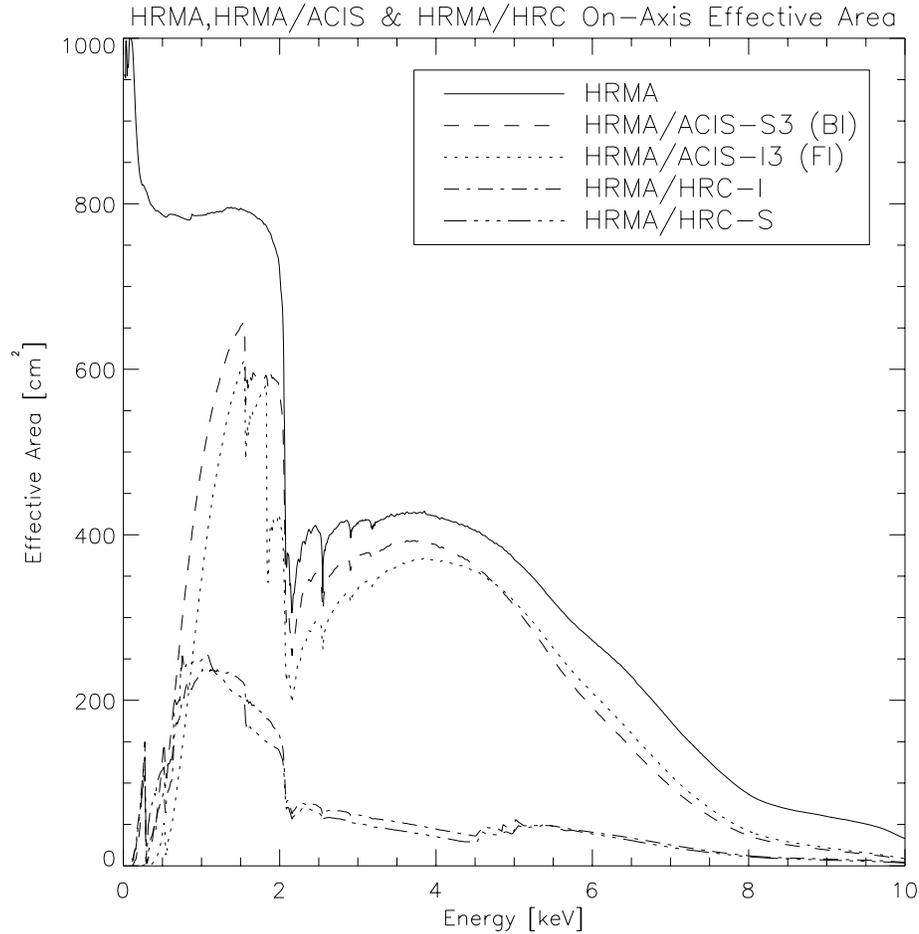
Figure 4.2: The HRMA HRMA/ACIS and HRMA/HRC effective areas versus X-ray energy in linear scale. The structure near 2 keV is due to the iridium M-edge. The HRMA effective area is calculated by the raytrace simulation based on the HRMA model and scaled by the XRCF calibration data. The HRMA/ACIS effective areas are the products of HRMA effective area and the Quantum Efficiency (QE) of ACIS-I3 (front illuminated) or ACIS-S3 (back illuminated). The HRMA/HRC effective areas are the products of HRMA effective area and the QE of HRC-I or HRC-S at their aimpoints, including the effect of UV/Ion Shields (UVIS).
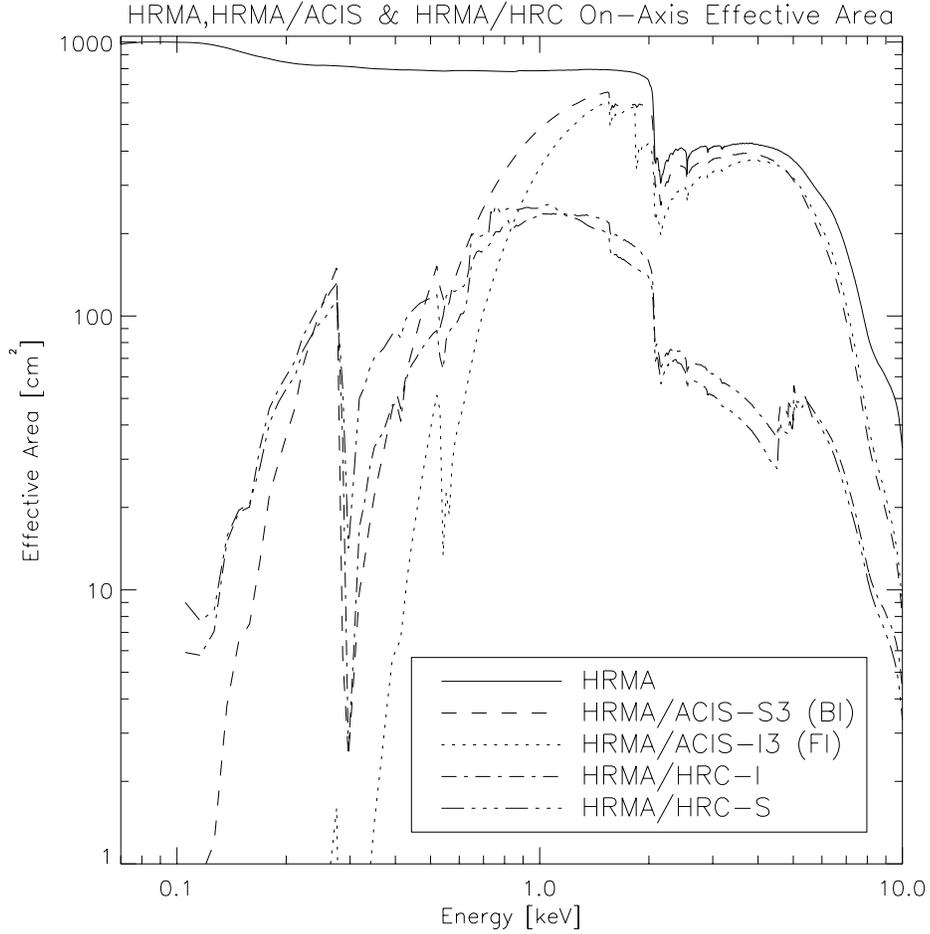
Figure 4.3: The HRMA HRMA/ACIS and HRMA/HRC effective areas versus X-ray energy in log-log scale. The structure near 2 keV is due to the iridium M-edge. The HRMA effective area is calculated by the raytrace simulation based on the HRMA model and scaled by the XRCF calibration data. The HRMA/ACIS effective areas are the products of HRMA effective area and the Quantum Efficiency (QE) of ACIS-I3 (front illuminated) or ACIS-S3 (back illuminated). The HRMA/HRC effective areas are the products of HRMA effective area and the QE of HRC-I or HRC-S at their aimpoints, including the effect of UV/Ion Shields (UVIS).
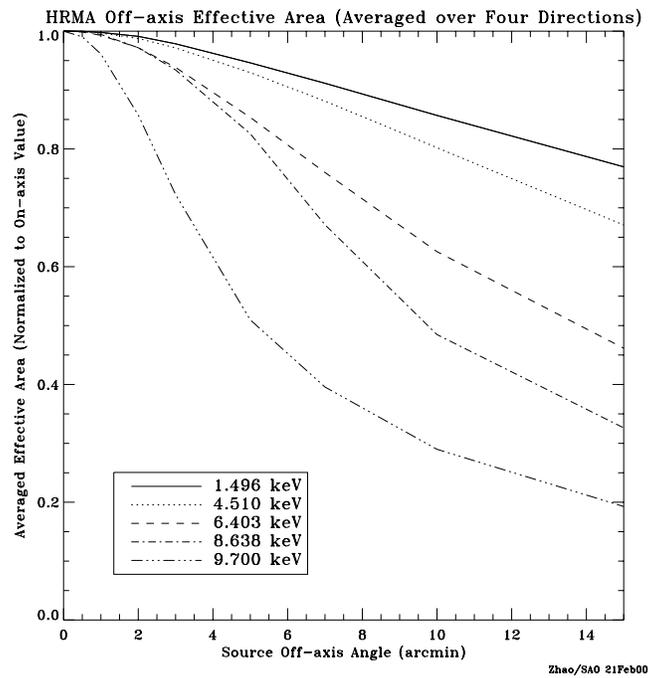
Figure 4.4: The HRMA effective area versus off-axis angle, averaged over azimuth, for selected energies, normalized to the on-axis area for that energy.
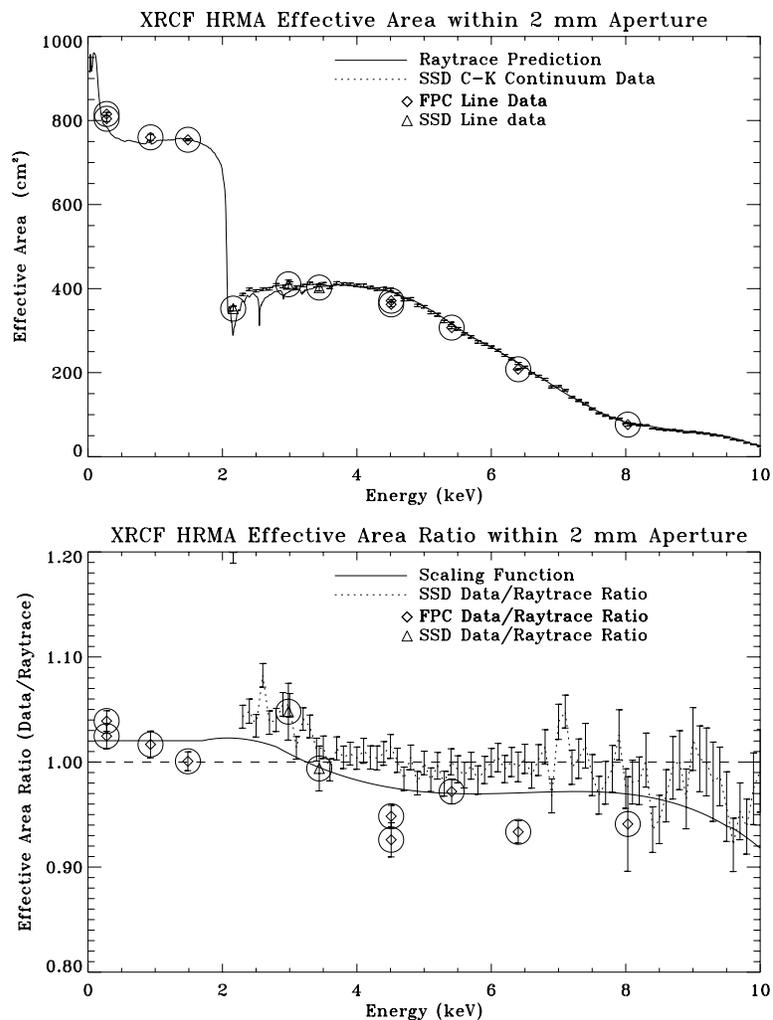
Figure 4.5: The HRMA effective area measured at the XRCF. In the upper panel: the solid line is the raytrace simulation of the HRMA effective area within a 2 mm diameter aperture at the focus; the dashed line with error bars shows data taken with a solid state detector (SSD) with a C-K continuum source; the diamonds and triangles show data taken with a flow proportional counter (FPC) and SSD data with spectral line sources. The lower panel shows deviation of data from the raytrace: the dashed line with error bars is the ratio of SSD C-K continuum data vs. the raytrace; the diamonds and triangles show the ratio of FPC and SSD spectral line data vs. the raytrace; the solid line is a polynomial function, which gives equal weight to the deviations of the continuum and line measurements, for scaling the raytrace simulation to provide the predicted HRMA effective area.

Table 4.2: HRMA Encircled Energy Performance

X-ray:		Encircled Energy Fraction	
E	λ	Diameter	
kev	Å	$1''$	$10''$
0.1085	114.2712	0.7954	0.9979
0.1833	67.6401	0.7937	0.9955
0.2770	44.7597	0.7906	0.9929
0.5230	23.7064	0.7817	0.9871
0.9297	13.3359	0.7650	0.9780
1.4967	8.2838	0.7436	0.9739
2.0424	6.0706	0.7261	0.9674
2.9843	4.1545	0.6960	0.9560
3.4440	3.6000	0.6808	0.9479
4.5108	2.7486	0.6510	0.9319
5.4147	2.2898	0.6426	0.9300
6.4038	1.9361	0.6365	0.9344
8.0478	1.5406	0.5457	0.9185
8.6389	1.4352	0.5256	0.9151
10.0000	1.2398	0.4971	0.8954

4.2.3   Point-Spread-Function and Encircled Energy Fraction

The *Chandra* HRMA point-spread function (*PSF*) has been simulated with numerical ray-trace calculations based upon the model previously discussed. A most useful parameter is the encircled energy fraction (the two-dimensional integral of the *PSF*) as a function of radius from the image center. The *PSF* and the encircled energy fraction for a given radius depend upon off-axis angle and energy.The HRMA optical axis is defined for practical purposes, and calibrated in flight, as the direction of the narrowest *PSF*. The *PSF* broadens, and the encircled energy fraction decreases, as the off-axis angle increases because of mirror aberrations. The performance also degrades as the X-ray energy increases because of larger X-ray scattering.

On-axis Response

Figure 4.6 shows the encircled energy fraction as a function of image radius for on-axis rays and for different energies. The resulting increase in image size with energy is apparent. The fraction contained within one and ten arc seconds diameters for on-axis rays is shown as a function of energy in Figure 4.7 and in Table 4.2.
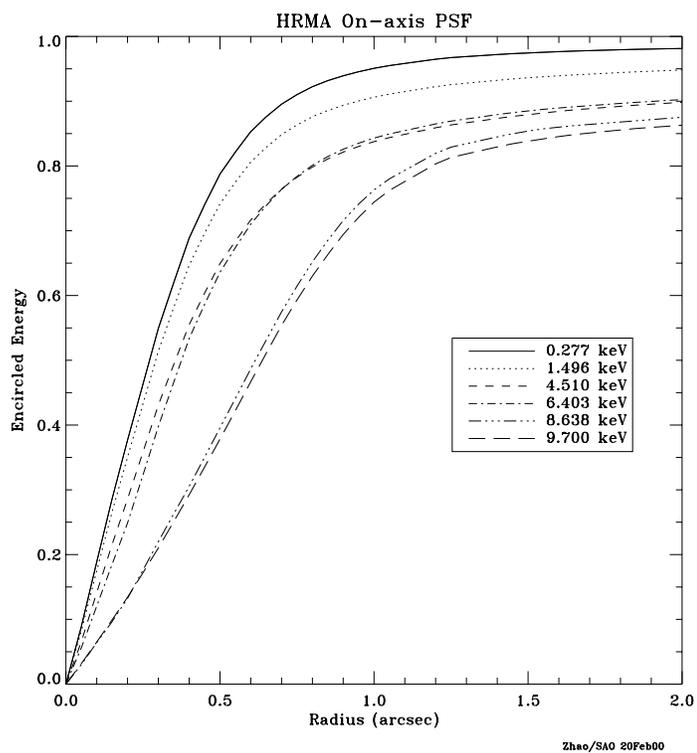
Figure 4.6: The fractional encircled energy as a function of angular radius calculated for an on-axis point-source, at selected X-ray energies. The curves are the combined response of the four nested mirror pairs.
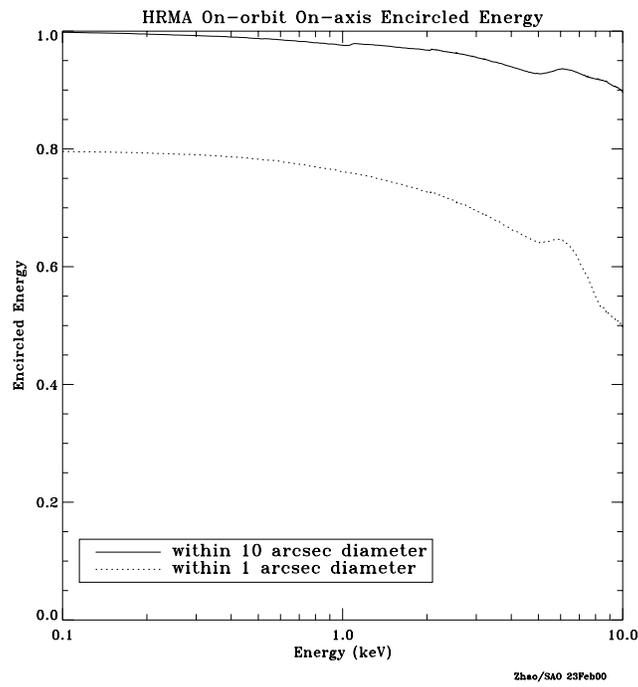
Figure 4.7: On-orbit performance prediction for encircled energy, calculated from model derived from ground-based calibration data.

Pre-flight measurements and also images taken at the XRCF show that there is a slight ($\approx 500\mu$m) offset between the optical axes of the paraboloids and hyperboloids, and that pair 6 is slightly tilted with respect to the other three. Consequently, the image from mirror pair 6 is not as symmetrical as the images from the other shells. The effect of this asymmetry on images depends on energy because of the different relative contribution of mirror pair 6.

Figure 4.8 shows simulated HRMA/HRC-I images at four energies. The effect of the mirror pair 6 alignment errors can be seen in the 8.6 keV image; note that the core of this image is not centered in the distribution. This $0.2''$ effect is not important compared to other sources of image degradation encountered in flight such as uncertainties in the aspect solution.

Off-axis Response

The *PSF* broadens for off-axis sources, and there is considerable distortion in the image even for a perfect mirror set. This distortion is due to the aberrations of Wolter type I optics and to the different focal surfaces for the four mirror pairs. The increase in image size with off-axis angle is greatest for the inner shell, and hence is larger for higher X-ray energies.

Figure 4.9 shows the dependence of encircled energy radii on off-axis angle on the HRC-I with the HRMA focus at the HRC-I aimpoint. Because the HRC-I is axially symmetric with respect to the HRMA optical axis, the off-axis encircled energy radii are almost azimuthally symmetric, except some small asymmetry due to the imperfect HRMA as mentioned above. The figure gives the averaged radii for 1.49 keV and 6.40 keV at 50% and 90% encircled energy. The blurs due to the HRC-I spatial resolution and the *Chandra* aspect error (FWHM: $0.22''$) are included.

The ACIS-I surface is not axially symmetric with respect to the HRMA optical axis, because the HRMA aimpoint is located at the inner corner of one of the four ACIS-I chips – I3. Thus the off-axis encircled energy radii are not azimuthally symmetric. Figure 4.10 shows the dependence of encircled energy radii on off-axis angle on the four ACIS-I chips. The figure gives the encircled energy radii for 1.49 keV and 6.40 keV at 50% and 90% encircled energy in four azimuthal directions – from the aimpoint to the outer corners of the four ACIS-I chips. The blurs due to the ACIS-I spatial resolution and the *Chandra* aspect error are included.

Figure 4.11 contains simulated HRMA images of point sources $5'$ and $10'$ off-axis, on the flat HRC-I surface, with and without the HRC-I detector effects. At $10'$ off-axis the separation between the flat detector surface and the curved focal surface is significant. Cusps in the HRMA images are due to a slight misalignment of the parabolic and hyperbolic mirrors.
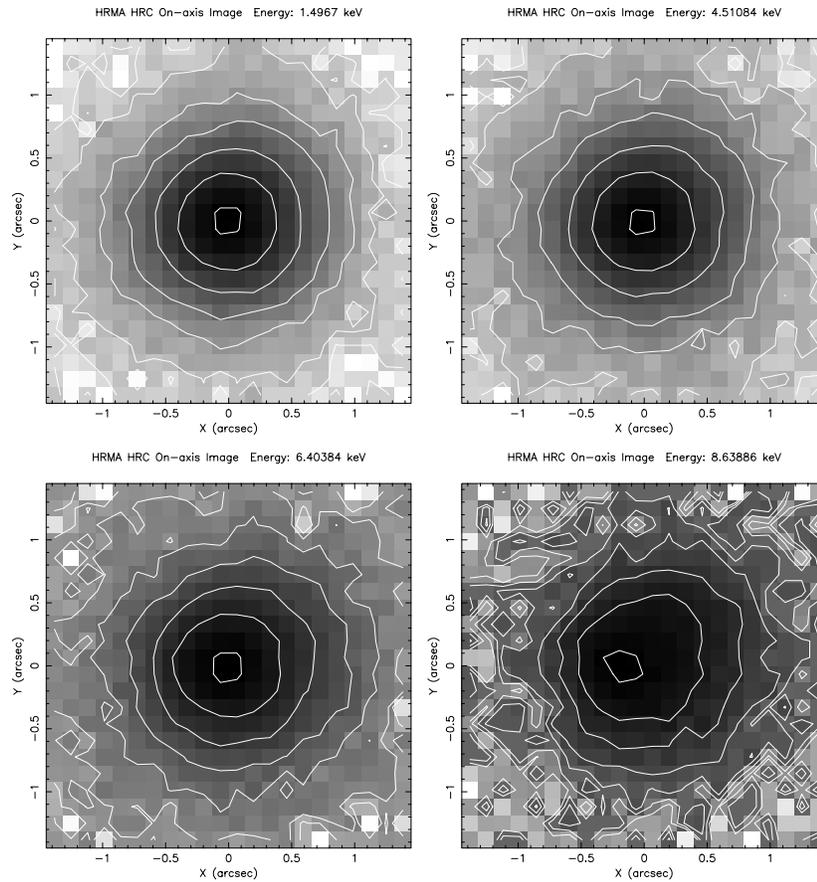
Figure 4.8: Simulated on-axis HRMA/HRC-I on-axis images of mono-energetic point sources without aspect blurring. Energies (reading like a book) are 1.49, 4.51, 6.40, and 8.63 keV. Surface brightness contours are logarithmic and spaced in factors of 3. The innermost contour is at 90% of the peak brightness. The 8.6 keV image core is off-center due to the shell 6 misalignment. Each panel is 3″ square.
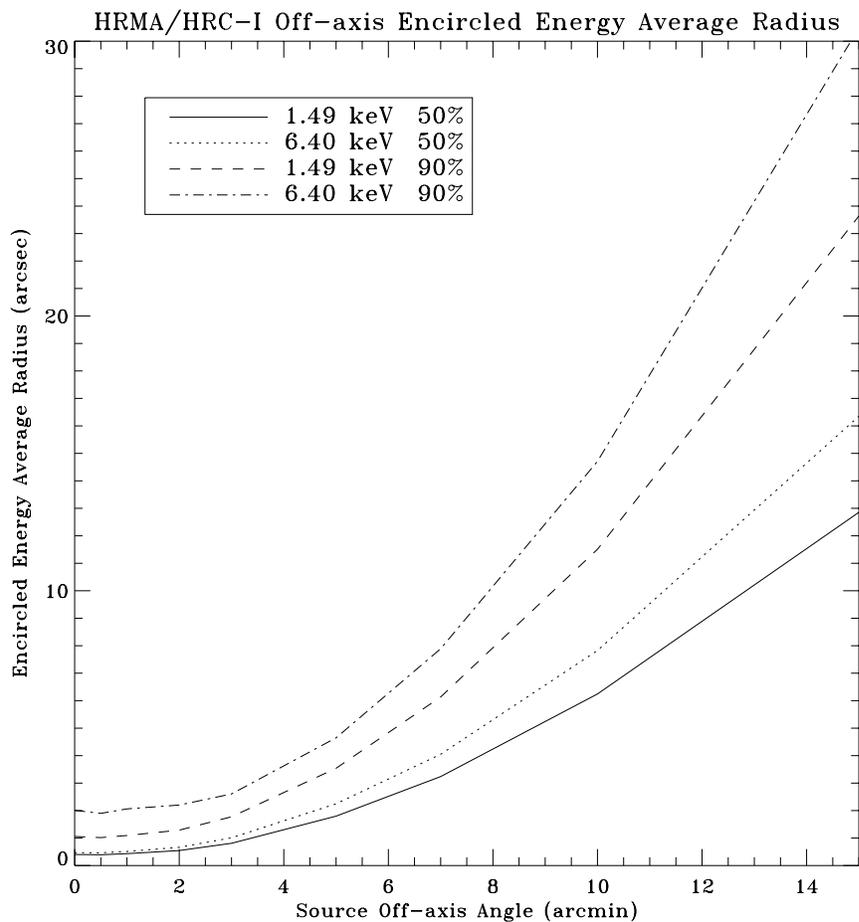
Figure 4.9: HRMA/HRC-I encircled energy average radii for circles enclosing 50% and 90% of the power at 1.49 and 6.40 keV as a function of off-axis angle. The HRC-I surface is a flat plane perpendicular to the optical axis, which does not follow the curved *Chandra* focal plane. These curves include the blurs due to the HRC-I spatial resolution and the *Chandra* aspect error.

HRMA/ACIS−I Off−axis Encircled Energy Radius
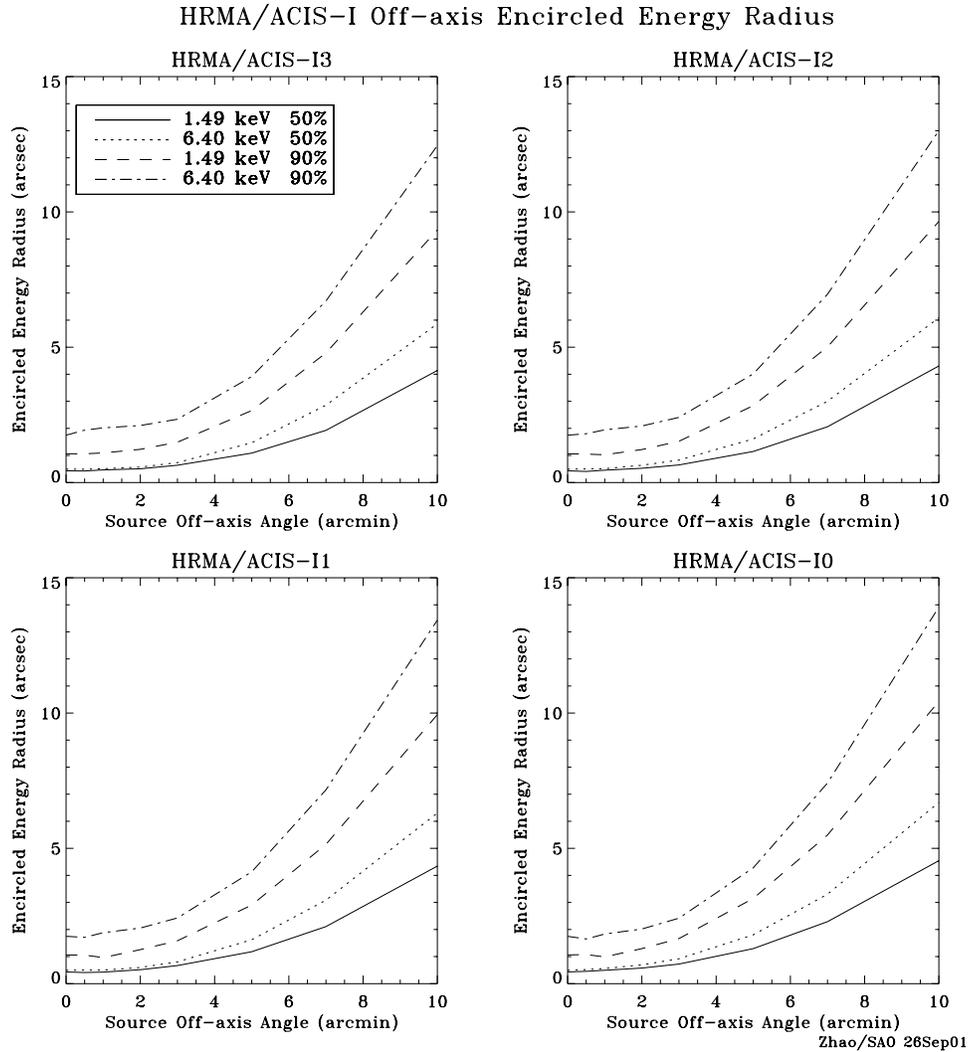
Figure 4.10: HRMA/ACIS-I encircled energy radii for circles enclosing 50% and 90% of the power at 1.49 and 6.40 keV as a function of off-axis angle. The ACIS-I surface is composed by four tilted flat chips which approximate the curved *Chandra* focal plane. The HRMA optical axis passes near the aimpoint which is located at the inner corner of chip I3. Thus the off-axis encircled energy radii are not azimuthally symmetric. The four panels show these radii's radial dpendence in four azimuthal directions – from the aimpoint to the outer corners of the four ACIS-I chips. These curves include the blurs due to the ACIS-I spatial resolution and the *Chandra* aspect error.
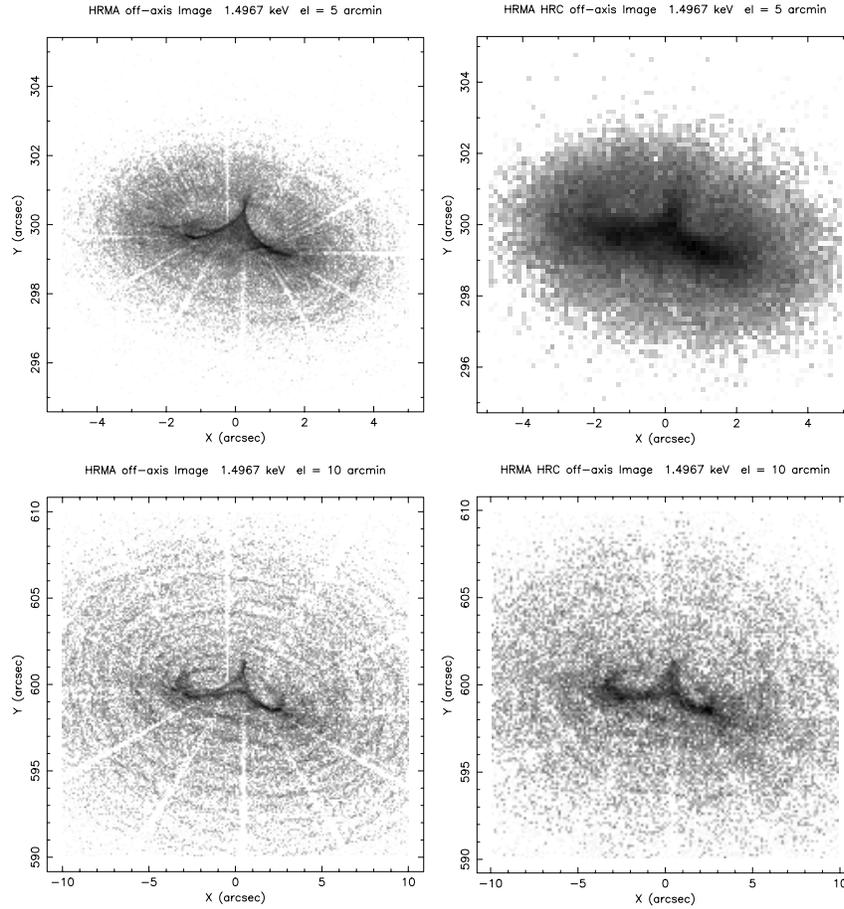
Figure 4.11: Simulated 1.49 keV images, for the HRMA only (at left, the pure mirror effects) and the HRMA/HRC-I combination (at right, mirror effects plus the HRC-I blur and pixelization), of a point source 5′ (at top) and 10′ (at bottom) off-axis. Panels are 11″ and 22″ square for 5′ and 10′ off-axis, respectively, much larger than the panels in figure 4.8. Spokes in the images are due to shadowing by mirror support struts. Cusps in the HRMA images are due to a slight misalignment of the parabolic and hyperbolic mirrors.

4.2.4   Effective Area in Flight

There was a concern that the effective areas might change between ground calibration and flight due to accumulation of contaminants or degradation of the reflecting surfaces. A Flux Contamination Monitor (FCM) was added to evaluate these effects. The FCM consisted of radioactive sources embedded in the forward contamination cover. The ACIS response to these sources was measured in the XRCF at the end of ground calibration, and again in orbit before the forward contamination cover was removed. No change in performance was detected.

The FCM is described in Elsner et al., 1998. The *Chandra* detectors are not exposed to the FCM now that the forward contamination cover has been opened.

4.3   Ghost Images

Baffles prevent non-reflected or singly reflected rays from impinging on the focal plane within the central $30'$ diameter of the field of view. Outside of this region, however, singly reflected rays from strong off-axis sources may appear. Figure 4.12 shows a simulated ghost image in which the off-axis angle was chosen to give the closest approach of singly-reflected rays to the focal point. In this situation, the outermost ray could extend into the HRC field of view. The area extending from the optical axis to a diameter of about $30'$ is free from ghost images.

4.4   Effects of Aspect and Instrument Uncertainties

The HRMA performance discussed in the previous sections will be slightly degraded by uncertainties in the aspect solution and the details of the imaging detector spatial response function. The ground software system also deliberately adds a small random position error to reduce image artifacts which result from instrument and data system integer location values (these can be removed if desired.) These effects are illustrated for the HRC-I and HRC-S instruments in Figures 4.13 and 4.14 respectively. These figures also show the fractional encircled energy as a function of radius actually observed in flight compared to model calculations at 0.277 and 6.403 keV. A aspect error of $0.22''$ (FWHM) was included in the model calculations. The agreement between the observations and the lower energy model predicted curve is quite good. The HRC efficiency and typical spectral photon number densities both decrease with energy, so the higher energy response curve would not be expected for most sources.

Similar calculations have been performed for the ACIS-S(S-3) over a wider range of energies; the results are shown in Figure 4.15. The simulation accounted for the typical spacecraft jitter, so the location of the instrument pixel boundaries has little effect. There

HRMA Off−axis Image & Ghost Rays   1.4967 keV
Source: Azimuth = 0 arcmin   Elevation = 53 arcmin
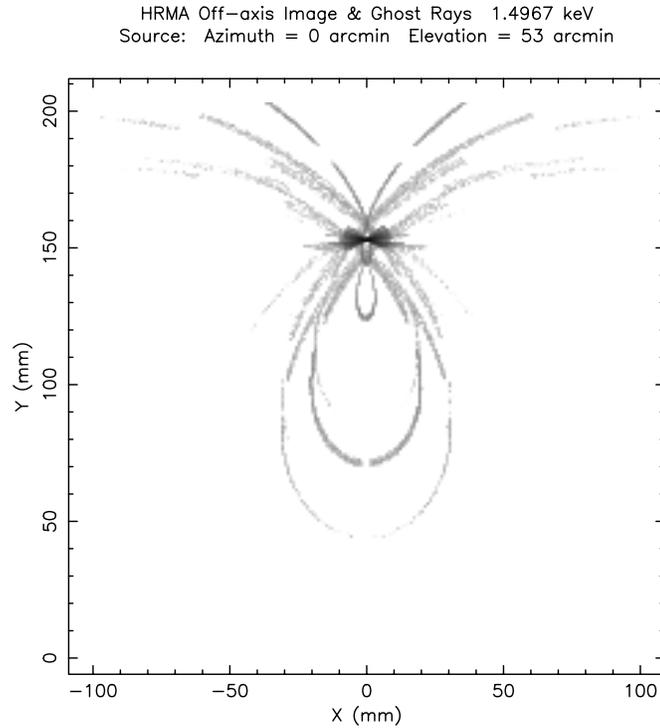
Figure 4.12: Calculated image of a source on the HRC-I at 53′ off-axis. The aimpoint is at position (0,0) at bottom center of the figure. The horizontally elongated bright region at (0,150) is the image produced by doubly reflected rays. The other curved lines in the figure are due to single reflections from different mirror segments. These lines comprise the "ghost image". If the HRC-I detector were centered on (0,0) with diagonal vertical, the upper corner of the field would be at (0,64). As this figure shows the ghost ray can be as close as (0,44) which is within the HRC-I field of view.
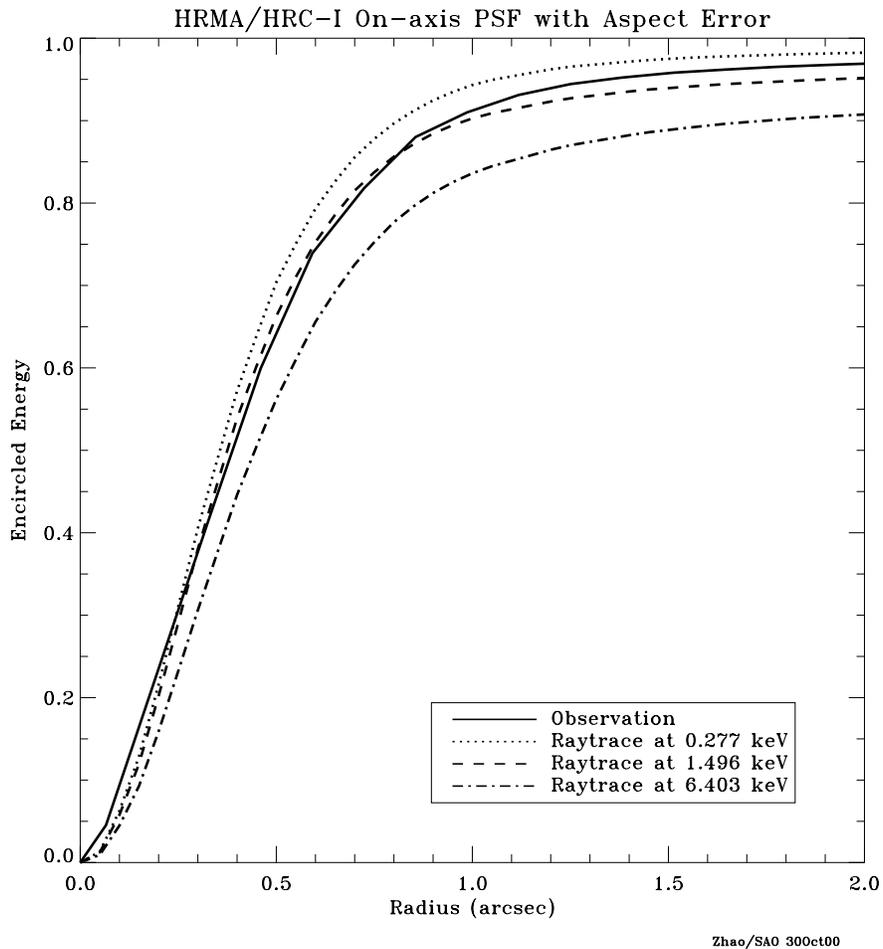
Figure 4.13: The fractional encircled energy as a function of angular radius observed in flight compared to model calculations for an on-axis point-source at selected X-ray energies. The curves are the combined response of the four nested mirror pairs, typical aspect uncertainties, and the HRC-I response function.
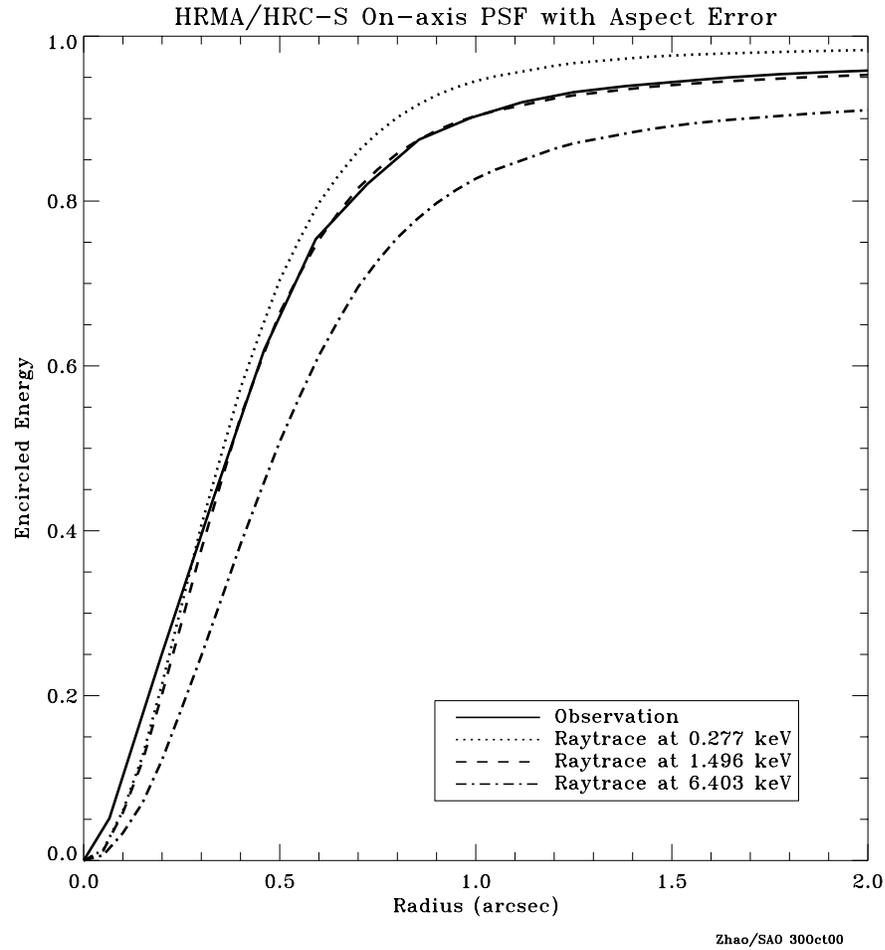
Figure 4.14: The fractional encircled energy as a function of angular radius observed in flight compared to model calculations for an on-axis point-source at selected X-ray energies. The curves are the combined response of the four nested mirror pairs, typical aspect uncertainties, and the HRC-S response function.

is, however, a small effect of the location of the source compared to the data system pixel boundaries. These particular calculations were performed for a point source centered on the boundary between two data system pixels. The ACIS-I instrument response is similar.

The curves of this section, Figures 4.13, 4.14, and 4.15 may be compared with Figure 4.6 to estimate the image performance degradation due to non-HRMA effects.

4.5 HRMA background material

4.5.1 Heritage

The *Chandra* mirrors represent a logical progression from those of the *EINSTEIN* (HEAO-2) (Giacconi et al. 1979) and *Rosat* (Trümper 1983; Aschenbach 1991) missions. Each of these previous X-ray observatories utilized nested Wolter Type-I optics with about 4 arcsec angular resolution. The *EINSTEIN* mirror assembly had considerably less geometric area than *Chandra*, while *Rosat* had comparable area ($1100 \, \mathrm{cm}^2$) at low energies ($< 1 \, \mathrm{keV}$).

The Validation Engineering Test Article-I (VETA-I) was constructed to verify the technology required for the spatial resolution of *Chandra*. VETA-I contained the $P_1 H_1$ proto-flight mirror shells constructed to final tolerances, but uncoated and with ends uncut. The VETA-I tests included the image full-width-half-maximum, encircled energy, effective area, and ring focus properties (for azimuthal and low spatial-frequency figure). Many of the results of these tests appear in SPIE Proceedings 1742, e.g. Hughes et al. 1992. Zhao et al. 1993, give a good overview of the VETA tests. A series of papers in SPIE Proceedings 3113, e.g. Zhao et al. 1997, report on the XRCF calibration of the HRMA assembly.

4.5.2 Exit cone angles

An annular on-axis beam enters each mirror pair, is reflected from paraboloids and hyperboloids and exits to converge to a focus. The angle θ between the direction of the reflected ray and the optical axis lies between two angles θ_c and θ_d; these limits are listed in Table 4.3.

4.5.3 Sub-assembly Calibration

Extensive measurements of the mirror shapes and of the surface characteristics were made at Hughes-Danbury Optical Systems (HDOS) during fabrication of the mirror segments and during assembly at Eastman-Kodak Co. HRMA throughput depends critically on the coating of the individual mirror elements carried out at Optical Coating Laboratory, Santa Rosa, California. Mirror flats were present in the coating chamber and coated with iridium at the same time as the HRMA mirror elements. Reflectivity of X-rays from these
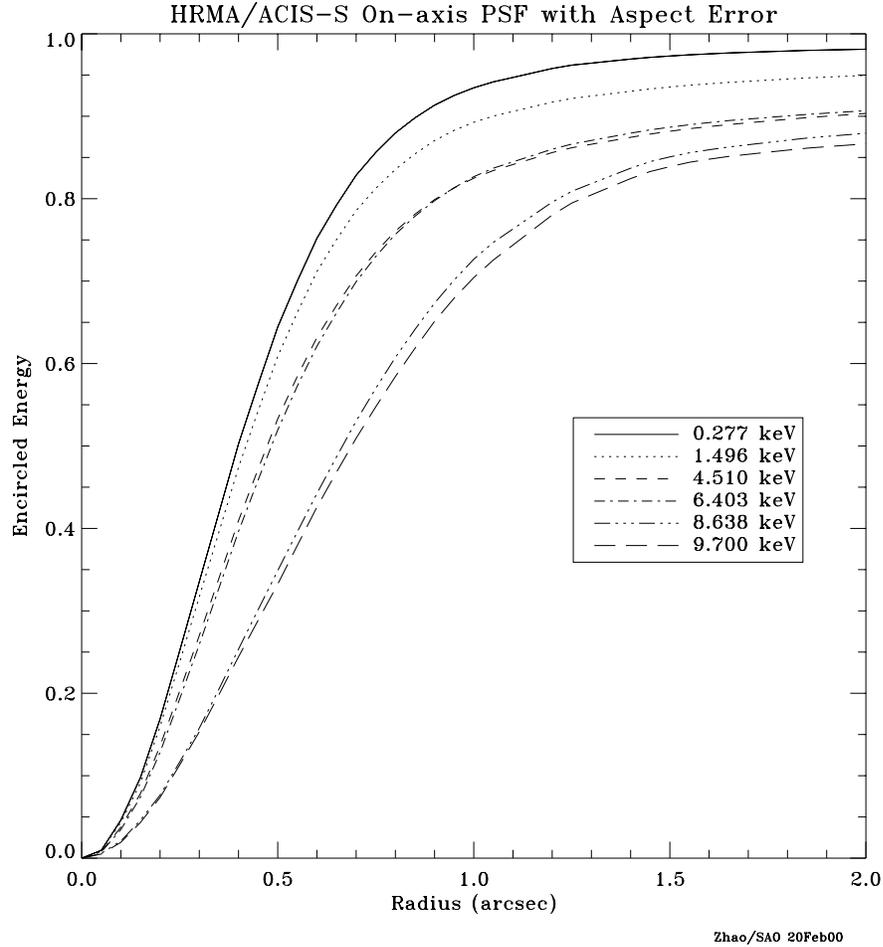
Figure 4.15: The fractional encircled energy as a function of angular radius expected for in flight ACIS-S(S3) measurements for an on-axis point-source at selected X-ray energies. The curves are the combined response of the four nested mirror pairs, typical aspect uncertainties, and the ACIS response function.

Table 4.3: Exit cone angles for each hyperboloid.

| Hyperboloid | θ_c | | θ_d | |
Mirror	[rad]	[deg]	[rad]	[deg]
1	0.05961	3.42	0.06115	3.50
3	0.04795	2.75	0.04923	2.82
4	0.04223	2.42	0.04237	2.49
6	0.03144	1.80	0.03232	1.90

witness flats was measured, and some results have been described in the 1997 July/Aug SPIE meeting proceedings.

4.5.4   Operating Environment

Insulation and heaters maintain the HRMA temperature at 70° Fahrenheit on-orbit to minimize changes from the assembly and alignment environments.

4.6   References

Aschenbach, B., 1985, Rep. Prog. Phys, 48, 579.

Aschenbach, B., 1991, Rev. Mod. Astron. 4, 173.

Edgar, R.J. , 1997, SPIE Proceedings, 3113, 124.

Elsner, R.F, et al., 1998, SPIE Proceedings, 3444, 177.

Gaetz, T.J., et al., 1997, SPIE Proceedings, 3113, 77.

Gaetz, T.J., et al., 2000, Orbital verification of the CXO high resolution mirror assembly alignment and vignetting, SPIE Proceedings, 4012, 41.

Giacconi, R., et al., 1979, Ap.J. 230, 540.

Graessle, D. E., et al., 1998, SPIE Proceedings, 3444, 140.

Henke, B.L., et. al., 1993, Atomic Data and Nuclear Data Tables 54, 181.

Hughes, J.P., et al., 1992, SPIE Proceedings, 1742, 152.

Jerius, D., et al., 2000, Orbital measurement and verification of the Chandra X–ray Observatory's PSF, SPIE Proceedings, 4012, 17.

Kolodziejczak, J.J., et al., 1997, SPIE Proceedings, 3113, 65.

O'Dell, S.L. and Weisskopf, M.C., 1998, SPIE Proceedings, 3444, 2.

Olds, C.R. and Reese, R.P., 1998, SPIE Proceedings, 3356, 910.

Schwartz, D.A., et al., 2000, Absolute effective area of the Chandra high-resolution mirror assembly, SPIE Proceedings, 4012, 28.

Trümper, J., 1983, Adv. Space Res. 2(4), 241.

Van Speybroeck, L., et al., 1997, SPIE Proceedings, 3113, 89.

Weisskopf, M.C. and O'DELL, S.L., 1997, SPIE Proceedings, 3113, 2.

Weisskopf, M.C., et al., 2000, Chandra X-Ray Observatory (CXO): overview., SPIE Proceedings, 4012, 2.

Zhao, P. and Van Speybroeck, L., et al., 1995, SPIE Proceedings, 2515, 391.

Zhao, P., et al., 1993, SPIE Proceedings, 2011, 59.

Zhao, P., et al., 1997, SPIE Proceedings, 3113, 106.

Zhao, P., et al., 1998, SPIE Proceedings, 3444, 234.

Postscript copies of various aspects of the HRMA calibration can be obtained from the *CXC* HRMA Calibration Group:

http://hea-www.harvard.edu/MST/simul/xrcf/report/index.html

Further information can be obtained from the MSFC *Chandra* calibration page http://wwwastro.msfc.nasa.gov/xray/xraycal/

Chapter 5

Pointing Control and Aspect Determination System

5.1   Introduction

The total system of sensors and control hardware that is used to point the observatory, maintain the stability, and provide data for determining where the observatory had been pointing is called the Pointing Control and Aspect Determination (PCAD) system. Unlike the Hubble Space Telescope, *Chandra* pointing requirements are much less stringent. This is because *Chandra* detectors are essentially single-photon counters and as long as one knows where the spacecraft was pointing when each photon was detected, it is possible to determine the celestial location. The mapping of photon positions from detector to relative and absolute positions on the sky is often referred to as "image reconstruction".

   In this chapter we briefly discuss the hardware that comprises the PCAD system, how it is used, and the in-flight performance. Further information can be found on the Aspect Information web page within the main *CXC* Science web site (http://cxc.harvard.edu/cal/ASPECT).

5.2   Physical configuration

The main components of the PCAD system are:

Aspect camera assembly (ACA) – 11.2 cm optical telescope, stray light shade, two CCD detectors (primary and redundant), and two sets of electronics

Inertial reference units (IRU) – Two IRUs, each containing two 2-axis gyroscopes.

Fiducial light assemblies (FLA) – LEDs mounted near each science instrument (SI) detector which are imaged in the ACA via the FTS

Fiducial transfer system (FTS) – The FTS directs light from the fid lights to the ACA, via the retroreflector collimator (RRC) mounted at the HRMA center, and a periscope

Coarse sun sensor (CSS) – All-sky coverage of the sun

Fine sun sensor (FSS) – 50 degree FOV and 0.02 degree accuracy

Earth sensor assembly (ESA) – Conical scanning sensor, used during the orbital insertion phase of the mission

Reaction wheel assembly (RWA) – 6 momentum wheels which change spacecraft attitude

Momentum unloading propulsion system (MUPS) – Liquid fuel thrusters which allow RWA momentum unloading

Reaction control system (RCS) – Thrusters which change spacecraft attitude

Since data from the CSS, FSS, and ESA are not normally used in the processing of science observations these are not discussed. However, in the unlikely event of a complete failure of the ACA, we would attempt to use CSS and FSS data.

5.2.1   ACA

The aspect camera assembly (Figure 5.1) includes a sunshade ($\sim$2.5 m long, $\sim$55 cm in diameter), a 11.2 cm, F/9 Ritchey-Chretien optical telescope, and light-sensitive CCD detector(s). This assembly and its related components are mounted on the side of the HRMA. The camera's field of view is 1.4×1.4 deg and the sun-shade is designed to protect the instrument from the light from the Sun, Earth and Moon, with protection angles of 47, 20 and 6 deg, respectively.

The aspect camera focal plane detector is a 1024×1024 Tektronix CCD chip, with 24×24 micron ($5 \times 5''$) pixels, covering the spectral band between 4000 and 9000 Å. The CCD chip is deliberately out of focus (point source FWHM = 9 arcsec) to spread the star images over several pixels in order to increase accuracy of the centering algorithm, and to reduce variation in the point response function over the field of view. There is a spare identical CCD chip, which can be illuminated by activating a rotating mirror.

The ACA electronics tracks a small pixel region (either 4×4, 6×6, or 8×8 pixels) around the fiducial light and star images. There are a total of eight such image slots available for tracking. Typically five guide stars and three fiducial lights (section 5.2.2) are being tracked. The average background level is subtracted on-board, and image centroids are calculated by a weighted-mean algorithm. The image centroids and fluxes are used

ASPECT CAMERA ASSEMBLY
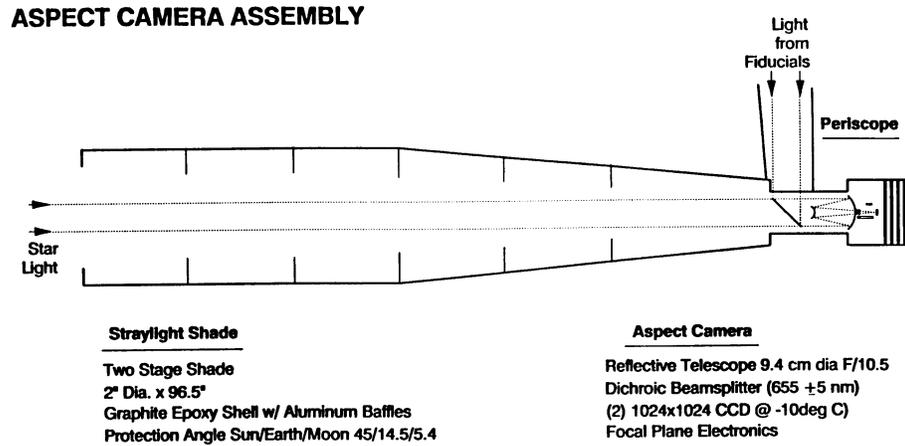
Figure 5.1: Aspect camera assembly

on-board by the PCAD, and are also telemetered to the ground along with the raw pixel data.

The spectral response of the CCD detector (Figure 5.2) is such that faint cool stars (e.g. type N0), with visual magnitudes lower than the limit of the Guide Star Catalog (i.e., 13) can produce large numbers of counts. These so-called "spoiler stars" are detected as part of the on-ground aspect "pipeline" data processing, and subsequent centroiding removes any bias that the spoilers may have introduced.

5.2.2   Fiducial lights and Fiducial Transfer System

Surrounding each of the SI detectors is a set of fiducial Light Emitting Diodes. Each fiducial light produces a collimated beam at 635 nm which is imaged onto the ACA CCD via the RRC, the periscope, and the fiducial transfer mirror (Figure 5.3). The images of the fiducial lights are used to locate the instrument position relative to the HRMA nodal axis and the guide stars.

5.2.3   IRU

Two Inertial Reference Units (IRU) are located in the front of the observatory on the side of the HRMA. Each IRU contains two gyros, each of which measures an angular rate about 2 gyro axes. This gives a total of eight gyro channels. Data from four of the eight channels can be read out at one time. The gyros are arranged within the IRUs and the IRUs are oriented such that all 8 axes are in different directions and no three axes lie in the same plane. The gyros output pulses represent incremental rotation angles. In high-rate mode,

Figure 5.2: Spectral response of the ACA CCD. The same signal-to-noise is achieved for a V=11.7 magnitude N0 star as for a V=10 magnitude G0V star. Also shown are the spectra and the standard visual response for the two stars.

Figure 5.3: Fiducial Transfer System

each pulse nominally represents $0.75''$, while in low-rate mode (used during all normal spacecraft operations) each pulse represents nominally $0.02''$.

5.2.4   Momentum control – RWA and MUPS

Control of the spacecraft momentum is required both for maneuvers and to maintain stable attitude during science observations. Momentum control is primarily accomplished using 6 Teldix RDR-68 reaction wheel units mounted in a pyramidal configuration. During observing, with the spacecraft attitude constant apart from dither, external torques on the spacecraft (e.g. gravity gradient, magnetic) will cause a buildup of momentum in the RWA. Momentum is then unloaded by firing the MUPS and simultaneously spinning down the reaction wheels.

5.3   Operating principles

The *Chandra* aspect system serves two primary purposes: on-board spacecraft pointing control and aspect determination and post-facto ground aspect determination, used in X-ray image reconstruction and celestial location.

The PCAD system has 9 operational modes (6 normal and 3 safe modes) which use different combinations of sensor inputs and control mechanisms to control the spacecraft and ensure its safety. These modes are described in Section 5.8.1. In the normal science pointing mode, the PCAD system uses sensor data from the ACA and IRUs, and control torques from the RWAs, to keep the X-ray target within $\sim$30" of the telescope boresight. This is done using a Kalman filter which optimally combines ACA star centroids (typically 5) and angular displacement data from two 2-axis gyroscopes. On short time scales ($\sim$seconds) the spacecraft motion solution is dominated by the gyroscope data, while on longer timescales it is the star centroids that determine the solution.

The post-facto aspect determination in done on the ground and uses more sophisticated processing and better calibration data to produce a more accurate aspect solution. The suite of *CXC* tools to perform this processing is called the aspect pipeline. The key improvements over PCAD aspect come from better image centroiding and using Kalman smoothing (which uses all available data over the observation period – as opposed to historical data). In addition, the aspect pipeline folds in the position of the focal-plane instrument.

5.4   Performance

The important PCAD system performance parameters and a comparison to the original requirements are shown in Table 5.1. Absolute celestial pointing refers to the accu-

racy with which the *Chandra* line of sight (the line connecting the nominal aimpoint and the HRMA node) can be pointed toward a particular target location on the sky, and is about $3''$ in radius. This is based on a small sample of 17 (ACIS-S) observations taken prior to February, 2000. It should be noted that the $3''$ value represents the repeatability of absolute pointing on timescales of less than approximately one year. During the first 1.5 years of the mission, there was an exponentially decaying drift in the nominal aimpoint of about $6''$, probably due to a long-term relaxation in the spacecraft structural alignment. The drift rate has subsequently slowed to less than $2\,\mathrm{arcsec}$ per year (http://cxc.harvard.edu/cal/ASPECT/fid_drift)

The PCAD 10-second pointing stability performance is measured by calculating the RMS attitude control error (1-axis) over successive 10 second intervals. The attitude control error is simply the difference between the ideal (commanded) dither pattern and the actual measured attitude. Flight data show that 95% of the RMS error measurements are less than $0.04''$ (pitch) and $0.03''$ (yaw). Systematic offsets are not included in this term.

The image reconstruction performance measures the effective blurring of the X-ray *PSF* due to aspect reconstruction. Analysis of flight X-ray data shows that if the resolution and focus of the HRMA and SIs were perfect, the reconstructed image of an X-ray point source (within the central 5 arcminutes) would have an RMS diameter of less than $0.3''$. Equivalently, aspect reconstruction effectively convolves the *PSF* with a gaussian having FWHM of less than $0.25''$.

Celestial location accuracy measures the absolute accuracy of Chandra X-ray source locations. Based on observations of point sources with accurately known coordinates, the source location error circle (1-σ) has a radius of $0.6''$. As various errors have been found from time to time, the user is urged to check for cautions and updates on the *CXC* Aspect Information web page (http://cxc.harvard.edu/cal/ASPECT/).

5.5   Heritage

The *Chandra* aspect camera design is based on the Ball CT-601 star tracker, which is currently operating on the XTE mission. The *Chandra* IRUs are nearly identical to the SKIRU V IRUs, some 70 of which have been built by the manufacturer - Kearfott. These IRUs are similar to those used on CGRO.

5.6   Special Characteristics

The ACA CCD detectors will degrade in performance due to radiation damage (as for ACIS). This will produce an increase in dark current, read noise, and charge transfer inefficiency (CTI). The first two factors increase centroiding uncertainty, while CTI produces

Table 5.1: Aspect System Requirements and Performance

Description	Requirement	Actual	References
Absolute celestial pointing	30.0″ (99.0%, radial)	3.0″	*Chandra* PRD, SE31 §6.3
PCAD 10 sec pointing stability	0.25″ (RMS, 1-axis)	0.043″ (pitch) 0.030″ (yaw)	*Chandra* PRD, SE31 §6.4.1.1.2
Image reconstruction	0.5″ (RMS diameter)	0.3″	*Chandra* PRD, SE31 §4.3
Celestial location	1.0″ (RMS radius)	0.6″	*Chandra* PRD, SE31 §4.4

systematic centroid shifts. The CTI-induced shifts can, to some extent, be removed by on-orbit calibration (Section 5.7.3).

Contamination buildup on the CCD surface is expected to result in a mean throughput loss of 9% by EOL, which is within margin. However, the calculation of this number is complicated, and the actual degradation may differ. Furthermore, it is difficult to predict the uniformity of the contaminants. Non-uniform contamination would especially impact the star centroiding accuracy, and hence degrade the accuracy of the aspect solution. The buildup of contaminants is tracked by a trending analysis of expected versus observed star brightnesses. Non-uniform contamination (and other effects) are searched for by trending analysis of the aspect accuracy and looking for anomalous changes. To date, these trending analyses show no indication of contamination build-up. In the event that the 0.5″ image reconstruction requirement (Section 5.4) cannot be maintained in the future, we will consider "baking-out" the CCD on-orbit. In this procedure the current on the CCD thermo-electric cooler is reversed so as to *heat* the device to approximately 30 C for a period of several hours. After bake-out the CCD would be returned to its nominal operating temperature of -10 degrees centigrade.

5.7   Calibration

5.7.1   Pre-launch calibration

IRU component testing at Kearfott provided calibration data necessary for accurate maneuvers and for deriving the aspect solution. The key parameters are the scale factor (arcsec/gyro pulse) and the drift rate stability parameters. The stability parameters specify how quickly the gyro readout random-walks away from the true angular displace-

ment. These terms limit the aspect solution accuracy during gyro hold observations (Section 5.9.2).

ACA component testing at Ball provided calibration data necessary for on-orbit pointing control and for post-facto ground processing. On-orbit, the ACA uses CCD gain factors, the plate scale factor, and temperature dependent field distortion coefficients to provide the control system with star positions and brightnesses. In ground processing, the *CXC* aspect pipeline makes use of those calibration data as well as CCD read noise, flat-field maps, dark current maps, and the camera *PSF* in order to accurately determine star positions.

5.7.2   Orbital activation and checkout calibration

Orbital activation and checkout of the PCAD occurred during the first 30 or so days of the *Chandra* mission. During the first phase of OAC, before the HRMA sunshade door was opened it was possible to use the ACA to observe the fiducial lights (period 1). After the sunshade door was opened it was possible to fully check the aspect camera using star light (period 2).

Chandra activation produced the following aspect system calibration data:

- Bias, alignment, scale factor of the CSS and FSS (period 1)

- Coarse gyro bias (period 1)

- ACA CCD dark current map (period 1)

- Fiducial light intensity, image, and centroid at nominal voltage (periods 1 and 2)

- IRU bias, alignment, scale factor (period 2)

- ACA alignment and field distortion coefficients (period 2)

5.7.3   On-orbit calibrations

During the *Chandra* science mission, aspect system components require on-orbit calibration to compensate for alignment or scale factor drifts, and ACA CCD degradation due to cosmic radiation. The IRU calibration coefficients were updated once (July-2002) based on analysis of PCAD data for 3105 maneuvers during the course of the mission. The following ACA calibrations are performed, as-needed, based on the trending analyses of aspect solution data.

Dark current

Cosmic radiation damage will produce an increase in the mean CCD dark current as well as the dark current non-uniformity (i.e., pixel-to-pixel variations). If uncalibrated, the latter term can significantly degrade aspect solution accuracy by up to $0.4''$ (image reconstruction RMS diameter). During OAC, dark current calibrations were performed shortly before sun-shade door opening. These indicated a substantial increase in the number of "warm" CCD pixels (due to radiation damage), relative to ground testing. However, as was shown in Table 5.1 there has been no impact on performance, because software within the aspect pipeline detects and compensates for these warm pixels. Dark current calibrations are performed up to several times per year.

Because the ACA has no shutter, a dark current calibration must be done with *Chandra* pointing at a star field which is as free from optical sources as possible. Furthermore, in order to minimize dark current accumulation during the CCD readout, only a small portion (typically 128 rows) of the CCD is actually digitized after each 30 second integration. A minimum of three full-frame CCD maps are collected, each with slight pointing offsets in order to allow removal of field stars. The entire calibration procedure takes between 30 minutes and 2 hours, depending on the number of repeats, integration time, and number of rows per integration.

Charge transfer inefficiency (CTI)

Radiation damage degrades the efficiency with which charge is transferred in the CCD by introducing dislocations in the semiconductor which trap electrons and prevent their transfer. The most important consequence is a "'streaking" or "trailing" of star images along the readout column(s), which can introduce systematic centroid shifts. These shifts depend primarily on CCD transfer distance to the readout and star magnitude.

The procedure for calibrating the mean CTI is to dither a faint star across the CCD quadrant boundary and observe the discontinuity in centroid (the CCD is divided electrically into four quadrants).

Field distortion

The precise mapping from ACA CCD pixel position to angle relative to the ACA boresight is done with the "ACA field distortion polynomial". This includes linear plate scale factors as well as non-linear temperature-dependent terms. In order to verify that no mechanical shift in the ACA had occurred during launch, a field distortion calibration was performed during the orbital activation and checkout phase. A mechanical shift would result in degraded celestial location accuracy, but the on-orbit calibration revealed no shift.

The calibration was done by observing a dense field of stars with the spacecraft in normal pointing mode. Two reference stars were observed continuously, while sets of 4

Table 5.2: PCAD modes

Mode	Sensors	Control	Description
Standby	—	—	OBC commands to RWA, RCS, and SADA disabled, for initial deployment, subsystem checkout, etc.
Normal Pointing	IRU, ACA	RWA	Point at science target, with optional dither
Normal Maneuver	IRU	RWA	Slew between targets at peak rate of $2°$ per minute
Normal Sun	IRU, CSS, FSS	RWA	Acquire sun and hold spacecraft -Z axis and solar arrays to the sun
Powered Flight	IRU	RCS	Control *Chandra* during Liquid Apogee Engine burns
RCS Maneuver	IRU	RCS	Control *Chandra* using the RCS
Safe Sun	IRU, CSS, FSS	RWA	Safe mode: acquire sun and hold spacecraft -Z axis and solar arrays to the sun
Derived Rate Safe Sun	IRU, CSS, FSS	RWA	Similar to Safe Sun Mode, but using only one gyro (two axes) plus sun sensor data
RCS Safe Sun	IRU, CSS, FSS	RCS	Same as Safe Sun Mode, but using RCS instead of RWA for control

stars each were observed for 100 seconds. The calibration was completed after observing 64 stars over the ACA field of view, taking roughly 60 minutes. There are currently no plans to repeat this calibration.

5.8 Operations

5.8.1 PCAD modes

The PCAD system has 9 operational modes (6 normal and 3 safe) which use different combinations of sensor inputs and control mechanisms to control the spacecraft and ensure its safety. These modes are listed in Table 5.2. Normal science observations are carried out in Normal Pointing Mode (NPM), while slews between targets are done in Normal Maneuver Mode (NMM).

5.8.2   Operational constraints

The ACA will meet performance requirements when the ACA line of sight is separated from: the Sun by 47 degrees or more; the limb of the bright Earth by 20 degrees or more; and the dark Earth or Moon by 6 degrees or more. If these restrictions are violated, the star images may be swamped by scattered background light, with resulting noise on star position that exceeds the $0.360''$ requirement (1-σ, 1-axis).

5.8.3   Output data

The important output data from the ACA are the scaled raw pixel intensities in a region (4×4, 6×6, or 8×8 pixel) centered on the star and fiducial light images. These data are placed in the engineering portion of the telemetry stream, which is normally allocated $8\,\text{kbit s}^{-1}$. During an ACA dark current calibration (Section 5.7.3), *Chandra* utilizes a $512\,\text{kbit s}^{-1}$ telemetry mode (in real-time contact) to enable read-out of the entire CCD(1024×1024 pixels). The key data words in telemetry from the IRU are the 4 accumulated gyro counts (32 bits every 0.256 sec).

5.9   Performing an Observation

5.9.1   Star acquisition

After maneuvering at a rate of up to $2°$/minute to a new celestial location using gyroscope data and the reaction wheels, *Chandra* begins the star acquisition sequence, a process which typically takes from 1 to 4 minutes. First the OBC commands the ACA to search for up to 8 acquisition stars, which are selected to be as isolated from nearby stars as possible. The search region size is based on the angular size of the slew, which corresponds to the expected uncertainty in attitude. If two or more acquisition stars are found, an attitude update is performed using the best (brightest) pair of stars. This provides pointing knowledge to $3''$ ($3\,\sigma$ per axis). Next the guide star search begins. Depending on the particular star field configuration, the star selection algorithm may choose guide stars which are the same as the acquisition stars. In this case the acquisition time is somewhat reduced. When at least two guide stars have been acquired and pointing control errors converge, the on-board Kalman filtering is activated and the transition to Normal Point Mode is made, at which point sensing of the fiducial lights begins.

5.9.2   Science pointing scenarios

The on-board PCAD system is flexible and allows several different *Chandra* science pointing scenarios, described in the following sections.

NPM dither

The large majority of observations are performed using Normal Point Mode, with dither selected. In this case the *Chandra* line-of-sight will be commanded through a Lissajous pattern. Dithering distributes photons over many detector elements (microchannel pores or CCD pixels) and serves several purposes: reduces uncertainty due to pixel to pixel variation in quantum efficiency (QE); allows sub-sampling of the image; and, in the case of the HRC, distributes the total exposure over many microchannel pores - useful since the QE of a pore degrades slowly with exposure to photons. The dither pattern parameters are amplitude, phase, and period for two axes. Each of the six parameters is separately commandable and differ for the two different instruments (See Chapters 6 and 7). The default values for these parameters are given in Table 5.3. The minimum dither rate required to maintain the health of the HRC is $0.02''$/sec, and the maximum rate tolerated by PCAD to maintain pointing stability is $0.1''$/sec.

Table 5.3: Default dither parameters

Parameter	HRC	ACIS
Phase (pitch)	0.0 rad	0.0 rad
Phase (yaw)	0.0 rad	0.0 rad
Amplitude (pitch)	20.0 arcsec	8.0 arcsec
Amplitude (yaw)	20.0 arcsec	8.0 arcsec
Period (pitch)	768.6 sec	707.1 sec
Period (yaw)	1087.0 sec	1000.0 sec

NPM steady

This mode is identical to NPM dither, but without the dither.

Pointing at solar system objects

Observations of moving solar system objects are done using a sequence of pointed observations, with the object moving through the field of view during each dwell period. Except in special circumstances, each pointing is selected so that the object remains within $5'$ of the *Chandra* line-of-sight. Most solar system objects move slowly enough so that a single pointed observation will suffice.

Raster scan

Survey scans of regions larger than the instrument field of view are specified simply with a list of target coordinates giving the field centers. The fields can optionally overlap, depending on the science requirements of the survey.

Offset and gyro hold

In special circumstances it will be necessary to perform observations without tracking guide stars. It may occur that a field has no suitable guide stars, although this situation has not been encountered to date. A more likely situation is that a very bright object, such as the Earth or Moon, saturates the ACA CCD and precludes tracking stars. In this case *Chandra* will first be maneuvered to a nearby pointing which has guide stars to establish fine attitude and a gyro bias estimate. A dwell time of approximately 25 minutes is needed to calibrate the bias estimate, which is the dominant term in the drift equation below. *Chandra* will then be maneuvered to the target. The default automatic transition to NPM will be disabled, and the spacecraft will hold on the target attitude in NMM.

While holding on gyros only, the spacecraft attitude will drift due to noise in the gyros, which results in an an aspect solution error. The variance of the angle drift for each gyro axis, in time t, is given by

$$\sigma^2 = \sigma_b^2 t^2 + \sigma_v^2 t + \sigma_u^2 t^3/3$$

Ground test data for gyro noise parameters indicate worst case values of $\sigma_u = 1.5 \times 10^{-5}$ arcsec sec$^{-3/2}$ and $\sigma_v = 0.026$ arcsec sec$^{-1/2}$. Analysis of the residual Kalman filter bias estimate gives $\sigma_b = 0.002$ arcsec sec^{-1}. This results in 1-σ angle drift errors of: $0.3''$ for 0.1 ksec; $2.2''$ for 1 ksec; $11''$ for 5 ksec; and $22''$ for 10 ksec. After a maximum of 5 ksec, *Chandra* will be maneuvered back to the nearby field with guide stars in order to re-establish fine attitude and update the gyro drift rate.

5.9.3 PCAD capabilities (advanced)

Monitor star photometry

The ACA has the capability to devote one or more of the eight image slots to "monitor" particular sky locations. This allows simultaneous optical photometry of one or more X-ray targets in the field of view. These optical sources can be slightly fainter than the ACA guide star limit of $m_{ACA} = 10.2$ mag. The bright-end limit for monitor star photometry is $m_{ACA} = 6.2$ mag. However, since there are a fixed number of image slots, devoting a slot to photometry instead of tracking a guide star results in a degradation of the image reconstruction and celestial location accuracy (Section 5.4). Using a monitor slot represents a 15 - 25% increase in the aspect image reconstruction RMS diameter , depending on the particular guide star configuration. For two monitor slots, the increase is

about 50 - 60%. The photometric accuracy which can be achieved depends primarily on the star magnitude, integration time, CCD dark current, CCD read noise, sky background, and the CCD dark current uncertainty.

Dark current uncertainty ultimately limits the photometric accuracy at the faint end, and results from uncalibrated pixel-to-pixel changes in dark current due to radiation damage. This includes both changing background pixels as Chandra dithers, as well as intrinsic flickering in the radiation-damaged CCD pixels. This flickering, which occurs on time scales from less than 1 ksec to more than 10 ksec, poses fundamental problems for accurate photometry since the background dark current is a strong random function of time. With straightforward data processing, the noise introduced by the dark current variations (both spatial and temporal) is approximately 300 e-/sec. A star with an ACA magnitude of 12.0 produces about 1100 e-/sec, giving a S/N of 3.7. This represents the practical faint limit for ACA monitor star photometry. Somewhat improved S/N could be obtained with a more sophisticated analysis which tracks the time-dependent dark current of each pixel.

The zero instrument magnitude is defined as the Aspect Camera response to a zero magnitude star of spectral class G0V. The conversion from V and B magnitude to ACA instrument magnitude, based on flight data, is given approximately by

$$m_{ACA} = V + 0.428 - 0.774(B - V) + 0.283(B - V)^2 - 0.267(B - V)^3$$

5.10   Ground Processing

For each science observation, the aspect system data described in Section 5.8.3 are telemetered to the ground to allow post-facto aspect determination by the *CXC* aspect pipeline, as part of the standard *CXC* data processing pipeline. The important components of the pipeline are:

Gyro process: Filter gyro data, gap-fill, and calculate raw spacecraft angular rate

ACA process: Filter bad pixels, make CCD-level corrections (e.g. dark current), find spoiler stars, centroid, make camera-level corrections, convert to angle

Kalman filter and smooth: Optimally combine ACA and gyro data to determine ACA celestial location and image motion

Combine ACA and fids: Derive fid light solution, and combine with ACA solution, to generate image motion and celestial location at the focal plane science instrument.

5.10.1   Data products

The data products which are produced by the aspect solution pipeline are listed in Table 5.4. Key data elements include: IRU accumulated counts; raw pixel data for 8 images;

Table 5.4: Aspect pipeline data products

Product	Description
ASPSOL	Final aspect solution with errors
ASPQUAL	Aspect solution quality indicators
AIPROPS	Aspect Intervals
ACACAL	ACA calibration data from ODB and CALDB
GSPROPS	Guide star properties, both from the AXAF Guide and Acquisition Star Catalog, and as actually observed with the ACA
FIDPROPS	Fiducial light properties, as commanded and as observed
ACADATA	Aspect camera telemetry (including ACA housekeeping), and images after CCD -level correction
ACACENT	Image centroids and associated fit statistics
GYROCAL	Gyro calibration data from ODB and CALDB
GYRODATA	Gyro raw and gap-filled, filtered data
KALMAN	Intermediate and final data in Kalman filter and smoother

observed magnitudes, pixel positions of the aspect stars and fiducial lights versus time; and aspect solution versus time. The star data are used to determine the RA, Dec, and roll (and corresponding uncertainties) of the HRMA axis as a function of time. The fid light images are used to track any drift of the SIM away from the nominal position. One cause of such drift is thermal warping of the optical bench assembly. The Kalman filtering routines also calculate an optimal estimate of the gyro bias rate as a function of time.

5.10.2   Star catalog

The Aspect system uses the *AGASC* (AXAF Guide and Aspect Star Catalog). Further information about the *AGASC*, as well as access to catalog data, can be found on the *CXC AGASC* web page (http://cxc.harvard.edu/agasc). The *AGASC* was prepared by the *CXC* Mission Planning group, and is a compilation of the Hubble Guide Star Catalog, the Positions and Proper Motion Catalog and the Tycho Output Catalog.

Chapter 6

ACIS: Advanced CCD Imaging Spectrometer

6.1 Introduction & Layout

The Advanced CCD Imaging Spectrometer (ACIS) offers the capability to simultaneously acquire high-resolution images and moderate resolution spectra. The instrument can also be used in conjunction with the High Energy Transmission Grating (HETG) or Low Energy Transmission Grating (LETG) to obtain higher resolution spectra (see Chapters 8 and 9). ACIS contains 10 planar, 1024 x 1024 pixel CCDs (Figure 6.1); four arranged in a 2x2 array (ACIS-I) used for imaging, and six arranged in a 1x6 array (ACIS-S) used either for imaging or as a grating readout. Two CCDs are back-illuminated (BI) and eight are front-illuminated (FI). The response of the BI devices extends to energies below that accessible to the FI chips. The chip-average energy resolution of the BI devices is, currently, better than that of the FI devices. Any combination of up to 6 CCDs may be operated simultaneously. Operating six chips increases the chances of serendipitous science but at the price of increased total background counting rate and therefore a somewhat enhanced probability of saturating telemetry.

The Instrument Principal Investigator for ACIS is Prof. Gordon Garmire (Pennsylvania State University). ACIS was developed by a collaboration between Penn State, the *MIT* Center for Space Research and the Jet Propulsion Laboratory, and was built by Lockheed Martin and *MIT*. The *MIT* effort was led by Dr. George Ricker. The CCDs were developed by *MIT*'s Lincoln Laboratory.

ACIS is a complex instrument having many different characteristics and operating modes. Radiation damage suffered by the FI chips has had a negative impact on their energy resolution – the BI devices were not impacted – thus altering the basic considerations as to how to make best use of the instrument (see Section 6.7.) We will review the

ACIS FLIGHT FOCAL PLANE
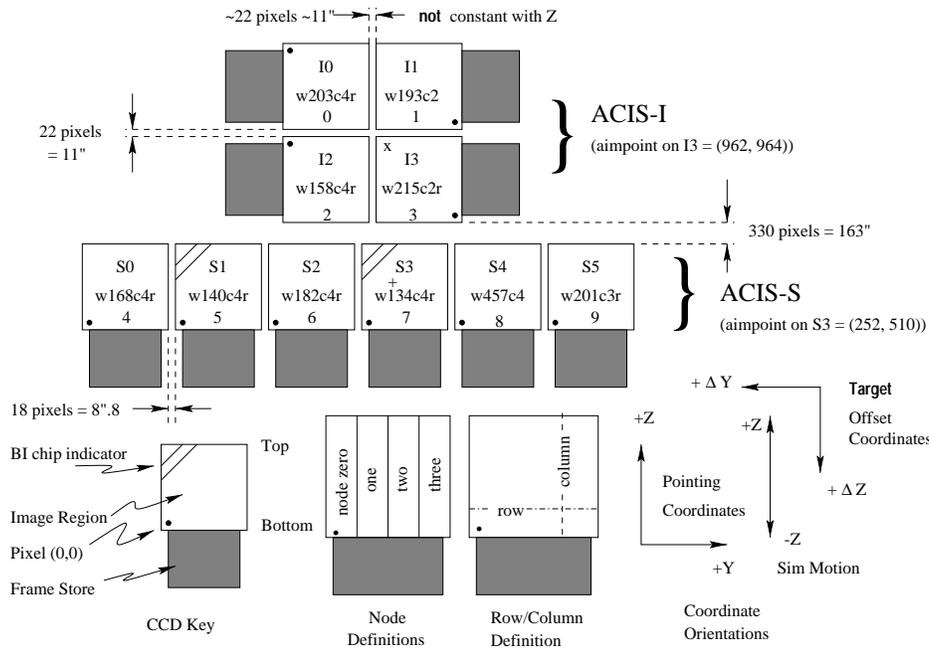
Figure 6.1: A schematic drawing of the ACIS focal plane; insight to the terminology is given in the lower left. Note the nominal aimpoints: on S3 (the '+') and on I3 (the 'x'). On S3, it has become standard practice to add an observatory Y-offset of -20″ (41 pixels) from the true aimpoint (252,510) in the direction of S4 for all ACIS-S observations in order to move the source flux away from the node 0-1 boundary. Note the differences in the orientation of the I and S chips, important when using Subarrays (Section 6.12.3). Note also the (Y, Z) coordinate system and the target offset convention (see Chapter 3) as well as the SIM motion (+/-Z). The view is along the optical axis, from the source towards the detectors, (-X). The numerous ways to refer to a particular CCD are indicated: chip letter+number, chip serial number, and ACIS chip number. The node numbering scheme is illustrated lower center.

tradeoffs elsewhere in this Chapter. Software methods for improving the energy resolution of the FI CCDs are discussed in Section 6.7.2.

Many of the characteristics of the ACIS instrument are summarized in Table 6.1.

6.2   Basic Principles

A CCD is a solid-state electronic device composed primarily of silicon. A "gate" structure on one surface defines the pixel boundaries by alternating voltages on three electrodes spanning a pixel. The silicon in the active (depletion) region (the region below the gates wherein most of the absorption takes place) has an applied electric field so that charge moves quickly to the gate surface. The gates allow confined charge to be passed down a "bucket brigade" (the buried channel) of pixels in parallel to a serial readout at one edge by appropriately varying ("clocking") the voltages in the gates.

The ACIS front-illuminated CCDs have the gate structures facing the incident X-ray beam. Two of the chips on the ACIS-S array (S1 and S3) have had treatments applied to the back sides of the chips, removing insensitive, undepleted, bulk silicon material and leaving the photo-sensitive depletion region exposed. These are the BI chips and are deployed with the back side facing the HRMA.

Photoelectric absorption of an X-ray in silicon results in the liberation of a proportional number of electrons (an average of one electron-hole pair for each 3.7 eV of photon energy absorbed). Immediately after the photoelectric interaction, the charge is confined by electric fields to a small volume near the interaction site. Charge in an FI device can also be liberated below the depletion region (in an inactive substrate) from where it diffuses into the depletion region. This charge may easily appear in two or more pixels.

Good spectral resolution depends upon an accurate determination of the total charge deposited by a single photon. This in turn depends upon the fraction of charge collected, the fraction of charge lost in transfer from pixel to pixel during read-out, and the ability of the readout amplifiers to measure the charge. Spectral resolution also depends on read noise and the off-chip analog processing electronics. The ACIS CCDs have readout noise less than 2 electrons RMS. Total system noise for the 40 ACIS signal chains (4 nodes/CCD) ranges from 2 to 3 electrons (rms) and is dominated by off-chip analog processing electronics.

The CCDs have an "active" or imaging Section (see Figure 6.1) which is exposed to the incident radiation and a shielded "frame store" region. A typical mode of the ACIS CCD operation is: (1) the active region is exposed for a fixed amount of time (full frame $\sim$ 3.2 s); (2) at the end of the exposure the charge in the active region is quickly ($\sim$ 41 ms) transferred into the frame store; (3) the next exposure begins; (4) simultaneously, the data in the frame store region is passed to a local processor which, after removing bias (the amount of charge in a pixel in the absence of any X-ray induced signal),

Focal plane arrays:	
I-array	4 CCDs placed to lie tangent to the focal surface
S-array	6 CCDs in a linear array tangent to the grating Rowland circle
CCD format	1024 by 1024 pixels
Pixel size	24.0 microns (0.4920 ± 0.0001 arcsec)
Array size	16.9 by 16.9 arcmin ACIS-I
	8.3 by 50.6 arcmin ACIS-S
On-axis effective Area	110 cm^2 @ 0.5 keV (FI)
(integrated over the *PSF*	600 cm^2 @ 1.5 keV (FI)
to >99% encircled energy)	40 cm^2 @ 8.0 keV (FI)
Quantum efficiency	> 80% between 3.0 and 5.0 keV
(frontside illumination)	> 30% between 0.8 and 8.0 keV
Quantum efficiency	> 80% between 0.8 and 6.5 keV
(backside illumination)	> 30% between 0.3 and 8.0 keV
Charge transfer inefficiency(parallel)	FI: $\sim2\times10^{-4}$; BI: $\sim2\times10^{-5}$
Charge transfer inefficiency(serial)	S3(BI): $\sim7\times10^{-5}$; S1(BI): $\sim1.5\times10^{-4}$; FI: unmeasurable
System noise	$<\sim$ 2 electrons (rms) per pixel
Max readout-rate per channel	$\sim$ 100 kpix/sec
Number of parallel signal channels	4 nodes per CCD
Pulse-height encoding	12 bits/pixel
Event threshold	FI: 38 ADU ($\sim$140 eV)
	BI: 20 ADU ($\sim$70 eV)
Split threshold	13 ADU
Max internal data-rate	6.4 Mbs (100 kbs $\times4 \times 16$)
Output data-rate	24 kb per sec
Minimum row readout time	2.8 ms
Nominal frame time	3.2 sec (full frame)
Allowable frame times	0.2 to 10.0 s
Frame transfer time	40 μsec (per row)
Point-source sensitivity	4×10^{-15}ergs cm^{-2} s^{-1} in 10^4 s
	(0.4-6.0 keV)
Detector operating temperature	-90 to $-120°$C

Table 6.1: ACIS Characteristics

32	64	128
8	0	16
1	2	4

Figure 6.2: Schematic for determining the grade of an event. The grade is determined by summing the numbers for those pixels that are above their thresholds. For example, an event that caused all pixels to exceed their threshold is grade 255. A single pixel event is grade 0.

identifies the position and amplitude of any "events" according to a number of criteria depending on the precise operating mode. These criteria always require a local maximum in the charge distribution above the event threshold (see Table 6.1). The position and the amount of charge collected, together with similar data for a limited region containing and surrounding the pixel are classified ("graded") and then passed into the telemetry stream.

6.3   Event Grades

During the first step in the algorithm for detecting X-ray events, the on-board processing examines every pixel in the full CCD image (even in the continuous clocking mode (Section 6.12.5)) and selects as events regions with bias-subtracted pixel values that both exceed the event threshold and are greater than all of the touching or neighboring pixels (i.e., a local maximum). The surrounding 3x3 neighboring pixels are then compared to the bias-subtracted split-event threshold; those that are above the threshold establish the pixel pattern. On the basis of this pattern, the event is assigned a grade. Depending on the grade, the data are then included in the telemetry. On-board suppression of certain grades is used to limit the telemetry bandwidth devoted to background events (see Section 6.10.1).

The grade of an event is thus a code that identifies which pixels, within the three pixel-by-three pixel island centered on the local charge maximum, are above certain amplitude thresholds. The thresholds are listed in Table 6.1. Note that the local maximum threshold differs for the FI and the BI CCD. A Rosetta Stone to help one understand the ACIS grade assignments is shown in Figure 6.2, and the relationship to the *ASCA* grading scheme is given in Table 6.2.

It is important to understand that most, if not all, calibrations of ACIS are based on a specific subset of ACIS grades. This "standard" set comprises *ASCA* grades 0,2,3,4, and 6 – G(02346). In the absence of pileup, this particular grade selection appears to optimize the signal-to-background ratio, but this conclusion depends on the detailed spectral

Table 6.2: ACIS and *ASCA* Grades

ACIS Grades	*ASCA* Grade	Description
0	0	Single pixel events
64 65 68 69	2	Vertical Split Up
2 34 130 162	2	Vertical Split Down
16 17 48 49	4	Horizontal Split Right
8 12 136 140	3	Horizontal Split Left
72 76 104 108	6	"L" & Quad, upper left
10 11 138 139	6	"L" & Quad, down left
18 22 50 54	6	"L" & Quad, down right
80 81 208 209	6	"L" & Quad, up right
1 4 5 32 128	1	Diagonal Split
33 36 37 129	1	
132 133 160 161	1	
164 165	1	
3 6 9 20 40	5	"L"-shaped split with corners
96 144 192 13 21	5	
35 38 44 52 53	5	
97 100 101 131	5	
134 137 141 145	5	
163 166 168 172	5	
176 177 193 196	5	
197	5	
24	7	3-pixel horizontal split
66	7	3-pixel vertical split
255	7	All pixels
All other grades	7	

Table 6.3: Average source positions summarized in pixels (chip-x, chip-y)

ACIS-I :	(962, 964) in I3	no offsets
ACIS-S :	(252, 510) in S3	no offsets
ACIS-S :	(293, 510) in S3	if invoking the suggested -20″ ΔY offset

properties of the source. Further, most of the scientifically important characteristics of ACIS (effective area, sensitivity, point spread function, energy resolution, etc.) are grade- and energy-dependent.

6.4 Aimpoints

Aimpoints are the nominal positions on the ACIS where the flux from a point source with zero commanded target offsets is placed. There are two nominal aimpoints, indicated in Figure 6.1 - one on the corner of I3 on the ACIS-I array (the ACIS-I aimpoint), and one near the boundary between nodes 0 and 1 on S3 of the ACIS-S array (the ACIS-S aimpoint). Their exact positions are given in Table 6.3. Note that the aimpoint is not the same as the on-axis position, which is defined as the position of the narrowest PSF and found approximately 20" from the aimpoints. For zero SIM-Z offsets, the optical axis crosses ACIS-I at the I3 chip coordinates (984,995), and ACIS-S, at the S3 chip coordinates (221,532).

Approximate contours of constant encircled energy for ACIS-I and ACIS-S observations for the default aimpoints are shown in Figures 6.4 and 6.5. If required, other aimpoints can be selected along the Z-axis.

It is important to note that it has become standard practice to add an observatory Y-offset=ΔY=-20″=41 pixels, in the direction of S4, for all ACIS-S observations in order to assure that the dithered flux from a (now almost) on-axis point source is placed entirely on a single node (node 1) of the S3 CCD. This was done both to simplify and improve the analysis of data from a point source by avoiding dealing with the response functions from two nodes. The shift has a negligible impact on image quality because the diameter of the circle, for which >90% of the encircled energy lies within 2″, is $\sim$2′.4.

Note that for some observations, typically those with gratings, it is suggested to translate the SIM such that the S3 aimpoint is shifted in the negative Z direction – towards the readout node (see Table 6.4 for recommended offsets.)

These new aimpoints should be kept in mind if selecting the use of subarrays in gratings' observations, since the standard subarrays (see Section 6.12.3) will not center the zeroth order.

Table 6.4: Recommended SIM-Z offsets

Observation Mode	SIM-Z Offset	New Source Position (w/ -20″ ΔY Offset)
ACIS-S w/ HETG TE mode:	-3mm = -1.02389′	(293, 385)
ACIS-S w/ HETG CC mode:	-4mm = -1.36519′	(293, 344)
ACIS-S w/ LETG TE mode:	-8mm = -2.73038′	(293, 177)
ACIS-S w/ LETG CC mode:	-8mm = -2.73038′	(293, 177)

Lastly, it should be kept in mind that the observatory is typically dithered about the aimpoint with an 8″ half-amplitude (see Section 6.6.)

6.5   Spatial Resolution & Encircled Energy

The spatial resolution for on-axis imaging with ACIS is limited by the physical size of the CCD pixels (24.0 μm square $\sim$0.492 arcsec) and not the HRMA. This limitation applies regardless of whether the aimpoint is selected to be the nominal point on I3 or S3 (Figure 6.1). Approximately 90% of the encircled energy lies within 4 pixels (2 arcsec) of the center pixel at 1.49 keV and within 5 pixels (2.5 arcsec) at 6.4 keV. Figure 6.3 shows an in-flight calibration. There is no evidence for any differences in data taken with either S3 or I3 at the nominal focus. The ACIS encircled energy as a function of off-axis angle is discussed in the HRMA Chapter (see Section 4.2.2 and Figure 4.10.)

Off-axis, the departure of the CCD layout from the ideal focal surface and the increase of the HRMA *PSF* with off-axis angle become dominating factors. Since the ideal focal surface depends on energy, observers, for whom such considerations may be important, are urged to make use of the MARX simulator to study the impact on their observation.

6.6   Dither

Unless specially requested, the spacecraft is dithered during all observations. The dither pattern is a Lissajous figure. For observations with ACIS, the dither pattern spans 16 arcsec peak to peak. The dither serves two purposes: (1) to provide some exposure in the gaps between the CCDs, and; (2) to smooth out pixel-to-pixel variations in the response. The dither is removed during high-level ground processing of the data. Obviously the exposure time in the gaps between chips (and at the outside edges) will be less than that for the remainder of the field.
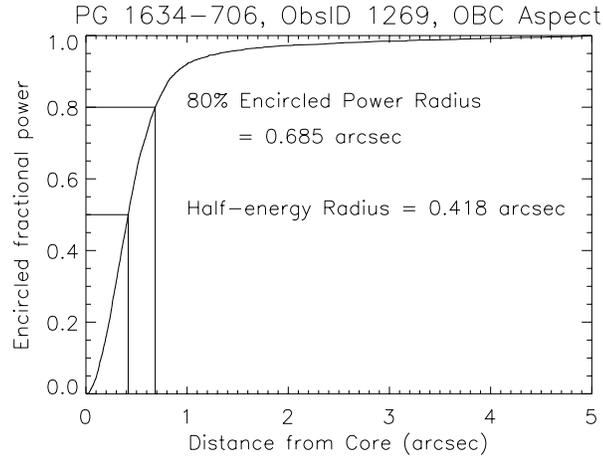
Figure 6.3: The on-orbit encircled broad-band energy versus radius for an ACIS observation of point source PG1634-706. The effective energy is 1 keV.
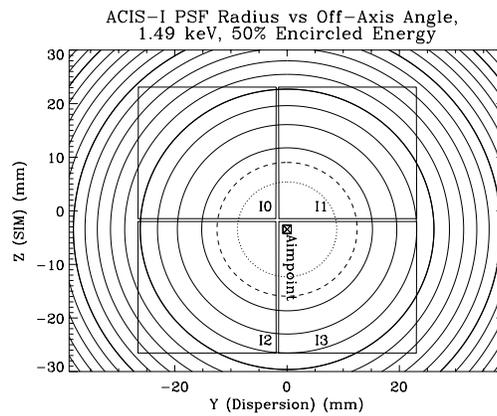
Figure 6.4: Approximate contours of constant 50% encircled energy at 1.49 keV when the ACIS-I default aimpoint is selected. The dotted line is 1 arcsec, the dashed line is 1.5 arcsec. The remainder are 1 arcsec intervals. The thicker solid lines highlight the 5, 10, and 15 arcsec contours.
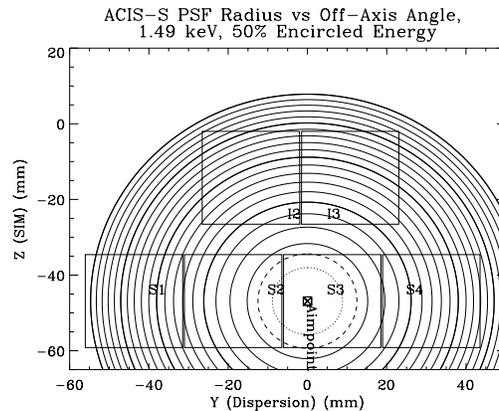
Figure 6.5: Approximate contours of constant 50% encircled energy at 1.49 keV when the ACIS-S default aimpoint is selected. The dotted line is 1 arcsec, the dashed line is 1.5 arcsec. The remainder are 1 arcsec intervals. The thicker solid lines highlight the 5, 10, 15 and 20 arcsec contours.

6.6.1   Gaps between the CCDs

The approximate sizes of the various gaps between chips are shown in Figure 6.1. Note that the Y-gaps in the ACIS-I array vary with Z due to the way the CCDs are tilted.

6.7   Energy Resolution

The ACIS FI CCDs originally approached the theoretical limit for the energy resolution at almost all energies, while the BI CCDs exhibited poorer resolution. The pre-launch energy resolution as a function of energy is shown in Figure 6.6. Subsequent to launch and orbital activation, *the energy resolution of the FI CCDs has become a function of the row number*, being near pre-launch values close to the frame store region and substantially degraded in the farthest row. An illustration of the dependence on row is shown in Figure 6.7.

   The CTI was caused by low energy protons, encountered during radiation belt passages and reflecting off the x-ray telescope onto the focal plane. Subsequent to the discovery of the degradation, operational procedures were changed, the ACIS is not left at the focal position during radiation belt passages. (The HRC is left at the focal position, but with door partially closed for protection.) Since this procedure was initiated, no further degradation in performance has been encountered beyond that predicted from pre–launch models. The BI CCDs were not impacted and this result is consistent with the proton-damage scenario – it is far more difficult for low-energy protons from the direction of the HRMA to deposit their energy in the buried channels of the BI devices, since the channels
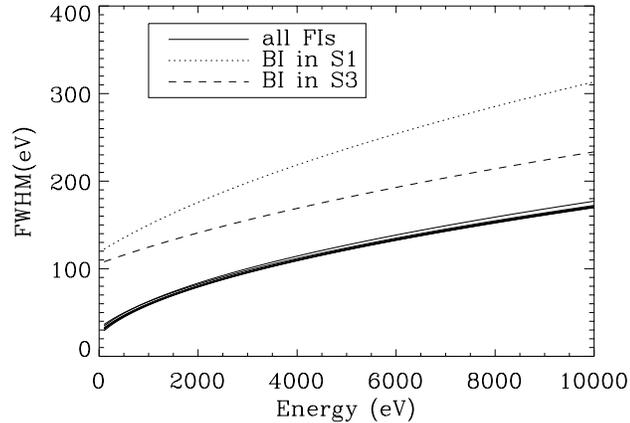
Figure 6.6: The ACIS pre-launch energy resolution as a function of energy. (Source: *CXC* Calibration group).

are near the gates and the gates face in the direction opposite to the HRMA. Thus the energy resolution for the two BI devices remains at their pre-launch values (the difference in energy resolution of the BI flight devices compared to pre-launch is < 1 ADU at the time of writing). The position-dependent energy resolution of the FI chips depends significantly on the ACIS operating temperature. Since activation, the ACIS operating temperature has been lowered in steps, based on considerations of molecular contamination, and is now set at the lowest temperature thought safely and consistently achievable ($\sim -120°$C).

6.7.1   Updated BI Response Matrices

The response matrices for the BI CCDs have been updated since their pre-launch versions. The new version of the S3 matrix for -120 C was released on August 7, 2001 in the CALDB 2.7 and was accompanied by an updated version of *CIAO* (2.1.3). Observers are encouraged to read the release notes on the *CXC* web page. The new version of the S3 matrix has an improved model of the spectral redistribution function, including the low-energy tail and the "shelf" feature of a typical pulse-height distribution, and an improved calibration of the gain at energies below 1 keV. There has been no change to the QE of the S3 CCD. The largest difference between the old and new matrices will be noticed for soft (E< 1 keV), line-dominated spectra. For harder line-dominated spectra, continuum spectra, or heavily-absorbed spectra, users will notice virtually no difference in the fitted parameters between the old and new matrices. The release notes web page includes sample fits to various spectra with the old and new matrices.
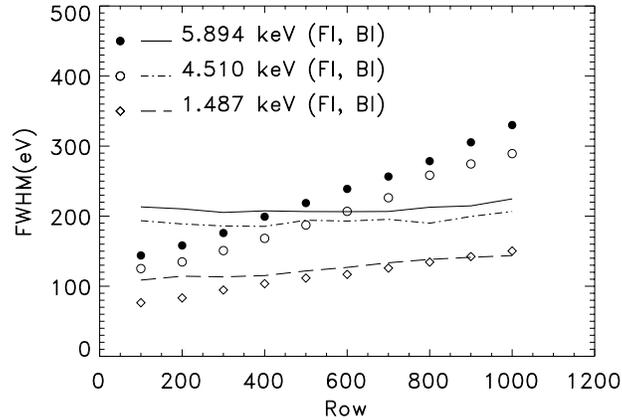
Figure 6.7: The energy resolution of S3 and I3 as a function of row number. These data were taken at $-120°$C. Note that these curves are representative of the variation - but they do not account for the row-dependent gain variation which also increases the energy resolution by about 10-15%, especially for the larger row numbers.

6.7.2   Correcting the energy resolution of the FI CCDs

The ACIS instrument team has developed a correction algorithm for the FI CCDs. The correction significantly improves the spectral resolution of the FI CCDs at all energies. Observers analyzing data from extended sources or across the ACIS-I array may find it advantageous to apply this correction. This CTI adjustment has been incorporated in acis_process_events in *CIAO* 2.3. An example of the application of the *CXC* CTI-corrector is shown in Figure 6.7.2.

Alternative software to apply the CTI correction, and response matrices appropriate for corrected data, has been developed by the IPI team at Penn State University. This is available from the contributed SW exchange web page at the *CXC* site and also at the Penn State ACIS page http://www.astro.psu.edu/users/townsley/cti/install.html.

6.8   Optical Blocking Filter & Optical Contamination

Since the CCDs are sensitive to optical as well as X-ray photons, optical blocking filters (OBFs) are placed just over the CCDs between the chips and the HRMA. The filters are composed of polyimide (a polycarbonate plastic) sandwiched between two thin layers of aluminum. The nominal thicknesses of the these components for the two arrays are given
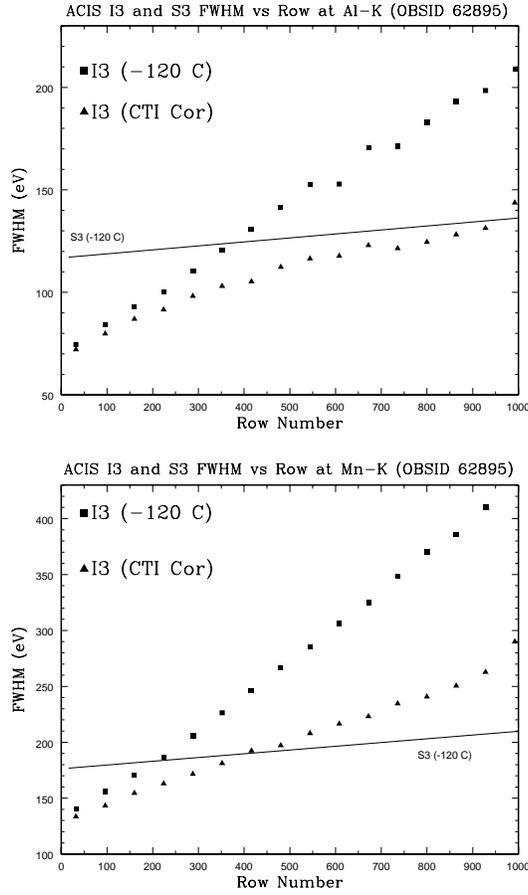
Figure 6.8: An example of the application of the *CXC* CTI-corrector in two energy bands. The first plot shows data for the Al-K line, and the second for Mn-K. The square data points are the FWHM of lines accumulated in 32-row bins. The triangle data points are the FWHM of CTI-corrected lines accumulated in 32-row bins. The line shows the nominal performance of the S3 chip. This data is from March 2000.

Table 6.5: Nominal Optical Blocking Filter Composition and Thicknesses

ACIS-I	Al/Polyimide/Al	1200Å 2000Å 400Å
ACIS-S	Al/Polyimide/Al	1000Å 2000Å 300Å

in Table 6.5. Details of the calibration of these filters may be found in the ACIS calibration report at http://www.astro.psu.edu/xray/docs/cal_report/node188.html.

The threshold for optical contamination (a 1 ADU (3.4 eV) shift in the bias level) has been revised based on on-orbit calibrations of a number of stars with different optical spectra. The threshold for detectable visible light contamination varies according to source color and is lowest for red stars observed on ACIS-S The detection threshold for an M star on the ACIS-S array is V∼8.1 for the nominal 3.2 second exposure or V∼6.3 for a 0.4s, 1/8 chip subarray. The thresholds are about 5 visual magnitudes brighter for the ACIS-I array. Proposers are urged to check the CXC web site for any further updates.

6.9   Quantum Efficiency and Effective Area

The chip-averaged quantum efficiencies for the ACIS CCDs for the standard grade set, including the optical blocking filters, are shown in Figure 6.9. Note that the quantum efficiency for the FI chips varies somewhat with row number (not shown), and decreases by ∼5-15% farthest from the readout at energies above 4 keV. This is due to the migration of good grades to bad grades induced by the effect of CTI. The QE variation with row number for the BI chips is much smaller. See also the discussion in the HRMA chapter (Section 4.2.2, and Figures 4.2 and 4.3), and the following subsection on the low-energy QE degradation in ACIS.

The combined HRMA/ACIS on-axis effective areas are shown in Figures 6.10 (log energy scale) and 6.11 (linear energy scale). The calculations are for a point source and 20 arcsec diameter detection cell.

Figure 6.12 shows the vignetting at several off-axis angles using flight data.

6.9.1   Low Energy QE Degradation in ACIS

An examination of archived astronomical observations and data acquired from the on-board ACIS calibration source (55Fe) shows that there has been a slow continuous degradation in the ACIS QE since launch. Our best interpretation is that this is due to molecular contamination building up on the cold optical blocking filter, and/or the CCD chips. This degradation is the most severe at low energies. Above 1 keV, the degradation is less than 10% to date. Analysis of the on-board calibration source shows that the L-complex (about half Mn-L and half Fe-L lines) to Mn-K alpha line ratio has decreased at a steady rate
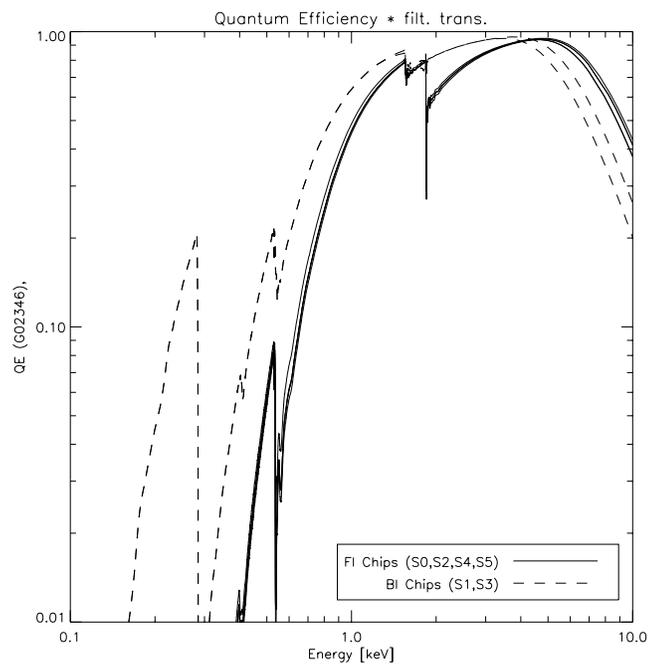
Figure 6.9: The quantum efficiency, convolved with the transmission of the appropriate optical blocking filter, of the FI CCDs (from a row nearest the readout) and the two BI CCDs as a function of energy. S3 is somewhat thicker, hence more efficient, than S1.
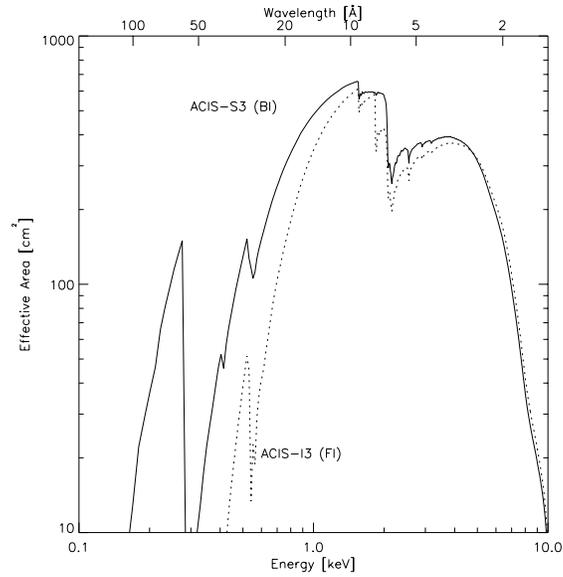
Figure 6.10: The HRMA/ACIS predicted effective area versus the energy on a log scale. The dashed line is for the FI CCD I3, and the solid line is for the BI CCD S3.
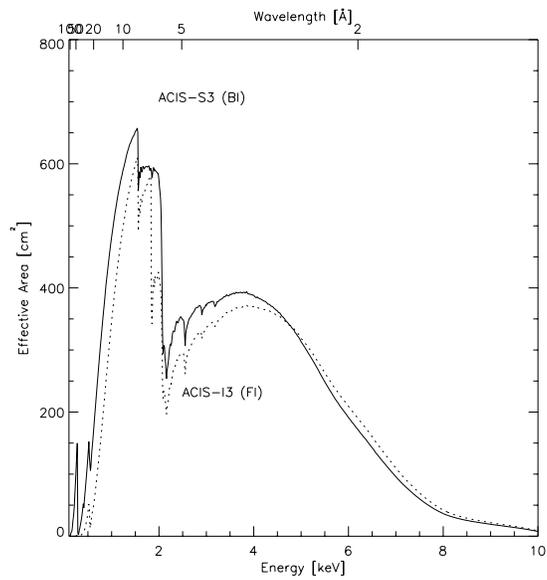
Figure 6.11: The HRMA/ACIS predicted effective area versus the energy on a linear scale. The dashed line is for the FI CCD I3, and the solid line is for the BI CCD S3.
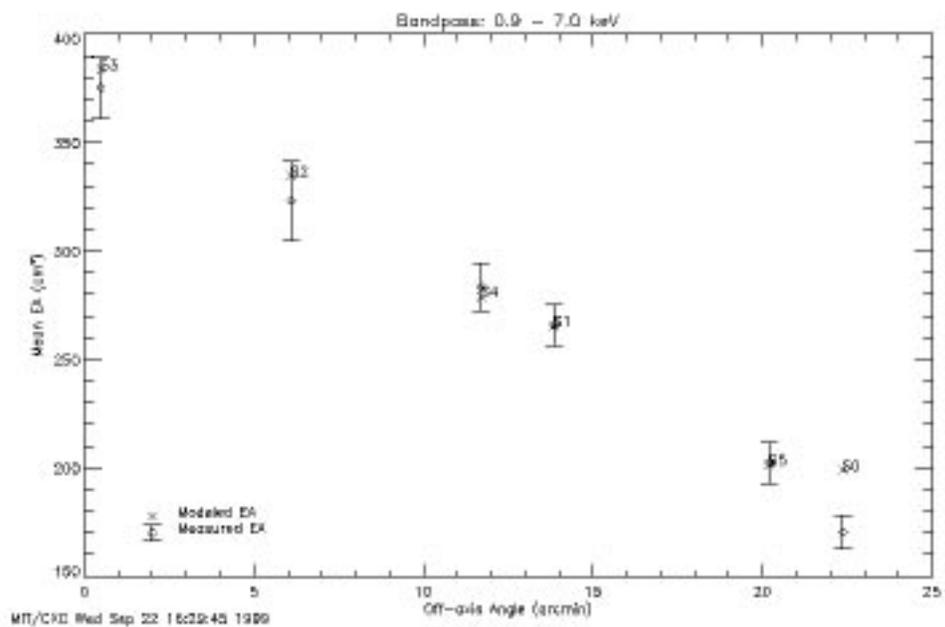
Figure 6.12: A comparison of the predicted and observed effective area (0.9 -7.0 keV) versus off-axis angle for flux at the center of each chip of the ACIS-S array. Standard grades G02346 have been included in this analysis.

since launch corresponding to a decrease in the QE at 670 eV of about 10% per year. Using periodic calibration observations of PKS2155-304 with the LETG we find that the contamination build-up on ACIS amounts to an increase of 0.41 optical depths per year at the C K-edge (284 eV). In the most recent PKS2155-304 observation (taken June 11, 2002), excess absorption at the O K-edge (543 eV) is clearly detected, and there is some suggestion of excess absorption at the N-K edge (410 eV). All indications are that the contamination is uniform across both ACIS-I and ACIS-S.

With the contamination rate constrained, and an assumed hydrocarbon model for the contaminant, a spectral absorption model (*ACISABS*) has been developed that can be adjusted to a specific observing date based on the measured rate of QE degradation at 670 eV. This model can be added as an extra component when fitting ACIS spectra with an uncorrected effective area file (.arf). The tool (corrarf) has been developed and directly applies the *ACISABS* absorption profile to the effective area file generated by the *CIAO* tool 'mkarf'. Using 'corrarf' eliminates the need for observers to include an extra model in their spectral analysis. On the web page (see below) we present several examples that demonstrate the improvement in the spectral analysis of ACIS imaging data using the 'corrarf' tool. Directions on how to obtain and execute these tools are also given below . Since the calibration uncertainties are more pronounced in gratings data, we recommend that the observer include the *ACISABS* model as an additional component in their spectral analysis, with an uncorrected effective area file. This procedure provides more flexibility in analyzing gratings data.

This degradation in the low energy QE may affect the feasibility of some proposals. The effective area curves in *PIMMS*, this document, and those available for use in *MARX* all *predict* ACIS effective area in the middle of AO5.

Caveats, examples, additional information and obtaining tools:

http://cxc.harvard.edu/cal/Acis/Cal_prods/qeDeg/index.html

Gratings & discovery of the problem:

Setting the QE for gratings' analysis:

http://cxc.harvard.edu/ciao/threads/mkgarf_letgacis/#qeset

6.10   On-Orbit Background

There are three components to the on-orbit background. The first is that due to the diffuse X-ray background (most of which may resolve into discrete sources during an observation with *Chandra*). The second component is commonly referred to as the charged particle background. This latter arises both from charged particles, photon, and other neutral particle interactions that ultimately deposit energy in the instrument. The third component depends on the flux from the very objects under observation and is a consequence of the
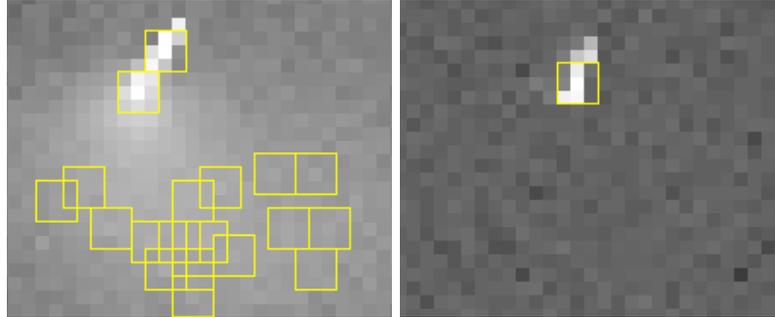
Figure 6.13: Enlarged view of an area of a FI chip I3 (left) and a BI chip (right) after being struck by a charged particle. There is far more "blooming" in the FI image since the chip is thicker. The overlaid 3x3 detection cells indicate that the particle impact on the FI chip produced a number of events, most of which end up as *ASCA* Grade 7, and are thus rejected with high efficiency. The equivalent event in the BI chip, is much more difficult to distinguish from an ordinary x-ray interaction, and hence the rejection efficiency is lower.

"trailing" of the image discussed in Section 6.12.4. Strictly speaking, this last component is only "background" to the extent that one doesn't recognize that it is signal.

The background rates differ between the BI and the FI chips, in part because of differences in the efficiency for identifying charged particle interactions. Figure 6.13 illustrates why.

6.10.1   The non-X-ray background

In September 2002 a 53 ksec 'observation' was carried out with the ACIS in the stowed position but collecting data in normal TE VF mode at -120C. The SIM position was chosen so that the on-board calibration source did not illuminate the ACIS chips. This allowed us to characterize the non-celestial contribution to X-ray background (ie. from charged particles). The resulting spectra is shown in in Figure 6.10.1. Standard grade filtering has been applied; additional VF mode cleaning was not applied. Chip S2 is similar to I023 and not shown for clarity

The flight grade distributions of early measurements the non-X-ray background for the two types of CCDs are shown in Figure 6.15. Although subsequent to these early measurements the CCD temperature has been lowered and the FI devices suffered the effects of the radiation damage, the background is still dominated by the same grades. Based on these data, events from flight grades 24, 66, 107, 214, and 255 are routinely discarded on-board. The total rate of the discarded events is available in the data stream.
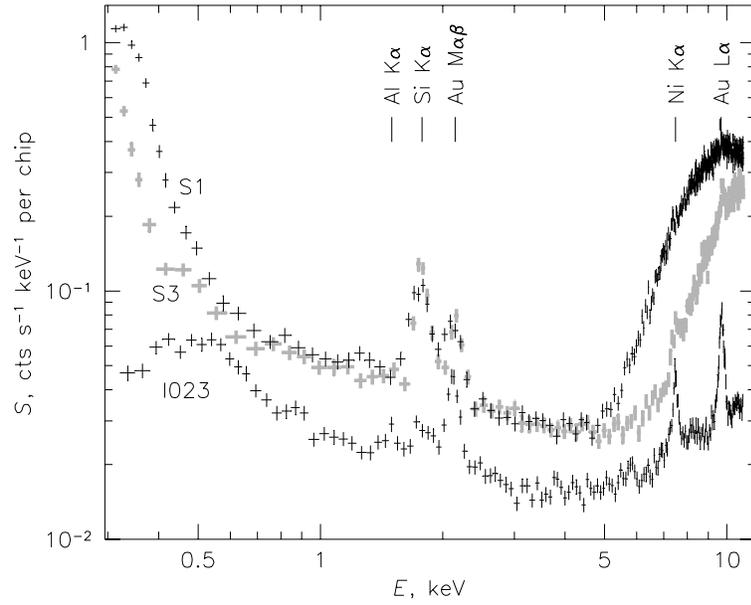
Figure 6.14: Energy spectra of the charged particle ACIS background (standard grade filtering) with ACIS in the stowed position. Line features are due to fluorescence of material in the telescope and focal plane.
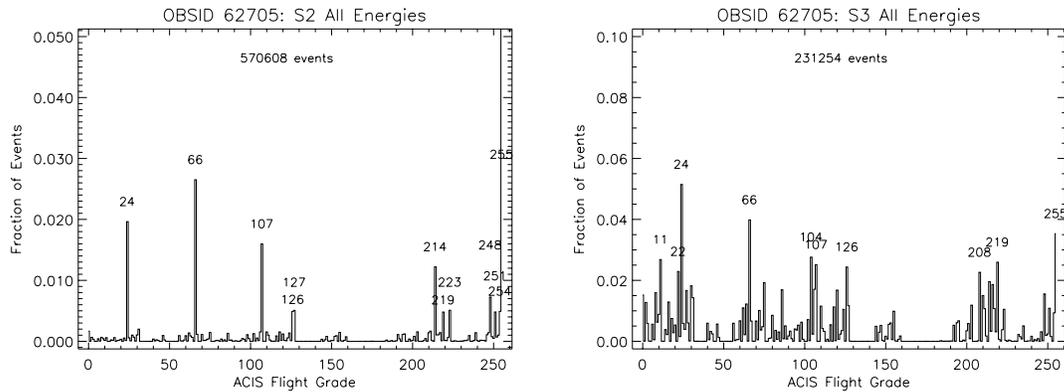
Figure 6.15: Fraction of ACIS background events as a function of grade from early in-flight data for an FI chip (S2) (left) and a BI chip (S3) (right).

6.10.2 The total background

Once the HRMA doors were opened, two more components to the background came into play. The first is the cosmic X-ray background which, for moderately long ($\sim$ 100 ks) observations will be mostly resolved into discrete sources, but, nevertheless, contributes to the overall counting rate. The second is due to any charged particles that may reflect from the telescope and have sufficient momentum so as not to be diverted from the focal plane by the magnets included in the observatory for that purpose, or from secondary particles. Figure 6.16 shows a representative "quiescent" background spectra for both types of CCDs taken after the doors were opened and with no bright sources in the field. The total background counting rates in various energy bands and for the standard grades are given in Tables 6.6 and 6.7. Insertion of the gratings makes little measurable difference in the background rates. Although these rates are slowly changing on the timescale of months, Tables 6.6 and 6.7 can be used for rough sensitivity estimates. Note that Table 6.10.2 includes **all** grades which are telemetered (see Section 6.3 and 6.10.1).

To aid in estimating the probability of telemetry saturation, Table 6.10.2 gives total background count rates for each type of chip, including *all* grades that are telemetered (see Section 6.3). These rates have been declining until Summer 2000, then flat until Summer 2001, and may be starting to increase, apparently anti-correlating the solar cycle.

For aid in planning background-critical observations, the *CXC* has combined a number of deep, source-free exposures (including all components of the background) into experimental quiescent background event files for different time periods. These datasets can be found on the web off the calibration page (http://cxc.harvard.edu/cal/Acis/Cal_prods/bkgrnd/current/background.html).

For data from low counting rate sources taken using the Very Faint (VF) telemetry format (Section 6.13.2), the background can be further reduced in data processing by screening out events with significant flux in border pixels of the 5×5 event islands. This screening leaves the data from faint sources essentially the same while reducing the FI background at different energies: a factor of $\sim$1.4 (E> 6 keV);$\sim$1.1(1-5 keV); and $\sim$2 (near $\sim$0.5 keV). For the BI chips the reductions are: 1.25 (E> 6 keV);$\sim$1.1(1-5 keV); and $\sim$3 (near $\sim$0.3 keV). This screening also eliminates almost all spurious "afterglow" events, caused by the slow leakage of charge deposited from particularly bright cosmic ray hits in subsequent frames. The screening algorithm has been incorporated into the *CIAO* tool "acis_process_events". Further discussion may be found at

http://cxc.harvard.edu/cal/Acis/Cal_prods/vfbkgrnd/index.html

Proposers should be aware that telemetry saturation is more likely for VF format observations, and that they may need minimize the number of CCDs in operation to avoid problems. Proposers should also be aware that if there are bright point sources in the field of view, that the flux is more likely to be piled up in the VF format if the above VF mode screening is applied. However, there is no intrinsic increase of pileup in VF

Table 6.6: Approximate on-orbit standard grade background counting rates with ACIS positioned at the ACIS-I aimpoint, T=-120C. The background rateare cts/s/chip, using only *ASCA* grades 02346, excluding background flares, bad pixels/columns and celestial sources identifiable by eye, Feb 2000 - Oct 2000 without gratings.

Energy Band (keV)	Bkgrd rates (cts/sec)						
	I0	I1	I2	I3	S2	S3	I0123 avg
0.3-10	0.27	0.28	0.27	0.28	0.29	0.74	0.27
0.5-2	0.06	0.06	0.07	0.06	0.07	0.14	0.06
0.5-7	0.16	0.16	0.16	0.17	0.17	0.32	0.16
5.0-10	0.14	0.14	0.13	0.14	0.14	0.42	0.14
10-12	0.08	0.08	0.08	0.08	0.08	0.51	0.08

data, and the screening software can be selectively applied to regions, excluding bright point-like sources. The screening criterion discussed above is then more likely to remove source events (albeit piled up) if the source is bright. Point sources should have count rates *significantly* less than 1 count/sec to be unaffected.

6.10.3   Background variability

In general the background counting rates are stable during an observation. Occasionally, however, there are significant variations, especially in the BI chips as illustrated in Figure 6.17. An early measure (August 1999) showing the frequency of such variations when compared to the quiescent level is shown in Figure 6.18. The user should note the finite probability that the counting rate in the BI CCDs can significantly increase in these circumstances, and thus possibly saturate telemetry – hence the advice to avoid turning on the BI chip(s) unless, of course, necessary for accomplishing the particular scientific objective.

6.10.4   Background in Continuous Clocking Mode

Apart from compressing the data into one dimension (Section 6.12.5), there is essentially no difference in the total background in this mode and that encountered in the timed exposure mode. The background per-sky-pixel, however, will be 1024 times larger, since the sky-pixel is now 1 x 1024 ACIS pixels.
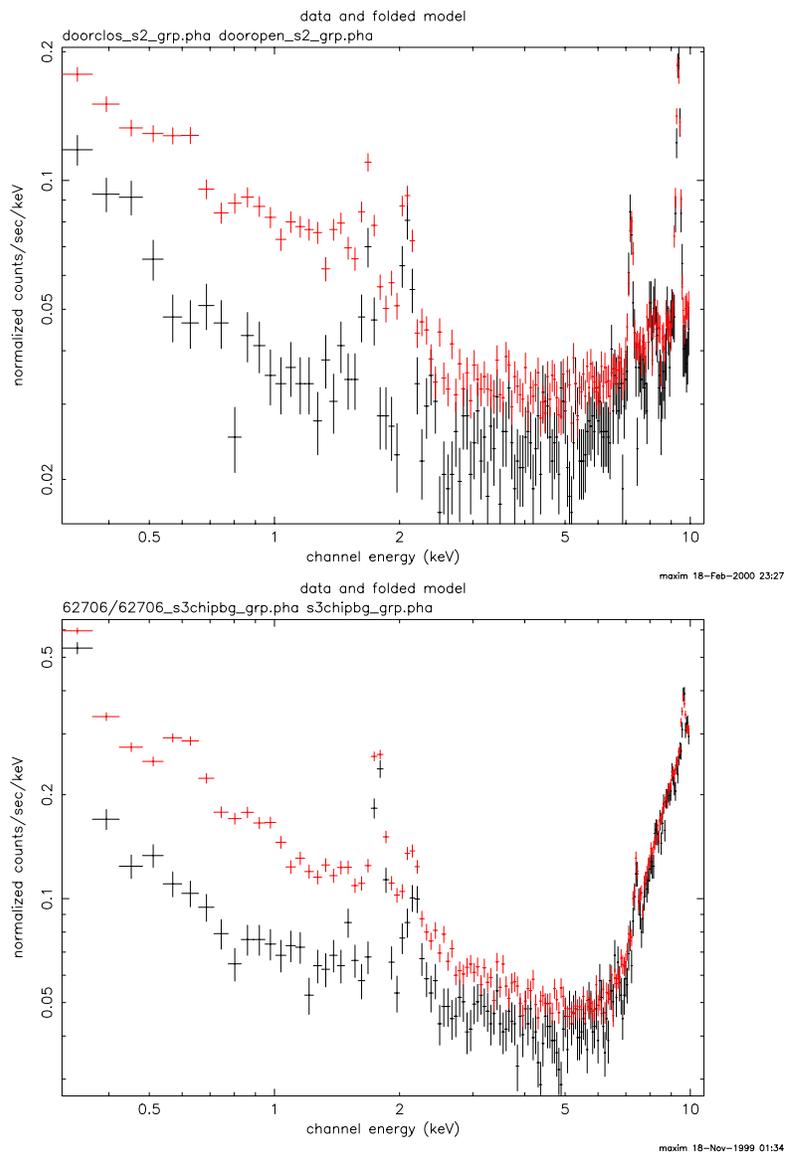
Figure 6.16: ACIS quiescent background spectrum for an FI CCD (s2) (top) and a BI CCD (S3)(bottom). The lower curve shows the spectrum before the HRMA doors were opened; the upper curve after. Both curves have G02346 filtering.

Table 6.7: Approximate on-orbit standard grade background counting rates with ACIS positioned at the ACIS-S aimpoint, T=-120C.

Energy Band (keV)	Bkgrd rates (cts/sec)*						
	I1	I2	I3	S1	S2	S3	S4
0.3-10	0.29	0.29	0.29	1.41	0.33	0.79	0.34
0.5-2	0.07	0.08	0.07	0.19	0.09	0.16	0.10
0.5-7	0.17	0.17	0.17	0.44	0.20	0.35	0.21
5.0-10	0.15	0.14	0.14	0.96	0.16	0.44	0.15
10-12	0.08	0.08	0.08	0.72	0.09	0.53	0.09

*Cts/s/chip, using only *ASCA* grades 02346, excluding background flares, bad pixels/columns and celestial sources identifiable by eye, Feb 2000 - Oct 2000 without gratings.

Table 6.8: Typical total quiescent background rates (cts/s/chip), including *all* grades that are telemetered (not just standard *ASCA* grades), by chip type and upper energy cutoff.

Period	Aug 1999	Fall 2000 – Summer 2001		
Upper E cutoff	15 keV	15 keV	13 keV	10 keV
Chip S2 (FI)	10	6.3	5.8	5.0
Chip S3 (BI)	11	7.7	5.0	2.5
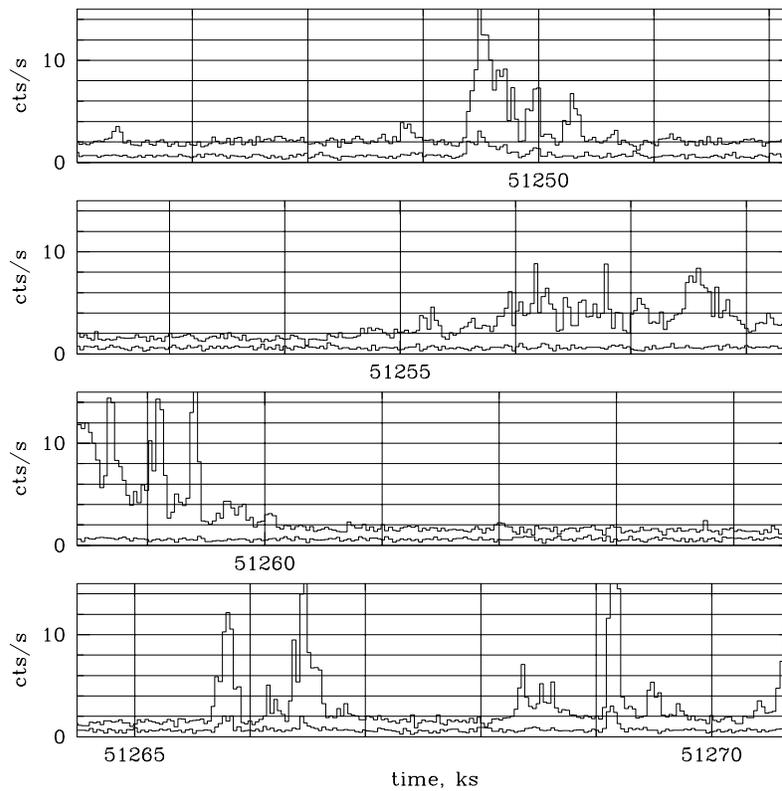
Figure 6.17: An example of the ACIS background counting rate versus time - BI chip (S3; top curve) and an FI chip (I2; bottom curve). These are for the standard grades and the band from 0.3 - 10 keV.
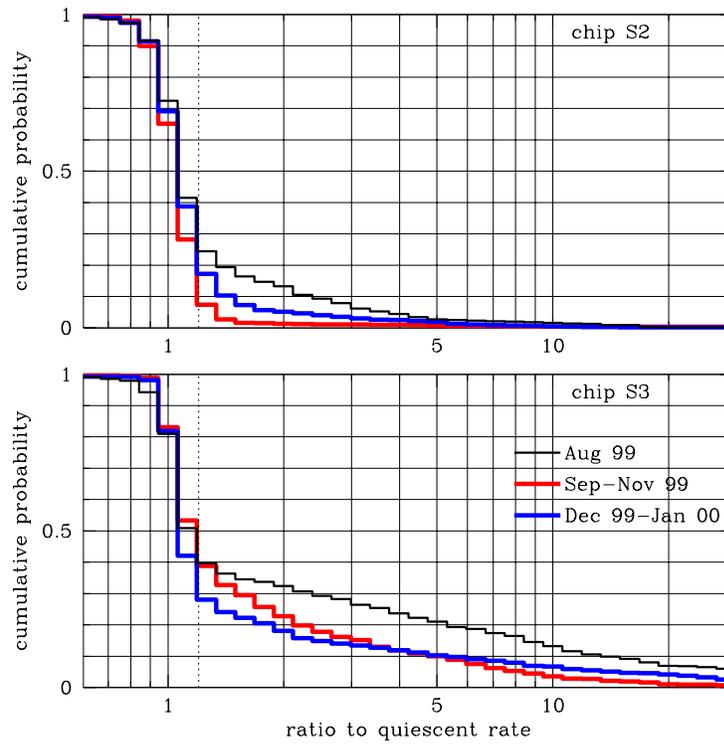
Figure 6.18: An estimate of the cumulative probability that the ratio of the background counting rate to the quiescent background counting rate is larger than a given value for three different time windows. Upper plot for a representative FI chip - S2, and the lower curve for a representative BI chip - S3. The vertical dotted line is a limiting factor 1.2 used in creating the background data sets.
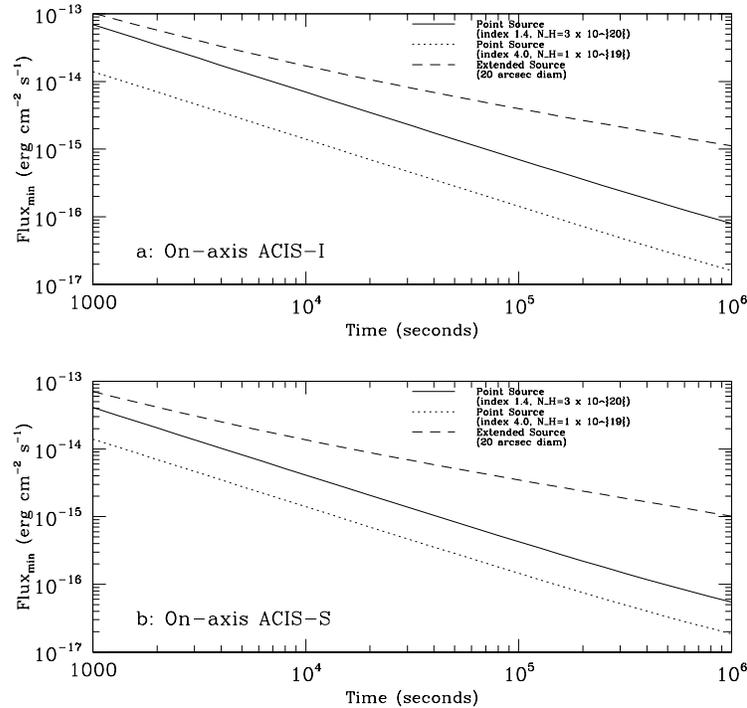
Figure 6.19: The minimum detectable flux as a function of exposure time for an on-axis observation of a point source using an FI chip (top) and a BI chip (bottom). The calculation assumes a 3σ 2-10 keV absorbed *flux* detection criterion in a 5x5 pixel detection cell and *no* pileup. The power law index is a photon index. The extended source spectrum assumed the -1.4 index power law and corresponding column.

6.11   Sensitivity

The ACIS sensitivity for detecting a point source, on axis, during times of quiescent background is approximately $4\text{x}10^{-15}$ ergs cm^{-2} s^{-1} in a 10 ks exposure in the 0.4–6.0 keV band. Necessarily, the sensitivity is a function of energy and depends on which CCD FI(I3) or BI(S3) is selected. Figure 6.19 shows the minimum detectable flux, for a point source and a 20"-diameter extended source for different choices of spectral parameters.

6.12   Operating Modes

Note that the selected operating mode (TE/CC) for the ACIS CCDs applies to all selected CCDs . It is not possible to operate CCDs in different modes simultaneously.

6.12.1   Timed Exposure Mode

A timed exposure refers to the mode of operation wherein a CCD collects data (integrates) for a preselected amount of time - the Frame Time. Once this time interval has passed, the charge from the 1024 x 1024 active region is quickly ($\sim$ 41 ms) transferred to the framestore region and subsequently read out through (nominally) 1024 serial registers.

6.12.2   Frame Times - Full Frames

Frame times are selectable within a range of values spanning the time interval from 0.2 to 10.0 seconds. If the data from the entire CCD are utilized (full frame) then *the nominal (and optimal!) frame time is 3.2s*. Selecting a frame time *shorter* than the nominal value (e.g. to decrease the probability of pileup - Section 6.16) has the consequence that there will be a time during which *no* data are taken, as 3.2s are required for the readout process regardless of the frame time. The fraction of time during which data are taken is simply the ratio of the selected frame time to the sum of this and the nominal frame time – *e.g.* for a new frametime of n ($<$3.2) secs, the fraction of time during which data are taken is n/(3.2+n). We note, strictly speaking, the full-frame time depends on how many CCD s are on – see the equation in Section 6.12.3 – but the differences are very small.

6.12.3   Frame Times & Subarrays

It is also possible for one to select a *subarray* - a restricted region of the CCD in which data will be taken. A subarray is fully determined by specifying the number of rows separating the subarray from the framestore region (q) and the number of rows in the subarray (n). Examples of subarrays are shown in Figure 6.20. The nominal frame time for a subarray depends on (q), (n), and the total number of CCDs that are activated (m) – see Table 6.9. The nominal frame time is given by:

$$T(msec) = 41 \times \text{m} + 2.84 \times \text{n} + 5.2 + 0.040 \times (\text{m} \times \text{q}).$$

As with full frames (Section 6.12.2), selecting a frame time less than the optimum results in loss of observing efficiency. Frame times are rounded up to the nearest 0.1 sec, and can range from 0.2 to 10.0 sec

6.12.4   Trailed Images

It takes 40 μsec to transfer the charge from one row to another during the process of moving the charge from the active region to the framestore region. This has the interesting consequence that each CCD pixel is exposed, not only to the region of the sky at which the observatory was pointing during the long (frame time) integration, but also, for 40 μsec each, to every other region in the sky along the column in which the pixel in question

Table 6.9: CCD Frame Time (seconds) for Standard Subarrays

Subarray	ACIS-I (no. of chips)		ACIS-S (no. of chips)	
	1	6	1	6
1	3.0	3.2	3.0	3.2
1/2	1.5	1.8	1.5	1.8
1/4	0.8	1.1	0.8	1.1
1/8	0.5	0.8	0.4	0.7
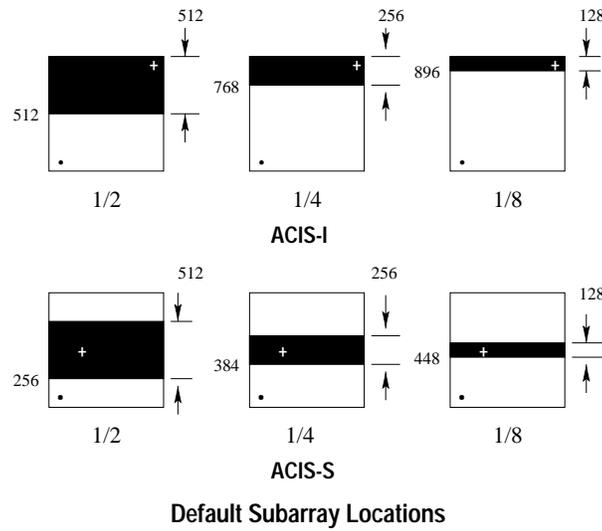
Figure 6.20: Examples of various subarrays. The heavy dot in the lower left indicates the origin
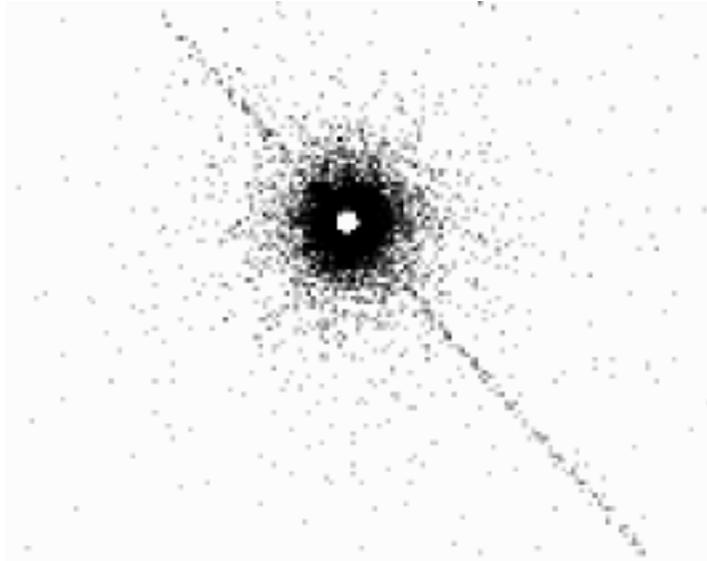
Figure 6.21: Trailed image of a strong X-ray source. The core of the image is faint due to pileup. Most events here are rejected because of bad grades. The readout direction is parallel to the trail.

resides. Figure 6.21 is an example where there are bright features present, so intense, that the tiny contribution of the flux due to trailing is stronger than the direct exposure - hence the trailed image is clearly visible. The user needs to be aware of this phenomenon as it has implications for the data analysis - e.g. estimates of the background. In some cases, the trailed image can be used to measure an unpiled spectrum and can also be used to 40 microsecond timing analyses (of really bright sources).

6.12.5   Continuous Clocking Mode

The continuous clocking mode is provided to allow 3 msec timing at the expense of one dimension of spatial resolution. In this mode one obtains 1 pixel x 1024 pixel images, each with an integration time of 3 msec. Details as to the spatial distribution in the columns are lost - other than that the event originated in the sky along the line determined by the length of the column.

   In the continuous clocking mode, data is continuously clocked through the CCD and framestore. The instrument software accumulates data into a buffer until a virtual detector of size 1024 columns by 512 rows is filled. The event finding algorithm is applied to the data in this virtual detector and 3 x 3 event islands are located and recorded to telemetry in the usual manner. This procedure has the advantage that the event islands

are functionally equivalent to data accumulated in TE mode, hence differences in the calibration are minimal. The row coordinate (called CHIPY in the FITS file) maps into time in that a new row is read from the framestore to the buffer every 2.85 msec. This does have some minor impacts on the data. For example, since the event-finding algorithm is looking for a local maximum, it cannot find events on the edges of the virtual detector. Hence CHIPX cannot be 1 or 1024 (as in TE mode). Moreover, CHIPY cannot be 1 or 512. In other words, events cannot occur at certain times separated by 512*2.85 msec or 1.4592 sec. Likewise, it is impossible for two events to occur in the same column in adjacent time bins.

6.13 Bias Maps and Telemetry Formats

6.13.1 Bias Maps

In general the CCD bias, the amplitude of the charge in each pixel in the absence of external radiation, is determined at various times - every change of mode when ACIS is in place at the focus of the telescope. These bias maps have proven to be remarkably stable and are automatically applied in routine data processing.

6.13.2 Telemetry Formats

There are a number of telemetry formats available. Specifying a format determines the type of information that is included in the telemetry stream. The number of bits per event depends on which mode and which format is selected. The number of bits per event, in turn, determines the event rate at which the telemetry will saturate and data will be lost until the on-board buffer empties. The formats available depend on which mode (Timed Exposure or Continuous Clocking) is used. The modes, associated formats, and approximate event rates at which the telemetry saturates and one begins to limit the return of data, are listed in Table 6.10. The formats are described in the following paragraphs. Event "arrival time" is given relative to the beginning of the exposure in TE mode, or relative to read out in CC mode.

Faint   Faint format provides the event position in detector coordinates, an arrival time, an event amplitude, and the contents of the 3 x 3 island that characterizes the event grade. The bias map is telemetered separately. Note that certain grades may be not be included in the data stream (Section 6.10.1).

Graded   Graded format provides event position in detector coordinates, an event amplitude, the arrival time, and the event grade. Note that certain grades may be not be included in the data stream (Section 6.10.1).

Table 6.10: Telemetry Saturation Limits

Mode	Format	Bits/event	Events/sec*	Number of Events in full buffer
CC	Graded	58	375.0	128,000
CC	Faint	128	170.2	58,099
TE	Graded	58	375.0	128,000
TE	Faint	128	170.2	58,099
TE	Very Faint	320	68.8	23,273

*(includes a 10% overhead for housekeeping data)

Very Faint   Very Faint format provides the event position in detector coordinates, the event amplitude, an arrival time, and the pixel values in a 5 x 5 island. As noted in Table 6.10, this format is only available with the Timed Exposure mode. Events are still graded by the contents of the central 3 x 3 island. Note that certain grades may be not be included in the data stream (Section 6.10.1). This offers the advantage of reduced background after ground processing (see Section 6.10.2) but only for sources with low counting rates that avoid both telemetry saturation and pulse pileup.

6.14   Calibration

Calibration of ACIS includes laboratory calibrations, a system-level ground calibration of the HRMA and ACIS at the X-Ray Calibration Facility (XRCF) at MSFC, and on-orbit calibration using celestial and on-board radioactive X-ray sources.

The on-orbit calibration of ACIS is an on-going activity. All calibration data are, or will be, described in detail, at http://cxc.harvard.edu/cal/

The user is urged to consult the WWW site and its pointers for the latest information.

6.15   Hot Pixels and Columns

Hot columns and pixels are defined to be those which produce a high spurious or saturated pulse-height for a large number of consecutive frames of data. These depend on operating conditions such as temperature. One should always refer to the *CXC* web site for the most recent list. To date, S1 is the device with the largest number of such pixels and columns.

on axis

2 arcmin off axis

4 arcmin off axis

7 arcmin off axis
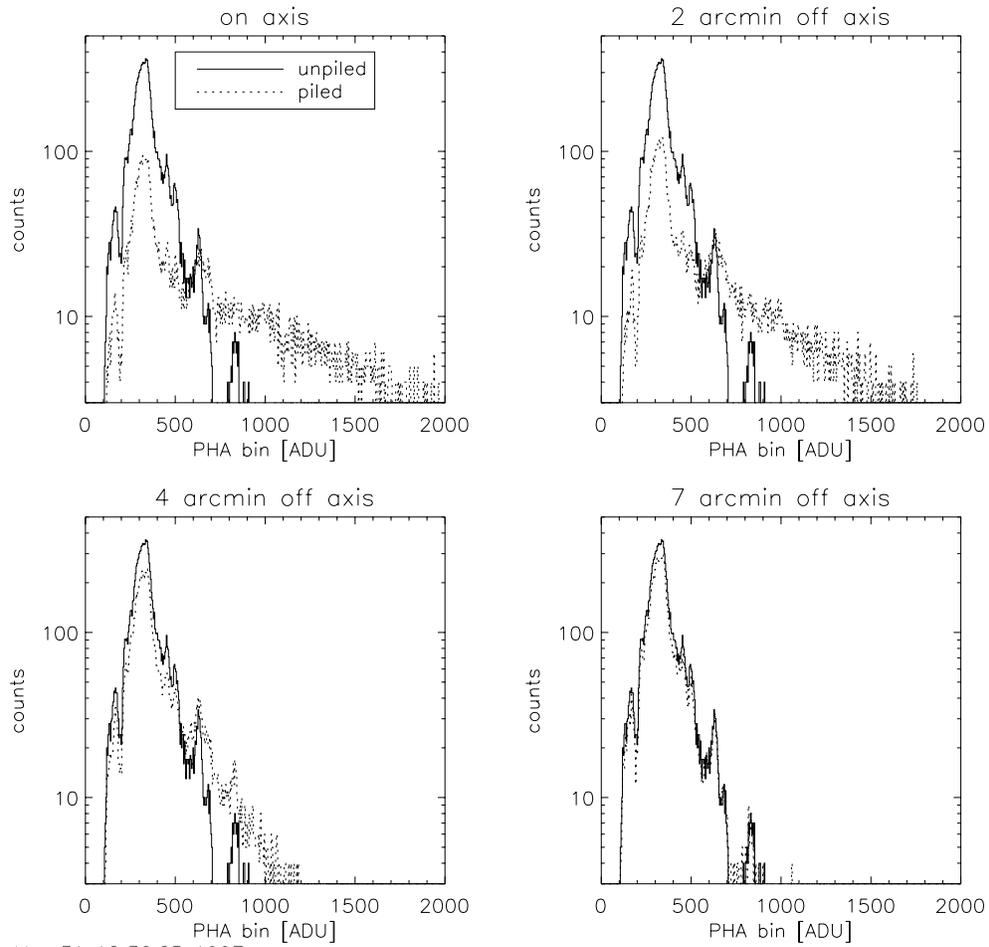
Mon Mar 31 12:36:25 1997

Figure 6.22: MARX simulations of the effect of pileup on the shape of the spectrum. The true (solid line) and the detected (dotted line) spectra are shown for four different viewing angles. The corresponding "pileup fractions" - see Section 6.16.2 - are 46%, 40%, 15%, and 2% as the image is moved progressively further off-axis. (Source: J. Kastner and M. Wise, *CXC*)
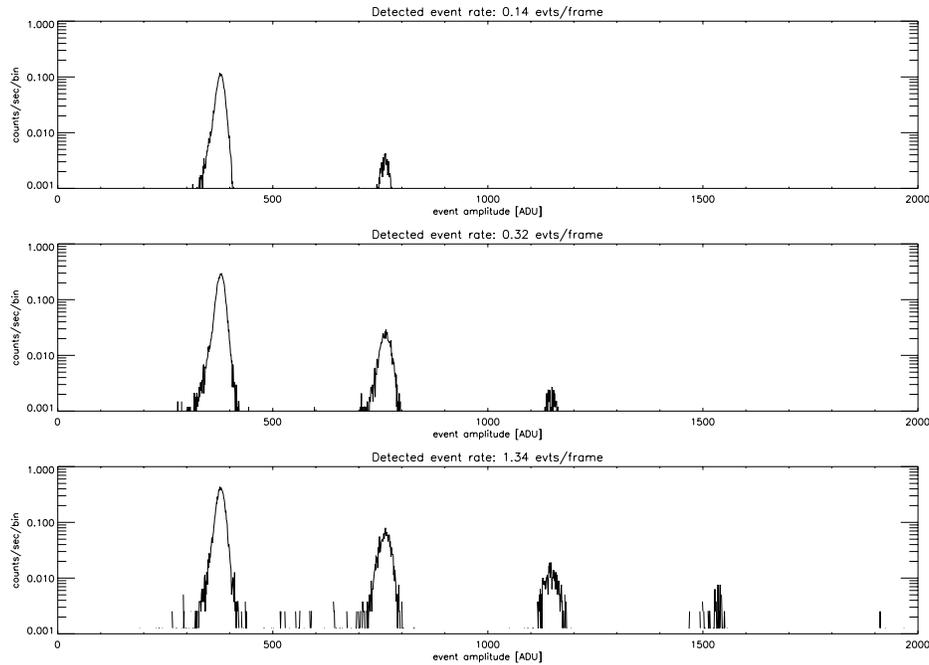
Figure 6.23: The effects of pileup at 1.49 keV (Al Kα) as a function of source intensity. Data were taken during HRMA-ACIS system level calibration at the XRCF. Single-photon events are concentrated near the pulse height corresponding to the Al Kα line ($\sim$ 380 ADU), and events with 2 or more photons appear at integral multiples of the line energy.

6.16   Pileup

Pileup results when two or more photons are detected as a single event. The fundamental impacts of pileup are: (1) a distortion of the energy spectrum - the apparent energy is approximately the sum of two (or more) energies; and (2) an underestimate as to the correct counting rate - two or more events are counted as one. A simple illustration of the effects of pileup is given in Figure 6.23. There are other, somewhat more subtle impacts discussed below (6.16.1).

The degree to which a source will be piled can be estimated roughly from *PIMMS*. Somewhat more quantitative estimates can be obtained using the pileup models in *XSPEC* ,*Sherpa* and *ISIS* . If the resulting degree of pileup appears to be unacceptable given the objectives, then the proposer should employ some form of pileup mitigation (Section 6.16.3) as part of the observing strategy. In general, pileup should not be a problem in the observation of extended objects, the Crab Nebula being a notable exception, unless the source has bright knots or filaments.

Table 6.11: *ASCA* Grade Distributions for different Incident Fluxes at 1.49 keV (Al-Kα, based on data taken at the XRCF during ground calibration using chip I3; *CXC* Calibration Group)

Incident Flux*	G0	G1	G2	G3	G4	G5	G6	G7
9	0.710	0.022	0.122	0.053	0.026	0.009	0.024	0.035
30	0.581	0.057	0.132	0.045	0.043	0.039	0.029	0.073
98	0.416	0.097	0.127	0.052	0.050	0.085	0.064	0.108
184	0.333	0.091	0.105	0.040	0.032	0.099	0.077	0.224

*arbitrary units

6.16.1 Other consequences of pileup

There are other consequences of pileup in addition to the two principal features of spurious spectral hardening and underestimating the true counting rate by under counting multiple events. These additional effects are grade migration and pulse saturation, both of which can cause distortion of the apparent *PSF*.

Grade migration Possibly the most troubling effect of pileup is that the nominal grade distribution that one expects for X-ray events changes. The change of grade introduced by pileup has become to be referred to as "grade migration". Table 6.11 shows an example of grade migration due to pileup as the incident flux is increased. In this simple test, which involved only monoenergetic photons, the largest effect is the depletion of G0 events and the increase of G7 events. In general, as the incident flux rate increases, the fraction of the total number of events occupying a particular event grade changes as photon-induced charge clouds merge and the resulting detected events "migrate" to other grades which are not at all necessarily included in the standard (G02346) set. If one then applies the standard calibration to such data, the true flux will be under-estimated.

Pulse Saturation One consequence of severe instances of pileup is the creation of a region with no events! In this case the pileup is severe enough that the total amplitude of the event is larger than the on-board threshold (typically 15 keV) and is rejected. Holes in the image can also be created by grade migration of events into ACIS grades (e.g. 255) that are filtered on-board.
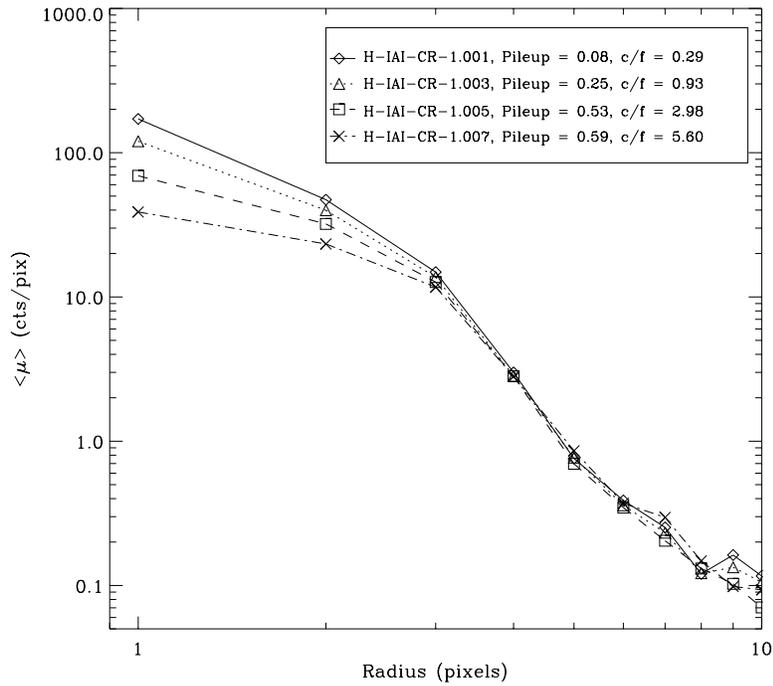
Figure 6.24: The effects of pileup on the radial distribution of the *PSF* are illustrated. These data were taken during ground calibration at the XRCF. The specific "OBSIDs", the counting rate per CCD frame ("c/f"), and the "pileup fraction" as defined in Section 6.16.2 are given in the inset.

PSF **distortion**   Obviously the effects of pileup are severest when the flux is highly concentrated on the detector. Thus, the core of the *PSF* suffers more from pileup induced effects than the wings. Figure 6.24 illustrates this point.

6.16.2   Pileup Estimation

It is clearly important in preparing a *Chandra* observing proposal to determine if the observation will be impacted by pileup, and if so, decide what to do about it (or convince the peer review why the specific objective can be accomplished without doing anything). There are two approaches to estimating the impact of pileup on the investigation. The most sophisticated uses the pileup models in *XSPEC* , *Sherpa* , and *ISIS* to create a simulated data set which can be analyzed in the same way as real data. A less sophisticated, but very useful, approach is to use the web version of *PIMMS* to estimate pileup or to use the figures in this chapter.

Simple Pileup Estimates   The pileup fraction is the ratio of the number of detected events that consist of more than one photon to the total number of detected events. An estimate of the pileup fraction can be determined from Figure 6.25. The algorithm parameterizes the HRMA+ACIS   *PSF* in terms of the fraction of encircled energy that falls within the central 3×3 pixel event detection cell, ϵ, and assumes that the remaining energy is uniformly distributed among the 8 surrounding 3×3 pixel detection cells. The probabilities of single- and multiple-photon events are calculated separately for the central and surrounding detection cells and subsequently averaged (with appropriate weighting) to obtain the pileup fraction as a function of the true count rate - the *solid* line in Figure 6.25. The model was tested against data taken on the ground under controlled conditions - also shown in Figure 6.25.

As a general guideline, if the estimated pileup fraction is $> 10\%$ the proposed observation is very likely to be impacted. The first panel (upper left) in Figure 6.22 qualitatively illustrated the effect on a simulated astrophysical x-ray spectrum. *However, the degree of pileup that is acceptable for a particular objective will depend on the particular scientific goals of the measurement, and there is no clear-cut tolerance level.* If one's scientific objective demands precise flux calibration, then the pileup fraction should probably be kept well below the 10% number discussed above.

The PIMMS tool provides the pileup fraction using the algorithm described here, both for direct observation with ACIS and also for the zeroth-order image when a grating is inserted.

Simulating Pileup   John Davis at MIT has developed an algorithm for modeling the effects of pileup on ACIS spectral data. The algorithm has been implemented in *XSPEC* V11.1 and in *Sherpa* V2.2. The algorithm can be used to attempt to recover
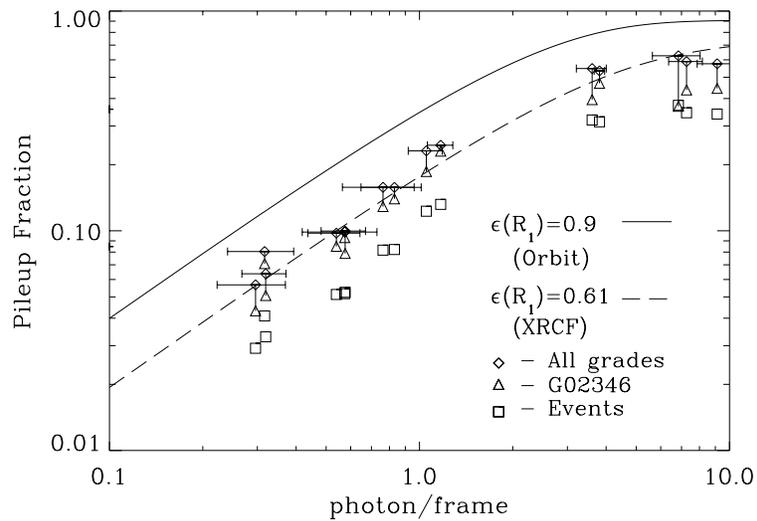
Figure 6.25: The pileup fraction as a function of the the counting rate (in the absence of pileup in units of photons/frame). The solid line is for on-orbit, the dashed line and the data points are for, and from, ground-based data respectively. The difference between the ground and flight functions are a consequence of the improved *PSF* on-orbit, where gravitational effects are negligible - see Chapter 4. Note that when pileup occurs there are two or more photons for each event, so the fraction of events with pileup is always less than the fraction of photons with pileup.

the underlying spectrum from a source, or to simulate the effects of pileup for proposal purposes.

The algorithm has been tested by comparing CCD spectra with grating spectra of the same sources. Care should be taken in applying the algorithm - for example, using the appropriate regions for extracting source photons and avoiding line-dominated sources. A description of the algorithm can be found in Davis 2001 (Davis, J.E. 2001, ApJ, 562, 575). Details on using the algorithm in *Sherpa* will be given in a *Sherpa* "thread" for *CIAO* V2.2 on the CXC CIAO web page: http://cxc.harvard.edu/ciao/.

6.16.3 Reducing Pileup

We summarize here various methods which can be used to reduce pileup.

Shorten exposure time: By cutting back on CCD exposure time, the probability of pileup decreases. The user is advised to select the best combination of a subarray and frametime in order to avoid losing data as discussed in Section 6.12.3.

Use the Alternating Exposure option: This option simply alternates between exposures that are subject to pileup and those that are not. The capability was originally developed for use with certain grating observations to allow one to spend some time obtaining useful data from a zeroth order image, which would otherwise be piled up.

Use CC mode If two-dimensional imaging is not required, consider using CC mode (Section 6.12.5).

Insert a transmission grating: Inserting either the HETG (Chapter 8) or the LETG (Chapter 9) will significantly decrease the counting rate as the efficiency is lower. The counting rate in the zero order image may then be low enough to avoid pileup.

Offset point: Performing the observation with the source off-axis spreads out the flux and thus decreases the probability of pileup at the price of a degraded image. Figure 6.22 illustrated the impact.

Defocus: The option is only listed for completeness, the option is *not* recommended or encouraged.

6.17 Bright Source X-ray Photon Dose Limitations

Pre-Flight radiation tests on devices similar to the ACIS chips have shown that ~200 krads of X-ray photon dose can positively damage the CCDs. The mechanism for the damage is the trapped ionization in the dielectric silicon oxide and nitride separating the

gates from the depletion region. Since the charge is trapped, the damage is cumulative. Because the structure of the BI's differs significantly from that of the FI's, the two sets of chips have different photon dose limitations. Specifically, the BI's are more than 25 times as tolerant of X-ray photon dose as compared to the FI's since the former have 40 μm of bulk Si 'protecting' the gate layer.

Simulations of several realistic astrophysical sources have yielded a very conservative spectrally-averaged correspondence of 100 counts/pix = 1 rad. (By 'counts' in this context we mean all photons that impinged on the detector, whether or not they were piled-up and discarded.)

In consultation with the IPI team the CXC has adopted the following mission allowances, per pixel of the two types of chips:

FI chips: 25 krads   2,500,000 cts/pix

BI chips: 625 krads 62,500,000 cts/px

If your observation calls for observing a bright point-like source close to on-axis, we suggest you use the *MARX* simulator (with the parameter DetIdeal=yes & dither, typically, on) to calculate whether your observation may reach 1% of the above mission limits in any one pixel. If so, please contact the *CXC* HelpDesk in order to custom design an observational strategy which may accommodate your science aims, while maintaining the health & safety of the instrument.

6.18   Observing Planetary and Solar System Objects with ACIS

Chandra has successfully observed several solar system objects, including Venus, the Moon, Mars, Jupiter and several comets. Observation of planets and other solar system objects is complicated because these objects move across the celestial sphere during an observation and the optical light from the source can produce a significant amount of charge on the detectors (this is primarily an issue for ACIS-S observations). Some information regarding observation planning and data processing is given here. Users are encouraged to contact the *CXC* for more detailed help.

6.18.1   Observations with ACIS-I

Any solar system object can be observed with ACIS-I. Previous solar system observations with ACIS-I have not revealed significant contamination from optical light. However, proposers are encouraged to work with the *CXC* when planning the specifics of a given observation. Since the source moves across the celestial sphere in time, an image of the event data will exhibit a "streak" associated with the source. The *CIAO* tool sso_freeze

can be used to produce an event data file with a pair of coordinates that have the motion of the source removed.

6.18.2   Observations with ACIS-S

The ACIS-Sarray can be used with or without a grating. The back-illuminated CCDs in the S array (chips S1 and S3) are more sensitive to soft X-rays than the I array CCDs, but the entire S array suffers from the disadvantage that its optical blocking filter is thinner than for ACIS-S and may transmit a non-negligible flux of visible light onto the CCDs. It is thus necessary to estimate the amount of charge produced in the CCDs due to the optical light. More detailed information can be found at http://www.astro.psu.edu/xray/docs/cal_report/ and from the *CXC* via Helpdesk.

If the optical light leak is small enough, it can be mitigated by simply shortening the frame time. This leads to a linear drop in the number of ADU due to optical light. If possible, VF mode should be used, since in this mode the outer 16 pixels of the 5x5 region allows a "local" bias to be subtracted from the event to correct for any possible light leakage.

The optical light also invalidates the bias taken at the beginning of the observation if a bright planet is in the field. It is therefore desirable to take a bias frame with the source out of the field of view. This bias map is useful even when processing 5x5 pixels in VF mode since it can be employed as a correction to the local average "bias" computed from the 16 outer pixels, thereby correcting for hot pixels, cosmetic defects etc.

A more sophisticated approach to dealing with excess charge due to optical light is to make an adjustment to the event and split thresholds. Event grades are described in more detail in Section 6.3. Excess charge (in adu) due to optical light will be added to the event and split counters on-board. Without an adjustment to the thresholds (or a large enough one), many of the X-ray events may have all nine pixels of a 3 pixel X 3 pixel event detection cell above the split threshold, in which case the event will not be telemetered to the ground. If the adjustment is too large, X-ray events may not be detected because they may not exceed the event threshold.

Users should be aware that if the detection thresholds are adjusted, standard *CXC* processing of planetary data will give inaccurate estimates of event pulse heights and GRADEs. A thorough understanding of the energy calibration process and manual massaging of the data will be required

6.19   Observing with ACIS- the input parameters

This section describes the various inputs that either must be, or can be, specified in order to perform observations with ACIS. The sub-sections are organized to match the RPS form. We have added some discussion as to some of the implications of the possible

choices. As emphasized at the beginning of the Chapter, ACIS is moderately complex and the specific characteristics of the CCDs and their configuration in the instrument lead to a number of alternatives for accomplishing a specific objective - *detailed trade-offs are the responsibility of the observer.* Thus, e.g. it might seem obvious that observations of a faint point source may be best accomplished by selecting the ACIS-S array with the aim point on S3, the BI device that can be placed at the best focus of the telescope, and the CCD with the best average energy resolution. On the other hand, perhaps the science is better served by offset pointing (by a few arcminutes) the target onto S2, very near to the framestore, where the FI energy resolution is better than that of S3. On the other hand, if the object is very faint, so that the number total number of photons expected is just a handful – not enough to perform any significant spectroscopy – the advantage of S2 nor S3 may not be so obvious considering the smaller field of view, and perhaps the ACIS-I array, which would optimize the angular resolution over a larger field, may be more attractive.

6.19.1   Required Parameters

There are certain ACIS input parameters that must be specified: the number and identity of the CCDs to be used, the Exposure Mode, and the Event Telemetry Format. If pileup and telemetry saturation are not considered to be a problem for the observation, then these are the only parameters that need to be specified.

• **Number and Choice of CCD**

Up to six CCDs can be operated at once. Specifying ACIS-S turns on S0-S5 and sets the aimpoint. Specifying ACIS-I turns on I0-I3, S2 and S3, and sets the aimpoint. For any other combination, the identity of the CCDs and the desired aimpoint will have to be specified.

• **Exposure Mode**

There are only two choices: Timed Exposure (Section 6.12.1) or Continuous Clocking (Section 6.12.5).

Timed Exposure Mode   The timed exposure mode with the default nominal (and optimal) frame time of 3.2s is the typical mode for ACIS observations. Note that the option of selecting frame times shorter than nominal reduces observing efficiency, and hence the number of photons collected for a given observation time.

Continuous Clocking Mode   The Continuous Clocking mode is useful when timing data are so critical and/or pileup is such a problem that the sacrifice of one dimension of

spatial data is warranted. The use of continuous clocking may also lead one to consider specifying a particular satellite roll orientation (see Chapter 3) in order to avoid having two different sources produce events in the same CCD column.

6.19.2   Optional Parameters

Alternating Exposures   This option applies *only* to Timed Exposures. The parameters specifying an Alternating Exposure are:

- the number of secondary exposures per primary exposure (1-15)

- the primary exposure frame time

- the secondary exposure frame time (default the optimum frame time)

Frame times and efficiencies in TE mode are discussed in Sections 6.12.2 and 6.12.3.

Energy Filtering

It is possible to remove events from the telemetry stream, and thus avoid telemetry saturation, by specifying an energy acceptance filter within which detected events will be telemetered. The default discards events above 3750 ADU (nominally 15 keV). The total per-chip background rates for different upper energy cut-offs are in Table 6.10.2.

Spatial Windows

A more sophisticated approach to removing data from the telemetry stream, and thus avoiding telemetry saturation, is by the use of a Spatial Window. This option offers a good deal of flexibility. One may define up to 6 Spatial Windows per CCD. Each window can be placed anywhere on the chip. Note there is a significant difference between a Spatial Window and a Subarray (Section 6.12.3): Subarrays affect the transmission of CCD data to the on-board ACIS processors; Spatial Windows select events detected by the processors and only impact the telemetry rate. The user may also specify the window energy threshold and energy range.

Spatial windows can be inclusive or exclusive - in which case the sample rate is irrelevant. A Spatial Window could be used to eliminate a bright, off-axis source that would otherwise overwhelm the telemetry stream. The order in which the spatial windows are specified is important if they overlap.

6.19.3   Non-ACIS Parameters Relevant to an Observation with ACIS

There are a small number of additional parameters that need to be considered in specifying an observation with ACIS: (1) the off-axis pointing (if required), which reduces the flux, and spreads out the image; (2) the roll angle (Chapter 4; (3) time constraints (if any); and (4) time monitoring intervals (if any).

Chapter 7

High Resolution Camera (HRC)

7.1   Introduction and Instrument Layout

The High Resolution Camera (HRC) is a microchannel plate (MCP) instrument comprised of two detectors, one optimized for imaging (HRC-I), and one (HRC-S) serves as a readout for the Low Energy Transmission Grating (LETG) discussed in Chapter 9. The HRC-I provides the largest field-of-view ($\sim 30' \times 30'$) of any detector aboard *Chandra*, and its response extends to energies below the sensitivity of the ACIS (Chapter 6), albeit without comparable spectral resolution. The time resolution of the HRC detectors (16 μsec) is the best on the observatory, but can only be exploited under certain conditions as discussed in Section 7.10.

A schematic of the HRC layout is shown in Figure 7.1, and a summary of the characteristics is given in Table 7.1. A cross-section of the HRC-S layout, the relationship to the optical axis and to the LETG Rowland circle is shown in Figure 7.2.

The HRC is a direct descendant of the Einstein (Giacconi *et al.* 1979) and ROSAT High Resolution Imagers (HRIs) (David *et al.* 1996). The ROSAT HRI had the same coating (CsI) as the HRC.

The Instrument Principal Investigator is Dr. Stephen S. Murray of the Smithsonian Astrophysical Observatory.

7.2   Basic Principles

Figure 7.3 illustrates the features of the HRC MCPs. X-rays enter through an UV/Ion shield, necessary in order to reduce/avoid signals from UV light, ions, and low energy electrons. Most of these X-rays are then absorbed in the CsI-coated walls of the first (input) of two consecutive MCPs. The axes of the millions of tubes that comprise the input and output MCPs are not parallel to the optical axis but are canted ("biased") at
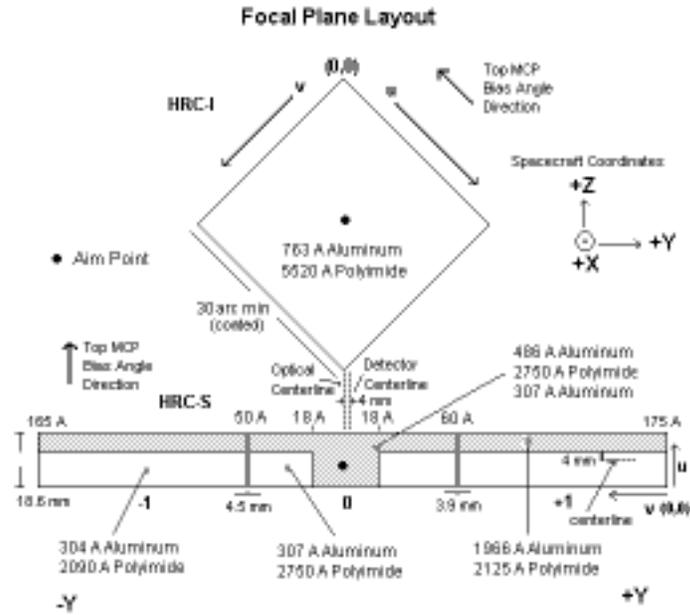
Figure 7.1: A schematic of the HRC focal plane geometry as viewed along the optical axis from the telescope towards the focal plane.
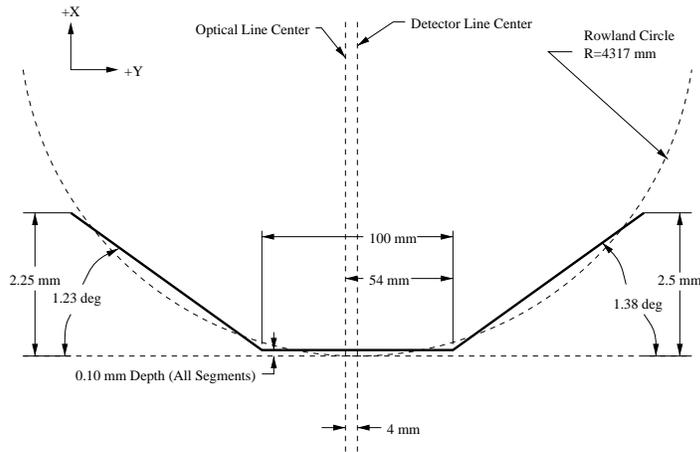
Figure 7.2: A schematic cross-section of the HRC-S MCP (not to scale). The HRC-S is shifted 0.1 mm forward of the tangent plane, so the Rowland circle intersects each segment at two points.

Table 7.1: HRC Parameters

Focal Plane Arrays		
HRC-I:	CsI-coated MCPpair	90×90 mm coated
		$(93 \times 93$ mm open)
HRC-S:	CsI-coated MCPpairs	3-100 $\times$ 20 mm
Field of view	HRC-I:	$\sim 30 \times 30$ arcmin
	HRC-S:	6×99 arcmin
MCP Bias angle:		$6°$
UV/Ion Shields:		
	HRC-I:	5520 Å Polyimide, 763 Å Al
	HRC-S:	
	Inner segment	2750 Å Polyimide, 307 Å Al
	Inner segment "T"	2750 Å Polyimide, 793 Å Al
	Outer segment	2090 Å Polyimide, 304 Å Al
	Outer segment (LESF)	2125 Å Polyimide, 1966 Å Al
Spatial resolution	FWHM	$\sim 20\mu$m, ~ 0.4 arcsec
	HRC-I: pore size	10μm
	HRC-S: pore size	12.5μm
	HRC-I: pore spacing	12.5μm
	HRC-S: pore spacing	15μm
	pixel size (electronic readout)	6.42938μm
		$[0.13175$ arcsec pixel$^{-1}]$
Energy range:		$0.08 - 10.0$ keV
Spectral resolution	$\Delta E/E$	~ 1 @1keV
MCP Quantum efficiency		30% @ 1.0 keV
		10% @ 8.0 keV
On-Axis Effective Area:	HRC-I, @ .277 keV	$133\,\text{cm}^2$
	HRC-I, @ 1 keV	$227\,\text{cm}^2$
Time resolution		16 μsec (see Section 7.10)
Limiting Sensitivity	point source, 3σ detection in 3×10^5 s	$9 \times 10^{-16}\text{erg}\,\text{cm}^{-2}\,\text{s}^{-1}$
	(power law spectrum: $\alpha = 1.4$,	
	$N_H = 3 \times 10^{20}$ cm^{-2})	
On-orbit	HRC-I	9×10^{-6} cts s^{-1} arcsec^{-2}
quiescent background	HRC-S	1.8×10^{-4} cts s^{-1} (res. elm.)$^{-1}$
(prior to ground processing)		(0.07Å$\times$ 0.1 mm)
Intrinsic dead time		50 μs
Constraints:	telemetry limit	184 cts s^{-1}
	maximum counts/observation/aimpoint	450000 cts
	linearity limit (on-axis point source)	
	HRC-I	~ 5 cts s^{-1} (2 cts s^{-1} pore^{-1})
	HRC-S	~ 25 cts s^{-1} (10 cts s^{-1} pore^{-1})
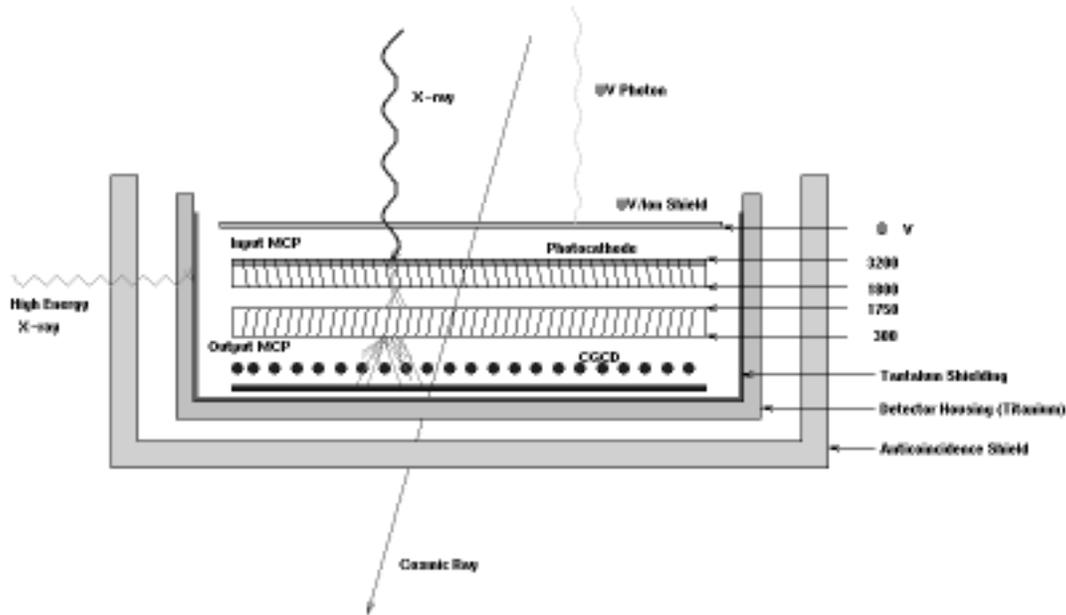
Figure 7.3: A schematic of the HRC Micro-channel-Plate detector.

an angle of 6°, but in opposite directions as shown. This bias is introduced to improve the probability of an interaction. The CsI coating serves to enhance the photoemission over that from a bare MCP. The resulting photoelectrons are then accelerated by an applied electric field. The next interaction with the walls releases several secondary electrons and so on until a cascade of electrons is produced.

One purpose of the second (output) MCP is to provide additional gain. In addition, reversing the direction of the second MCPs bias angle with respect to the first removes a clear path for positive ions, and hence reduces the possibility of (positive) ion feedback - wherein an accelerated ion moving in the opposite direction as that of the electrons ends up causing the release of electrons and starts the process all over again.

The electron cloud — typically about 2×10^7 electrons per photon — that emerges from the output MCP is accelerated towards a position-sensitive charge detector. The HRC employs two types of charge detectors: HRC-I uses a crossed grid charge detector; the HRC-S uses a hybrid where one axis is comprised of wires, while the other has gold lines deposited on a ceramic substrate. Adjacent wires (or lines) are resistively connected and every eighth wire is attached to a charge-sensitive amplifier, referred to as a "tap", as illustrated in Figure 7.4.

The X-ray position is determined by calculating the centroid of the charge cloud exiting

the rear MCP via the "three tap algorithm". In short, the three tap algorithm determines the charge cloud centroid using a combination of digital and analog electronics and off-line processing. Fast discriminators and logic circuits first determine a "coarse" position, which is based on the amplifier with maximum detected charge. Analog switches then select the three amplifiers centered on that coarse position and steer them to analog to digital converters. The coarse position and three digitized values are then telemetered to the ground and used off-line to calculate the event position. This process is performed for each axis. The reconstructed X-ray position can then be written as the sum of a coarse position and a charge centroid term centered on the coarse position:

$$pos = cp_i + (\frac{Q_{cp_{i+1}} - Q_{cp_{i-1}}}{Q_{cp_{i-1}} + Q_{cp_i} + Q_{cp_{i+1}}}) \times \Delta \tag{7.1}$$

where cp is the coarse position, $Q_{cp_{i+1}}$ is the charge measured on the cp_{i+1} tap, and Δ is the distance between taps. Since the charge cloud extends beyond the two outer taps, each of the outer amplifiers underestimates the amount of charge needed to calculate the true centroid. For an event perfectly centered on the middle tap, the amount of charge missed by the two outer taps cancel in the equation. If however, the event position is not over the center of a tap, the fractional amount of missing charge is different and produces a small systematic error in the reconstructed position. The small systematic positional error combined with the coarse position logic produce "gaps" in the HRC images. These gaps are perfectly aligned with the detector axes and correspond to positions exactly half-way between amplifier taps. The gaps are systematic and are removed in data processing.

The three-tap position algorithm described above can be improved upon by making use of the predictability of the shape of the charge cloud exiting the rear MCP. The spatial distribution of the charge cloud leaving the rear of the 2nd MCP has a very specific shape for X-ray induced events. This shape has often been modeled as the combination of a Gaussian and a Lorentzian distribution. Due to this specific shape, it has been observed and simulated via Monte Carlo techniques that the fine position term:

$$(\frac{Q_{cp_{i+1}} - Q_{cp_{i-1}}}{Q_{cp_{i-1}} + Q_{cp_i} + Q_{cp_{i+1}}}) \tag{7.2}$$

and the complementary term:

$$(\frac{Q_{cp_i}}{Q_{cp_{i-1}} + Q_{cp_i} + Q_{cp_{i+1}}}) \tag{7.3}$$

are highly correlated. In fact, the shape of a scatter plot of the two quantities for X-ray induced events closely describes a hyperbola. Non X-ray events, primarily those due to the passage of charged particles, produce charge distributions that are often larger and are spatially extended and complex. As such, it is possible to remove many non-X-ray
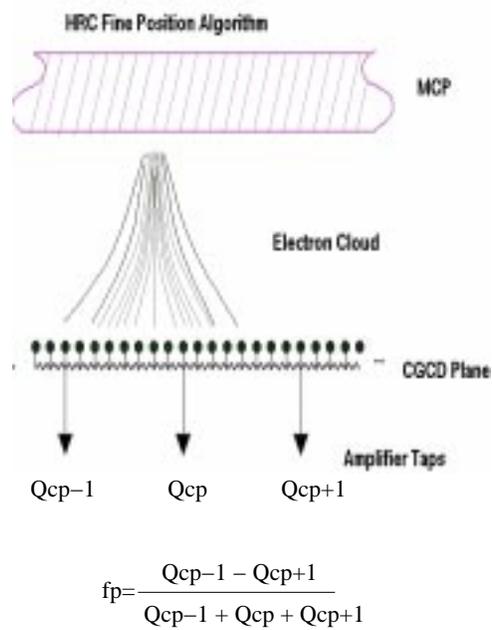
Figure 7.4: Schematic representation of event position determination for one axis of the crossed grid charge detector (CGCD). The electron cloud is divided between several amplifiers. The position of the event relative to the central coarse position is calculated from the difference between the signals on either side of the coarse position divided by the sum of the three signals.

background events by screening those events that do not fit the hyperbola. Furthermore, since the charge distribution is centrally peaked, the complement Q_{cp_i} term is larger and less susceptible to noise induced errors than the $Q_{cp_{i+1}} - Q_{cp_{i-1}}$ difference term. It is therefore possible to use the complement term, and the best fit hyperbolic locus to correct those events where instrumental noise has compromised the three-tap fine position. A much more detailed explanation of this technique is presented in Murray, *et al.* (2000).

For more details concerning the HRC see Murray & Chappell (1989) and Zombeck *et al.* (1995) and references therein.

7.2.1 Aimpoints

The aimpoints are the positions on the instrument where the flux from a point source with no commanded offsets is placed. Note that the on-axis position is offset approximately 20" from the aimpoint. There are two nominal aimpoints as indicated in Figure 7.1 - one at the approximate center of the HRC-I, and the other slightly off-center on HRC-S. The HRC-S aimpoint Z-offset places the LETG-dispersed image along the centerline of the two white rectangles in the diagram. The HRC-S aimpoint Y-offset is slightly off-center, so that the boundaries between the three HRC-S segments correspond to different wavelengths of the grating-dispersed spectrum (See Chapter 9 for details).

7.3 Dither

The spacecraft is dithered during all observations in a Lissajous figure. For observations with the HRC, the dither amplitude is 40 arcsec peak-to-peak, with nominal periods of 1087 (in Y) and 768 (in Z) seconds. Dither serves the purpose of smoothing pixel-to-pixel variations in the response. The dither also eliminates gaps in coverage caused by the HRC-S inter-segment spaces near -50 A and +60 A (see Figure 7.3). The effects of dither are removed during high-level ground processing of the data.

7.4 Spatial Resolution & Encircled Energy

Imaging with the HRC is best performed with the HRC-I because of the much lower background (Section 7.8) and larger field of view. The intrinsic PSF of the HRC is well modeled by a gaussian with a FWHM of $\sim 20\mu$m (~ 0.4 arcsec). The HRC pixels, determined by the electronic readout and *not* the pore size, are 6.42938μm (0.13175 arcsec). The HRC response is thus well matched to the intrinsic HRMA resolution (Chapter 4).

Approximately 90% of the encircled energy lies within a 14 pixel diameter region (1.8 arcsec) from the center pixel for the observation of AR Lac shown in Figure 7.5. The

measured PSF is as good or better than the simulations because a very conservative pre-flight estimate of the aspect solution was used in the simulations.

The imaging resolution of the HRC-I/HRMA combination degrades off-axis for two reasons: the HRMA PSF increases with increasing off-axis angle and the deviation increases between the flat HRC-I detection surface and the curved HRMA focal surface. The off-axis imaging behavior of the HRC-I/HRMA is shown in Figure 7.6. The nominal best-focus of the HRC-I is chosen to provide the best image quality in the center of the field-of-view.

7.5   Energy Resolution

The pulse-height amplitude of each event is telemetered. However, the energy resolution is poor. Figure 7.7 shows the HRC-I pulse height distributions for six energies obtained during sub-assembly calibration. The pulse-height distributions for the HRC-S detector are somewhat narrower. There is significant spatial variation in the gain across both instruments.

7.6   UV/Ion Shields

The placement, composition, and thickness of the various UV/ion shields (filters) are shown in Figure 7.1. Tables and plots of the UVIS transmission as a function of energy can be found at http://hea-www.harvard.edu/HRC/calib/uvismodel.html.

The shields are useful in suppressing out-of-band (outside the X-ray band) radiation from the ultraviolet through the visible. The detector response to out-of-band light for an object in its field-of-view is a possible source of unwanted signal. Suppressing out-of-band radiation is particularly important for observing sources which have bright XUV and UV fluxes. The HRC has strongly reduced sensitivity in this spectral region, as shown in Figure 7.8. As part of the in-flight calibration program the bright A star Vega (A0V, U=0.02, B=0.03, V=0.03) was observed with both the HRC-I and HRC-S. The predicted count rate for HRC-I was 7×10^{-4} cts s^{-1}. The observed upper limit is 1×10^{-3} cts s^{-1}. The image of Vega was also placed on three regions of the HRC-S - the inner segment "T", the thin aluminum inner segment, and on one of the thin aluminum outer segments. The predicted count rates were 1, 400, and 2000 cts s^{-1}, respectively. The corresponding observed rates were 0.2, 240, and 475 cts s^{-1}. Sirius was observed with the HRC-S/LETGS in order to obtain a soft X-ray spectrum of Sirius B (white dwarf) and Sirius A (A1V, V=-1.46, B-V=0.01) was seen in zeroth order at about the expected count rate. Based upon these sets of observations, the UV/Ion shields are performing as designed. Other stars will be observed as part of future calibration activities. For a detailed discussion of the out-of-band response of the HRC to stars, the reader is referred to http://hea-
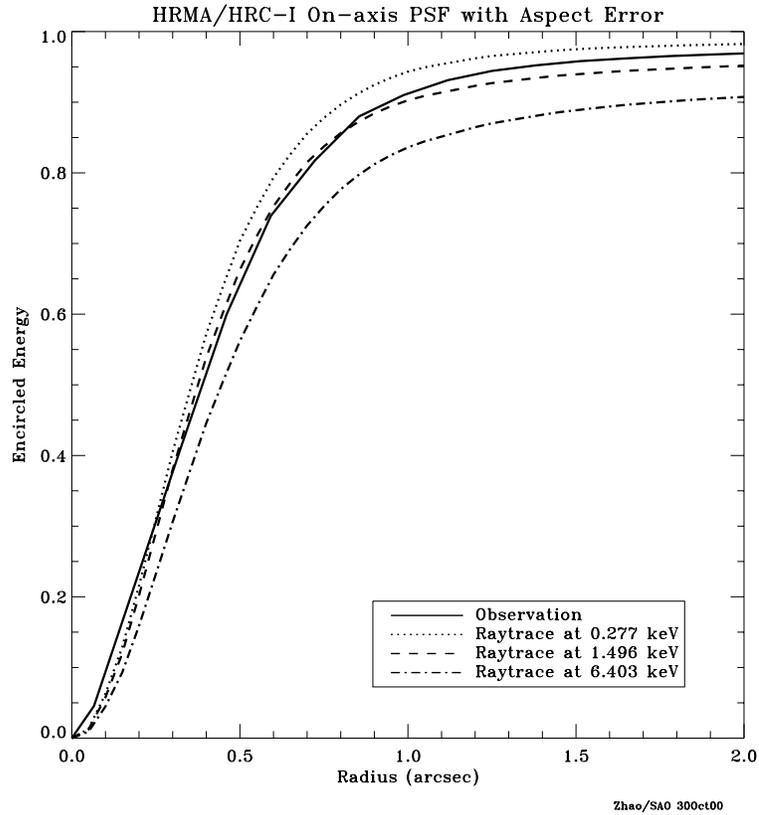
Figure 7.5: The predicted and observed fractional encircled energy as a function of radius for an on-axis point source observed with the HRMA/HRC-I. The calculations (at two energies, 0.277 keV and 6.40 keV) include a very conservative estimate of the aspect solution (FWHM = 20μm ($0.41''$)). Flight data from an observation of AR Lac are also shown.
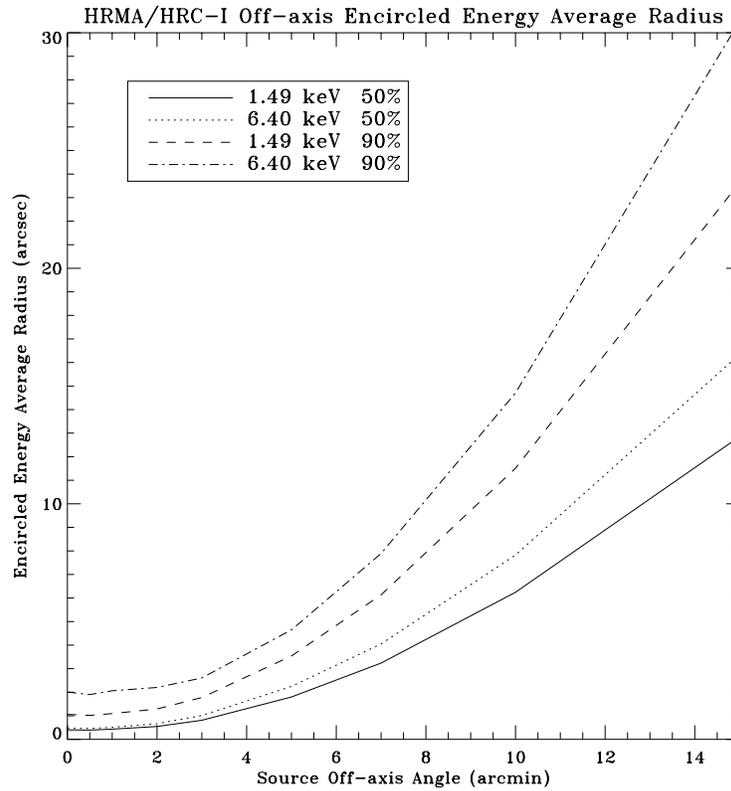
Figure 7.6: Encircled energy as a function of source off-axis angle for 50% and 90% encircled energy for 1.49 and 6.40 keV for the combined HRMA/HRC-I. A conservative contribution from the aspect solution is included (FWHM $= 20\mu$m $(0.41'')$). A plot for the combined HRMA/HRC-S would be almost identical since the PSFs of the two instruments are virtually identical and independent of off-axis angle.
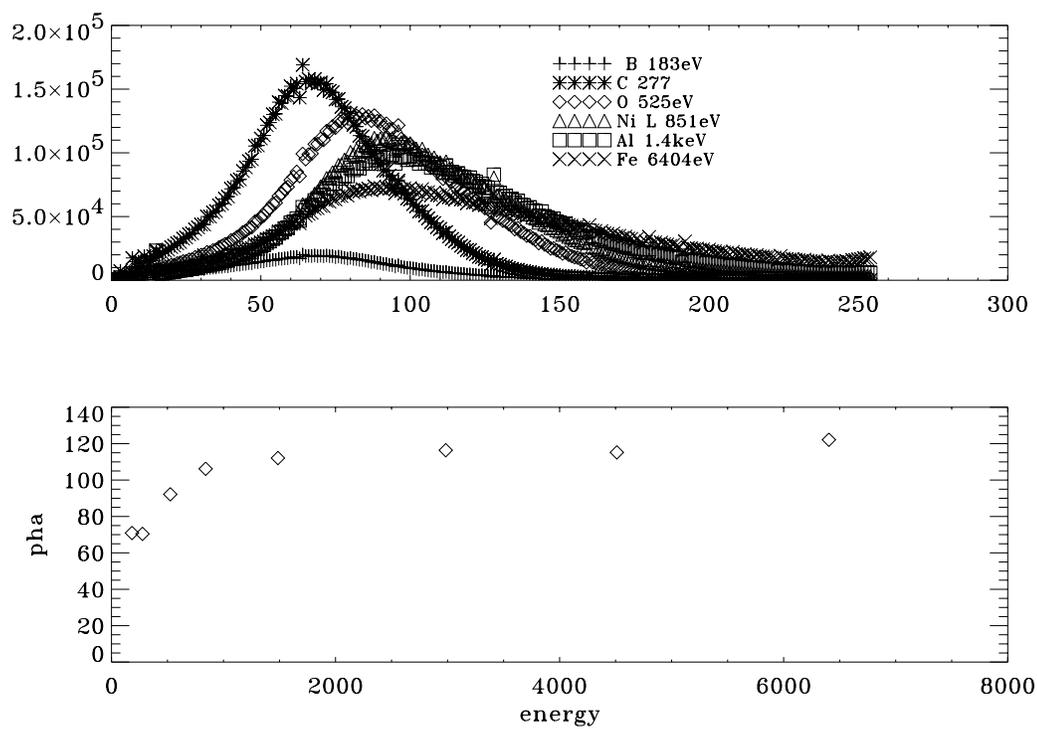
Figure 7.7: The pulse height versus energy for the HRC-I detector and the centroid of the pulse height distribution versus energy. This data set was obtained at SAO during flat field, normal-incidence-illumination tests. The voltage settings have been changed in-flight and thus the applicability of these data is questionable and they are presented here for purposes of illustration only.
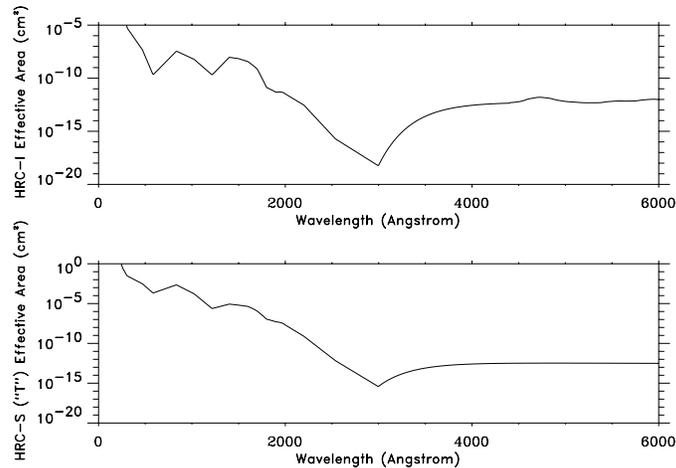
Figure 7.8: The HRC-I (top) and the center section of the HRC-S (bottom) UV/Ion shield effective area as a function of wavelength.

www.harvard.edu/HRC/calib/palermopaper.ps. Plots of the out-of-band count rate for any star for which T_{eff}, V, and N_H are known, are given.

Scattered UV, far-UV (FUV), and extreme-UV (XUV) light from the Sun or bright Earth may cause a background strongly dependent on viewing geometry. The spacecraft was designed to limit the contribution from stray scattered radiation to 0.01 cts cm^{-2} s^{-1} (2.4×10^{-7} cts arcsec^{-2} s^{-1}) on the HRC. The imaged components of scattered radiation are dependent on the solar cycle, but are at most ~ 0.01 cts cm^{-2} s^{-1} for most lines of sight.

7.7   Quantum Efficiency and Effective Area

The quantum efficiency of the HRC detector is the product of the appropriate UV/Ion shield transmission and the quantum efficiency of the CsI coated MCP. Pre-flight flat field measurements show a 10% variation in the QE across the HRC-I. The HRC-S also exhibits QE variations of the same magnitude, where the complex structure of the HRC-S UVIS contributes to the spatial variations.

The combined HRMA/HRC-I and -S effective areas – the product of the HRMA effective area, the quantum efficiency of the HRC and the transmission of the appropriate UV/Ion shield – are shown, integrated over the point spread function, in Figure 7.9. See also the discussion in the HRMA chapter (Section 4.2.2, and Figures 4.2 and 4.3.) Analysis of data from in-flight calibrations is ongoing (See http://cxc.harvard.edu/cal/Hrc/).
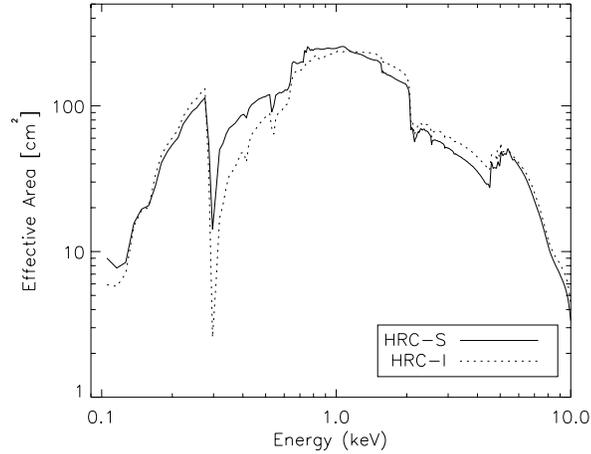
Figure 7.9: The effective area of the HRMA/HRC-I (dashed line) and the central segment of the HRMA/HRC-S in imaging mode (solid line) integrated over the full PSF. Absorption edges are due to the iridium coating of the telescope, the CsI MCP coating, and the polyimide/Al of the UVIS. The results of the low energy in-flight QE calibration have been incorporated into these curves.

7.8   On-Orbit Background

7.8.1   HRC-I

The HRC-I total counting rate on orbit is about 250 cts s^{-1}due mostly to cosmic ray events which are detected in the anti-coincidence shield (antico) and flagged. The observed cosmic ray event rate is about twice what was assumed pre-launch and corresponds to $\sim$2 cts cm^{-2} s^{-1}. Because a rate of 250 cts s^{-1} saturates the telemetry limit of 184 events sec^{-1}, the on-board veto function has been activated. This reduces the valid event rate to about 50 c/s over the field yielding a background telemetered rate of 10^{-5} cts s^{-1} arcsec^{-2}. The background is generally flat, or at least smoothly varying over the field with no more than a 20% difference between the center (higher) and edges (lower) of the detector. Note, the total event rate remains unchanged, but detector events in coincidence with antico events no longer enter the telemetry data stream. Before launch the expected rate, after vetoing the effects of cosmic rays, was 10-20 cts s^{-1} composed of mainly the internal rate of the MCPs (10-15 cts s^{-1}), and a small contribution from cosmic rays due to antico inefficiency. There is additional background in the HRC-I that is not well understood. However, for point source detection and exposure times of 100 ks or less the background is virtually negligible. For studies of extended objects of low surface brightness, however,

even this relatively low rate can become significant depending on the specific details of the feature.

Ground based data analysis screening techniques have been developed to further reduce the non-X-ray background in the HRC detectors. These techniques are described in detail in Murray *et al.* (2000), Juda *et al.* (2000) and Wargelin *et al.* (http://cxc.harvard.edu/cal/Letg/Hrc_bg/). The net result is that for the HRC-I, non-X-ray background is reduced by ~ 40 % compared to non-screened data while the corresponding reduction in X-ray events is reduced by less than a few percent. For the HRC-S, non-X-ray background is decreased by ~ 50 % and the X-ray loss is 1 to 2 %. Furthermore, the screening process makes the spatial distribution of the detector background more uniform. The screening algorithms have the added benefit of removing saturated events which were responsible for a faint secondary "ghost" images (see Section 7.10).

The HRC IPI team continues to work on the screening/processing techniques and to develop new ones. These event screening procedures have been incorporated by the Data Systems Group into the standard CXO/HRC data pipeline and are transparent to the users. Proposers interested in the details of the screening procedures are encouraged to read the aforementioned papers and references contained therein.

7.8.2 HRC-S

The anti-coincidence shield of the HRC-S is not working because of a timing error in the electronics. The error is not correctable. As a result the event rate is very high and exceeds the telemetry rate limit. To cope with this problem the HRC Team has defined a "spectroscopy region" which is about 1/2 of the full width and extends along the full length of the HRC-S detector. The spectroscopy region is ~ 10 mm x 300 mm in size. The region is imposed by using the edge blanking feature of the electronics. With this change, the telemetered quiescent background rate is about 85 cts s^{-1}.

As with the HRC-I, this background can be further reduced in ground data processing by using pulse height filtering that preferentially selects X-rays over the cosmic ray events. A reduction in background of a factor of about three for dispersed spectra is possible. Thus there are two relevant background rates for the HRC-S: a telemetry rate of 85 cts s^{-1} and a post-processing rate for calculating signal to noise. The latter is discussed in detail in Chapter 9 (see especially Figure 9.28).

7.8.3 Temporally Variable Background

Both the HRC-I and HRC-S experience occasional fluctuations in the background due to charged particles. These times of enhanced background are typically short (a few minutes to a few tens of minutes) and are anywhere from a factor a 2 to a factor of 10 over the quiescent rates. The increased background appears to be uniformly distributed over the
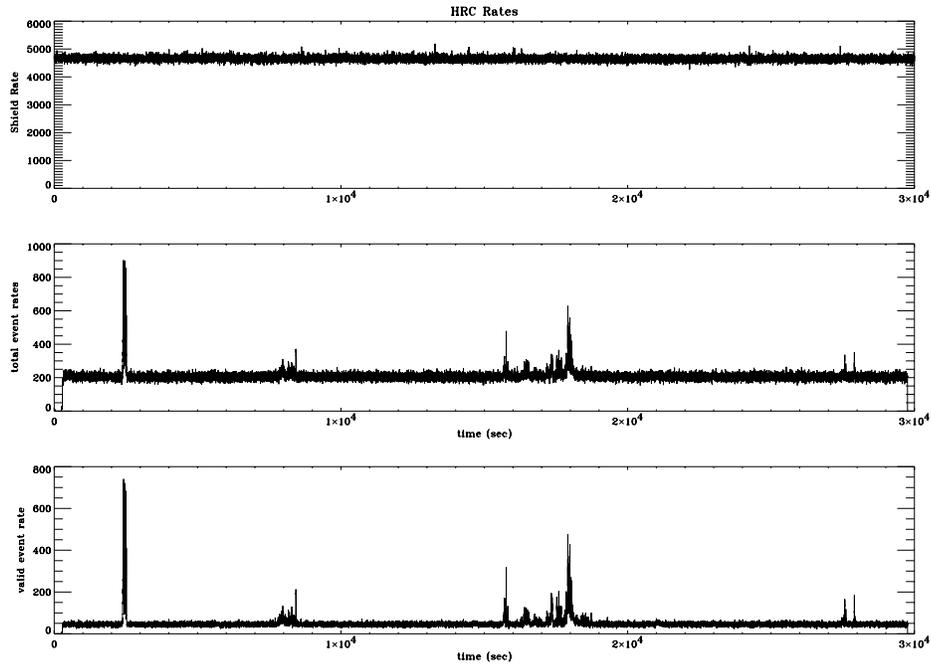
Figure 7.10: An example of the background variability during a ∼30 ks HRC-I observation of the SNR G21.5-09 taken on 1999-10-25. The total event rate and the valid event rate show correlated bursts up to ∼800 cts s^{-1}. The data in the bursts are uniformly distributed over the detector. The anti-coincidence shield exhibits no correlated enhancements. The total rate and the valid rate differ by ∼200 cts s^{-1} due primarily to cosmic ray events that are vetoed and don't appear as valid events in the telemetry.

detector and introduces no apparent image artifacts. On the average it seems that no more than about 20% of the observing time is affected by these events, and they are easily recognized in the secondary science rate data and so can be filtered out if desired. An example of this behavior is shown in Figure 7.10. The reader is referred to Juda *et al.* (2002) for more information on the HRC background.

7.9 Source Sensitivity

Examples of the minimum flux detectable by the HRC-I in a 1 arcsec radius circle on-axis and for a 20″ diameter extended source are shown as a function of observing time and spectral form in Figure 7.11.
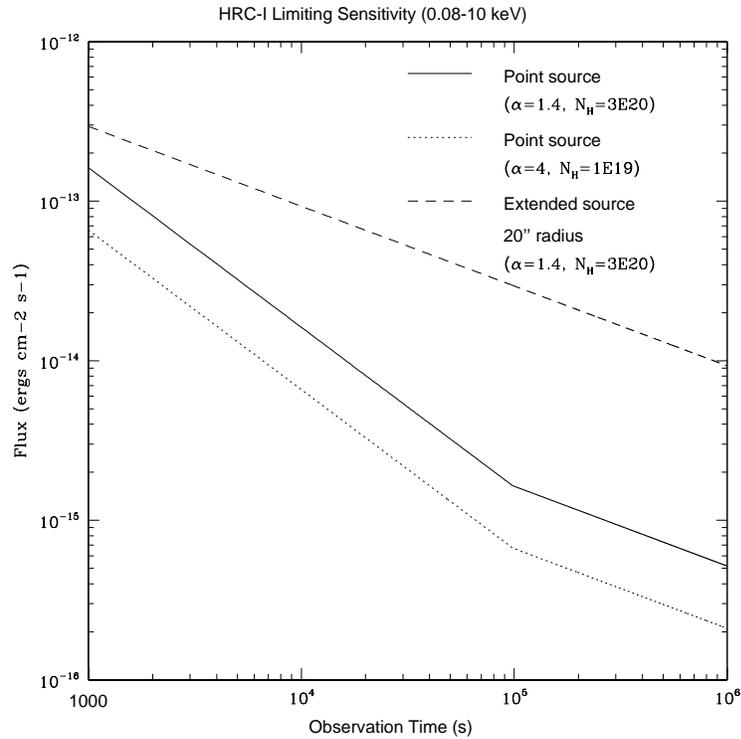
Figure 7.11: Predicted minimum detectable flux as a function of exposure time using HRC-I at best focus for two sample point sources of differing spectra and one sample extended source in the 0.08 to 10 keV bandpass. We require a minimum of 5 source counts of a 3 sigma measurement above background for detection of a source. The spectral parameters are summarized in the figure. For the point sources, we have used a detect cell of $1''$ radius, which corresponds to 90% of the encircled energy on-axis. The background is assumed to be 9×10^{-6} cts arcsec^{-2} s^{-1}.

7.10 Instrument Anomalies

Initial observations with the HRC-I detector showed a faint secondary "ghost" image associated with the PSF. This "ghost" image was a displaced, weaker ($\sim 3\%$) image $\sim 10''$ on one side of every source in the HRC-I field of view. The cause of this imaging anomaly was determined to be saturation of fine position amplifiers. The previously mentioned event processing algorithms which are now part of the CXO/HRC data pipeline have reduced the relative intensity of the ghost image to $< 0.1\%$ effectively eliminating this anomaly. A similar "ghost" image existed in the HRC-S, but at a much reduced intensity.

A problem has been discovered in HRC event times. A wiring error in the detector causes the time of an event to be associated, not with that event, but with the following event, which may or may not be telemetered. The result is an error in HRC event timing such that the accuracy is degraded from about 16 microseconds to a time which is more or less the mean time between events. To date, the total HRC-I rate has been dominated by the background, and is about 250-300 events/sec. Thus, if the time tag of each event is shifted, it turns out (verified by laboratory tests and simulations) that the average uncertainty in the time of any event is just the mean time between events. For example, if the trigger rate is 250 events/sec, then the average uncertainty in any time tag is less than 4 milliseconds.

The HRC Team has worked out a special operating mode that allows high precision timing to be achieved (see Section 7.13.1). This new timing mode uses only the central segment of the HRC-S. Disabling the outer two segments lowers the total counting rate by two-thirds, dropping it below the telemetry saturation limit for most sources. Thus, there is a high probability that all events will be telemetered. In this case, once the time tag of each event has been appropriately shifted in ground processing, the original timing accuracy (16 microseconds) can be recovered. In using this approach, it is prudent to be sure that the total counting rate, source plus background, is somewhat below the telemetry saturation limit to avoid the effects of statistical fluctuations.

In addition to the primary science data for individual events, the rate of microchannel plate triggers (total rate) and triggers (valid rate) that pass on-board validity tests are telemetered to the ground. The valid rate is used to correct the primary rate for dead-time and telemetry saturation effects. As long as the primary rate is below saturation, the primary rate itself can be used to make the small ($<1\%$) correction, since the event processing dead-time is known. However, when the event rate exceeds saturation, a not uncommon occurrence because of the flaring background from low energy protons, the valid rate is necessary to correct the event rate. Unfortunately, the total and valid event rates are overestimated by about 15% for normal operation of the HRC-S . The problem is caused by an overshoot in occasional large trigger pulses. This results in double counting in the total and valid event on-board scalers. The primary science event is not affected, since once event processing starts with the initial trigger pulse, a gate rejects further pulses

until processing is complete. The HRC-I does not have the overshoot problem. A scheme that corrects the HRC-S valid event rate based upon the fraction of event pulse amplitudes that are above a given threshold (segment dependent) has been developed but not yet implemented in the standard processing software.

7.11 Calibration

Calibration of the HRC included laboratory calibrations, a system-level ground calibration with the HRMA and HRC at the X-ray Calibration Facility (XRCF) at MSFC, and on-orbit calibration using celestial and on-board radioactive X-ray sources. The on-orbit calibration of the HRC is an on-going activity. All calibration data are, or will be, described in detail on our web site (http://cxc.harvard.edu/cal).

The user is urged to consult the WWW site and its pointers for the latest information.

7.12 Operational considerations and constraints

In addition to the general Chandra observatory level constraints (Chapter 3), there are a handful of HRC-specific considerations and constraints that must be taken into account in planning an observation.

7.12.1 Total Count limits

Both the gain and the quantum efficiency are adversely affected by the total amount of charge extracted from the MCP at the point of extraction. To minimize such effects, the high voltage on the detector is lowered during passage through the radiation belts and at times of very high particle radiation. To limit the impact from X-ray sources themselves, a 450,000 count limit distributed over the dither pattern from an on-axis source at a given aimpoint has been imposed. *Users anticipating to exceed this value should so note in the comments section of the RPS form when submitting their proposal.* In this case, the *CXC* will establish new aimpoints as necessary. Offsets in the pointing may be imposed, if necessary, in order to limit the accumulated dose to a given region of the MCP.

7.12.2 Count rate limits

There are two counting rate limits:

Telemetry Limit

The maximum telemetered counting-rate is 184 cts s^{-1}. This is a limitation on the total count rate received over the full field-of-view rather than for one individual source within

the field. It is possible to exceed this limit and to subsequently correct the total count rate by using the secondary science rates, which keep track of the actual detected rate, to determine the deadtime correction (see Section 7.10). The resulting deadtime fraction increases rapidly with valid event rates above 184 cts s^{-1}. For example, at 200 cts s^{-1} the deadtime fraction is 8%, at 250 cts s^{-1} 26%, and at 300 cts s^{-1} 39%. In the following we list some methods of dealing with situations where the telemetry limit is exceeded.

1. *Bright target:*

   - Insert either the LETG or the HETG as appropriate and perform the investigation viewing the zeroth-order image. This solution may be so dramatic as to substantially increase the required observing time.

   - Offset point. To be effective, this solution may result in substantially reduced spatial resolution.

2. *Bright nearby source*

   - Depending on the proximity, an appropriate choice of roll angle and/or aim point can position the problematical source (or sources) off the detector. Note that in order to limit the use of mechanical systems, a request for an off-nominal aimpoint is discouraged if an equally scientifically useful alternative is feasible. Note, this option is not available if one also wants to use the HRC precise-timing mode (see Section 7.10).

   - Request a rectangular window for the on-board data so that events produced by the nearby bright source (or sources) do not contribute to the telemetry limit.

   - Select a roll angle which allows use of the HRC shutters to block the light from a bright source near the edge of the field of view. Observers should contact the *CXC* to investigate this possibility and enter their requirements in the Comment field of the RPS form. This request should only be made if all other proposed solutions - included accomplishing the objective with a different instrument - fail.

There are of course, other combinations and situations that can lead to telemetry saturation - numerous faint sources on the field, a too-bright extended source, etc.

Linearity limit

The HRC-I was found to be linear for incident photon rates up to ~ 2 cts s^{-1} pore^{-1}, which translates to ~ 5 cts s^{-1} for an on-axis point source (see Kenter *et al.* 1997, Figure 7). The HRC-S was found to be linear for rates five times greater. (We note that in the

case of the HRC-I there is no evidence that linearity does not extend beyond the stated limit, only that no data were taken for higher incident fluxes.)

It is important to be aware that *avoiding telemetry saturation does not guarantee that linearity limits are not exceeded.* There are only three approaches to assure oneself that the linearity limit is not exceeded:

- Offset point to smear the image out.

- Insert a transmission grating to reduce the flux and offset point (if also necessary).

- Defocus – only mentioned for completeness – the option is not recommended or encouraged.

7.13 Observing with HRC- Operating Modes

For many observations, it is necessary only to specify the instrument, the exposure time, and the target coordinates. No other parameters need to be provided. There are, however, a number of optional parameters that one might wish to consider invoking to optimize a particular observation. The observer is encouraged to make use of the various tools provided when planning an observation, and not to forget to include the background when estimating sensitivity.

7.13.1 Timing Mode

The HRC-S is normally operated in spectroscopy mode whereby signals from any of the three MCP segments can be recognized as triggers. An alternate mode of operation (timing) ties the signals from the outer segments to ground so that only signals from the center MCP generate triggers. A key distinction of this mode from using an edge-blanked region (described below) to select only the center MCP segment is that the timing mode selects events without using the on-board veto logic. This preferred method of doing high-precision timing observations reduces the active detector area thereby minimizing the total trigger rate. Provided that this rate is below telemetry saturation, all events will then be telemetered and the event time tags can be correctly assigned in ground processing (see Section 7.10).

The HRC-S, when used in this mode, provides about a 6 arcmin by 30 arcmin field of view.

7.13.2 Edge and Center Blanking

It is possible to define a rectangular region, other than the default region, on either HRC-I or HRC-S from which events either inside (edge-blanking) or outside (center-blanking)

the region are selected for telemetering. This would be done, for example, to prevent events from a nearby bright source from contributing to telemetry (see section 7.12.2). If a proposer wishes to define such a rectangular region, she/he should state this request in the "Remarks" field of the RPS form in order to prompt discussions with a *CXC* Support Scientist.

7.13.3 Zero-order Blocking

The HRC has a pair of blades that were designed so that quadrant focusing and mirror-tilt measurements could be performed on-orbit. The blades can be positioned to block the zero-order image in a grating observation. The positions of the blades can also be adjusted to block other portions of the field. If a proposer wishes to use the blades in a manner other than for zero-order blocking, she/he should state this request in the "Remarks" field of the RPS form in order to prompt discussions with a *CXC* Support Scientist.

7.14 REFERENCES

The following is a list of publications, documents, web pages, and memos containing information about the High Resolution Camera (HRC).

General

David, L.P., Harnden, F.R. Jr., Kearns, K.E, and Zombeck, M.V. "The ROSAT High Resolution Imager (HRI) Calibration Report", revised (1999). hea-www.harvard.edu/rosat/rsdc_www/hr

Fraser, G., "X-ray Detectors in Astronomy", 1989, Cambridge University Press.

Giacconi, R., *et al.*, 1979, Ap. J., 230, 540.

Murray, S.S., Chappell, J.H., Elvis, M.S., Forman, W.R., Grindlay, J.E., Harnden, F.R., Jones, C.F., Maccacaro, T., Tananbaum, H.D., Vaiana, G.S., Pounds, K.A., Fraser, G.W., and Henry, J.P., "The AXAF High Resolution Camera (HRC) and its use for observations of Distant Clusters of galaxies" Astro. Lett. Comm., 26, 113-125, 1987.

Murray, S.S., *et al.*, "In-flight Performance of the Chandra High Resolution Camera", SPIE, 4012, 2000. http://hea-www.harvard.edu/HRC/calib/ssmspie2000.ps

Zombeck, M.V., Chappell, J. H , Kenter, A, Moore, R., W., Murray, S. S., Fraser, G.W., Serio, S.,"The High Resolution Camera (HRC) on the Advanced X-ray Astrophysics

Facility (AXAF)", Proc. SPIE, 2518, 96, 1995.
http://hea-www.harvard.edu/hrc_art/hrc_spie/hrcspie0.html

Position modeling, de-gap corrections, and event screening

Murray, S.S., Chappell, J.H., 1989, SPIE 1159, 460-475. "Position Modeling for the AXAF
    High resolution Camera (HRC)"

Kenter, A., "Degap as a Transformation of Probability Distribution Problem", 3/1/99.
    http://hea-www.harvard.edu/HRC/calib/degap.ps

Murray, S.S., *et al.*, "Event Screening for the Chandra X-ray Observatory High Resolution
    Camera (HRC)", SPIE Proceedings, 4140, 2000.
    http://hea-www.harvard.edu/HRC/calib/event_screening.ps

Juda, M., *et al.*, "Improving Chandra High Resolution Camera event positions via correc-
    tions to cross-grid charge detector signals", SPIE Proceedings, 4140, 2000.
    http://hea-www.harvard.edu/HRC/calib/spie2000_tap_correction.ps

Count rate limitations and linearity

Juda, M and Dobrzycki, A, "HRC Deadtime and Telemetry Saturation", 6/18/99.
    http://cxc.harvard.edu/contrib/juda/tlm_sat.html

Kenter, A.T., Chappell, J.H. Kobayashi,K.,Kraft,R.P., Meehan, G.R., Murray, S.S.,
    Zombeck, M.V., Fraser, G.W., Pearson, J.F., Lees, J.E., Brunton, A.N. and Pearce,
    S.E. Barbera, M., Collura, A., Serio, S., "Performance and Calibration of the AXAF
    High Resolution Camera I " SPIE 3114, 1997.

Juda, M., "Telemetered vs. Processed Events", memo, 12/7/01.
    http://hea-www.harvard.edu/~juda/memos/proc2valid/

Juda, M., "HRC-S Double Pulse Fraction", memo, 6/27/02.
    http://hea-www.harvard.edu/~juda/memos/proc2valid/pha_fraction.html

Zombeck, M. V., "Secondary Science Rate Double Counting", memo, 2/12/02.
    http://hea-www.harvard.edu/HRC/calib/doublecount.html

Calibration

cxc.harvard.edu/cal (CXC calibration site)

http://hea-www.harvard.edu/HRC/calib/calib.html(HRC IPI Team calibration site)

Meehan, G, "Calibration of the HRC-I UV/Ion Shield", 10/13/99. http://hea-www.harvard.edu/HRC/calib/hrci_cal_report.ps

Meehan, G.,"Calibration of the HRC-S UV/Ion Shields", 10/13/99. http://hea-www.harvard.edu/HRC/calib/hrcs_cal_report.ps

Kenter, A.T., Chappell, J., Kobayashi, K., Kraft, R.P., Meehan, G.R., Murray, S.S., Zombeck, M.V., "Performance and Calibration of the AXAF High Resolution Camera: I. Imaging Readout", SPIE, 3114, 26, 1997. http://hea-www.harvard.edu/HRC/calib/spie97_kenter.ps

Kenter, A., *et al.*, "In-flight Performance and Calibration of the Chandra High Resolution Camera Spectroscopic Readout (HRC-I)" SPIE, 4012, 2000. http://hea-www.harvard.edu/HRC/calib/ hrci.spie2000.ps

Kraft, R.P., Chappell, J., Kenter, A.T., Kobayashi, K., Meehan, G.R., Murray, S.S., Zombeck, M.V., "Performance and Calibration of the AXAF High Resolution Camera: II. the Spectroscopic Detector", SPIE, 3114, 53, 1997. http://hea-www.harvard.edu/HRC/calib/spie97_kraft.ps

Kraft, R., *et al.*, "In-flight Performance and Calibration of the Chandra High Resolution Camera Spectroscopic Readout (HRC-S)" SPIE, 4012, 2000. http://hea-www.harvard.edu/HRC/calib/hrcs.spie2000.ps

Meehan, G.R., Murray, S.S. , Zombeck, M.V., Kraft, R.P. Kobayashi, K., Chappell, J.H., and. Kenter, A.T.,"Calibration of the UV/Ion Shields for the AXAF High Resolution Camera", SPIE, 3114, 74, 1997. http://hea-www.harvard.edu/HRC/calib/spie97_meehan.ps

Murray, S. S.; Chappell, J.H.; Kenter, A. T.; Kobayashi, K.; Kraft, R. P.; Meehan, G. R.; Zombeck, M. V.; Fraser, G. W.; Pearson, J. F.; Lees, J. E.; Brunton, A. N.; Pearce, S, E.; Barbera, M.; Collura, A.; Serio, S., "AXAF High-Resolution Camera (HRC): calibration and recalibration at XRCF and beyond", SPIE, 3114, 11, 1997.

Background

Juda, M., "Time History of the HRC Background", memo, 5/22/01. http://hea-www.harvard.edu/∼juda/memos/hrc_bkg/time_history.html

Juda, M., "HRC Rates and High Solar Activity", memo, 5/21/01. http://hea-www.harvard.edu/∼juda/memos/hrc_bkg/high_solar.html

Juda, M., *et al.*, "Characteristics of the On-Orbit Background of the Chandra X-ray Observatory High Resolution Camera", Proc. SPIE 4851, August 2002.

http://hea-www.harvard.edu/∼juda/memos/spie2002/spie2002.html   http://hea-www.harvard.edu/∼juda/memos/spie2002/spie2002.ps

Detector coordinate systems

McDowell, J., "Coordinate Systems for Analysis of On-orbit Chandra Data, Paper I: Imaging", http://cxc.harvard.edu/contrib/jcm/ncoords.ps

Count life

Kenter, A.T., K.A. Flanagan, G. Meehan, S.S. Murray, M.V. Zombeck, G.W. Fraser, J.F. Pearson, J.E. Lees, A.N. Brunton, and S.E. Pearce, "Microchannel plate testing and evaluation for the AXAF high resolution camera (HRC)", Proc. SPIE, 2518, 356, 1995.

Out-of-band response

Zombeck, M.V., HRC-I out of band response.
        http://hea-www.harvard.edu/HRC/calib/hrci_cal.html/uv_vis

Zombeck, M.V., HRC-S out of band response.
        http://hea-www.harvard.edu/HRC/calib/hrcs_cal.html/uv_vis

Zombeck, M.V., *et al.*, Vega calibration observations.
        http://hea-www.harvard.edu/HRC/calib/vega/vega.html

Zombeck, M.V., *et al.*, "The Out-of-band Responses of the HRC on Chandra", X-ray 2000 Proceedings, Palermo, 2000.
        http://hea-www.harvard.edu/HRC/calib/palermopaper.ps

Zombeck, M. V., "Response of the HRC to Vega", memo, 10/28/02.
        http://hea-www.harvard.edu/HRC/calib/vega/vega_trend.html

Chapter 8

HETG: *Chandra* High Energy Transmission Grating

8.1 Instrument Overview

HETG is the High-Energy Transmission Grating. In operation with the High Resolution Mirror Assembly (HRMA) and a focal plane imager, the complete instrument is referred to as the HETGS — the High-Energy Transmission Grating Spectrometer. The HETGS provides high resolution spectra (with $E/\Delta E$ up to 1000) between 0.4 keV and 10.0 keV for point and slightly extended (few arc seconds) sources. Although the HETGS's operation differs from proportional counter and CCD spectrometers, standard processing of an HETGS observation produces familiar spectrometer data products: *PHA*, *ARF*, and *RMF* files. These files can then be analyzed with standard forward-folding model fitting software, *e.g.*, *Sherpa* , *XSPEC* , *ISIS* , *etc.*

The HETG itself consists of two sets of gratings, each with different period. One set, the Medium Energy Grating (MEG), intercepts rays from the outer HRMA shells and is optimized for medium energies. The second set, the High Energy Gratings (HEG), intercepts rays from the two inner shells and is optimized for high energies. Both gratings are mounted on a single support structure and therefore used concurrently. The two sets of gratings are mounted with their rulings at different angles so that the dispersed images from the HEG and MEG will form a shallow X centered at the undispersed (zeroth order) position; one leg of the X is from the HEG, and the other from the MEG. The HETG is designed for use with the spectroscopic array of the *Chandra* CCD Advanced Imaging Spectrometer (ACIS-S) although other detectors may be used for particular applications. A summary of characteristics is given in Table 8.1.

The Instrument Principal Investigator for the HETG is Dr. Claude Canizares of the MIT Center for Space Research.

Table 8.1: HETG(S) Parameters

HETGS Range:	$0.4 - 10.0$ keV, $31 - 1.2$Å
HEG Range:	$0.8 - 10.0$ keV, $15 - 1.2$ Å
MEG Range:	$0.4 - 5.0$ keV, $31 - 2.5$ Å
Effective Area (see plots):	$7 \, \mathrm{cm}^2$ @ 0.5 keV
(MEG+HEG first orders,	$59 \, \mathrm{cm}^2$ @ 1.0 keV
with ACIS-S)	$200 \, \mathrm{cm}^2$ @ 1.5 keV
	$28 \, \mathrm{cm}^2$ @ 6.5 keV
Resolving Power ($E/\Delta E$, $\lambda/\Delta\lambda$)	
HEG:	$1070 - 65$ (1000 @ 1 keV, 12.4 Å)
MEG:	$970 - 80$ (660 @ 0.826 keV, 15 Å)
Resolution:	
ΔE:	$0.4 - 77$ eV FWHM
$\Delta\lambda$, HEG:	0.012 Å FWHM
$\Delta\lambda$, MEG:	0.023 Å FWHM
Absolute Wavelength Accuracy:	
HEG	± 0.006 Å
MEG	± 0.011 Å
Relative Wavelength Accuracy:	
HEG	± 0.0028 Å
MEG	± 0.0055 Å
HEG angle on ACIS-S:	$-5.235° \pm 0.01°$
MEG angle on ACIS-S:	$4.725° \pm 0.01°$
HETGS Rowland Spacing	8632.65 mm (flight installed)
Wavelength Scale:	
HEG	0.0055595 Å / ACIS pixel
MEG	0.0111185 Å / ACIS pixel
HETG Rowland Diameter:	8633.69 mm (as machined)
Diffraction Efficiency:	2.5% @ 0.5 keV (MEG)
(single-side, first order)	19% @ 1.5 keV (MEG & HEG)
	9% @ 6.5 keV (HEG)
HETG Zeroth-order Efficiency:	4.5% @ 0.5 keV
	8% @ 1.5 keV
	60% @ 6.5 keV
Grating Facet Average Parameters	
HEG and MEG bar material:	Gold
HEG / MEG period:	2000.81 Å, / 4001.41 Å
HEG / MEG Bar thickness:	5100 Å, / 3600 Å
HEG / MEG Bar width:	1200 Å, / 2080 Å
HEG / MEG support:	9800 Å, / 5500 Å polyimide

8.1.1   Examples of Observations with the HETGS

An example of an HETGS observation is presented in Figure 8.1 using data from an observation of Capella, Obsid 1318. The top panel shows an image of detected events on the ACIS-S detector with the image color indicating the ACIS-determined X-ray energy (see WWW version if this is not in color.) In this detector coordinate image (TDETX, TDETY), the features are broad due to the nominal dither motion which serves to average over detector non-uniformities. The ACIS-S chips are numbered S0 to S5 from left to right, with the aim point in S3 where the bright zeroth-order image is visible and includes a vertical frame-transfer streak (a trailed image). The HRMA optical axis passes through S3 approximately 6 mm from the S2-S3 chip gap. For further information see Figure 6.1 and related text.

HETG-diffracted photons are visible in Figure 8.1 forming a shallow "X" pattern; the full opening angle between the HEG and MEG spectra is 9.96°. The back illuminated (BI) chips are S1 and S3. The S1 location was chosen to enhance the first order MEG spectrum since back illumination provides higher efficiency below 1 keV. The location of the zeroth-order for any particular observation, however, may be adjusted by offset pointing in order to select the energies of the photons that will be placed in the gaps between the chips. Details on gaps are presented in Section 8.2.1.

The middle panel of Figure 8.1 shows an image after the data have been aspect corrected and data filters applied to include only valid zeroth and first-order events. The lower set of panels shows an expanded view of the MEG minus-first-order spectrum with emission lines clearly visible. Wavelengths are assigned based on the diffraction angle of the events, that is, how far the events are from the zeroth-order image. Using the grating equation, below, absolute wavelengths can be assigned based on the dispersion angle. A spectrum of the source is then created by binning the events into energy or wavelength bins; the spectrum from another Capella observation is shown in Figure 8.2.

Note: The dispersion distance on the detector is essentially linear in wavelength. Thus, wavelength is the natural unit for this high-resolution x-ray spectrometer. The conversion between energy and wavelength is provided by the relation:

$$E \times \lambda = hc = 12.39852 \text{ keV\AA}$$

Both energy and wavelength photon measures are used in this document.

Each of the "arms" of the HETGS diffracted X pattern yields a first-order spectrum identified by type (HEG or MEG) and sign of the order (plus or minus.) Using *ARF*'s (ancillary response files) and *RMF*'s (response matrix files) these spectra can be analyzed in an *XSPEC*-like framework. Additionally, the *CXC* software package "Interactive Spectral Interpretation System" (ISIS, http://space.mit.edu/ASC/ISIS/) can be used to identify spectral lines, e.g., as seen in Figure 8.2.
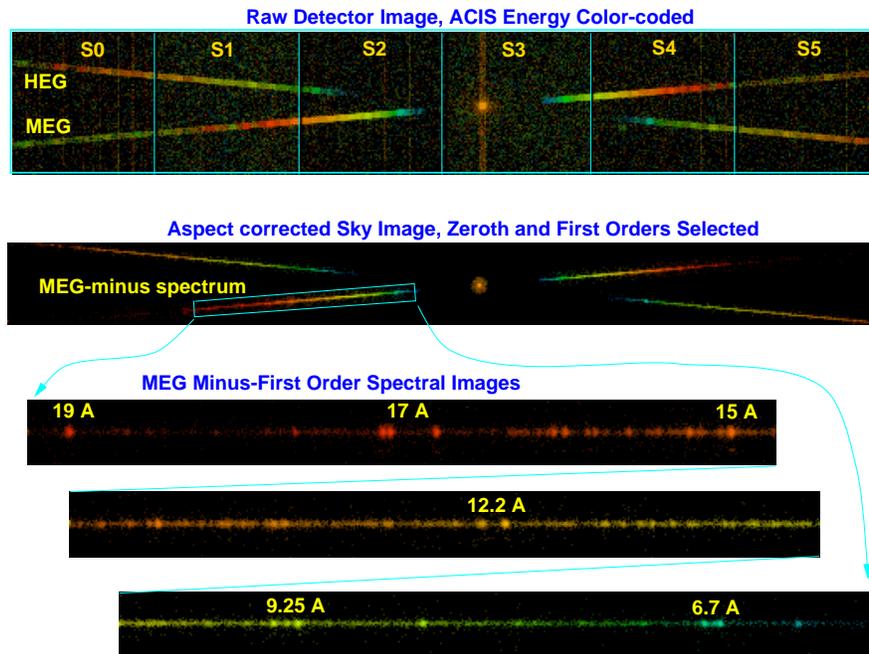
Figure 8.1: HETGS Observation of Capella, Obsid 1318. The top panel shows an image of detected events on the ACIS-S detector with the image color indicating the ACIS-determined X-ray energy. The bright zeroth-order image is visible on CCD S3 and includes a trailed image (the vertical frame-transfer streak). Diffracted photons are visible forming a shallow "X" pattern; the HEG and MEG spectra are indicated. The images are broad due to dither of the spacecraft. The middle panel shows an image after the data have been aspect corrected and selections applied to include only valid zeroth and first-order events. Finally, the lower panel shows an expanded view of the MEG minus-first-order spectrum with emission lines clearly visible.
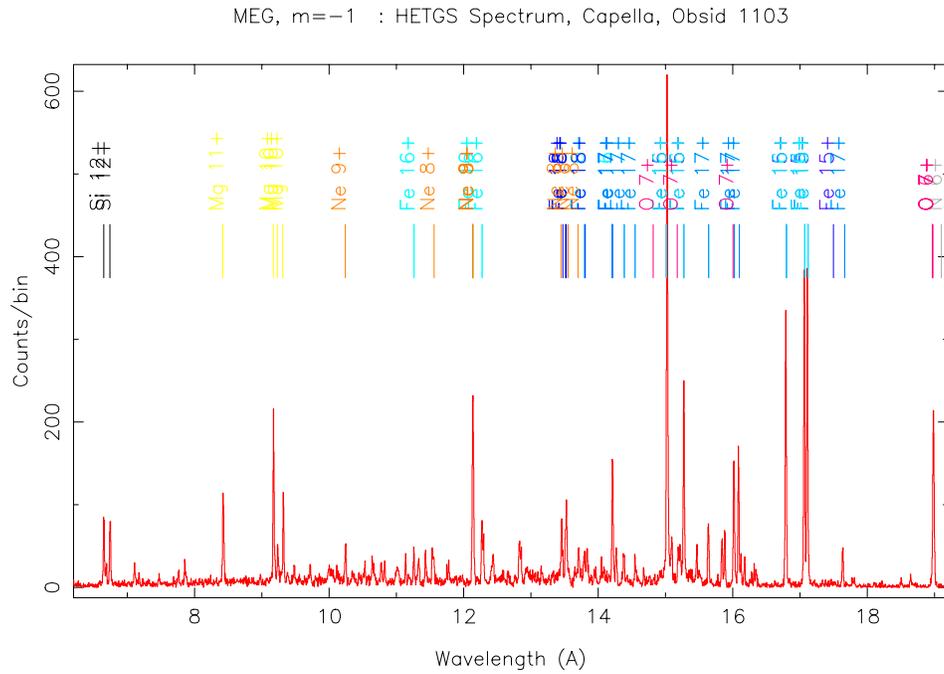
Figure 8.2: HETGS Capella spectrum, MEG $m = -1$, Obsid 1103. The first-order events identified in the MEG minus-side "arm" of the HETG X pattern are assigned wavelengths by *CXC* pipeline software according to the grating equation and known instrument parameters. These values are then binned to produce a pulse height analysis spectrum (`pha2.fits` file) which is plotted here. The `ISIS` software package available from the *CXC* has also been used to indicate the location of expected emission lines based on a simple source model.

8.1.2 Scientific Objectives and Grating Heritage

The HETGS allows one to probe the physical parameters of emitting regions of all classes of X-ray sources, including stars, X-ray binaries, supernova remnants, galaxies, clusters of galaxies, quasars, and interstellar and intergalactic material. Plasma diagnostic techniques applied to emission lines, absorption lines and absorption edges will convey source properties such as temperatures, ionization states, densities, velocities, elemental abundances, and thereby structure, dynamics, and evolution of various classes of sources. The energy band amenable to observation is extremely rich in lines from both coronal and photo-ionized plasmas, containing the L-shell lines from ionization stages of Fe XVII to Fe XXIV and the K-shell lines of hydrogenic and helium-like ions of oxygen through nickel. The 6 keV Fe K lines are well within the observable band. The highest resolutions available will also allow detailed study of motions through Doppler line shifts in supernova remnants, X-ray binaries, turbulent intra-cluster or intra-galactic gas, or early-type galaxies in clusters.

Although gratings have flown on Einstein and EXOSAT, the HETGS shares only the basic operating principles with these. Advanced grating technology has enabled achievement of greater efficiency and increased dispersion. The Rowland geometry of the grating plate and spectroscopic arrays maintains the telescope focal properties in the dispersion direction by minimizing dispersed image aberrations and hence contributes to improved spectral resolution.

8.1.3 HETGS Operating principles

The HETG is mounted, and can be inserted, just aft of the HRMA as shown in the schematic of the HRMA-HETG-detector system, Figure 8.3. The HETG provides spectral separation through diffraction. X-rays from the HRMA strike the transmission gratings and are diffracted (in one dimension) by an angle β given according to the grating equation,

$$\sin\beta = m\lambda/p,$$

where m is the integer order number, λ is the photon wavelength in angstroms, p is the spatial period of the grating lines, and β is the dispersion angle. A "normal" undispersed image is formed by the zeroth-order events, $m = 0$, and dispersed images are formed by the higher orders, primarily the first-order, $m = 1$.

The HETGS-Faceted Rowland design is shown in Figure 8.4. The "Rowland circle" is a circle whose diameter is simply the distance from the grating that would lie on the optical axis to the point in the focal plane, where the zeroth order image is placed. The "Rowland torus" is formed by rotating the circle about the line in the dispersion direction going through the on-axis focus. Individual grating facets are mounted such that their centers lie on the torus. In the figure, the axis of the torus is perpendicular to the page

for the side view and lies in the plane of the top view. Ideally, the detector is shaped to follow the counterpart Rowland torus in the image plane. The result is that the telescope focal properties in the dispersion direction are maintained for a large range of diffraction angles, β, thereby minimizing any grating-added optical aberrations.

An important parameter of the HETGS is the Rowland Spacing, the distance from the outer intersection of the HETG axis and Rowland Circle to the HRMA focus. This parameter was introduced since the HETG was built to a particular Rowland circle whose diameter was not the precise value for the as-assembled observatory. The slight difference between the Rowland diameter and spacing introduces negligible effects on the HETGS performance. The Rowland spacing is, however, what determines the value of β in the grating equation. The values of the various Rowland parameters are listed in Table 8.1.

Order overlap and source confusion can be discriminated by the intrinsic energy resolution of the CCD detector (ACIS-S is the preferred detector for HETG spectroscopy since it has intrinsic energy resolution and so can separate orders; HRC can also be used for high time resolution). The form of a spectral image on the ACIS-S array is shown in Figure 8.1. The spectroscopic array spans about 8 arc minutes × 48 arc minutes of the sky, though image quality and resolving power degrade rapidly for sources more than about 4 arcmin off-axis. For an on-axis source, the detector edge in the dispersion direction causes a low energy cutoff of the spectrum at about 0.4 keV for the MEG and 0.8 keV for the HEG. Order selection and chip gaps are described more fully in Section (8.2.1).

A "grating" coordinate system has been defined in the AXAF-I to SI Interface Control Document (ICD). Various *Chandra* coordinate systems have been summarized in the CXC document, "ASC Coordinates, Rev. 4.1" (J. McDowell, 27 Feb 1997).

8.1.4   HETG Physical Configuration

The HETG support structure (HESS) is a circular aluminum plate (110 cm diameter by 6.35 cm thick) which can be swung into operation behind the HRMA. Mounted on the HESS are 336 grating facets, each about 25 mm square. The position and orientation of the HESS mounting surfaces have been designed and machined to place each grating center on a Rowland torus of diameter 8633.69 mm. A detailed drawing of the HETG (HESS plus facets) is shown in Figure 8.5.

The gratings cover the annular regions through which the X-rays pass. The 192 grating facets on the outer two annuli (MEG) have a period of 4001.41 Å . Tiling the inner two annuli are 144 (HEG) gratings, which have a period of 2000.81 Å (see Table 8.1). The two sets of gratings are mounted with their rulings at different angles so that the dispersed images from the HEG and MEG will form a shallow X centered at the undispersed (zeroth order) position; one leg of the X is from the HEG, and the other from the MEG.

The HETG grating facets are composed of electro-plated Gold bars supported on a polyimide substrate, as shown schematically in Figure 8.6. The grating bar design
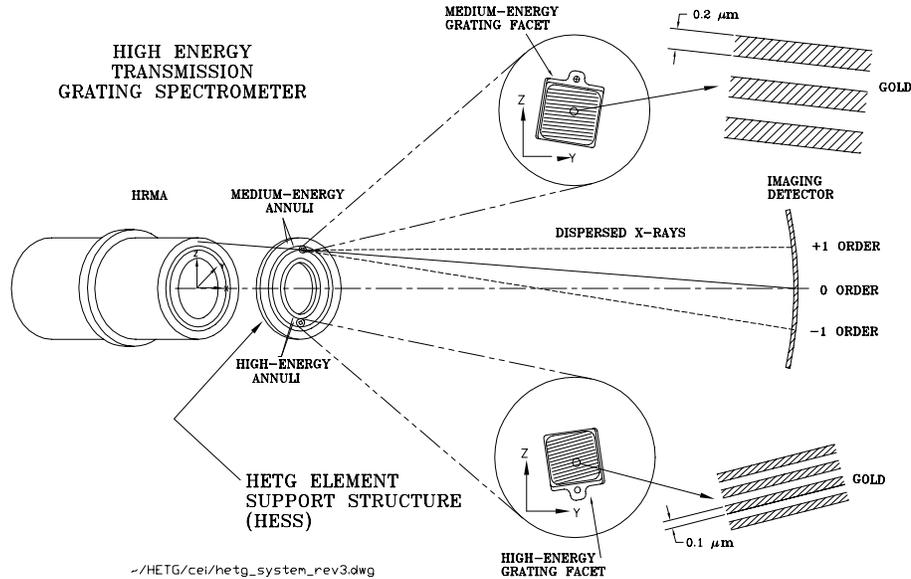
Figure 8.3: A schematic layout of the High Energy Transmission Grating Spectrometer. (Dimensions shown are approximate.)

parameters, height and width, are nominally chosen to reduce zeroth-order and maximize first-order intensities. Choosing to have the bar width one-half of the grating period suppresses even orders and provides maximum 1st order efficiency for a rectangular profile; this is closely achieved for the MEG gratings. For the HEG gratings, the bar is wider and results in a higher 2nd order efficiency and reduced 3rd order efficiency. The bar height choice "tunes" the efficiency peak in energy by allowing X-rays to constructively interfere in first order in the region where the gold is partially transparent primarily, above 1.2 keV.

8.2   Instrument Characteristics

The operation of the HETGS is modeled by combining detailed models of the HRMA, HETG, and ACIS in a ray-trace code, such as the "Model of AXAF Response to X-rays" simulation software, *MARX*. A large set of parameters and constants define this model and are the basis for the instrument characteristics. However, the HETGS as a spectrometer can be described at a basic level by a throughput measured by the *Effective Area* (how many events are diffracted into the "X") and a *Line Response Function* (the distribution of dispersed photons from a monochromatic input.) In addition an HETGS observation will include *Background* events which must be accounted for in analyses and
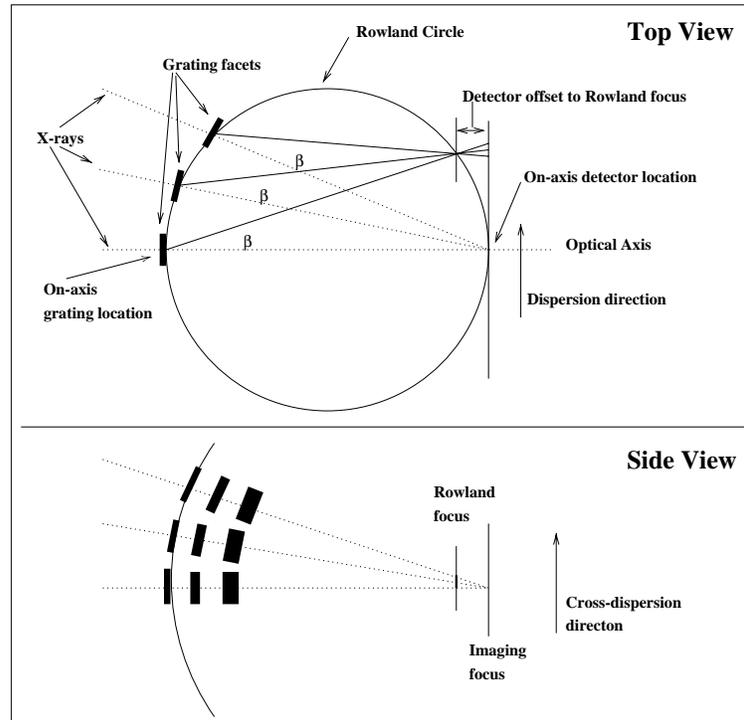
Figure 8.4: The Rowland geometry is shown schematically. In the "Top" view, we are looking across the dispersion direction. The diffraction angle is β. The geometry is such that converging rays diffracted at a specific angle by the gratings (which are located on the Rowland circle) will converge to a point that is also on the Rowland circle. The dotted lines represent zeroth-order rays and the solid lines the grating first-order diffracted rays. The bottom panel ("Side" view) looks along the dispersion direction at rays from a set of gratings arranged perpendicularly to those in the "Top" view and schematically shows the astigmatic nature of the spectrally focused image: since the converging rays have not yet reached the imaging focus, they are extended across the dispersion (by less than 100 microns).
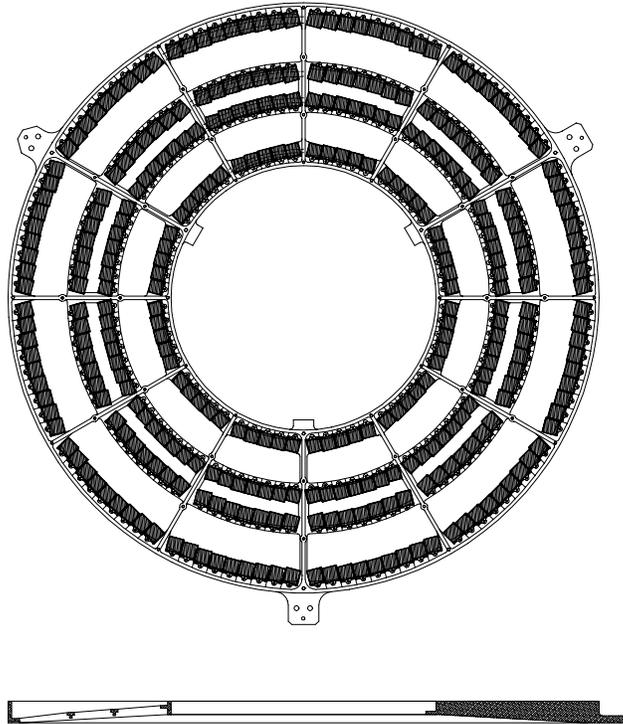
Figure 8.5: An (upper) front and side (lower) view of the HETG support structure (HESS). The grating facets are mounted to intercept the X-rays as they exit the HRMA; the front view is from the HRMA i.e., what an approaching X-ray would see. In the side view, the left cross-section shows that the four support rings are in different planes due to the Rowland curvature. The right cross-section is through a radial rib at one of the three mounting "ears".
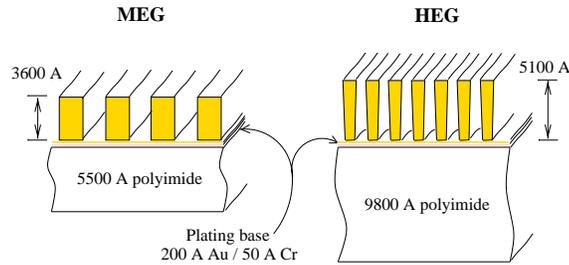
Figure 8.6: Cross-sections of the MEG and HEG membranes. The soap-bubble-thin membranes of the HETG consist of gold bars attached to a polyimide support layer. The MEG grating bars are close to rectangular, typically with a height of 3600 Å and a bar-to-period fraction of 52 % . The HEG bars have a crudely trapezoidal shape, typically 5100 Å high with an effective bar-to-period fraction around 60 % .

the *Absolute Wavelength* accuracy is of key interest. Summaries of these characteristics and related considerations are presented in the following sections. Flight calibration efforts to examine and improve the fidelity of the *MARX* parameters and these characteristics are presented in Section 8.3.4.

8.2.1   HETGS Effective Area

The HETGS effective area depends on the HETG efficiency coupled with the HRMA effective area and the ACIS efficiency. Additional effects can arise from the process of selecting events, the effect of chip gaps, and the use of "ACIS ENERGY" to do order sorting. In this chapter we use the term ACIS ENERGY to describe the energy deduced from the ACIS pulse height. Current values and assessments of these effects are described in Section 8.3.4.

Nominal HETGS *ARF*s

Combining the HETG diffraction efficiencies with the HRMA effective area and the ACIS-S detection efficiency produces the system effective area as a function of energy, described by an "ancillary response file" or *ARF*. Plots of HETGS *ARF*'s are shown in Figures 8.7 and 8.9 which are plotted with log vertical axes; the same plots with linear vertical scale are shown in Figures 8.8 and 8.10. The values are plotted from *ARF* files created by the *CXC* CIAO tool `mkgarf`.

   The plots shown here are for qualitative reference only; because the `mkgarf` tool also accounts for a variety of other effects, *e.g.*, dither motion, bad pixels, QE non-uniformity, etc., grating *ARF*s are custom made for a given observation. The calibration details of the *ARF* are presented in Section 8.3, Calibration. (For reference, the *ARF*s in these plots

were made based on the Capella Obsid 57 observation; *CIAO* version 2.2.1 software was used.)

Since first-order photons from both the HEG and MEG gratings provide information, to compare the HETGS with other instruments it is useful to plot the total HETGS effective area (the combined plus and minus first-order areas of both the HEG and MEG); this is shown by the solid curve in Figure 8.11. During an observation the zeroth-order photons from HEG and MEG form a single zeroth-order image; the effective area for this zeroth-order image is also plotted on this figure (dotted line).

Note the dips caused by the gaps between chips in these figures. The observatory is dithered in order to spread the signal across a large number of pixels. For HETGS observations sinusoidal motions with 8 arc second amplitude in spacecraft Y and Z axes are used with periods of 1000.0 and 707.0 seconds, respectively. When the combination of the chip gaps and dither are accounted for a "pitch fork" dip occurs at each gap region in the *ARF*s. Although effects of this motion are removed in on-ground processing, observers are advised to avoid placing spectral features of interest near the gaps. More information concerning gaps are in the next section. The effective areas shown in Figure 8.7-8.11 are based on an integration over the full LSF. Most of the flux in a line will be contained within a circle of diameter 4 arcsec. The user might wish to note that in data processing the pipeline software keeps only events that are in a spatial window that lies within 3 arcsec of the dispersion axis. This aperture guarantees that a high fraction, 97-99%, of the signal flux is retained while minimizing the contribution of the background. Further discussion of the spatial distribution of events can be found for the HRMA PSF in Chapter 4 and for the HETGS in Section 8.2.2 below.

The goal for HETGS effective area calibration is 10 % absolute and 3 % relative (e.g., for a line ratio). See Section 8.3.4 for a discussion of results of in-flight calibration.
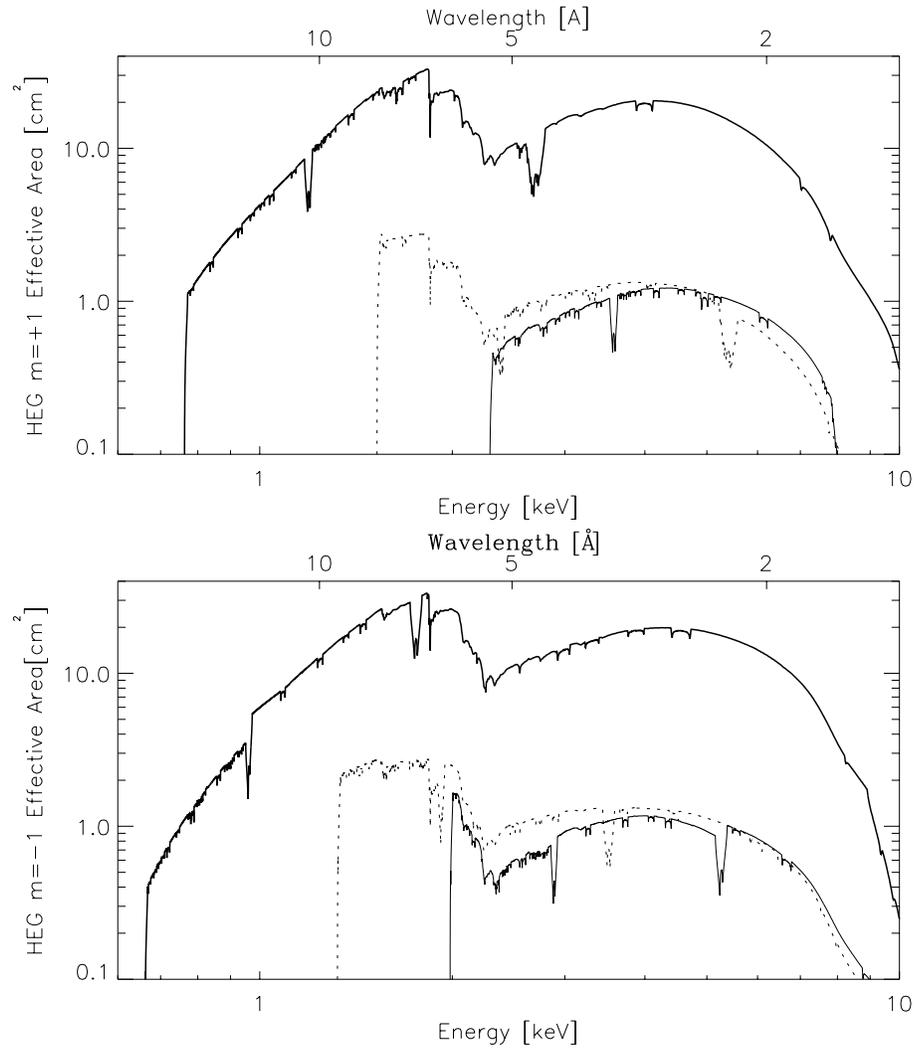
Figure 8.7: The HETGS HEG effective area, integrated over the PSF, is shown with energy and wavelength scales. The $m = +1, +2, +3$ orders (falling on ACIS chips S5, S4, S3; left to right) are displayed in the top panel and the $m = -1, -2, -3$ orders (falling on ACIS chips S0, S1, S2; left to right) are in the bottom panel. The thick solid lines are first order; the thin solid line is third order; and the dotted line is second order.
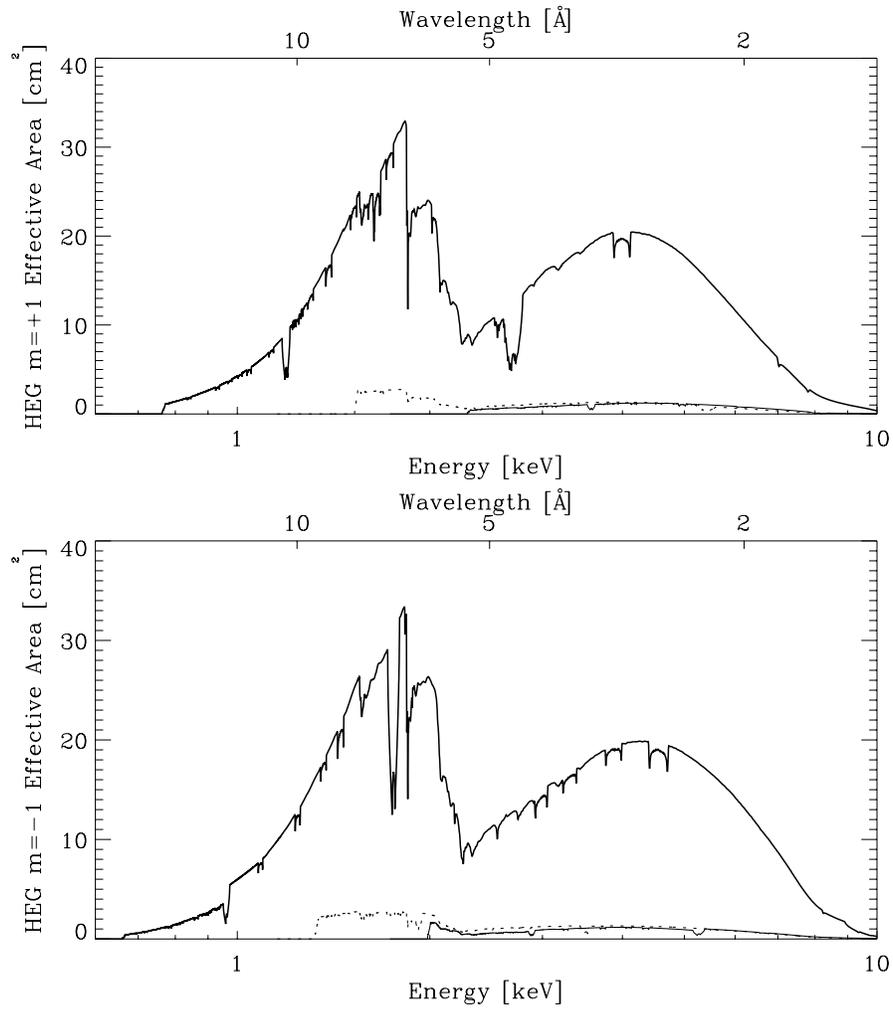
Figure 8.8: The HETGS HEG effective area: same caption as previous figure, except the vertical scale is now linear.
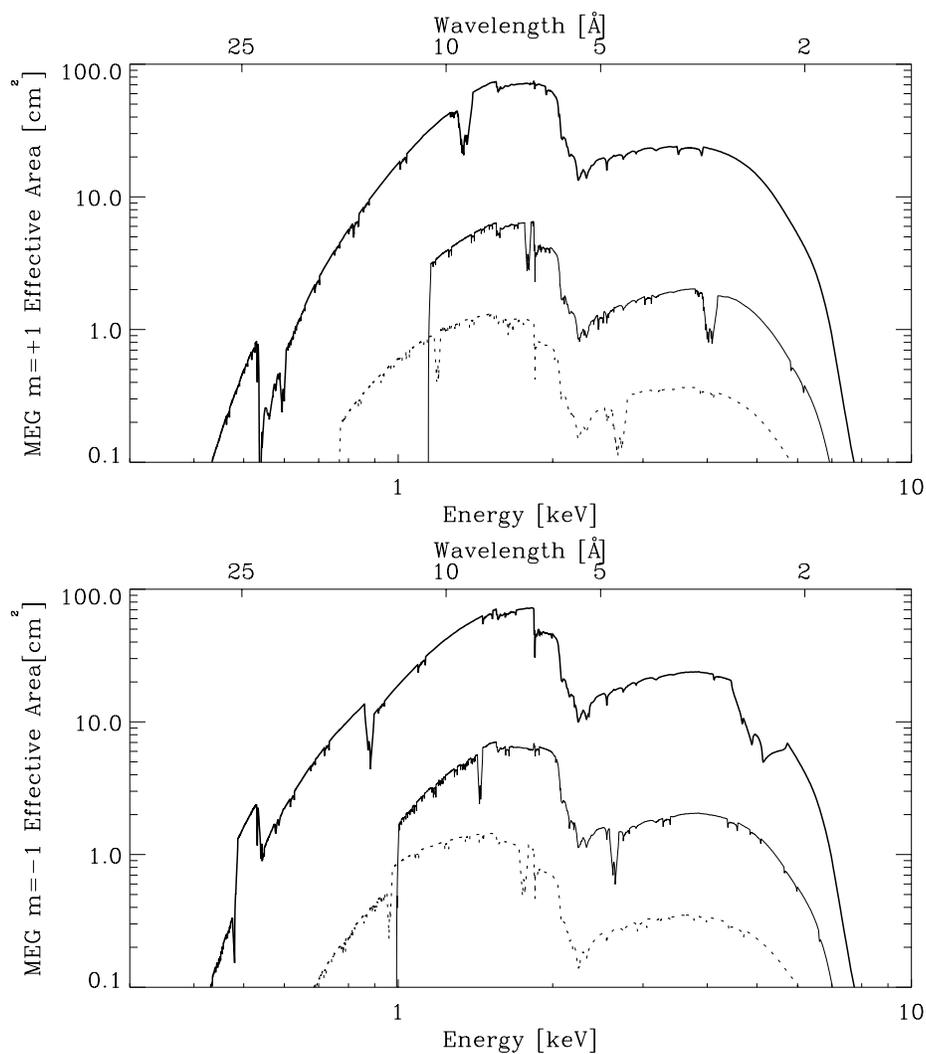
Figure 8.9: The HETGS MEG predicted effective area, integrated over the PSF, is shown with energy and wavelength scales. The $m = +1, +2, +3$ orders (falling on ACIS chips S5, S4, S3; left to right) are displayed in the top panel and the $m = -1, -2, -3$ orders (falling on ACIS chips S0, S1, S2; left to right) are in the bottom panel. The thick solid lines are first order; the thin solid line is third order; and the dotted line is second order.
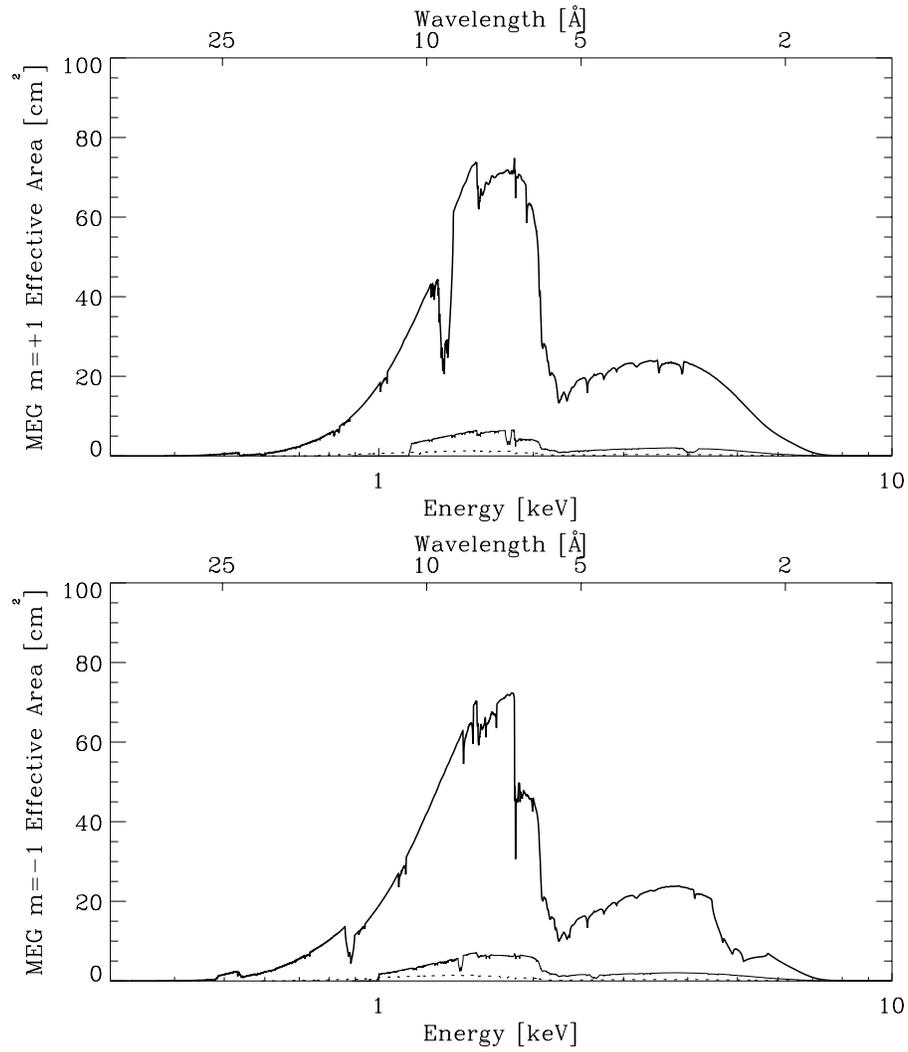
Figure 8.10: The HETGS MEG effective area: same caption as previous figure, except the vertical scale is now linear.
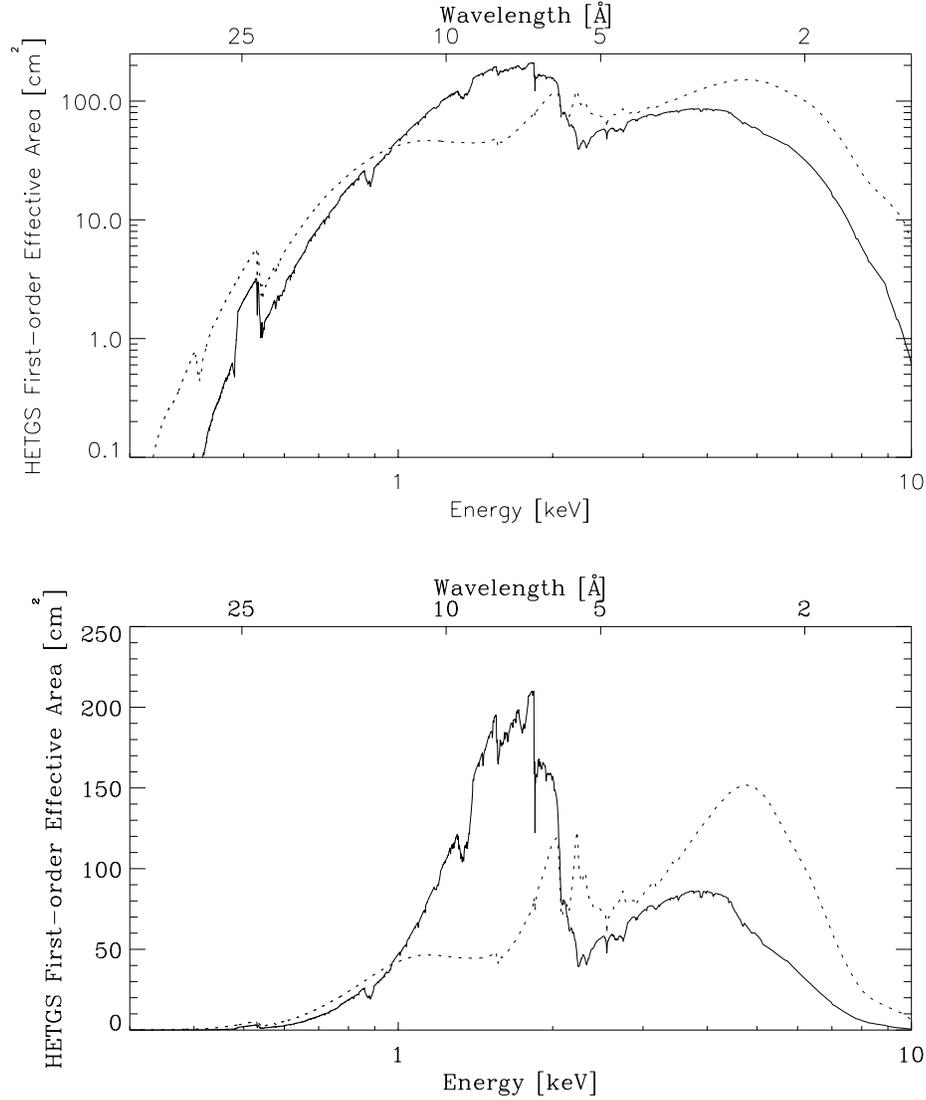
Figure 8.11: The modelled total first-order (solid curve) and zeroth-order (dotted curve) predicted effective area, integrated over the PSF, of the HRMA-HETG-ACIS-S combination, as a function of energy. The first-order data are the same as those plotted in Figures 8.7 and 8.9. The plotted first-order values are the sums of the area at a particular energy from both orders (+/-) of both MEG and HEG spectra. Both a log-log and a log-linear version are shown.

HETG Efficiency

The HETG contribution to the effective area comes in through the efficiencies of the HETG gratings; the values of these are shown in Figure 8.12. These efficiencies are currently based on laboratory measurements of each facet, synchrotron reference grating corrections, improved polyimide transmission models, and updated gold optical constants as described in Flanagan *et al.*, 2000.

ACIS-S Order Sorting Effects

One of the advantages of using the ACIS-S as the HETG readout detector is the ability of ACIS to determine the energy of detected X-rays. This crude (by HETGS standards) energy measure can be used to determine the diffraction order of the photon, i.e., perform "order sorting", as shown in the "banana plot" of Figure 8.13.

During data analysis this filtering is accomplished by utilizing two of the data columns supplied in the level 1.5 (or 2.0) FITS data file: the ACIS-determined energy, ENERGY, and the dispersion distance, $m\lambda$ = TG_MLAM. Ideally this order sorting would have perfect efficiency, that is, all first-order events would be correctly identified. In practice, a high sorting efficiency is achieved by accurately calibrating the ACIS ENERGY values and by accepting events in a large ENERGY range. The slight efficiency corrections that do arise are included in the *ARF* through values in an order sorting integrated probablility (osip) file.

ACIS-S Pileup Effects

Figure 8.14 shows a closeup of the "banana plot" (ACIS-determined energy versus the dispersion distance in units of wavelength) for MEG minus-order events for an observation which exhibits pileup (see the ACIS pileup section) and thus mimics higher-order photons. One can encounter pileup even in the dispersed spectra. The effect is most likely seen in first order spectra when observing bright continuum sources such as those fund in the Galactic bulge. Pileup, when it occurs, is most usually found in the MEG first order spectrum near the iridium edge at 2 keV where the HETGS effective area is the highest. Users analyzing data should note that not correcting for pileup may introduce an artificial absorption edge. In these cases users may well wish to examine the spectrum in the third order to either salvage or correct a result. Algorithms to correct for pileup are in development (J.E.Davis of the MIT/CXC)."

ACIS-S Chip Gap Effects

The nominal ACIS-S aim point is on chip S3, about $2.0'$ from the gap between chips S2 and S3. Energies of gap edges in both dispersed spectra for the nominal aim point and for
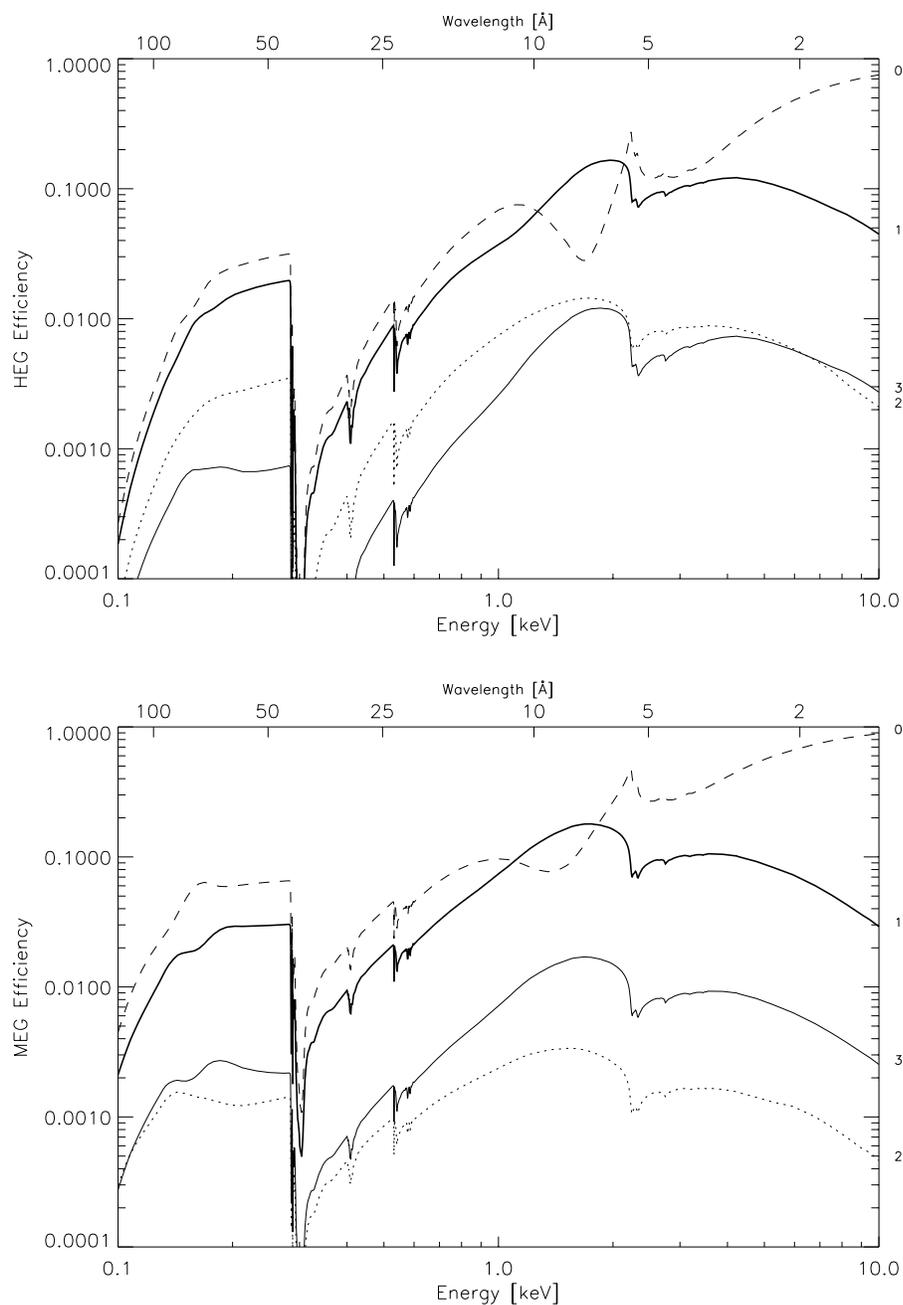
Figure 8.12: HEG (upper panel) and MEG (lower panel) efficiencies as a function of energy. The values plotted are the mirror-weighted efficiency into a single plus, minus, or zero order (labelled on the right edge). The dashed line is zeroth order; the thick solid line is first order. Note that the relative strengths of the third orders (thin solid lines) are comparable, whereas the second order strengths (dotted lines) are significantly different between the HEG and MEG.
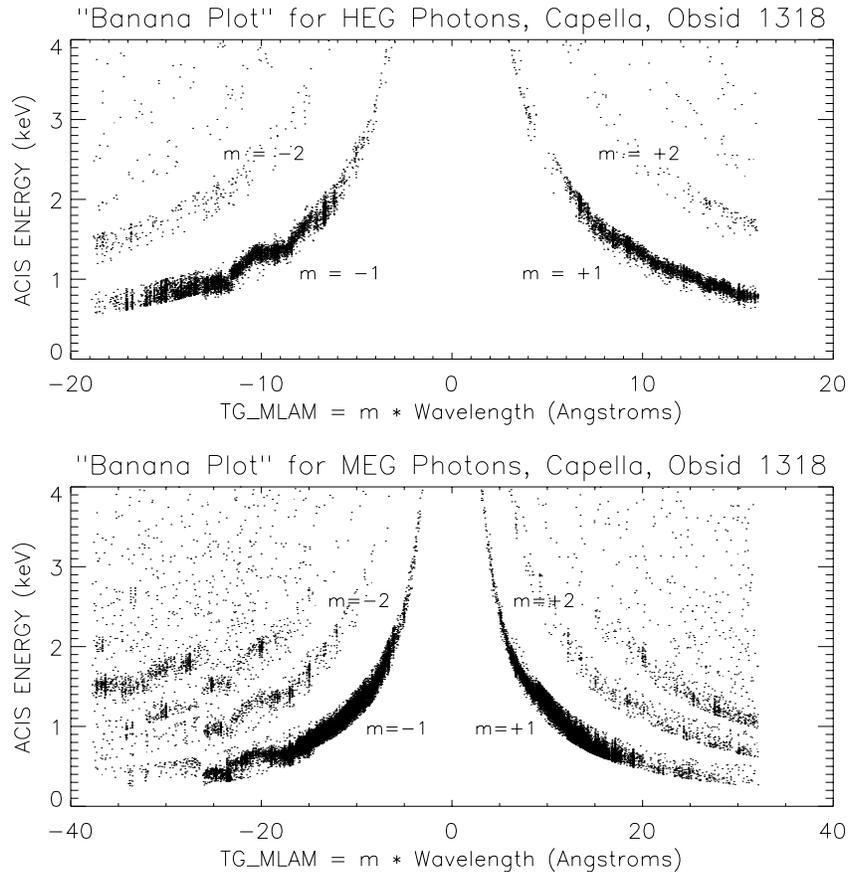
Figure 8.13: HEG (upper panel) and MEG (lower panel) "Banana Plots". A useful look at the HETGS data is obtained by plotting the ACIS-measured event ENERGY as a function of $m\lambda = $ TG_MLAM (or versus dispersion distance.) These "banana plots" are shown here for HEG and MEG parts of the Obsid 1318 Capella observation. The various diffraction orders show up as hyperbolae in these plots. Events can be assigned to a diffraction order based on their location in this space. By accurately calibrating the ACIS ENERGY and by taking an appropriate acceptance region, events can be order sorted with high confidence and efficiency. A "zig-zag" in the $m = -1$ events pattern is visible around -10 Å in the HEG plot and is due to uncorrected serial charge transfer inefficiency in the BI device S1 which produces a slow variation of gain across a node.
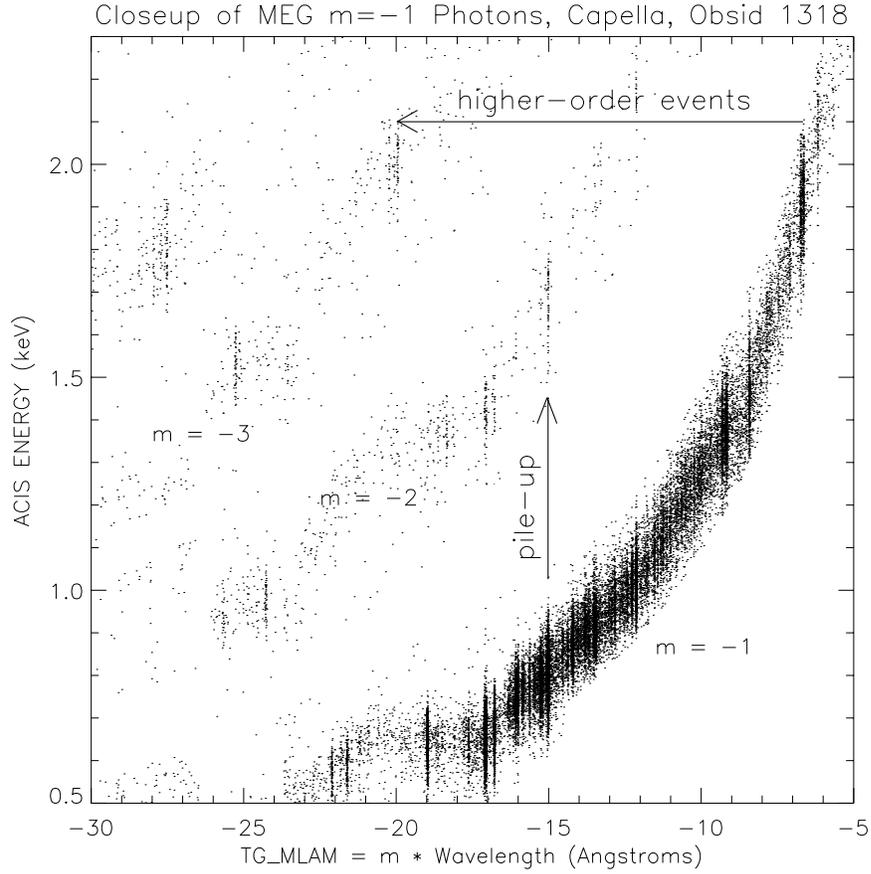
Figure 8.14: HETGS pile-up and higher-order events. Taking a close look at the MEG "banana plot" demonstrates how the ACIS ENERGY can be used to identify higher-order events and pileup in an HETGS spectrum. The 3rd order of the ≈ 6.7 Å lines are clearly visible; the lines are only weakly present in 2nd order because the MEG 2nd order is suppressed. In comparison, the 15 Å line (and others) are so bright in 1st order that a fraction of the events (≈ 6 % here) pile-up and produce events with twice the ACIS ENERGY. Note that the 6.7 Å lines are better resolved in the high order spectrum.

3 offsets in both (+/-) Y directions are given in Table 8.2. *Note well that when ACIS-S is placed in the focal plane, the standard procedure includes a -20 arcsec (-0.33 arcmin) offset to avoid placing the image of a point source on the boundary between the nodes in S3.* Table 8.2 gives the energies of gaps relative to the nominal aimpoint, not the standard offset position. For example, with zero order at this standard Y-offset position, the gap between chips S3 and S4 spans the energy range 1.519-1.477 keV in the MEG spectrum (lower energies on S4). With a +0.33 arc minute Y offset, the S2-S3 gap in the HEG spectrum is moved up to over 9 keV, so that the Fe-K line region is not affected.

These values are based on an effective gap size of 0.502 mm, corresponding to 10″ on the sky. It is "effective" in the sense that the gap includes columns 1 and 1024 of the devices from which no events are reported. This value for gap size is approximate and accurate to about 2 pixels. The actual gap sizes vary slightly; more accurate values of the ACIS-S chip geometry are given in the CXCDS CALDB file 'geomN0002 (and higher versions) and incorporated in *MARX* version 3.0 and higher.

The chip gaps were determined from early in-flight calibration data and were consistent with ground-based data taken at about the same temperature of the ACIS detector. Relative to S3, where zeroth order is normally placed, the chip placement accuracy of S2 and S4 is estimated to be of order 0.2 pixels (0.001 Å for the HEG and 0.002 Å for the MEG) but may be as large as 0.5 pixels for chips S0, S1, and S5 (0.0028 Å for the HEG and 0.0055 Å for the MEG). Chip placement may be the limiting factor in determining the relative accuracy of line wavelengths when measured on different chips. The chip placement accuracy will be revisited as more lines in flight calibration targets are identified with accurately known laboratory-measured wavelengths.

All HETGS observations are nominally dithered with an amplitude of ±8 arc seconds. There will thus be reduced coverage in the spectral regions within one gap-width on either side of the gaps.

Finally, the observer is advised to *try to avoid placing known features of interest within three gap widths of the tabulated gap edges.* Note that the nominal acquisition accuracy (Chapter 5) should also be taken into account.

8.2.2   HETGS Line Response Function

A high-resolution spectrum is created by the projection of events along the dispersion axis and binning the events into energy or wavelength bins as shown in Figure 8.2. The HETGS line response function (LRF) at a given wavelength is the underlying distribution which would result if the source were monochromatic at that wavelength. Examples from flight data are shown in Figures 8.16 and 8.17. To a good first approximation the core of the LRF can be modeled as a Gaussian, parameterized by a *Resolution*, ΔE or $\Delta \lambda$, given as the full-width at half-maximum of the Gaussian, 2.35σ. The *Resolving Power*,

Table 8.2: Table of HETGS Gap Locations

Y Offset		Grating	HETGS Gaps (keV)						
arc min.	mm		S0	S0-S1	S1-S2	S2-S3	S3-S4	S4-S5	S5
+1.00	+2.93	MEG		0.497	0.931	7.423	1.243	0.574	0.373
			0.341	0.502	0.948	8.629	1.215	0.568	
		HEG		0.993	1.861	14.834	2.485	1.146	0.745
			0.681	1.002	1.894	17.244	2.428	1.134	
+0.66	+1.93	MEG		0.488	0.900	5.812	1.304	0.586	0.378
			0.337	0.492	0.916	6.527	1.273	0.580	
		HEG		0.975	1.799	11.615	2.606	1.171	0.756
			0.673	0.984	1.830	13.043	2.543	1.159	
+0.33	+0.97	MEG		0.479	0.872	4.801	1.369	0.599	0.383
			0.333	0.484	0.886	5.279	1.334	0.592	
		HEG		0.958	1.742	9.595	2.735	1.197	0.766
			0.665	0.967	1.771	10.548	2.666	1.184	
0.00	0.00	MEG		0.471	0.845	4.090	1.440	0.612	0.389
			0.329	0.475	0.859	4.431	1.402	0.605	
		HEG		0.942	1.689	8.173	2.878	1.223	0.777
			0.657	0.950	1.716	8.855	2.802	1.209	
-0.33	-0.97	MEG		0.463	0.820	3.562	1.519	0.626	0.394
			0.325	0.467	0.833	3.818	1.477	0.619	
		HEG		0.926	1.638	7.118	3.036	1.251	0.788
			0.649	0.934	1.664	7.630	2.952	1.237	
-0.66	-1.93	MEG		0.456	0.796	3.155	1.608	0.641	0.400
			0.321	0.460	0.808	3.354	1.561	0.633	
		HEG		0.910	1.591	6.305	3.213	1.280	0.799
			0.642	0.918	1.615	6.703	3.118	1.265	
-1.00	-2.93	MEG		0.448	0.773	2.822	1.710	0.656	0.406
			0.317	0.452	0.785	2.981	1.657	0.648	
		HEG		0.895	1.545	5.640	3.418	1.312	0.812
			0.634	0.903	1.568	5.957	3.311	1.296	

$E/\Delta E = \lambda/\Delta\lambda$, is a useful dimensionless measure of the spectrometer performance. Plots of the HETGS resolving power are presented in Figure 8.18.

Of course the HETGS LRF is not simply a Gaussian and, as for other spectrometers, the response can be encoded at a higher level of fidelity through the use of response matrix files, *RMF*'s. As explained below, the LRF (*RMF*) of the HETGS depends on all system components as well as the source spatial properties. Thus, LRF creation is carried out using a system model, e.g., the *MARX* ray-trace software (Ver. 4.0). A set of RMF's for a point source and nominal telescope properties can be created based on the latest LRF library (LSFPARM, in the CALDB directory `tel/grating/hetg/cpf/lsf/`.) Version N0003 of LSFPARM includes two Gaussian and two Lorentzian components to describe the LRF as derived from realistic MARX simulations; for examples, see the fitted LRF models in Figures 8.16 and 8.17. (Note that a "canned" set of RMFS (Version N0004, CALDB directory `tel/grating/hetg/cpf/rmf`) were created from an earlier single Gaussian and single Lorentzian LRF model; these may be used for observation planning purposes but should not be used for analyzing real data.)

The line response function can be decoupled approximately into three contributing components: the telescope PSF, the HETG effects in the dispersion direction, and HETG effects in the cross-dispersion direction. These are described below. With the exception of "HEG scatter", all effects described here are included in *MARX* version 3.0 (and higher) ray-trace software.

LRF: Telescope PSF and Zeroth Order

The HETG itself does not focus the X-rays emerging from the HRMA. Rather, *the Rowland design attempts to maintain the focal properties of the HRMA in the dispersion direction even as the focus is deflected by the diffraction angle β.* The 1-D projection of the telescope PSF onto the dispersion axis is thus at the heart of the HETGS LRF and can be thought of as the "zeroth-order LRF". Ground testing showed no measurable effect on the telescope PSF due to the HETG insertion; this was taken advantage of in the now famous image of the Crab Nebula and its pulsar, Obsid 168, where the jet and swirling structure are seen in the zeroth-order HETGS image. Thus, the zeroth-order image in an HETGS observation can be used to determine the telescope contribution to the LRF.

Image quality depends on many factors, and so, while a nominal LRF can be modeled, the detailed LRF will be observation dependent at some level. Factors in the telescope PSF performance include: source size and spectrum, HRMA properties, focus setting, detector effects (e.g., pixel quantization), aspect solution and reconstruction effects, and data analysis operations (e.g., pixel randomization.) While all of these effects can be modeled, the "proof of the pudding" is in the as-observed zeroth order image.

As an example we show the results of the observation of Capella (Obsid 1318, Figure 8.1) in Figure 8.15. Both the zeroth-order event distribution and its 1-D projection

indicate that the zeroth-order is heavily piled up with an unpiled event rate of order 10 events per frame time (per few square ACIS pixels). The wings of the PSF are visible but the core shape and intensity have been severely distorted. However, because the ACIS-S CCDs have their columns perpendicular to the (average) dispersion axis, the "frame-transfer streak" events or "trailed image" (see Section 6.12.4 in Chapter 6) can be used to create an accurate zeroth order LRF that is not affected by pileup, as shown. For point-sources such as Capella, measurements of the FWHM of the zeroth-order streak events for selected observations over the first two years of HETGS operation show FWHM values generally in the range 1.46 to 1.67 ACIS pixels with an average of 1.57 ACIS pixels.Thus,by appropriately examining the zeroth-order image and its LRF, one can get a good idea of the expected width of a truly mono-chromatic spectral line, and determine whether or not any broadening seen in a dispersed order is a spectral property of the X-ray source.

LRF: Dispersion Direction

As mentioned, the profile in the dispersion direction defines the instrument spectral resolution, ΔE or $\Delta \lambda$. The resolution function has two main terms with different dependences on energy: the image blur from the mirror described above and that caused by grating period variations which come in through the dispersion relation and are described here.

From the grating equation, $m\Delta\lambda = p\Delta\beta cos\beta + \Delta p sin\beta \approx y\Delta p/R_s + p\Delta y/R_s$, where y is the dispersion distance and R_s is the (fixed) Rowland spacing. The two terms of interest are on the right side of $\lambda/\Delta\lambda = (\Delta p/p + \Delta y/y)^{-1}$. The grating fabrication process produced tightly distributed grating periods ($\Delta p/p < 2.5 \times 10^{-4}$) so that the first term is important in the spectral resolution only at very high dispersion (low energy). The mirror point response function has a nearly constant size Δy and dominates the resolution over most of the HETGS band, as shown in Figure 8.18. At very low energies there is a contribution from variation in the grating periods. These variations are taken into account in the *MARX* simulator.

During ground testing, we discovered that there is a low-level of incoherent dispersion (or "scattering") in HEG spectra. This scattering effect distributes a small amount of the flux along the dispersion direction. The total power involved is only 1.0% of the total in first order but the light is irregularly distributed between the coherently dispersed orders. Assuming that the power distribution scales with the first order dispersion distance, there is no more than 0.02% of the first order flux in any bin of width 0.01λ. There has been no scattering detected in the MEG spectra to a level of order 100 times fainter than in the HEG. See the HETG Ground Calibration Report listed at the end of this chapter for further details. The effects of scattering from the grating are likely to be negligible for most observations.
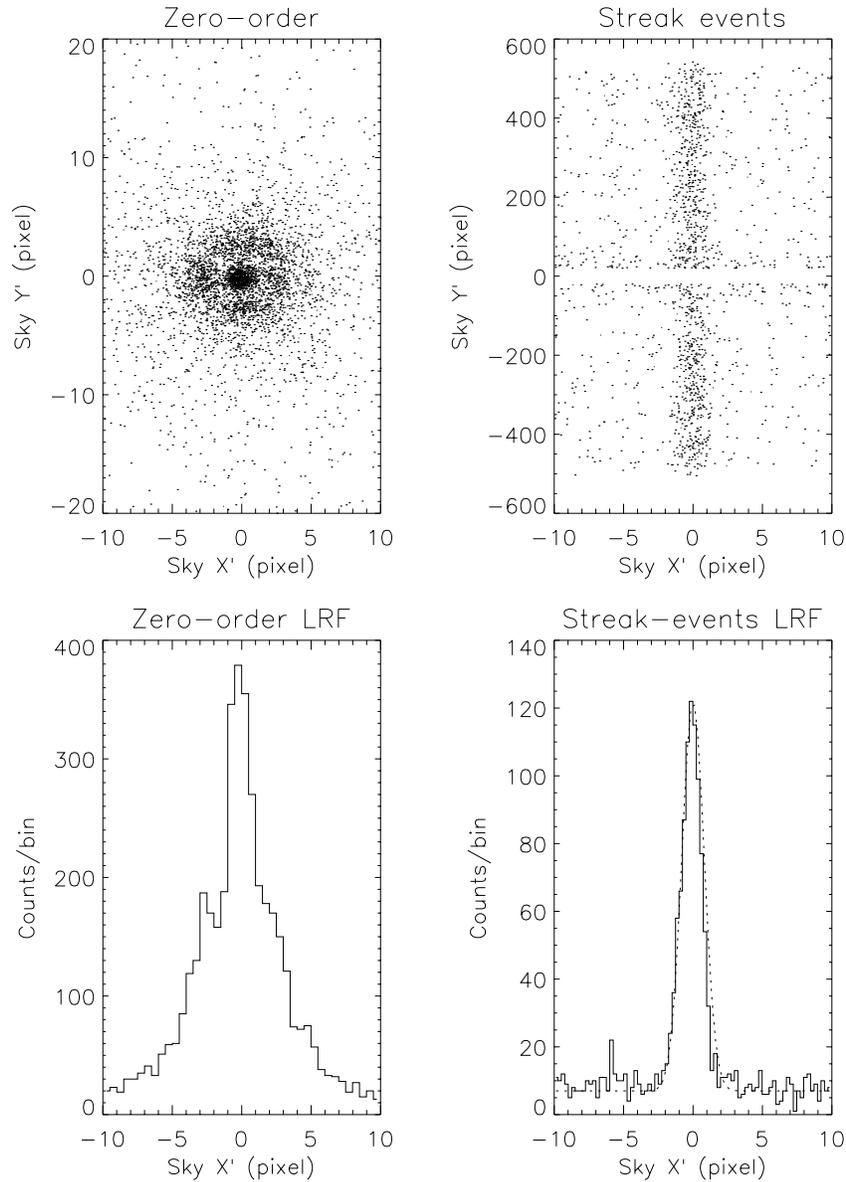
Figure 8.15: HETGS Zero order and Frame transfer Streak (trailed image) for Obsid 1318 of Capella. The sky coordinates, X, Y, have been rotated so that the frame-transfer streak is along the Y' axis, hence Y' is parallel to the CCD detector Y axis (`CHIPY`) and X' is approximately along the average HEG-MEG dispersion axis. The left-side panels show the detected zero-order events and their 1-D projection; pileup is evident by the enhanced wings relative to the suppressed PSF core. The right-side panels show the frame-transfer streak events and their 1-D projection; the dotted line is a Gaussian with FWHM of 1.33 ACIS pixels, or 0.65 arcsec.
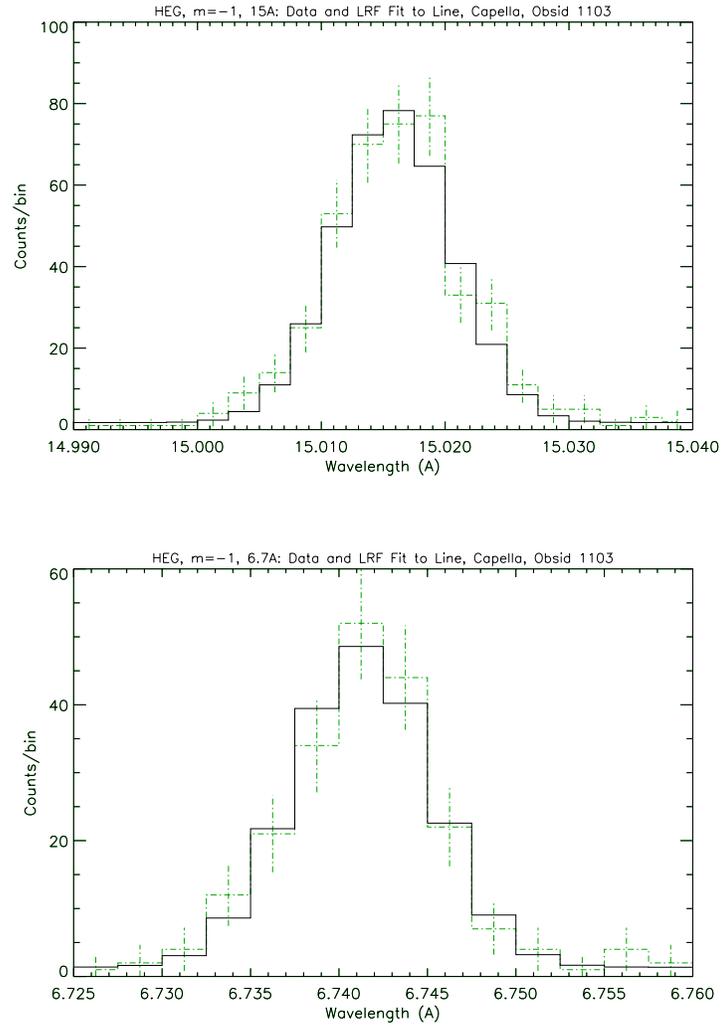
Figure 8.16: Representative Line Response Functions at two wavelengths for the HEG; 15 Å top, 6.7 Å bottom. Two of the bright lines in the HEG counterpart to the MEG Capella spectrum shown in Figure 8.2 have been fit by the instrumental LRF. The LRF is encoded in the HEG *RMF* created using *CXC* software and calibration parameters (`mkgrmf, lsfparmN0003.`)
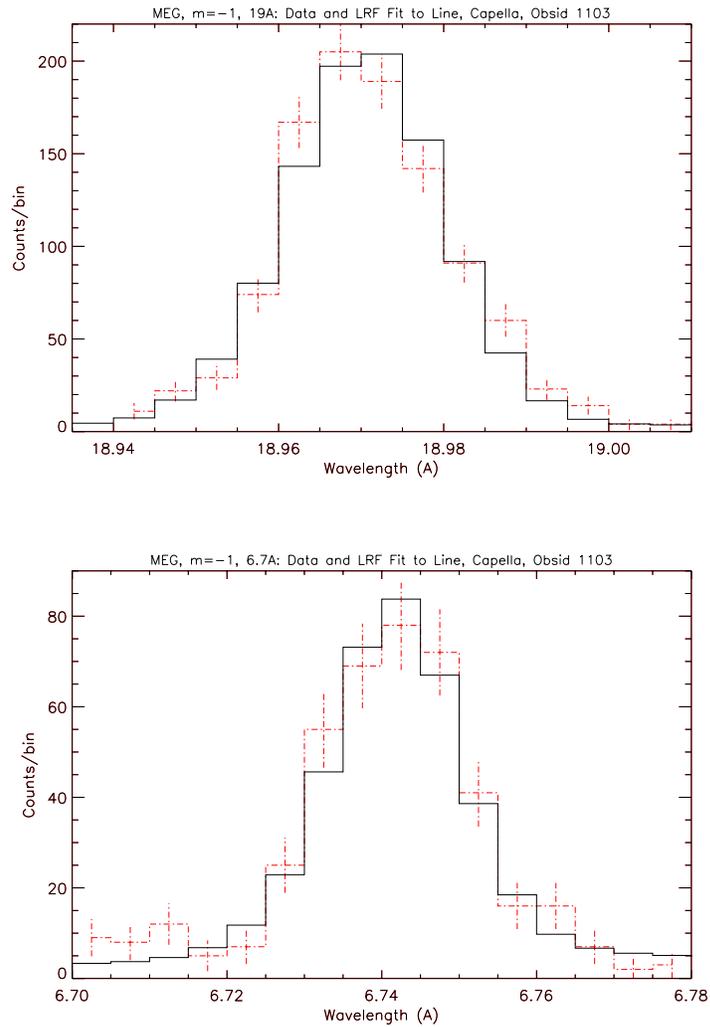
Figure 8.17: Representative Line Response Functions at two wavelengths for the MEG; 19 Å top, 6.7 Å bottom. Two of the bright lines in the MEG Capella spectrum shown in Figure 8.2 have been fit by the instrumental LRF. The LRF is encoded in the MEG *RMF* created using *CXC* software and calibration parameters (`mkgrmf, lsfparmN0003`.)
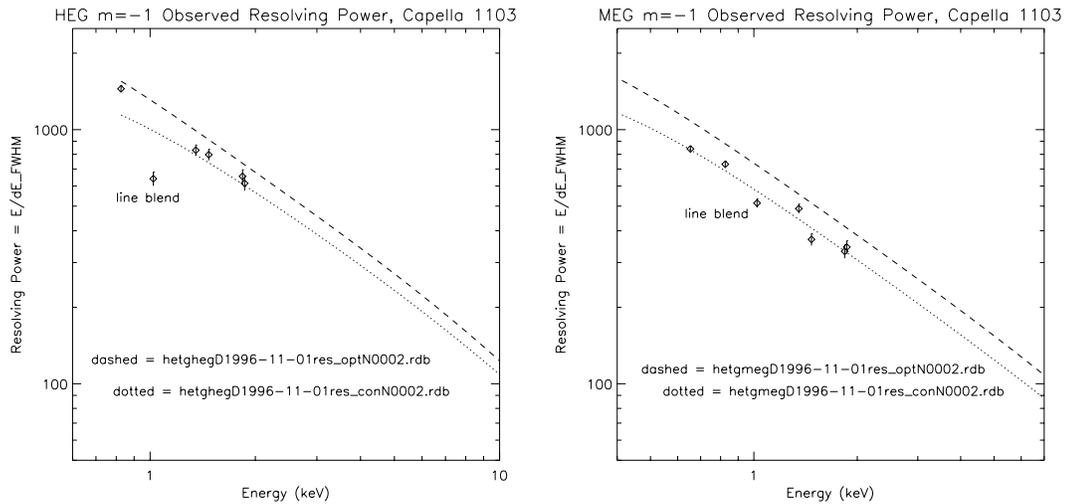
Figure 8.18: HEG and MEG Resolving Power ($E/\Delta E$ or $\lambda/\Delta\lambda$) as a function of energy for the nominal HETGS configuration. The resolving power at high energies is dominated by the telescope PSF; at low energies grating effects enter but do not dominate. The "optimistic" dashed curve is calculated from pre-flight models and parameter values. The "conservative" dotted curve is the same except for using plausibly degraded values of aspect, focus, and grating period uniformity. The cutoff at low-energy is determined by the length of the ACIS-S array. Measurements from the HEG and MEG $m = -1$ spectra, e.g., Figure 8.2, are typical of flight performance and are shown here by the diamond symbols. The values plotted are the as-measured values and therefore include any natural line width in the lines; for example, the "line" around 12.2 Å is a blend of Fe and Ne lines.

LRF: Cross-Dispersion Direction

The profile in the cross-dispersion direction is dominated by three effects: mirror blur, grating roll variations, and astigmatism (as a by-product of the Rowland design which optimizes spectral resolution). The cross-dispersion profile that results from astigmatism is slightly edge brightened, but quasi-uniform, with a length at the Rowland focus of $2R_f y^2/R_s^2$, where R_f is the radius of the ring of facets on the HETGS structure and dominates the size of the cross dispersion profile at large dispersion.

The spread of facet roll angles (defining the dispersion direction for each facet, and not to be confused with the spacecraft roll angle), $\Delta\phi$, contributes a cross-dispersion term of order $y\Delta\phi$. Sub-assembly measurements predicted $\Delta\phi$= 0.42 arc minutes rms. However, analysis of ground test measurements lead to a somewhat larger and more complex roll angle distribution for the gratings. In addition, six misaligned MEG facets were discovered during ground testing. The inferred facet roll angles were misaligned from the average dispersion direction by 5-23 arc min. On average, each facet contributes only 1/192 of the flux at any given energy, so the cross dispersion profile has small deviations in the form of peaks displaced from the main distribution.

In order to include explicitly the MEG misaligned gratings *MARX* uses "sector" files which allow the specification of grating alignment and period parameters for certain regions (sectors) of each of the four shells. Using these files, the agreement between ground calibration and flight data is very good. For the MEG the misaligned gratings are explicitly included and the rest of the gratings' $\Delta\phi$ term is modeled as the sum of two Gaussian distributions centered at +1 and -1 arc minute w.r.t. the nominal axis, each with an rms value of 1.5 arc minutes. For the HEG a more pronounced bi-gaussian distribution is observed and modeled: the Gaussians are offset by -1.35 and +1.65 arc minutes, each with a 1 arc minute rms, and in a relative ratio of 55:45.

In each case, these effects are accurately included in *MARX* version 3.0 (and above). Flight data for the Crab pulsar (Obsid 168) are shown in Figure 8.19 for the MEG and in Figure 8.20 for the HEG, respectively. Note that these profiles are on top of a significant baseline due to the presence of the Nebula. The asymmetry in the MEG profile caused by misaligned gratings is quite clear at large dispersions.

Finally, we show in Figure 8.21 how the total observed flux depends on the width of the extraction region in the cross-dispersion direction. The figure can be used to estimate the reduction in flux if analysis using a narrow extraction window, smaller than the nominal 4 arcsec full width, is planned.

Extended and Off-Axis Targets

The observation of extended sources with the HETGS adds complexity. Chiefly, the position of an event in the focal plane is not a unique function of the position within the
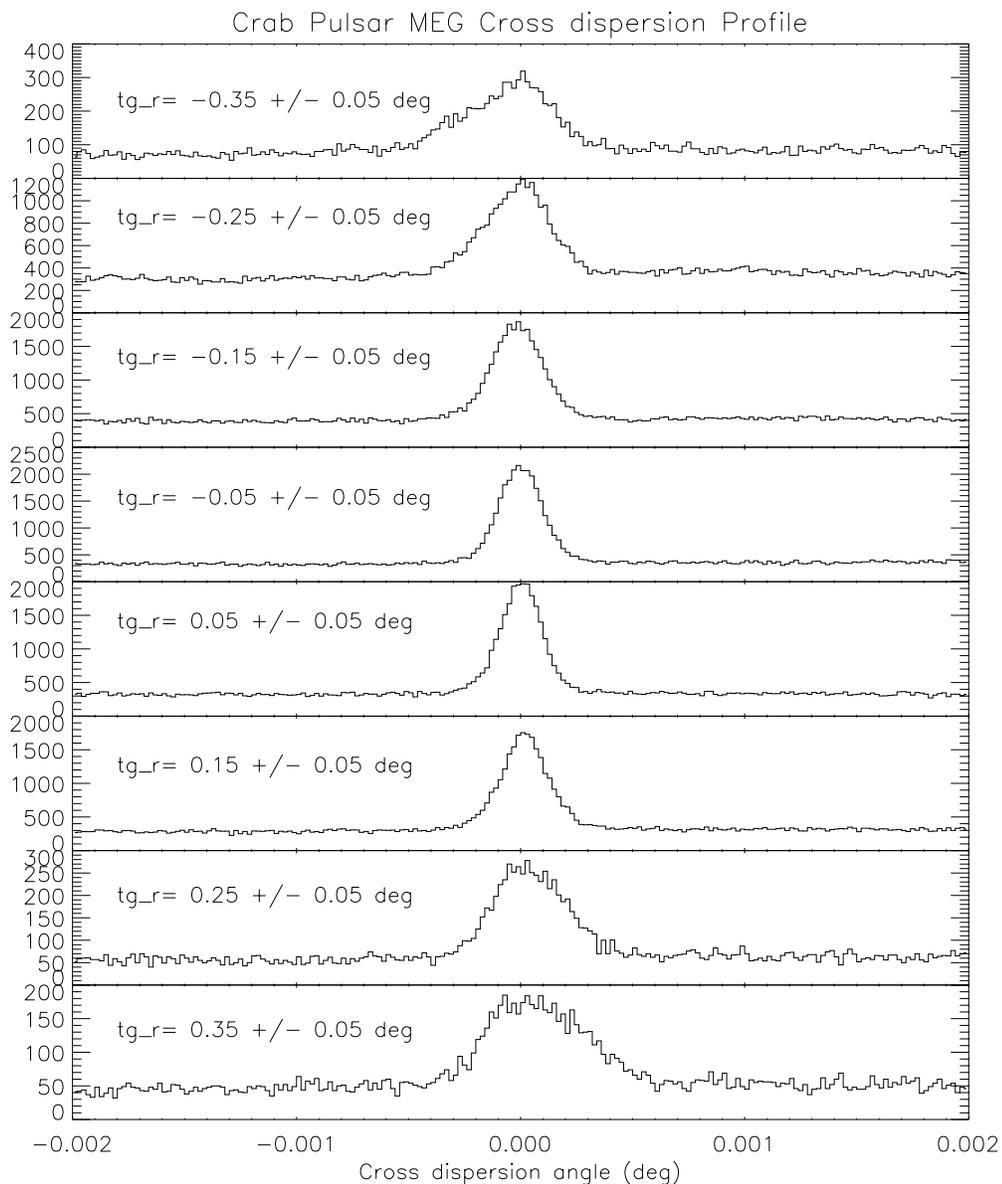
Figure 8.19: The cross dispersion profile is shown for eight slices of the dispersed MEG spectrum of the Crab pulsar. There is an asymmetry caused by misaligned gratings that becomes most evident at large dispersion.
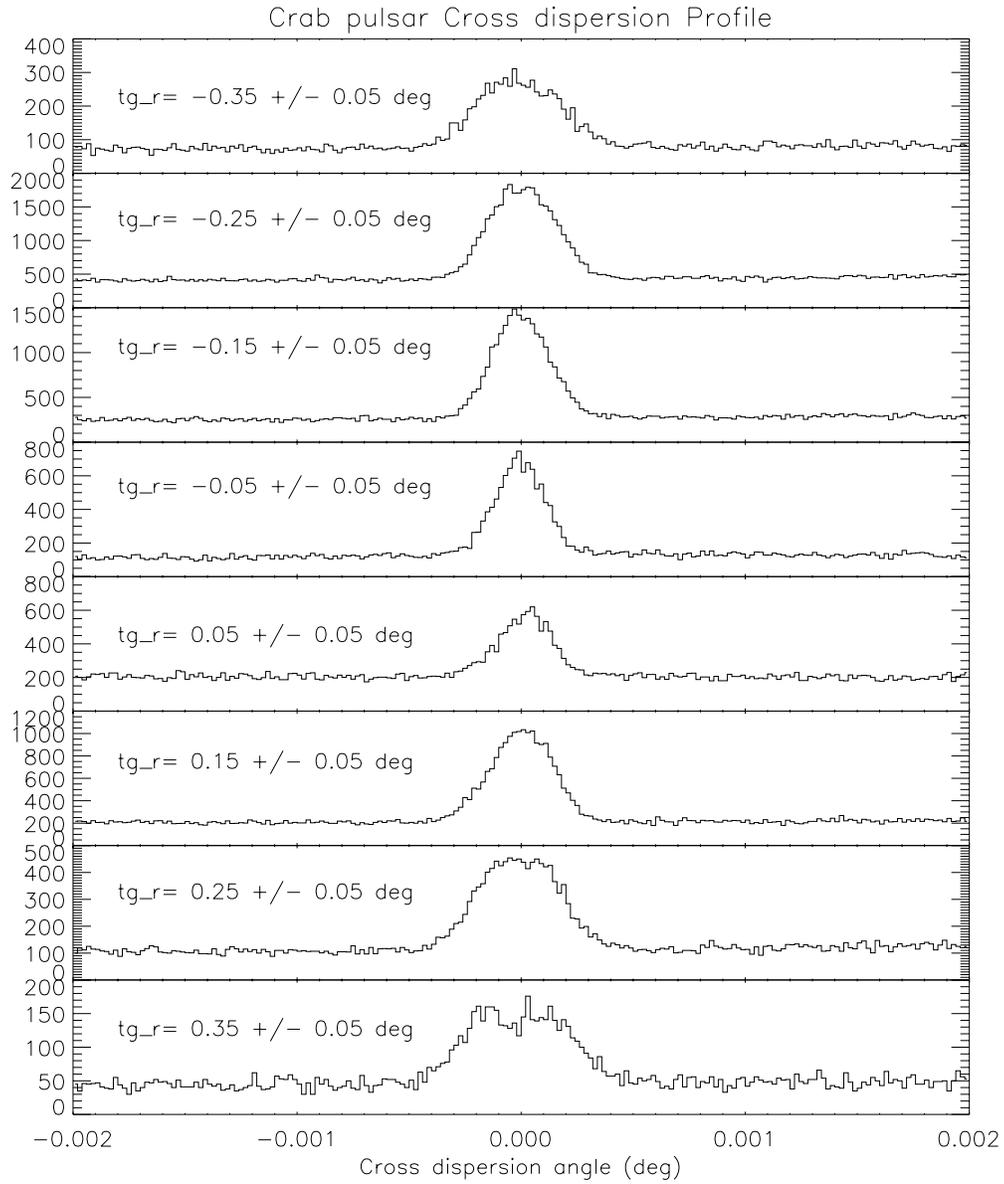
Figure 8.20: As in Figure 8.20, the cross dispersion profile is shown for the HEG spectrum of the Crab pulsar. The profile is symmetric but broadens significantly at large dispersion.
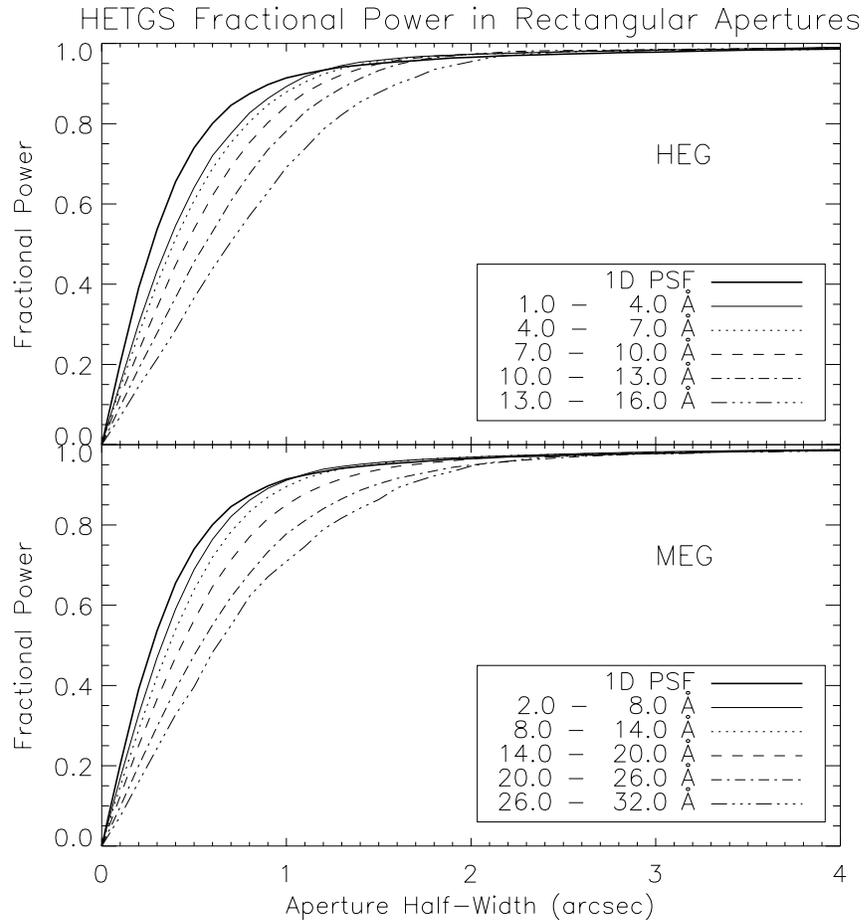
Figure 8.21: Enclosed power distributions are computed for five wavelength intervals for both the HEG (top) and the MEG (bottom). The observation of Mk 421 (observation ID 1714) was used.

source and the photon energy. The source extent, measured by the zeroth-order image size, can effectively increase in several ways: the telescope is out of focus, the source is off-axis, or there is a natural extent to the astrophysical source. Figure 8.22 illustrates the chief consequence for extended sources - a degradation of the apparent spectral resolution. In Figure 8.23 similar resolution curves are shown as a function of the source off-axis angle.

The discussion and plots above assumed that the source has no spatially dependent variations in the spectrum. The more general case of extended sources with spatially varying spectra is briefly discussed below in Section 8.5.3.

8.2.3 Background

Since the HETG is always used in conjunction with a focal-plane detector, spectra from the HETGS will have background events determined by the detector's intrinsic and environmental backgrounds. The cosmic background, folded through the HETGS response, will likewise contribute background events. In addition to these detector-dependent backgrounds, there are additional grating-dependent effects such as scattering from the gratings which will produce extraneous photons in locations unexpected on the basis of the simple grating equation. One such effect is the scattering along the dispersion direction described in Section 8.2.2.

Figure 8.24 shows the HEG and MEG spectra of the background for a long calibration observation of HR 1099 (observation ID 62538). The background was selected from regions 8-50 arcsec from the dispersion line in the HEG and 11-50 arcsec from the dispersion line in the MEG. The pulse height selection was simple, accepting events that satisfy the relation $|E_{ACIS}/E_{TG} - 1| < 0.30$, where E_{ACIS} is the energy derived from the ACIS-S pulse height and E_{TG} is the energy based on the dispersion distance. The background was normalized to an aperture of $\pm$ 3 arcsec (full size of 6 arcsec) and averaged at 0.1 A intervals. This plot can be used to estimate the background in a dispersed spectrum at a particular wavelength for proposal purposes.

There is considerable structure in the background. for $\lambda < 2$ Å ($E > 6$ keV), the background is dominated by high energy events that are included in the relatively wide pulse height selection. This background can be further reduced in data analysis because the pulse height selection can be somewhat narrower at high energies. As one would expect, the background is higher in the region near 8 Å in -1 order as this portion of the dispersed spectrum is detected with a BI chip (S1). "Streaks", short-lived events observed in the S4 detector, have been removed; otherwise, the background in +1 would be significantly higher and would show more structure.
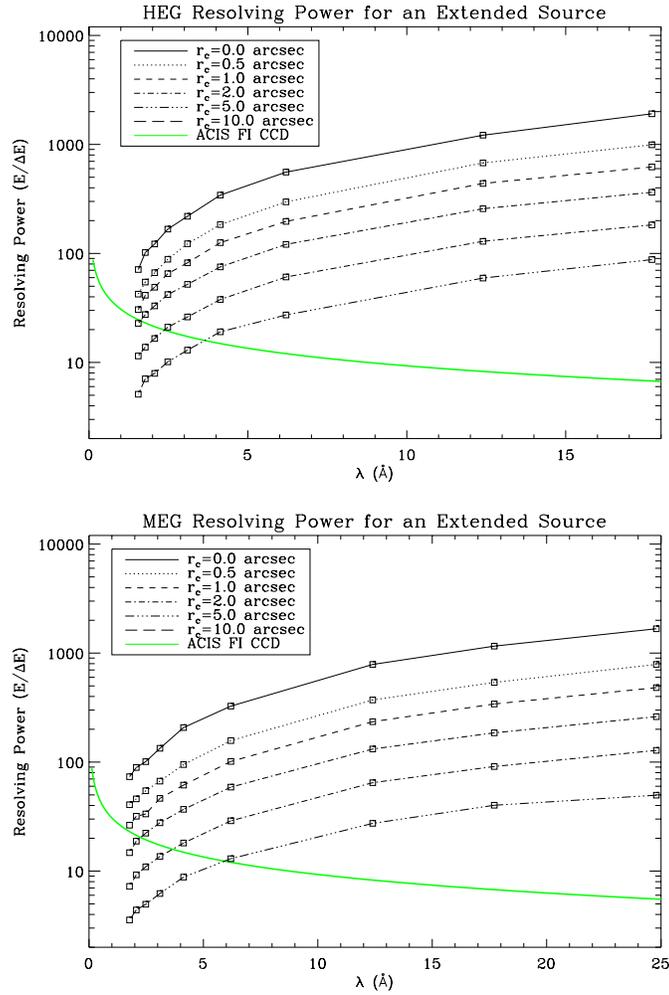
Figure 8.22: The effects of source size on the apparent HETGS spectral resolution. This *MARX* simulation uses a cluster (of galaxies) Beta model for the surface brightness profile. The Beta model is parameterized by a core radius (r_c) which represents the extension of the source. The effect on the apparent resolving power ($E/\Delta E$) is shown as a function of photon energy for source sizes of $0''$, $0.5''$, $1''$, $2''$, $5''$, and $10''$. The spectral resolution of an ACIS FI CCD near the framestore region is shown for comparison.
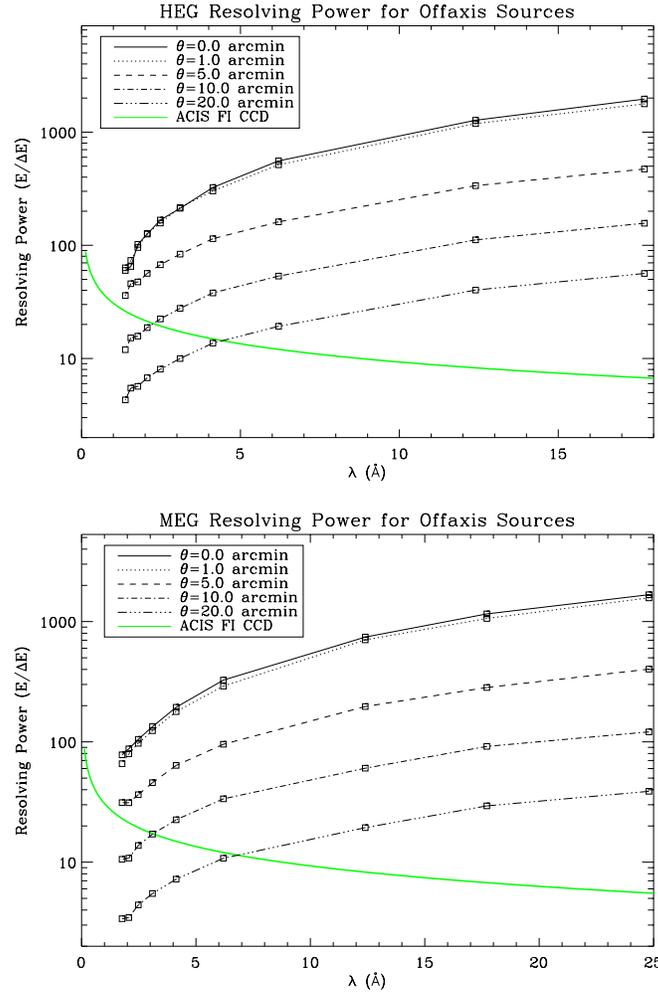
Figure 8.23: The effects of off-axis pointing on the HETG grating spectral resolution. Using *MARX*, we have simulated an observation of a point source at increasing off-axis positions. The effect on the resolving power (E/ΔE) is shown as a function of photon energy for off-axis angles of $0'$, $1'$, $5'$, $10'$, and $20'$. The spectral resolution of an ACIS Front Illuminated (FI) CCD at a point near the framestore region is shown for comparison.
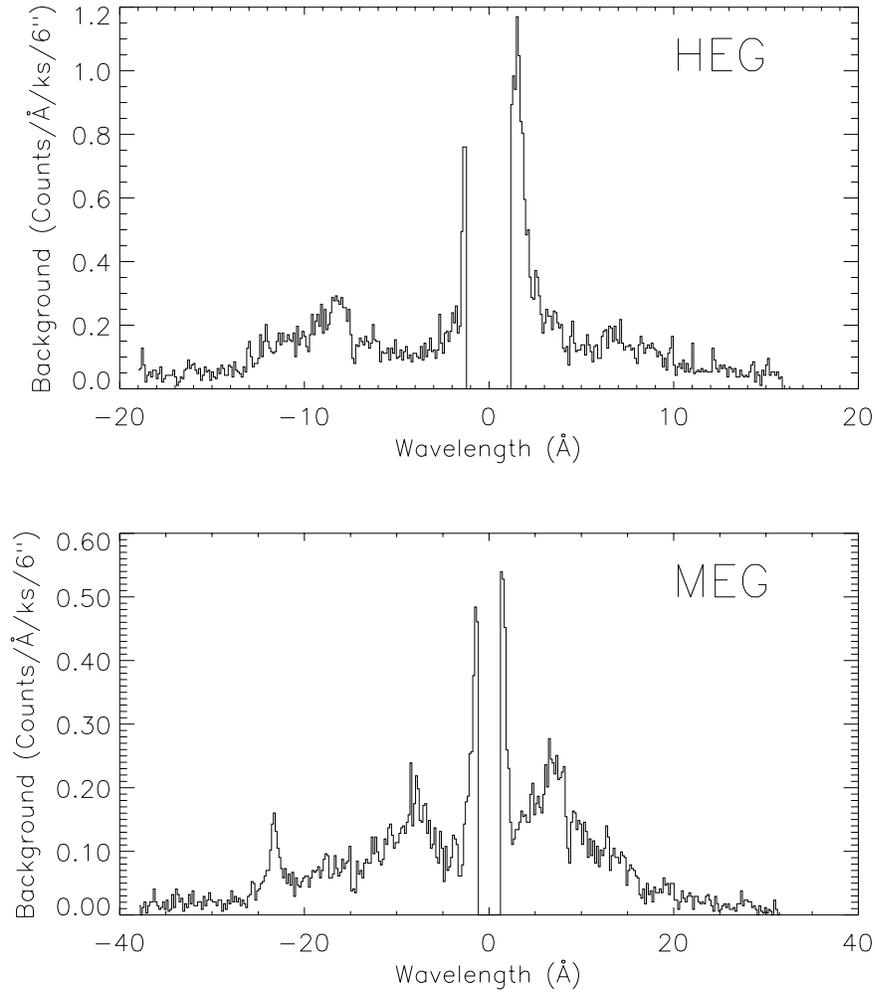
Figure 8.24: The background spectrum is plotted for the HEG (top) and MEG (bottom) for a long observation of the late-type star HR 1099 (observation ID 62538). The background was normalized to a 6 arcsec wide aperture but determined from a substantially larger region out to 50 arcsec from the source dispersion line. The spectrum was binned to 0.1 Å to show details of structure that may be observed in a typical HETGS observation. The spikes near zeroth order are due to increased background included in the pulse height selection at high energies.

8.2.4   Absolute Wavelength

The HETGS-measured wavelength depends, as the grating equation implies, on knowing the diffraction angle, the diffraction order, and the grating average period. The angle depends on knowing the HETGS geometry, specifically the Rowland Spacing and the ACIS-S pixel size and configuration. Preliminary comparisons between measured and expected emission line wavelengths indicates an agreement to the accuracies listed in Table 8.1. Systematic wavelength errors are now at the 100 km/s level, see Section 8.3.4.

8.3   Calibration

8.3.1   Introduction

Calibration includes the ground and flight activities whose purpose is to create data and models and associated uncertainties which accurately describe the instrument characteristics. Crudely, assessing the feasibility of an HETGS observation has more to do with the rough characteristics than their precise values; *e.g.*, whether the effective area is 100 cm^2 or 1.0 cm^2. However, scientific results may hinge on 10 % differences in a line width or line intensity so it is important to know if the calibration will allow a significant measurement. This section provides calibration details to help observers who may require a more precise evaluation of instrument characteristics.

The ultimate usefulness of the calibration activity is only achieved when the results are incorporated into parameters and files used to process and interpret the instrument data; in *CXC* parlance these files are refered to as "Analysis Reference Data" or ARDs. As instrument and calibration knowledge improves, new ARDs are created and released. The archived, released calibration products provide a central framework for calibration discsussions; for general details, see the *CXC* CALDB WWW link given in the references section. Section 8.3.2 gives an overview of HETGS-related ARDs. Ground calibration and on-going flight calibration are discussed in Section 8.3.3 and Section 8.3.4.

8.3.2   HETGS Calibration Data

The ARDs which are most relevant to HETGS calibration are listed in Table 8.3, organized by component (HRMA, ACIS, etc.). The "S/W id" column indicates which software uses the specific ARD as listed in Table 8.4. The "Version" column gives the relevant portion of the specific CALDB file name which includes a version number, *e.g.* N0004; in some cases these files may depend on the observation date or focal plane temperature, as indicated. The "F/G" column indicates whether the calibration values are based on Flight or Ground calibration.

Table 8.3: HETGS Analysis Reference Data (ARD).

ARD Description	S/W id	ARD (CIP) Version	F/ G	Comments
HRMA				
Axial Eff Area	6	axeffaN0006	G	issued 11/29/00
		'N0004	G	issued 5/10/99
Off-axis Vignetting	6	vignetN0003	G	from ray-trace
PSF width	2	wpsfN0001	G	approx, for detect use
HRMA geometry	0	—	G	detailed parameters
ACIS				
Mean QE	0,6	qeN000X	F	in process
including		'N0004	F	ACIS-LETG only, high-res
OBF trans.		'N0003	G	ver. "0700"
QE Uniformity	6	qeu vs. T	F	not yet examined
Gain Maps	0,1	gain vs. T	F	residual variations
Order-sorting	4,6	osipN0005	F	not yet examined
integrated prob.		vs. T		
Bad Pixels	1,6	badpix vs. T	F	—
HETG				
Efficiency	0,6	greffN0005	F	in process
		'N0004	G	4/00; final ground
dp/p variation	0	(coreN0002)	G	ground result
Angle variation	0	(sectorN0003)	G	ground result
RMF files	8	rmfN0005	F	FWHM from flight; wings
	7	lsfparmN0003	G	from *MARX* sim.s
ASPECT				
Aspect solution	0,4,6	'asol, 'aoff;	F	Aspect solution is
		vs ObsID		based on ARD below
PIXLIB				
Aim points	lots	aimptsN0001	F	—
ACIS geometry	0,1,4	geomN0004	F	pixel size at flight T, gaps
		geomN0002	G	pixel size room T, gaps
HETG Period	0,4	geomN0004	G	NIST referenced
HETG Angles	0,3,4	geomN0004	F	angles w.r.t. ACIS-S CHIPX
Rowland spacing	0,4	geomN0004	G	see text
Sky Coord.s	0,1	skyN0001	F	sky pixel size
SIM				
Default pos.s	1,4	posN0008	F	ACIS-S focus
PCAD				
Alignment	0,1,4	date coded	F	sky to det mapping

Table 8.4: HETGS Software list for ARD Table

id	Software	Purpose
0	`MARX`	create HETGS simulated observation
1	`acis_process_events`	creates level 1 ACIS event file
2	`tgdetect`	find zeroth-order sources
3	`tg_create_mask`	select events in HETG "X" on Sky
4	`tg_resolve_events`	create level 1.5 file with `TG_LAM`, etc.
5	`tgextract`	create pha files from event list
6	`mk[g]arf`	create custom *ARF* files
7	`mkgrmf`	create custom *RMF* files
8	`ISIS`	fit high-resolution line spectra

8.3.3   Pre-launch Calibration

Prelaunch calibration of the HETG and HETGS is extensively treated in the HETG Ground Calibration Report and the web pages where the reader is directed for more details - see listings at the end of this Chapter.

Laboratory measurements of X-ray efficiency and period uniformity have been made on each grating facet (Dewey et al. 1994; Markert et al. 1995; Flanagan et al. 1995). Synchrotron data has been collected on "reference" gratings. A laser-reflection diffractometer has measured period variations within and between gratings to order of $dp/p = 1 \times 10^{-4}$, and the temperature dependence of the period. Measurements have been made of the alignment of each grating to the support plate, and hence of the angle between the HEG and MEG spectra. The support vignetting factor and point-spread-function have also been measured.

The complete HRMA/HETG optics were ground tested at the X-ray Calibration Facility (XRCF) at the Marshall Space Flight Center in conjunction with various non-flight detectors and the flight science instruments (SIs). Tests were performed to measure the system spectral resolution and the cross-dispersion profile at several energies and orders and for a few off-axis angles to verify models of the HETG performance. As discussed previously (Section 8.2.2), two unexpected effects were observed: a small fraction of MEG facets are misaligned and the HEG shows some incoherently diffracted light between the orders. The average periods of the gratings were measured to a part in 10,000 or better, and the linear dispersion relation was verified to the measurement accuracy ($< 10 \ \mu$). Furthermore, many other tests were performed to verify the grating efficiencies and the overall system effective area.

Analysis of the ground calibrations have been completed and there are no additional HETG anomalies. XRCF measurements of the absolute effective area for the full HETGS

Table 8.5: HETGS Calibration Observations

Obsid(s)	Date(s)	Target	Comments
3456, 3457, 3573	6/5/02	3C 273	ACIS modes and SIM offsets
2583	4/29/02	Capella	Wavelength Stability
3167	11/30/01	PKS 2155-304	Effective Area
2463	6/13/01	3C 273	Effective Area
1014	3/28,29/01	PKS 2155-304	Effective Area
1010	2/11/01	Capella	Wavelength Stability
1705	5/31/00	PKS 2155-304	Effective Area
1714	5/29/00	Mkn 421	Effective Area
57	3/3/00	Capella	Wavelength Stability
169	2/29/00	3C 273	Effective Area
			ACIS temp = -120 C
459	1/10/00	3C 273	Effective Area
457	11/5/99	Mkn 421	Effective Area
1103, 1318	9/24,25/99	Capella	Emission Line Project
1102	9/23-24/99	Cyg X-2	Effective Area
62538, 1252	9/14,17/99	HR 1099	Emission Line Project
			ACIS temp = -110 C
170, 168	8/29/99	Crab Nebula	Effective Area and CC mode
1101, 1237	8/29/99	Capella	Focus set: "+0.2 mm"
1100, 1236	8/28/99	Capella	Focus set: "-0.2 mm"
1099, 1235	8/28/99	Capella	Focus set: "0.0 mm"
1098	8/28/99	Capella	HETGS First-light
			ACIS temp = -100 C

system agreed with predictions to better than 10-20%. Data obtained during illumination with a continuum source were used to search for unexpected spectral features and none were noted, confirming the detailed structure of the HETGS effective area model.

8.3.4 In Flight Calibration

There have been over twenty calibration observations made with the HETGS to date and these are summarized in Table 8.5. Several types of in flight calibration observations are included. HETG first light and focus tests were carried out with Capella. These observations were also used to measure the angles of the grating dispersion directions on ACIS-S (Table 8.1). The observations of the Crab Nebula and its pulsar serve as a baseline
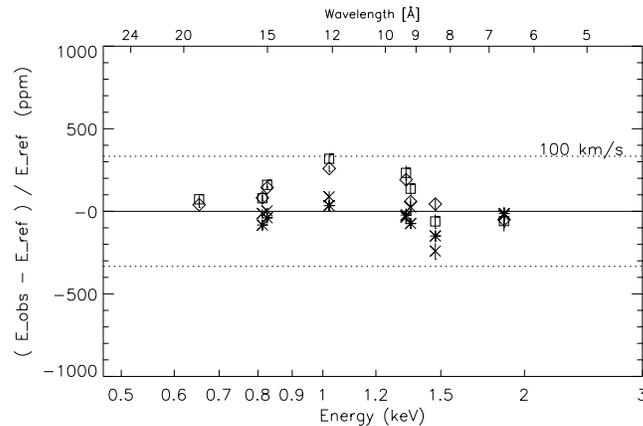
Figure 8.25: HETGS Wavelength accuracy for bright lines in the Capella spectrum are shown for Obsids 1318 and 1103 (from archived 'N002_evt2.fits files.) The lines are Si XIII, Mg XII, Mg XI, Ne X, Fe XVII, and O VIII, at 6.64795, 8.41930, 9.16875, 12.1322, 15.0140, 18.9672 Å, respectively. Open symbols (squares, diamonds) are the MEG plus-minus-order averaged values from each Obsid; asterisks and crosses are similar values from the HEG spectra. The difference between the measured wavelength and expected values is plotted in parts per million (ppm).

effective area data set and as a checkout of the continuous clocking (CC) readout mode.

For up-to-date flight calibration information see the HETG link on the *CXC* "Instruments and Calibration" web page:

http://cxc.harvard.edu/cal/

The following sections highlight some of the calibration analyses that have been carried out.

Absolute Wavelength

Two stars with active coronae, Capella and HR1099, have been observed with long exposures. These observations have served to confirm the resolving power of the HETGS, calibrate the ACIS-S chip gaps, and verify the dispersion relation. Many different emission lines have been observed and the centroids of the brightest can be measured to within 10^{-3} Å in first order. Figure 8.25 shows that the measured and expected wavelengths for a set of emission lines in the 0.6-2.0 keV range are within 300 ppm; thus, systematic errors in doppler velocities are less than 100 km/s.

The absolute wavelength accuracy is limited by the knowledge of the ACIS-S chip locations (see Section 8.2.1), which is of order 0.5 pixels: 0.0028Å for the HEG and 0.0055Å for the MEG. In addition, the location of the zeroth order image can be in error
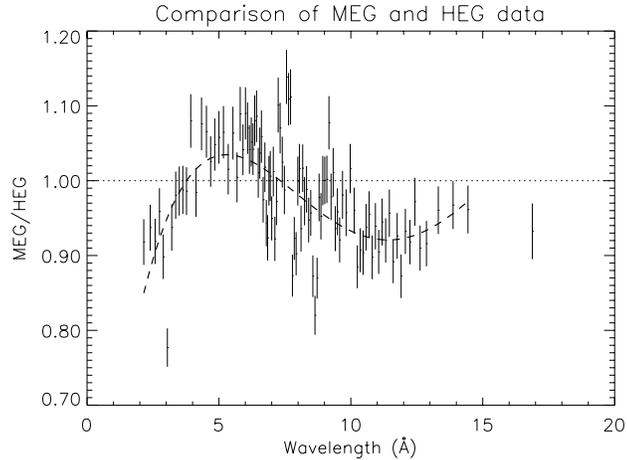
Figure 8.26: Four featureless continuum sources were used to compare fluxes derived from HEG data with those based on MEG data. After correcting for preliminary ACIS-S BI-FI QE inconsistencies, there are residual systematic errors of order 5-8% between the HEG and MEG. The data were adaptively binned to obtain a similar signal-to-noise ratio in each bin. A polynomial fit shown as the dashed line gives the ratio of the observed MEG to HEG efficiencies compared to the values in the ground-data-based version N0003.

by ~ 0.5 pixels, which translates to slight and opposite-signed shifts of the wavelengths derived from the plus and minus orders. (When analyzing actual data, it is good practice to check and compensate for this plus-minus order offset using averaging (as in the figure) or corrections based on a bright long-wavelength line if available.)

Note that there also appears to be a systematic offset between the HEG and MEG measured wavelengths in Figure 8.25 by of order 200 ppm; appropriate changes to the HEG and/or MEG periods will be made in order to obtain better agreement after a more thorough analysis of the flight calibration data to include more emission lines.

Effective Area

Continuum sources, 3C 273 and the X-ray binary Cyg X-2 have been observed to verify that there are no unexpected spectral edges and that contamination is small; Mk 421 was observed twice, the source was in a record low state in 11/99 so that this observation has minimal utility for calibration. Other targets were observed to help verify that the absolute effective area is correct: the Crab nebula was observed and 3C 273 was observed simultaneously with SAX, RXTE, and ASCA in order to compare the calibration with other X-ray observatories.

Based on analyses of these observations, the following accuracies apply to the current HETGS effective areas (*ARF*s) calculated from ground-data-only derived calibrations (specifically, for the products: HRMA=N0004, HETG=N0003, ACIS=N0003):

- 30% for $0.5 < E < 0.8$ keV (MEG only),

- 20% for $0.8 < E < 1.5$ keV (both MEG and HEG),

- 10% for $1.5 < E < 6$ keV (both MEG and HEG),

- 20% for $6 < E < 8$ keV (HEG only),

- 50% in the O-K edge region (0.525-0.57 keV) (MEG only).

- 20% in the Si-K edge region (1.83-1.84 keV) (both MEG and HEG),

The O-K edge region is still under investigation as a location for large systematic residuals.

We have determined that the MEG and HEG effective efficiencies (N0003 version) show inconsistencies at the 10 % level as shown in Figure 8.26.

If one applies these preliminary QE and efficiency correction factors, one obtains the spectra of 3C 273 shown in Figure 8.27. For this observation, a simultaneous ASCA observation was taken and analyzed by Tahir Yaqoob and the resultant model fit is shown as the heavy dashed lines. The agreement is better than 10% across the 0.7-7.0 keV band after applying these preliminary corrections.

Stability of Calibration

At periodic intervals, some of these targets are re-observed. For example: in March 2000, the Crab and Capella were re-observed in order to confirm that the effective area and dispersion relations are stable. Initial analysis shows that the wavelength scales between Obsid 1103 and Obsid 57 agree to 100 ppm. The effective area analyses described above combine and compare data sets widely spaced in time. To date the HETGS appears stable in its calibration.

8.4   HETG Operations

8.4.1   Flight Events and Anomalies

There have been no flight anomalies with the HETG per se. There have been some problems with the HETG and LETG grating insertion/retraction mechanisms. To date these have been limited to failure of some of the limit switches which are used to sense the gratings' position. In May 2000 there was failure of the HETG A-side electronics
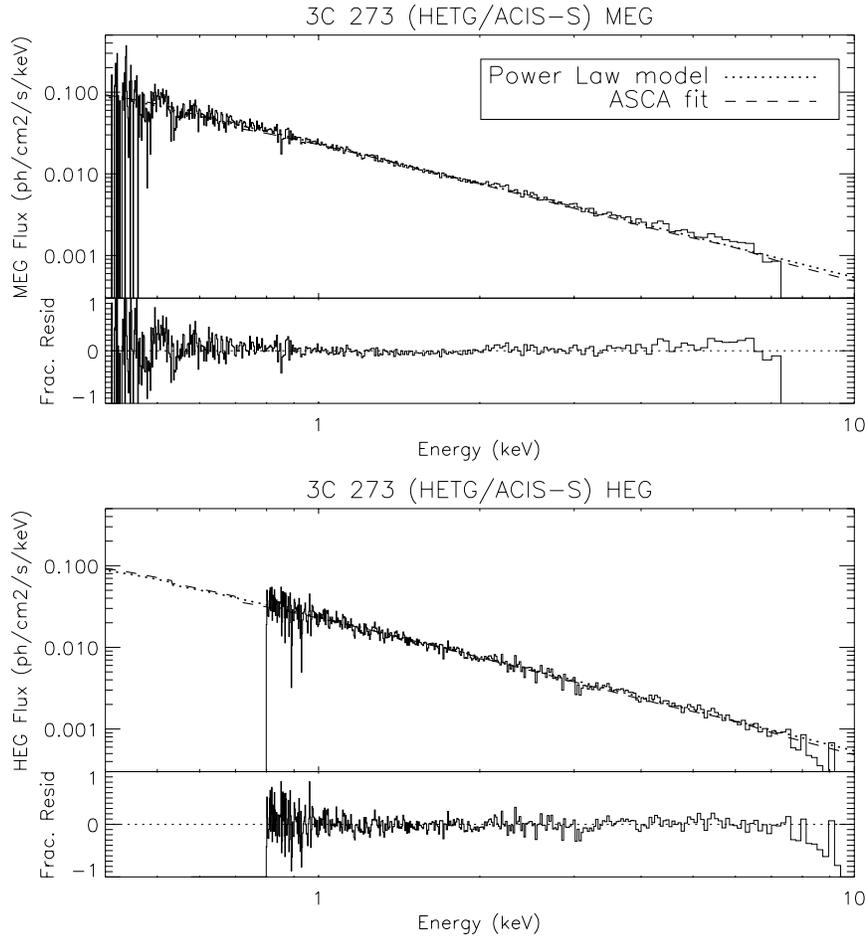
Figure 8.27: The calibration observation of 3C 273 is analyzed using preliminary calibration corrections to the ACIS-S BI QEs and the MEG efficiencies derived from in-flight data as described in the text. The residuals are generally small and show no large systematic deviations from a simple power law fit (heavy dotted lines). A simultaneous observation using ASCA was analyzed by Tahir Yaqoob and the resultant model fit is shown as the heavy dashed lines. The ASCA and Chandra HETGS observations agree to better than 10% across the 0.7-7.0 keV band and the MEG and HEG spectra are consistent. This example demonstrates the accuracy expected when future calibration products are released.

retraction limit switch indicating that the HETG was not retracted, when in fact it was. Switching to the redundant B-side limit switch worked until June 2000 when it too would not indicate that the HETG was retracted. Subsequently operational procedures have been changed in order to determine when the gratings are properly retracted. There have been no impacts to the science program.

Because the HETG insert limit switches continue to function and because the HETG is inserted against a hard stop, **these anomalies have had no effect on the HETG wavelength scale.**

8.4.2   Operational Constraints

There are no operational constraints for the use of the HETGS from the proposer's point of view. The HETG is placed in the stowed position during passage through the radiation belts, a time when no data can be taken. Additional functional constraints include preventing both the HETG and LETG from being simultaneously commanded into position, which could cause a mechanical interference. Finally, a "failsafe" command, once used, will permanently retract the grating. A decision to issue the failsafe command will not be taken without a thorough review including the Chandra Project and NASA Headquarters.

8.4.3   Output Data

There are no data from the HETG itself. The data are generated by the focal-plane imager in its format (e.g. Figure 8.1).

8.4.4   Performance Monitoring, Health and Safety

The HETG itself has only a few thermal and mechanical switch sensors associated with it. These sensors are examined routinely as part of the health and safety monitoring of the Observatory. HETGS performance is monitored by means of the calibration observations (Section 8.3.4).

8.4.5   Thermal response time

There is a negligible thermal time constant for the HETG to equilibrate from "near-wall" storage to "in-use" temperature environments. The temperature dependence of the resolution and energy scales have been minimized through use of low-expansion material ("Invar") and single-point-mounted facet-frames. Thus, the support structure may expand or contract, but the facets will not.

8.4.6   Observation frequency/duty cycle

There are no instrument limits on exposure time.

8.4.7   Radiation Considerations

The main radiation concern for the HETG is effects to the polyimide support material. Thin membranes of this material, used for proportional counter windows operating under a pressure differential, have been tested for the effects of radiation damage on leak rate. No increased leak rate was encountered after a dosage 9 krad. In these tests the mechanical integrity of the material, the key issue for the HETG, was severely tested by the ability of the window to maintain the pressure differential of order one atmosphere. Loss of mechanical integrity has been reported in the literature, but only after exposures of 1000 MRads. The estimated proton dose to the HETG polyimide is of order 1 kRad per orbit when the HETG is inserted, and much lower values when HETG is in its stowed position. Current practice is to have the HETG retracted during radiation passages; however, even if it were left inserted the total exposure would be $\approx$ 1 MRad over 10 years, well below the 1000 MRad level.

A secondary concern would be changes to the Gold grating bars (which, when in place, face the HRMA) due to sputtering by particles, particularly for the high-aspect ratio HEG gratings. Diffraction order ratios are sensitive to these changes. To date, after flight experience and laboratory radiation tests, there is no evidence that this concern is other than intellectual.

8.5   Observation Planning

The following sections provide assorted information and topics relevant to planning an HETGS observation.

8.5.1   Focal Plane Detector Considerations

The HETG was designed for use with the ACIS-S detector, although other detectors may be used for certain applications. Details concerning the detectors may be found in Chapters 6 and 7. Some considerations are:

- ACIS or HRC: ACIS provides energy resolution which is useful for order separation, background suppression, and discrimination between multiple sources. The HRC is likely to be useful if high time resolution is necessary especially if the ACIS mode is not helpful for the observation in question.

- Operating mode of ACIS-S: The ACIS-S array can operate in many modes, giving control over e.g., the read-area, pixel-binning, and read-frequency. The selection of the appropriate operating mode and its ramifications for the experiment is one of the most important that the user faces.

- Offset pointing: Pointing offsets may be specified and used to include or exclude nearby sources, to keep an important spectral feature clear of the gaps between chips, to put a particular low-energy feature on the higher efficiency BI chip S1, etc. Offsets greater than one or two arc minutes will, however, degrade the image quality - Chapter 4 - which in turn broadens the LRF (Section 8.2.2).

- Selecting the aimpoint: The capability of moving the SIM along the spacecraft Z-axis (the cross-dispersion direction) is useful for placing the image (dispersed spectra and zeroth order) closer to the ACIS-chip readouts. This placement minimizes the effects of the degraded energy resolution of the FI chips. For a point source, the recommended placements, stated as offsets from the nominal position are -3 mm (-1193 motor steps) and -4 mm (-1591 motor steps) for ACIS TE and CC modes respectively. The recommended shift in TE mode allows space for background data to be obtained on the readout side of the dispersed image. The CC mode, however, integrates over the columns, and so there is no advantage gained ,and thus the the image can be placed even closer to the readout. NB: Shifting the aimpoint may not be desirable if the target is extended or when there are several sources in the field.

- Orientation of multiple (or extended) sources: One may need to specify a restricted range of spacecraft roll-angles to avoid overlapping spectra from multiple targets in the field, or to arrange that the dispersed spectra from particular features of an extended target do not similarly overlap. Note that roll angle constraints usually will lead to restrictions as to the dates dates of target availability. See Chapter 3.

- Offset pointing - Optimizing zeroth-order data: Because the the nominal aimpoint is very close to the boundary between nodes 0 and 1 of S3, the user may wish to offset the telescope pointing direction along the Y axis by about 20 arcsec to insure that the dithered zeroth order image is always restricted to a single node of the CCD. Such placement simplifies the data-analysis. If the source is a point source and the > 7 keV region is of interest, an offset of $+0.33'$ is recommended. If the source has interesting extended emission that would otherwise fall into the S2-S3 gap, then the user may wish to offset by -0.33$'$. See the discussion in Section 8.2.1.

- ACIS subarray modes: It is possible that one might wish to reduce the ACIS-S frame time e.g. in order to minimize the effects of pileup. The user might consider a small subarray, especially if the source is point-like and the -3mm SIM shift will be used. In this case, there are at least 6 mm of ACIS-S rows that may not be necessary

(unless the user desires data from serendipitous sources). The reduced array could have 1024 - 250 = 774 rows starting at row 1 thus reducing the frame time to 2.5 s.

- Example of a set of parameters: It is instructive to examine the obscat entry for observation ID 1802 which shows observation parameters and values.
  (See http://cxc.harvard.edu/cgi-gen/target_param.cgi?1802.)
  The source is point-like and has flux down to 0.8 keV in the HEG, so all ACIS-S chips are on, the SIM has been shifted to minimize the impacts of the row-dependent CTI on the FI-chips, the aimpoint has been shifted by $+0.33'$, and a custom subarray is used to reduce the frame time to 2.5 s.

8.5.2   Complications from multiple sources

Multiple sources in the field of view can also lead to effects which impact the observation.

Faint background sources

The position of a faint second source might be such that the zeroth-order image falls directly on the dispersion pattern from the prime target. In this case, the zeroth-order image of the second source appears as a line in the dispersed image of the prime target. The ACIS energy spectrum can be used to minimize the contribution to the measured dispersed spectrum of the target. Also, the lack of a feature in the other side of the dispersion pattern will indicate that the "line" is spurious.

Two point sources of comparable intensity

The dispersed MEG and HEG spectra of two sources will cross if the objects are fairly close. When the two targets are less than about $3'$ apart, both will be nearly in focus, so the spectra appear like two flattened "X"s. Normally, the ACIS-S pulse heights of the events will be significantly different in the regions of overlap, so that one may distinguish the events from two sources in data analysis. There are specific roll angles, however, where the identification of the source is ambiguous; a rare occurrence, but one the user should be aware of.

An example is shown in Figure 8.28, where the MEG spectrum of the brighter object (source 1) overlaps the HEG spectrum of the fainter target (source 2). The first order energies at the overlap positions are a factor of 3 apart, so that $E_2 = 3 \times E_1$. An ambiguity arises from 3rd order photons from source 1 at $3 * E_1$, which cannot be discriminated by ACIS from photons of about the same energy but from source 2. For a given angular distance between sources, it is possible to specify the observatory roll angle so that collisions like the one shown in the top of Figure 8.29 are avoided.
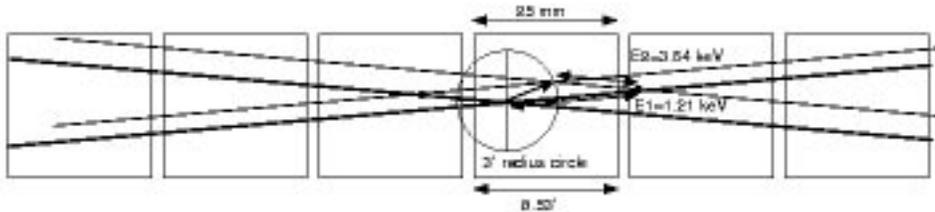
Figure 8.28: An idealized sketch of a 'collision' between two sources separated by 3 arcmin. At the 'collision' point, third-order photons from the on-axis source will have an energy 3x1.21=3.63 keV and ACIS can not distinguish these from the second source's first order photons, at 3.64 keV.

A strong source lying outside the field

The proposer should also take into consideration sources, other than the target, that are within the field of view of the telescope, but out of the field of view of the detector. Parts of the image of the dispersed spectrum may still fall onto the detector. If this situation presents a problem, a sensible choice of a range of allowable roll angles might ameliorate the situation.

8.5.3 Extended Sources and Spatial-Spectral Effects

The case of a simply extended, spectrally homogeneous source was described in Section 8.2.2, under the heading, "Extended and off-axis targets". Here more complex cases are briefly considered, generally these must be treated on a case-by-case basis.

For extended sources with multiple condensations, careful selection of the roll angle (see e.g. Section 8.5.2) might make the data easier to analyze and interpret. It may also be possible to model the spectrum given information from the zero order image and/or a short ACIS exposure with the grating retracted. The ACIS spectrum can then be used as an initial guess in modeling the dispersed HEG and MEG spectra.

The diffracted images of extended objects which lead to position dependent spectra are complicated. The complexity indicates that information is present but extracting the information is more difficult than for a point or an extended source with a uniform-spectrum. For example, the plus and minus order images may not have the same appearance. An example of this effect was seen in ground test data sets using the double crystal monochromator source, e.g., test image H-HAS-EA-8.003 which is schematically presented and described in Figure 8.30. For astrophysical sources, variations in temperature, abundances, Doppler velocities, cooling flows, etc. can all create spatial-spectral variations. For these
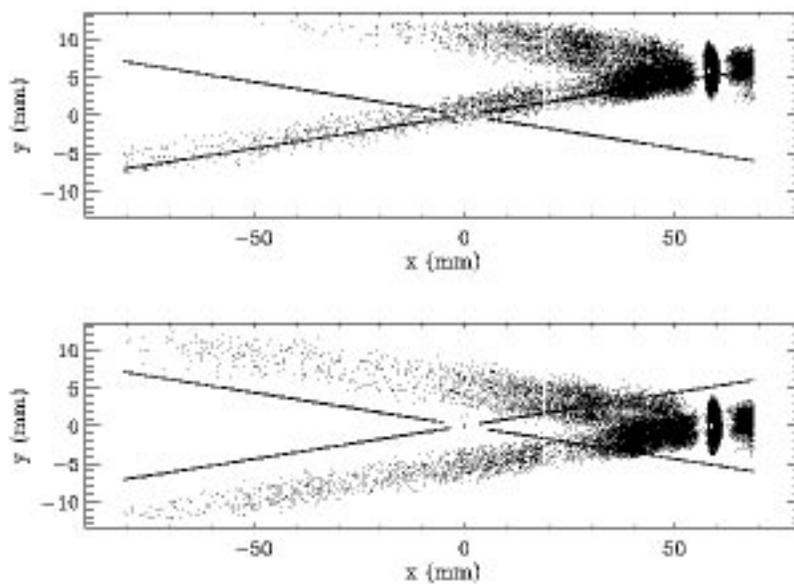
Figure 8.29: A simulation of spectral contamination caused by a second source in the field. The image of the dispersed spectrum from the second source is seen in the upper right hand corner for particular choice of roll angle. Note that the image is highly extended as the source is 20 arcmin off-axis. For this roll angle, there is significant overlap of the two images. In the lower panel we show the same situation, but for a different choice of roll angle. Here the overlap of the images is minimal and data analysis will be further aided through the use of energy discrimination provided by the ACIS-S detector.
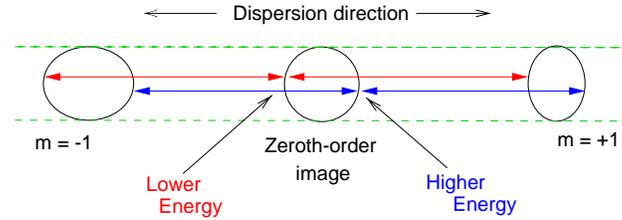
Figure 8.30: HETGS spatial-spectral effect example. In this schematic, a zeroth-order ring image emits at an energy which varies across the ring's diameter in the dispersion direction emitting lower-energy photons on the left and higher-energy photons on the right. The resulting diffracted images in ±1st orders have different appearances due to the spatial-spectral interaction. In the cross-dispersion direction, however, the images have the same extent.

complex objects general analysis techniques are not available and forward folding of the spatial-spectral model through *MARX* is the best way to study these effects and to plan potential observations.

8.5.4 Optimizing Detection of Isolated Emission Lines: Choice of Spectrometer

If the scientific objectives require detecting emission lines against a moderately bright source continuum, then the signal/noise ratio depends on the effective area of the instrument in combination with the spectrometer resolving power. Here, we compute the relative merits of each *Chandra* spectrometer in this context. Three cases where this analysis will not apply are when: (1) detecting weak lines that may blend with stronger lines, (2) observing significantly extended sources, and (3) observing lines that are substantially broadened. In case 1, the highest resolving power at the energy of interest would be indicated. Case 2 will require that the reduction of the grating resolution for extended sources, discussed in Section 8.2.2, be included.

When a line is isolated and appears against a "background" due primarily to the source continuum, then the signal/noise ratio is given by:

$$\frac{C_L}{\sigma_C} = \frac{A_E T W n_E}{[A_E T (dE)_E n_E]^{1/2}}$$

where C_L is the number of counts in the emission line, σ_C gives the uncertainty in this number, A_E is the instrumental effective area, T is the integration time, n_E is the photon flux in the continuum in units of photon cm^{-2} s^{-1} keV^{-1}, W is the equivalent width of the line in keV, and $(dE)_E$ is the spectral resolution of the spectrometer in keV. The signal-to-noise ratio per fractional equivalent width, $W_f = W/E$, is then:

$$\frac{C_L/\sigma_C}{W_f} = (Tn_EE)^{1/2}[\frac{A_E\ E}{(dE)_E}]^{1/2}$$

This last instrument-specific term is the figure of merit for the spectrometers:

$$F_E \equiv [A_E\ (E/dE)_E]^{1/2}$$

Observation and source parameters are taken out to show the dependence of the signal/noise ratio on the characteristic figure of merit, F_E, of the spectrometer which is, of course, a function of energy.

The merit functions F_E were computed for several grating-detector combinations and for the ACIS-S and the ACIS-I used without a grating. In the current context, the term 'ACIS-S' means that parameters for the back illuminated (BI) chips were used, whereas 'ACIS-I' indicates the use of front illuminated (FI) chip parameters. The results are shown in figures 8.31 and 8.32. The first of these figures indicates that the LETG with the HRC-S is preferred if the emission lines of interest have wavelengths longer than 20 Å (or 0.62 keV) while the HETGS is best for emission lines shorter than about 16 Å (or 0.78 keV). In the energy range from 0.62 keV to 0.78 keV, the LETG with ACIS-S would give the best results.

The second of these figures shows that although the grating spectrometers are better for detecting isolated lines at low energies, the ACIS detectors are comparable at high energies (at least near the readout edge of the CCDs where the energy resolution is the best).

Of course, all these considerations are tempered by the additional features of each instrument setup. For example, this calculation does not take into account instrumental background effects nor the additional continuum that may result from higher energy flux detected in higher orders when the LETG is used with the HRC-S. The reduction of the line detectability then depends on the source spectrum.
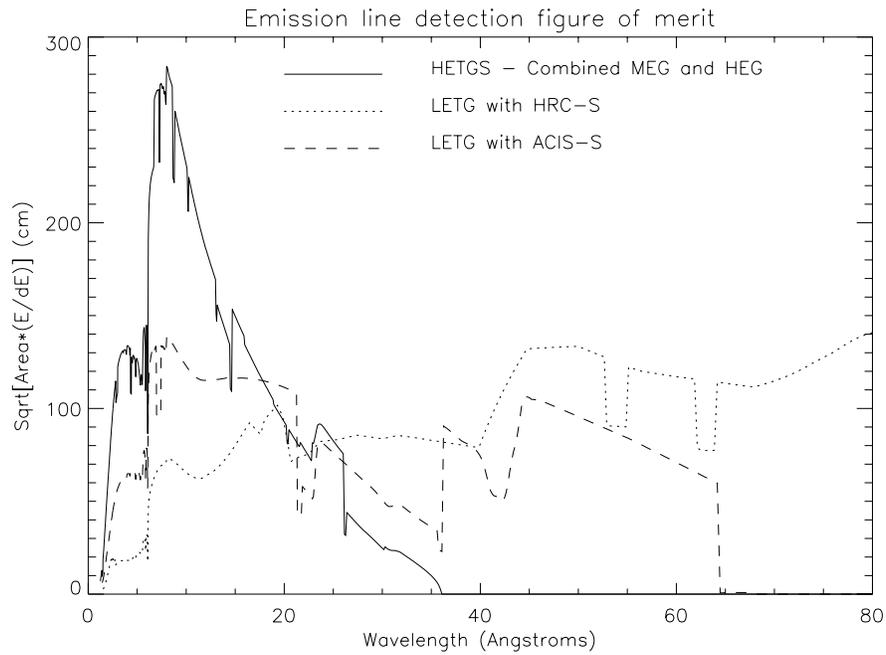
Figure 8.31: The figure of merit for detecting isolated emission lines computed according to the equations in Section 8.5.4 for the HETGS, LETG with HRC-S and for the LETG with ACIS-S. The results indicate that the LETG with the HRC-S is preferred if the emission lines of interest have wavelengths longer than 20 Å (or 0.62 keV) while the HETGS is best for emission lines shorter than about 16 Å (or 0.78 keV).
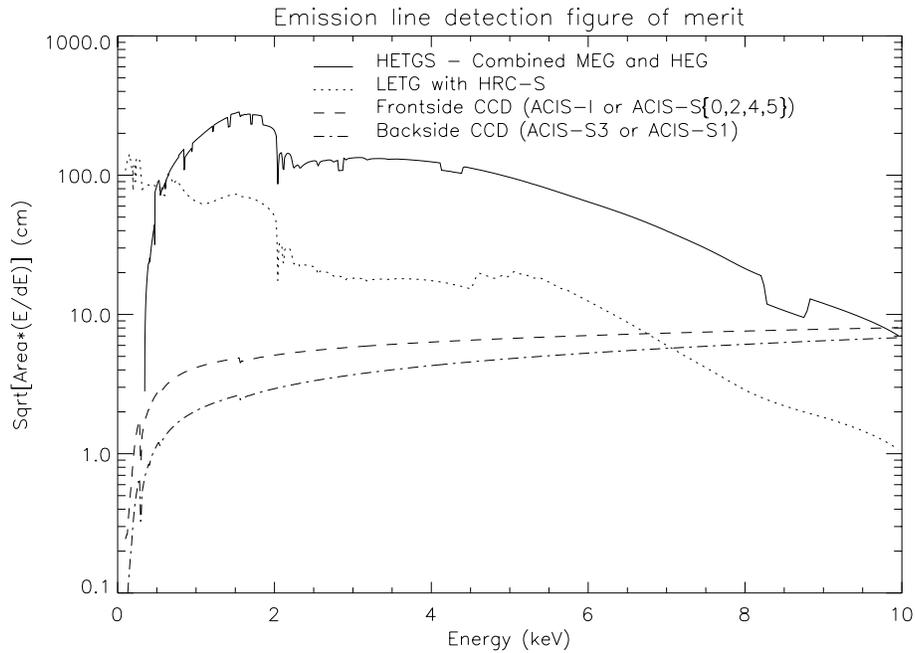
Figure 8.32: The figure of merit for detecting isolated emission lines computed according to the equations of Section 8.5.4 for the HETGS, the LETG with the HRC-S, and the ACIS without either grating. For the latter case, separate curves are given for FI and BI chips. Although the grating spectrometers are better for detecting isolated lines at low energies, the ACIS detectors are comparable at high energies. NB: the ACIS FI chips have suffered degradation in spectral resolution; the plotted curve is pre-launch and now pertains only to the area of each chip near the readout edge.

8.6   Simulations with *MARX*

For sources with spatial or spectral complexity, observation planning is best carried out using the *MARX* simulator to create a simulated data set. These data can then be analyzed with the same tools as flight data in order to demonstrate the feasibility of extracting useful results from a proposed observation.

MARX is a suite of programs designed to simulate the on-orbit performance of *Chandra*. It is built around a core program or engine which performs a raytrace of photon paths through all elements of the *Chandra* observatory. The user specifies a file containing the spectral energy distribution of the source to be simulated and then selects a model for the spatial distribution of the source, which can be a FITS image. More complicated "user source models" allow simulation of sources with spatial-spectral variations.

Once the source has been specified, *MARX* traces the path of photons through a model of the HRMA. Models for the High Energy Transmission Grating (HETG) and Low Energy Transmission Grating (LETG) can also be included and, in the focal plane, the user has the choice of all four *Chandra* detectors. The result of the simulation is converted with `marx2fits` into a FITS event file which can then be processed with standard CIAO tools.

The latest capabilities and instructions for use of *MARX* are given in the *MARX* User Guide at the *MARX* web site, http://space.mit.edu/CXC/MARX and in threads on the web.

8.7   Document History

- Dec 92; The original version was compiled by D. Huenemoerder.

- Nov 94; updated post PDR.

- Nov 96; updated.

- May 97: updated by D. Huenemoerder and N. Evans.

- Oct 97; reorganized and updated in preparation for NRA (D. Harris).

- Jul 99; merge Observatory Guide and Proposer's Guide (D. Harris).

- Dec 99; Re-arrange sections, update text and figures (D. Dewey).

- Nov 00; Updated to reflect flight calibration, etc. (H. Marshall, DD).

- Oct 01; Slight updates (D. Dewey, M. Weisskopf).

- Nov 02; LRF update, etc. (K. Ishibashi, DD).

Contributors to updates have been: C. Canizares, D. Davis, J.E. Davis, D. Dewey, N. Evans, D. Harris, D. Huenemoerder, K. Ishibashi, H. Marshall, F. Seward, A. Tennant, M. Wise, and M. Weisskopf.

8.8 REFERENCES

WWW resources http://
        cxc.harvard.edu/cal/ - *CXC* Instruments and Calibration page
        cxc.harvard.edu/caldb/ - *CXC* CALDB page
        space.mit.edu/HETG - HETG home page
        space.mit.edu/HETG/flight.html - HETG on-orbit page
        space.mit.edu/HETG/report.html - HETG ground cal report
        space.mit.edu/CXC - CXC at MIT, focusses on gratings
        space.mit.edu/CXC/calib/hetg_user.html - HETGS user information
        space.mit.edu/CXC/calib/hetgcal.html - HETGS calibration updates
        wwwastro.msfc.nasa.gov/xray/xraycal/ - MSFC ground cal site

Canizares, C.R. *et al.* 2000, "Initial Results from the Chandra High Energy Transmission Grating Spectrometer", Atomic Data Needs for X-ray Astronomy, M.A. Bautista, T.R. Kallman, and A.K. Pradhan, eds. http://heasarc.gsfc.nasa.gov/docs/heasarc/atomic/

Canizares, C.R. *et al.* 2000, ApJ, **539**, L41 .

Canizares, C.R., Schattenburg, M.L. and Smith, Henry I. 1985, SPIE, **597**, 253. "The High Energy Transmission Grating Spectrometer for AXAF"

Davis, J.E., H.L. Marshall, M.L. Schattenburg, and D. Dewey, "Analysis and Modeling of Anomalous Scattering in the AXAF HETGS", *X-Ray Optics, Instruments, and Missions*, Proc. SPIE, Vol. **3444**, 76–92 (1998).

Dewey, D., J.J. Drake, R.J. Edgar, K. Michaud, and P. Ratzlaff, "AXAF Grating Efficiency Measurements with Calibrated, Non-imaging Detectors", *X-Ray Optics, Instruments, and Missions*, Proc. SPIE, Vol. **3444**, (1998).

Dewey, D., Humphries, D. N., McLean, G. Y., and Moschella, D. A. 1994, SPIE, **2280**, pp. 257-271, "Laboratory Calibration of X-Ray Transmission Diffraction Gratings"

Flanagan, K. A., Dewey, D. and Bordzol, L. 1995, SPIE, **2518**, 438-456, "Calibration and Characterization of HETG Grating Elements at the MIT X-ray Grating Evaluation Facility"

Flanagan, K.A., et al., "Modeling the Chandra High Energy Transmission Gratings below 2 keV" *X-Ray Optics, Instruments, and Missions*, Proc. SPIE, Vol. **4140**, (2000).

Markert, T.H., Canizares, C.R., Dewey, D., McGuirk, M., Pak, C., and Schattenburg, M.L. 1994, SPIE, **2280**, 168. "The High Energy Transmission Grating for AXAF"

Markert, T. H. et al., 1995,**SPIE**, 2518, pp. 424-437, "Modeling the Diffraction Efficiencies of the AXAF High Energy Transmission Gratings"

Marshall, H.L. et al. *Grazing Incidence and Multilayer X-Ray Optical Systems, Proc. SPIE*, **3113**, (1997). "Towards the Calibration of the HETGS Line Response Function"

Marshall, H.L., D. Dewey, N.S. Schulz, and K.A. Flanagan, "Spectral Features in the AXAF HETGS Effective Area using High-signal Continuum Tests", *X-Ray Optics, Instruments, and Missions*, Proc. SPIE, Vol. **3444**, (1998).

Schattenburg, M.L. et al. 1991, Optical Engineering, **30**, 1590. "Transmission Grating Spectroscopy and the Advanced X-ray Astrophysics Facility"

Schattenburg, M.L., Ancoin, R.J., Flemming, R.C., Plotnik, I., Porter, J., and Smith, H.I. 1994, SPIE, **2280**, 181. "Fabrication of High Energy Transmission Gratings for AXAF"

Schulz, N.S., D. Dewey, H.L. Marshall, "Absolute Effective Areas of HETG", *X-Ray Optics, Instruments, and Missions*, Proc. SPIE, Vol. **3444**, (1998).

"X-ray Spectroscopy in Astrophysics", 1999, Springer-Verlag, ed. van Paradijs, J., & Bleeker, J. A. M. - This has a number of good reviews of collisional, photoionized, and non-equilibrium plasmas.

Chapter 9

LETG: Low Energy Transmission Grating

9.1 Instrument Description

The Low Energy Transmission Grating (LETG) was developed under the direction of Dr. A.C. Brinkman in the Laboratory for Space Research (SRON) in Utrecht, The Netherlands, in collaboration with the Max-Planck-Institut für Extraterrestrische Physik (MPE) in Garching, Germany. The grating was manufactured in collaboration with Heidenhaim GmbH.

The Low Energy Transmission Grating Spectrometer (LETGS) is comprised of the LETG, a focal plane imaging detector and the High Resolution Mirror Assembly discussed in Chapter 4. The *Chandra* High Resolution Camera spectroscopic array (HRC-S) is the primary detector designed for use with the LETG. The spectroscopic array of the *Chandra* CCD Imaging Spectrometer (ACIS-S) can also be used, though with decreased quantum efficiency below 0.6 keV and a smaller detectable wavelength range. The High Energy Transmission Grating (HETG) used in combination with ACIS-S offers superior energy resolution and quantum efficiency above 0.78 keV. The HRC is discussed in Chapter 7, the ACIS in Chapter 6, and the HETG in Chapter 8.

The LETGS provides high-resolution spectroscopy ($E/\Delta E > 1000$) between 80 and 175 Å (0.07 – 0.15 keV) and moderate resolving power at shorter wavelengths. The nominal LETGS wavelength range accessible with the HRC-S is 1.2 – 175 Å (0.07 – 10 keV); ACIS-S coverage is 1.2 – 65 Å (0.20 – 10 keV).

A summary of LETGS characteristics is given in Table 9.1.

Table 9.1: LETGS Parameters

Wavelength range	1.2–175 Å (HRC-S)
	1.2–65 Å (ACIS-S)
Energy range	70–10000 eV (HRC-S)
	200–10000 eV (ACIS-S)
Resolution ($\Delta\lambda$, FWHM)	0.05 Å
Resolving Power ($E/\Delta E$)	≥ 1000 (50–160 Å)
	$\approx 20 \times \lambda$ (3-50 Å)
Dispersion	1.148 Å/mm
Plate scale	48.80 μm/arcsecond
Effective area (1st order)	1–25 cm^2 (with HRC-S)
	4–200 cm^2 (with ACIS-S)
Background (quiescent)	$\sim$0.10 counts/pixel/100-ksec (HRC-S, on-orbit)
	$\sim$0.04 counts/pixel/100-ksec (HRC-S, after filtering)
	$\ll 0.01$ counts/pixel/100-ksec (ACIS-S, order sorted)
Detector angular size	3.37' $\times$ 101' (HRC-S)
	8.3' $\times$ 50.6' (ACIS-S)
Pixel size	6.43 $\times$ 6.43 μm (HRC-S)
	24.0 $\times$ 24.0 μm (ACIS-S)
Temporal resolution	16 μsec (HRC-S in Imaging Mode, center segment only)
	$\sim$10 msec (HRC-S in default mode)
	2.85 msec–3.24 sec (ACIS-S, depending on mode)

Rowland diameter	8637 mm (effective value, subject to revision)
	8632.31 $\pm$ 0.50 mm (preflight value)
Grating material	gold
Facet frame material	stainless steel
Module material	aluminum
LETG grating parameters	
Period	0.99125 $\pm$0.000087 μm
Thickness	0.474 $\pm$0.0305 μm
Width	0.516 $\pm$0.0188 μm
Bar Side Slope	83.8 $\pm$2.27 degrees
Fine-support structure	
Period	25.4μm
Thickness	2.5μm
Obscuration	$< 10\%$
Dispersion	29.4 Å/mm
Material	gold
Coarse-support structure	
Triangular height	2000μm
Width	68μm
Thickness	$< 30\mu$m
Obscuration	$< 10\%$
Dispersion	2320 Å/mm
Material	gold

9.1.1 Scientific Objectives

The LETGS provides the highest spectral resolving power (> 1000) on *Chandra* at low (0.08 – 0.2 keV) energies. High-resolution X-ray spectra of optically thin plasmas with temperatures between 10^5 and 10^7 K, such as stellar coronae, reveal a wealth of emission lines which provide diagnostics of temperature, density, velocity, ionization state, and elemental abundances and allow precise studies of structure, energy balance, and heating rates. Absorption features provides similar information in cases where bright compact X-ray sources are embedded in cooler, extended gas clouds.

The high resolution ($\Delta\lambda \approx 0.05$ Å) of LETGS spectra at longer wavelengths ($\gtrsim 100$ Å) also permit detailed studies of spectral line *profiles* in the X-ray region. These studies may provide non-thermal velocities of stellar coronae, flow velocities along active-region loops, orbital velocities in X-ray binaries, and upflow velocities in stellar flares.

The LETGS also allows time resolved spectroscopy, 1-D spatially resolved spectra, and spectra of multiple point sources within its 4 arcmin field of best focus.

Since the ultimate spectral resolution can only be achieved for point sources, the prime candidates for study in our Galaxy mainly comprise stellar coronae, white dwarf atmospheres, X-ray binaries, and cataclysmic variables. Extragalactic sources include relatively bright active galactic nuclei (AGN) and cooling flows in clusters of galaxies.

9.1.2 Heritage

Flat transmission gratings were flown aboard *EINSTEIN* and EXOSAT. The LETG grating elements are produced using a technique similar to that used for production of the EXOSAT gratings. However, the LETG shares only basic operating principles with earlier instruments. Advanced grating technology has enabled the achievement of greater efficiency and increased dispersion. The Rowland geometry (see Figure 8.4) of the grating plate and spectroscopic arrays reduces dispersed image aberrations and hence contributes to improved spectral resolution.

9.1.3 Operating principles

When inserted behind the HRMA, the LETG diffracts X-rays into a dispersed spectrum according to the grating diffraction relation, $m\lambda = p\sin\theta$, where m is the integer order number, λ the photon wavelength, p the spatial period of the grating lines, and θ the dispersion angle. Parameters are summarized in Table 9.1. The grating facets are mounted on an aluminum support plate which has been machined so that the centers of individual grating facets lie on a Rowland torus. The grating facets are aligned to produce a single dispersed image. Spectral resolution is determined, among other factors, by grating line density, line density variations, HRMA point-spread function, pointing stability, alignment
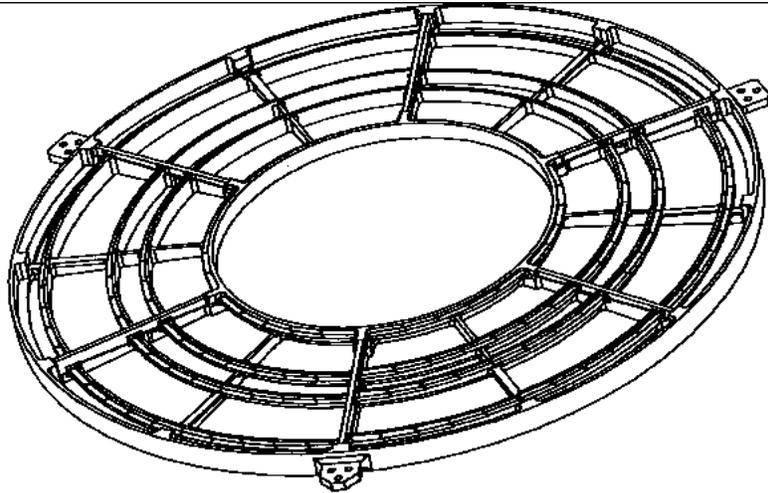
Figure 9.1: LETG Grating Element Support Structure, a machined aluminum plate approximately 110 cm in diameter which holds grating modules on a Rowland torus behind the *Chandra* mirrors.

accuracy, pixel size of the readout detector, and detector geometry. Spectra retain the timing and energy resolution of the readout detector.

9.1.4   Physical configuration

When the LETG is used, the Grating Element Support Structure (GESS), an aluminum frame approximately 110 cm in diameter and 6 cm thick, is inserted ∼300 mm behind the exit aperture of the HRMA and 1.4 m behind the HRMA mid-plane. The GESS holds approximately 180 trapezoidal grating modules, which measure about 13 × 50 mm. A design drawing of the full GESS is shown in Figure 9.1; a closer view, showing some mounted modules, is seen in Figure 9.2. Each grating module has three circular facet rings, each of which holds a grating facet. Figure 9.3 shows empty grating modules mounted on the GESS.

Within each grating facet the grating bars are supported by perpendicular "fine support" bars and triangular "coarse support" bars. The parameters of these structures are given in Table 9.1. A schematic of the grating structure is shown in Figure 9.4. Both the fine and coarse grating supports form long-period transmission gratings themselves. The fine support produces a dispersion pattern perpendicular to the grating dispersion direction, seen in Figure 9.22. The coarse support produces a six-pointed star pattern, shown in the 0-th order image of Sirius in Figure 9.26.
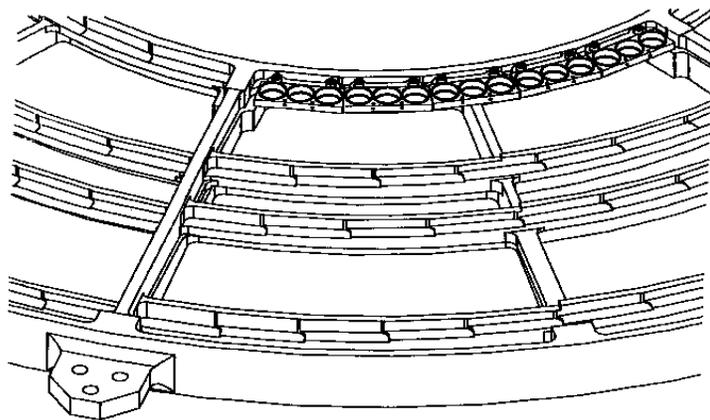
Figure 9.2: Detail of the LETG Grating Element Support Structure showing grating modules mounted on the inner annulus.
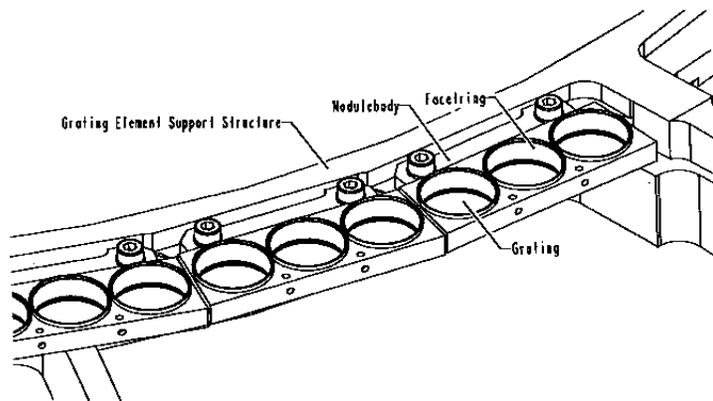
Figure 9.3: A closeup view of the LETG GESS showing two complete grating modules. Each module has three holes which hold the arrays of grating facets.
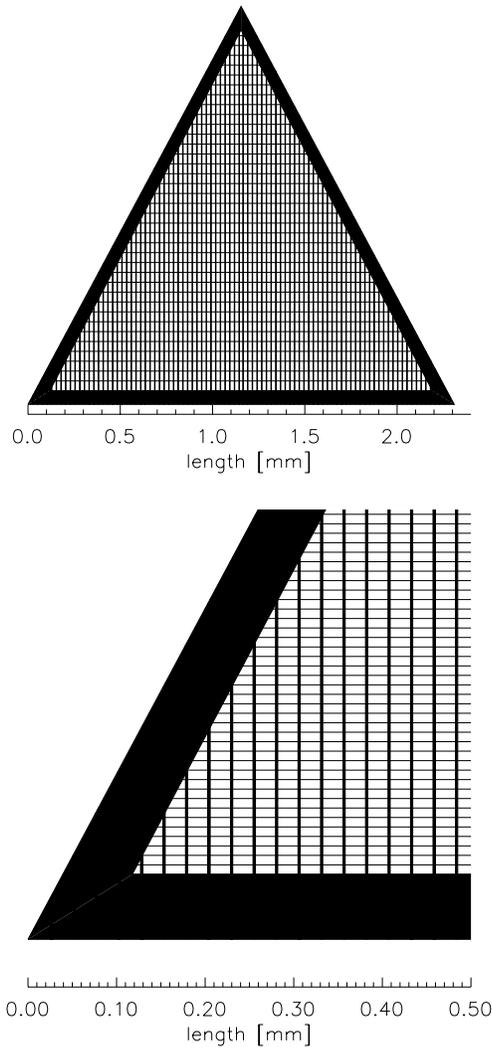
Figure 9.4: LETG facet structure schematic showing the basic shape of the individual grating elements and the relative sizes of the support structures. The upper view shows the entire facet, which is comprised of the triangular coarse support, the vertical fine supporting bars, and the (horizontal) grating bars. The grating bars themselves are not shown to scale. In the upper view every 50th grating bar is drawn, in the lower view every 10th bar.
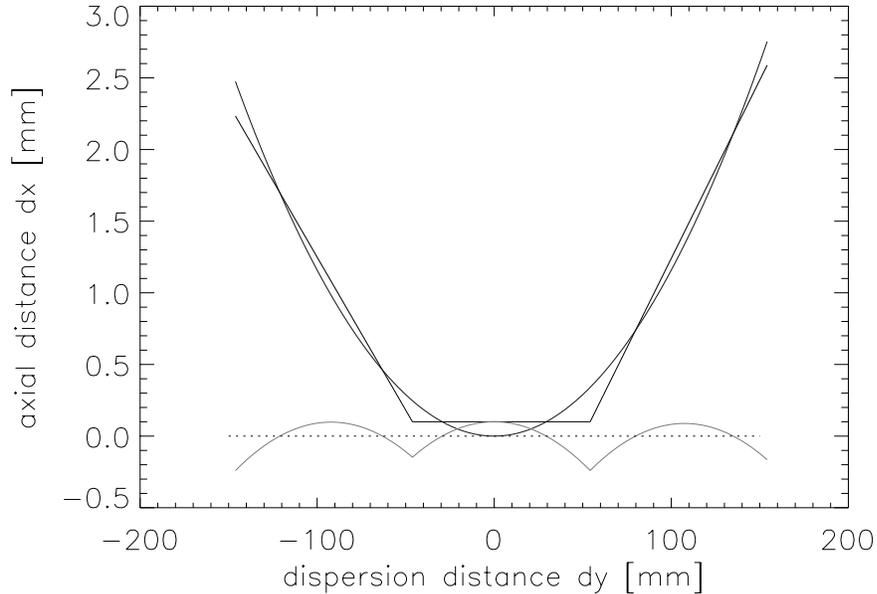
Figure 9.5: The front surfaces of the HRC-S detector segments and their relationship to the Rowland circle are shown schematically. The scalloped line beneath them is the difference between the detector surface and the Rowland circle.

In contrast to the HETG gratings, which have a substrate, the LETG gratings are free-standing wires held by a support mesh. Since the gratings are produced from a single master mask, there is negligible variation in the period between facets. The thickness of the gold of the grating bars on top of the support mesh determines the "phasing," or efficiency of redistribution of photons into each spectral order in wavelengths where the gold is partially transparent. The thickness is designed to optimize the first-order response at energies of interest.

To reduce aberrations, the GESS is shaped to follow the Rowland torus. The primary readout detector (HRC-S) is made of three tilted array segments which also follow the Rowland circle in the image plane (see Figure 7.2 in Chapter 7, and Figure 9.5). The secondary readout detector, ACIS-S, has 6 CCDs which are similarly tilted (Chapter 6). The readout detector position along the optical bench is adjusted so that the "average" focus is best. Since the detector array elements are flat, the distance from the Rowland circle changes with position, and hence the spectral resolution changes with wavelength. The relation between the HRC-S geometry and the Rowland circle is shown in Figure 9.5. The basics of the Rowland geometry are shown in Figure 8.4.

The arrangement of the HRC-S array is shown schematically in Figure 7.1. The HRC-S subtends about 7 by 101 arcmin, though image-quality degrades substantially more than about 4 arcmin off axis. The HRC-S edges in the dispersion direction correspond to dispersed wavelengths of about (negative) 165 and (positive) 175 Å for on-axis sources.

9.2　Calibration

9.2.1　Pre-launch Calibration

Prior to assembly, individual grating elements were tested using a visual light spectrograph at the Max-Planck-Institut. Laboratory calibration of grating period and resolution was performed for individual grating elements at optical wavelengths, and extrapolated to the X-ray range. Grating efficiencies at X-ray wavelengths were modeled using near-infrared spectrophotometry, and verified by X-ray measurements of a sample of facets. Grating facet and module alignment was also tested. LETGS efficiency, resolution, and line response function were tested at the X-ray Calibration Facility at *MSFC* in Huntsville, AL for both ACIS-S and HRC-S combinations. Absolute energy scale and off-axis response were also measured. Efficiency and the Line Spread Function (LSF) of the LETG and HRMA/LETG subsystem were also characterized using a detector system designed for HRMA calibration, the HRMA X-ray Detection System (HXDS). Details may be found at the first WWW reference at the end of this Chapter.

9.2.2　In Flight Calibration

In flight calibration was planned and is being executed by the *CXC* LETG team. LETG first light and focus observations were of the active late type binary Capella whose coronal spectrum is rich in narrow spectral lines (see section 9.3.7). LETGS effective area (EA) and HRC-S relative quantum efficiency (QE) studies have been performed using observations of Capella and the BL Lac and quasar continuum sources PKS 2155-304 and 3C 273 at shorter wavelengths (< 44 Å; > 0.28 keV), and using observations of the hot DA white dwarfs HZ 43 and Sirius B observations at longer wavelengths (> 44 Å; < 0.28 keV). In addition to these objects, the supernova remnants G21.5-0.9 and Cas A were used for HRC-S broadband effective area verification studies. Observations of Capella and the late type star Procyon (F5 IV) are also being used in calibration of the dispersion relation, resolving power, line response function, and HRC-S/LETG relative azimuthal orientation. The active late type eclipsing binary AR Lac is being observed for calibration of the HRC-S spatial characteristics, including resolution (point spread function) and gain variation. Finally, the bright A0 V star Vega is observed with the HRC-S to monitor detector optical and UV susceptibility (see Section 7.6); Betelgeuse is also observed to monitor the

Table 9.2: Planned LETGS Calibration Monitoring Observations

Target	Frequency (yr^{-1})	Purpose
Capella	1	HRC-S/LETG LRF, dispersion relation, relative QE, EA
PKS 2155-304	1	HRC-S/LETG QE, EA, ACIS-S/HRC-S cross calibration
HZ 43	2	HRC-S/LETG QE, EA
AR Lac	2	HRC-S spatial resolution, gain
G21.5-09	2	HRC-S gain, broadband QE, EA
Cas A	2	HRC-S gain, broadband QE, EA
Vega	2	UV susceptibility
Betelgeuse	2	optical susceptibility

HRC-S's optical response. Periodic calibration observations are being taken to monitor LETGS operation. Targets and monitoring frequencies are listed in Table 9.2.

9.3 LETGS Performance

9.3.1 Usage

Overview

The primary use of the LETG is expected to be for on-axis observations of point sources, which produce a zero-order image and a dispersed spectrum. Typical LETGS observations range from a few to several 100 ksec; substantially longer observations may require a "Large Project" (section 10.1.7) proposal. No real-time observations are allowed, and to reduce the (small) risk that the grating mechanism might fail, the frequency of use is minimized by concatenating grating observations into consecutive time blocks whenever possible.

Since use of the LETG attenuates the undispersed flux by roughly an order of magnitude, excessive counting rates should not generally be a concern with respect to exceeding detector count rate limits or telemetry saturation. However, some bright sources (e.g. Sco X-1) if observed for long exposure times could cause significant charge depletion in the HRC MCPs – see Chapter 7, especially section 7.12. Some observers may find it useful to insert the LETG for imaging observations simply to reduce the detected photon counting rate. Even moderate rates may cause pileup problems when using ACIS-S (see Section 6.16).

Detectors

In standard operation, the LETGS uses the HRC-S as its detector, covering a wavelength range of approximately -165 to +175 Å in first order for on-axis sources. This wavelength

range can be shifted somewhat by offset pointing, but image quality degrades substantially beyond about 4′. The HRC-S does not have sufficient energy resolution to allow sorting of overlapping spectral orders. In some cases it might be useful to use the HRC-S Low Energy Suppression Filter (LESF), as discussed in Section 9.4, in order to obtain a predominantly higher-order ($m > 1$) spectrum.

The ACIS-S detector can be used instead of the HRC-S, but effective wavelength coverage is reduced because of its smaller size in the dispersion direction (ACIS-S is only half as long as the HRC-S) and the fact that the two outermost chips (S0 and S5) have essentially zero QE for detecting first-order LETG photons (see Figure 9.6). Another consideration is that ACIS has lower temporal resolution than HRC, which may be important when observing periodic or rapidly varying sources. In some cases, however, those disadvantages may be outweighed by the lower effective background rate and intrinsic energy resolution of ACIS, which can be used to separate diffraction orders. The degraded energy resolution of the ACIS FI CCDs (section 6.7) does not pose a problem for LETG point-source observations, since the source position can be placed close to the ACIS readout, thus minimizing any effects.

In some specialized cases, the HRC-I may also be used with the LETG. A detailed discussion of the various merits of LETGS detector choices from a point of view of proposal planning is given in Section 9.4.

Off-Axis and Multiple Sources

Because the LETGS is essentially an objective-grating system, it is possible to do multi-object spectroscopy, although as noted above, the point-spread function degrades rapidly off axis. To include or reject secondary sources, or to avoid overlapping diffraction from multiple sources, observers may specify the orientation (roll angle) of the grating dispersion direction on the sky (see Chapter 3). Observations of extended sources are also possible, but at the expense of resolving power and with the loss of the simple relation between position and energy. In angular extent, the standard HRC-S spectroscopy readout region is 3.37′ x 101′, and ACIS-S covers 8.3′ x 50.6′. In special cases, a different detector "window" (up to twice as wide) may be selected, as described in Section 9.4.

9.3.2   Wavelength Coverage and Dispersion Relation

The active extent of the HRC-S in the dispersion direction is 296 mm, almost exactly twice that for the ACIS-S. The nominal 0th-order aimpoints for each detector are slightly offset from the detector center so that gaps between the three HRC-S segments (six ACIS-S segments) will occur at different wavelengths in negative and positive orders. In addition, a small offset of $-0.33′$ from the on-axis aimpoint is used as the default for grating observations with ACIS-S so that 0th order photons will fall entirely on one readout node.
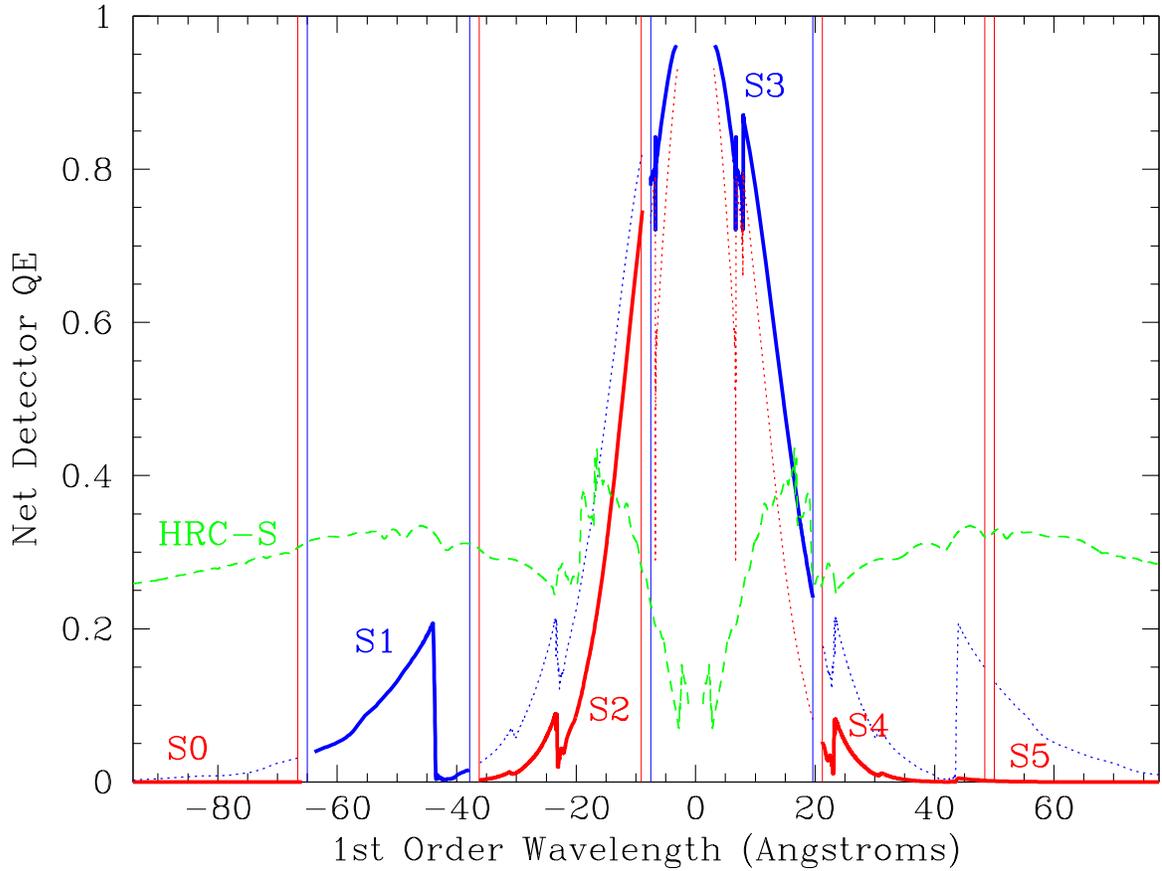
Figure 9.6: (Y-offset = 0 for HRC-S, -0.33' for ACIS-S). Dashed (green) line is for HRC-S, thick solid curves are for ACIS (updated for AO5 QE degradation). Y-offsets may be chosen to tailor the coverage of BI chips (S1 and S3; top/blue QE curve) and FI chips (S0,S2,S4,S5; bottom/red curve). Vertical lines indicate ACIS chip gaps (with dither, 1.5 Å). For clarity, -3 to +3 Å is not shown for ACIS.

With a dispersion of 1.148 Å/mm for the LETG, the standard wavelength range of the LETGS with HRC-S is −165 Å and +175 Å. Physical coverage with ACIS-S extends to −94 and +78 Å, but the poor low-E response of the outlying front-illuminated chips limits the effective wavelength range to −65 Å for negative first order and less than about +40 Å for the positive order (see Figure 9.6). Outlying chips may be useful, however, for collecting higher-order spectra.

Off-Axis Pointing and Detector Gaps

Wavelength coverage can be adjusted (with an increase in wavelength range on one side and a decrease on the other) by changing the central offset (the observatory 'y' coordinate - see the discussion in chapter 3), although spectral resolution degrades rather quickly beyond about 4′. From the information in Table 9.1, one can derive the relationship between angular offset (in the dispersion direction) and wavelength as 3.36 Å per arc minute, so an offset of 10′ would stretch the positive order HRC-S coverage to approximately 208 Å (60 eV). In addition to standard on-axis observations, flight LETG calibration data have been collected at 5′ off-axis (for resolution testing) and 10′ off-axis (for effective area calibration).

As noted before, there are gaps between detector segments which create corresponding gaps in wavelength coverage. The location of these gaps (without dither) are listed in Table 9.3. Dithering the spacecraft will partially smooth these gaps, but observers may wish to adjust the source pointing if a favorite line falls in a gap, or to tune the wavelength coverage of the higher-QE back-illuminated (S1 and S3) ACIS-S chips. (Please see the LETGS Observer Information web page[1] for further details on choosing ACIS-S offsets.) Standard HRC dither amplitude (full width, in both directions) is 40″ (1.95 mm), which covers 2.3 Å, and standard ACIS dither is 16″ (0.78 mm), or 0.9 Å.

Also listed in Table 9.3 is the location of the UV/Ion Shield (UVIS) inner "T" filter edge (see the HRC chapter - 7). Note that the boundaries between the regions of thick and thin aluminum coatings on the UVIS in the LESF – the upper part of the "T" in Figure 7.1 – lie in the gaps between detector segments.

Also note that all these detector features are position-specific, as opposed to fixed in wavelength; the corresponding wavelengths when using a given offset pointing (in the dispersion direction) are easily derived from the 3.36 Å/arc minute relationship mentioned above. Energy-dependent features (from absorption edges in the HRMA, LETG, or detector) do *not* depend on source position to any significant degree, and are discussed in section 9.3.5, and listed in Table 9.4.

---

[1]http://cxc.harvard.edu/cal/Letg/

Table 9.3: LETG Position-Dependent Spectral Coverage (1st Order). Listed values are for nominal pointing (on-axis for HRC-S and Y-offset = -0.33' for ACIS-S) without dither. Standard dithering will smear out feature edges over a range of 2.3 Å for HRC-S and 0.9 Å for ACIS-S. For offset pointing along the dispersion axis (see section 9.4.2), the associated wavelengths (in Å) are shifted by 3.36 times the Y-offset (in arcmin). Energies and wavelengths for the negative order are listed in parentheses. Note that the QE for Front-Illuminated ACIS chips is much lower than for Back-Illuminated chips at low energies, rendering S0, S4, and S5 of limited use (see Figure 9.6).

Detector	Section	Energy (eV)	Wavelength (Å)
HRC-S	UVIS Inner T (thick Al)	(690) - 690	(18.0) - 18.0
HRC-S	seg-1 (neg. $m\lambda$)	(75) - (217)	(165.5) - (57.0)
HRC-S	seg0	(238) - 205	(52.0) - 60.5
HRC-S	seg+1 (pos. $m\lambda$)	191 - 71	65.0 - 174.5
ACIS-S	S0 (neg. $m\lambda$)	(132) - (188)	(94.2) - (66.1)
ACIS-S	S1 (Back-illuminated)	(189) - (332)	(65.5) - (37.3)
ACIS-S	S2	(338) - (1440)	(36.7) - (8.6)
ACIS-S	S3 (Back-illuminated)	(1550) - 617	(8.0) - 20.1
ACIS-S	S4	599 - 254	20.7 - 48.9
ACIS-S	S5 (pos. $m\lambda$)	250 - 160	49.5 - 77.6

Dispersion Calibration

As of this revision, overall wavelength calibration is accurate to a level of a few parts in 10000. In order to obtain agreement between LETGS measurements and accurately known wavelengths of prominent lines (primarily from observations of Capella), the Rowland circle diameter assumed during data processing was changed in Oct 2000 from the preflight value of 8632.3 mm to 8637 mm.

This adjustment brings measured and expected wavelengths into good average agreement—typically about one part in 5000 for wavelengths shorter than 60 Å (lying on the centre plate of the HRC-S), but down to one part in 1000 at some locations longward of 60 Å (lying on the outer plates of the HRC-S). The small residual disagreements between expected and observed locations of spectral features has been found, through analysis of accumulated calibration and GO observations, to be caused by non-linearities in the imaging characteristics of the HRC-S.

These imaging non-linearities can be understood in terms of small errors in the positions of photon events on the detector, as determined by the combination of detector electronics and ground telemetry processing. Position errors occur in both dispersion and cross-dispersion axes, though for spectroscopy the latter are usually not important because spectra are generally summed in the cross-dispersion direction. The magnitude of position errors in the dispersion axis for the central HRC-S plate range from 0 to $\sim$ 0.05 Å, with typical errors of $\sim$ 0.01-0.02 Å. The outer plates ($>$ 60 Å) tend to exhibit larger errors of typically $\sim$ 0.02-0.08 Å. The size of the position errors changes over spatial scales of the HRC readout taps (see Chapter 7) for details of the HRC), which are 1.646mm apart. Spacecraft dither moves dispersed monochromatic photons of a given order over a region of the detector which is roughly 2mm square. Within any given dither region, then, monochromatic light will fall on detector regions that have different position determination errors. As a result, a narrow spectral line could suffer some distortion of its line profile (either widening or narrowing), and/or a small shift of its apparent wavelength by an amount as enumerated above. Such distortions or shifts could occur at the spacecraft dither frequency (see Chapter 5); observers should therefore exercise caution in interpretation of such periodic effects. Care should also be taken when interpreting the results of combined spectra from + and - orders, since these effects are not symmetrical about 0th order.

The position errors appear to be stable and to repeat in different observations; while the problem is not yet fully understood, it is therefore expected that significant improvements in event positions to a level of 0.01-0.02 Å can be achieved in the future through calibration efforts. For the purposes of observation planning at the present time, observers should assume that observed line wavelengths might be in error by 0.02 Å.

Systematic deviations in observed dispersion relation compared to the expected one, in the sense that spectral lines at wavelengths >60 Å appeared at wavelengths too long

by 0.01% , reported in earlier versions of the *Proposers' Observatory Guide*, have recently been traced to a *CXC* data processing software bug that will be fixed in a future software release. At that time, all affected archival data will be reprocessed to correct the problem.

9.3.3 Resolving Power

The dominant contribution to the LETGS line response function (LRF) and instrument resolving power is the HRMA point-spread function (*PSF*), which is ~ 25 μm FWHM, depending on energy. The next most important factor is the detector *PSF* , which is ~ 20 μm FWHM for the HRC-S, with 6.43-μm-wide pixels in the dispersion direction; ACIS pixels are 24 μm wide. Uncertainties in correcting photon event positions for the observatory aspect, which occurs during ground data processing, does add an additional small blurring term. In most cases, the contribution of aspect errors to the *PSF*/LRF is of order a few μm. Finally, the small errors in photon position determination resulting from HRC-S imaging non-linearities described above, can lead to some distortion, broadening, or narrowing of spectral line profiles. The size of these effects have not been fully quantified as yet, though generally affect the line FWHM to less than 25 % .

When all these effects are combined, the LETGS line response function is generally ~ 40 μm FWHM. With a conversion of 1.148 Å/mm for the LETG, a good figure of merit for LETGS resolution is therefore 0.05 Å. Because the three segments of the HRC-S can not perfectly follow the Rowland circle (see Figure 9.5), however, resolution varies slightly along the detector, and is lowest near the ends of each detector segment. Resolution degradation is almost negligible when using the ACIS-S, since its six segments more closely follow the Rowland circle, although the coarser ACIS pixel size (24 μm vs. ~ 40-μm-FWHM LRF) means that line profiles are barely sampled adequately. A plot of LETGS resolving power for an on-axis point source, based on results from an observation of Capella, is shown in Figure 9.7.

Plots of fits to the LETG+HRC-S LRF at zeroth order and at Fe XVII and XVIII lines at ~ 17 and 94 Å are given in Figure 9.8 and Figure 9.9. The fitted function is a beta model of the form:

$$I(\lambda) = [1 + \left(\frac{\lambda}{\lambda_c}\right)^2]^{-\beta}$$

which is a fairly good approximation of the LETG/HRC-S LRF. Figure 9.10 illustrates the χ^2 of fits to the zeroth order profile vs. β, and shows a best fit profile with an index of ~ 2.5. (The Lorentzian profile has $\beta = 1.0$.)

Extended Sources

If a source is extended, there is no longer a unique mapping between the position of an event in the focal plane and wavelength, which results in the apparent degradation of
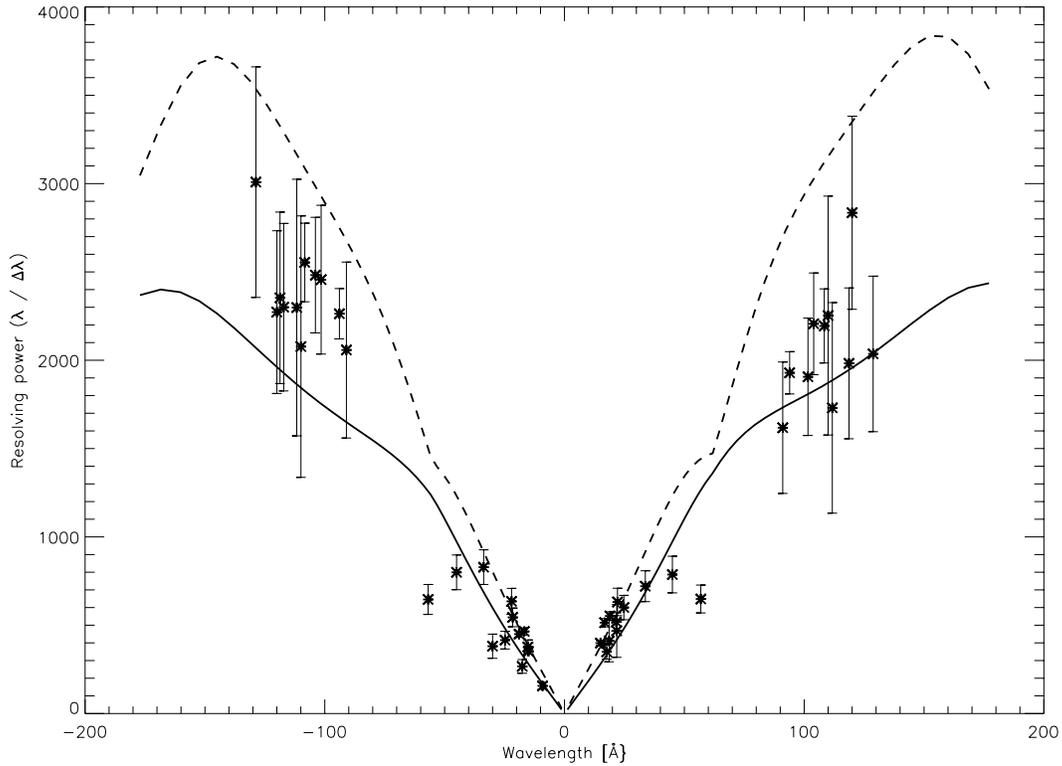
Figure 9.7: LETG spectral resolving power, as derived from observations of Capella (Obs ID's 1248, 1009, 58) and Procyon (Obs ID's 63, 1461) with the HRC-S. The analysis is based only on spectral lines thought not to be affected significantly by blending at the LETGS resolution. Measured line widths were corrected for source orbital, rotational, and thermal motions. The dashed line is an optimistic error budget prediction calculated from pre-flight models and instrument parameters. The conservative solid curve is based on plausible in-flight values of aspect, focus, and grating period uniformity. The deviations from approximate linearity near ±60 Å and at the longest wavelengths arise from deviations of the HRC surface from the Rowland circle (see Figure 9.5). Deviations in the experimental data from a smooth curve are likely caused by hidden blends not predicted by the radiative loss model.
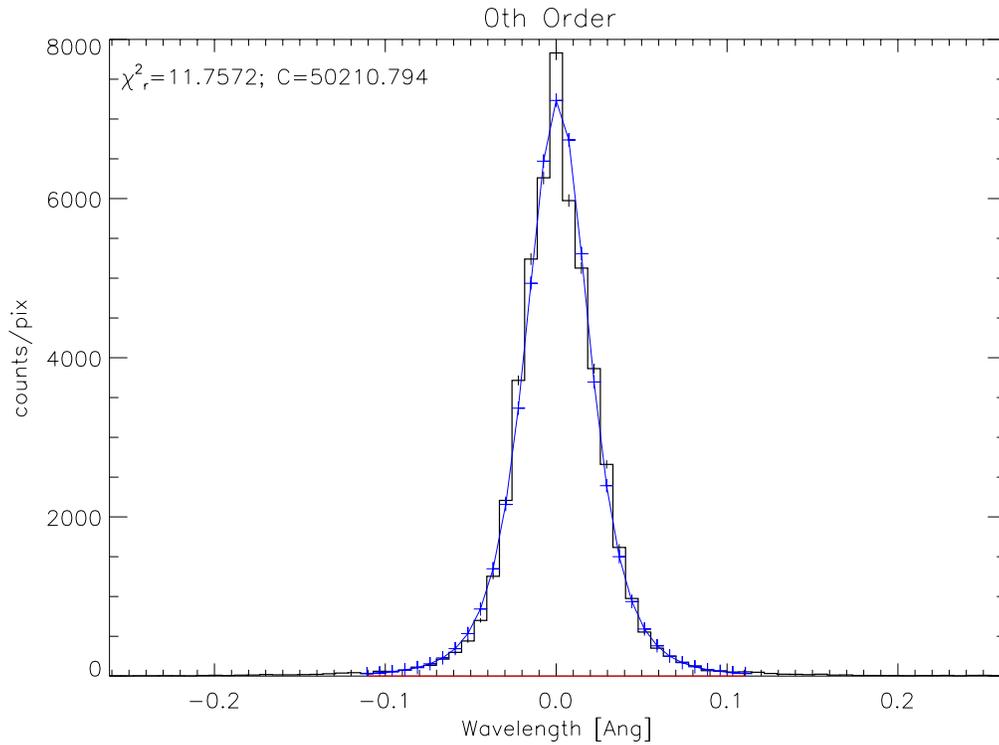
Figure 9.8: Observed LETG zeroth-order LRF from in-flight calibration observations of the active late-type binary Capella. The model profile, the continuous curve, is a beta model (see text) corresponding to the best fit value of $\beta = 2.5$. The reduced χ^2 of 11.8 certainly indicates a statistically poor fit to these very high S/N data, but the beta model is a good approximation to the LRF for weaker dispersed lines.
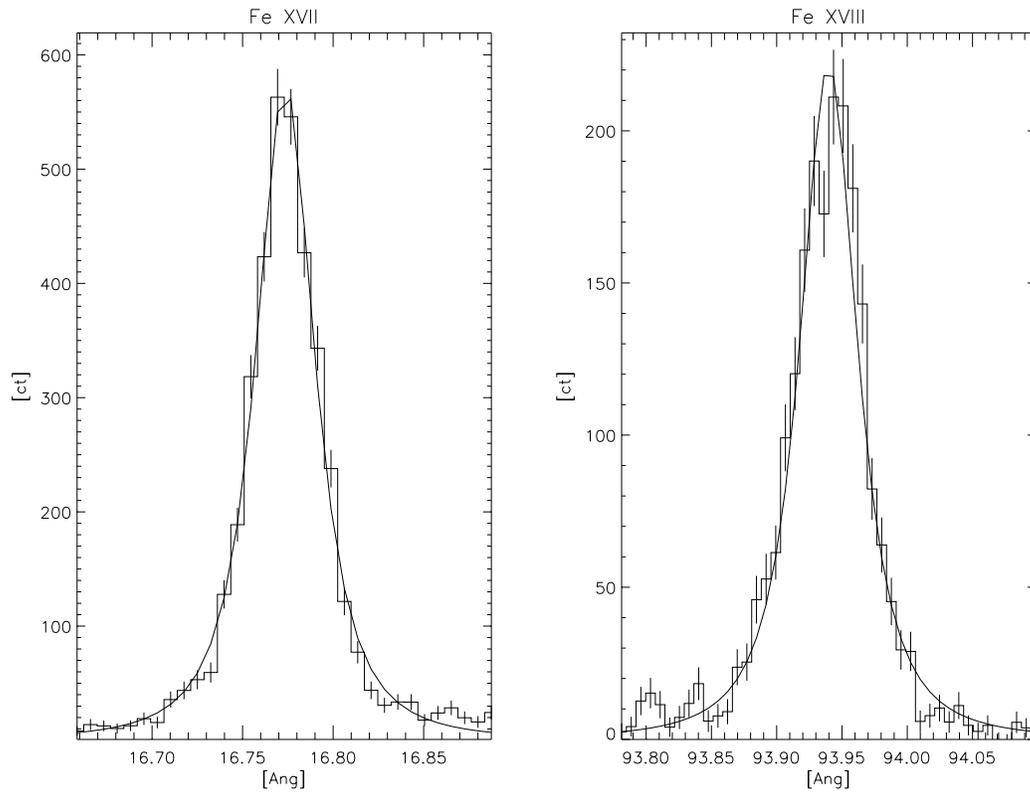
Figure 9.9: LETGS line response function as illustrated by two bright Fe lines (Fe XVII at ~ 17 Å and Fe XVIII at ~ 94 Å) using in-flight calibration observations of Capella. The solid curves are best fit beta models ($\beta = 2.5$).
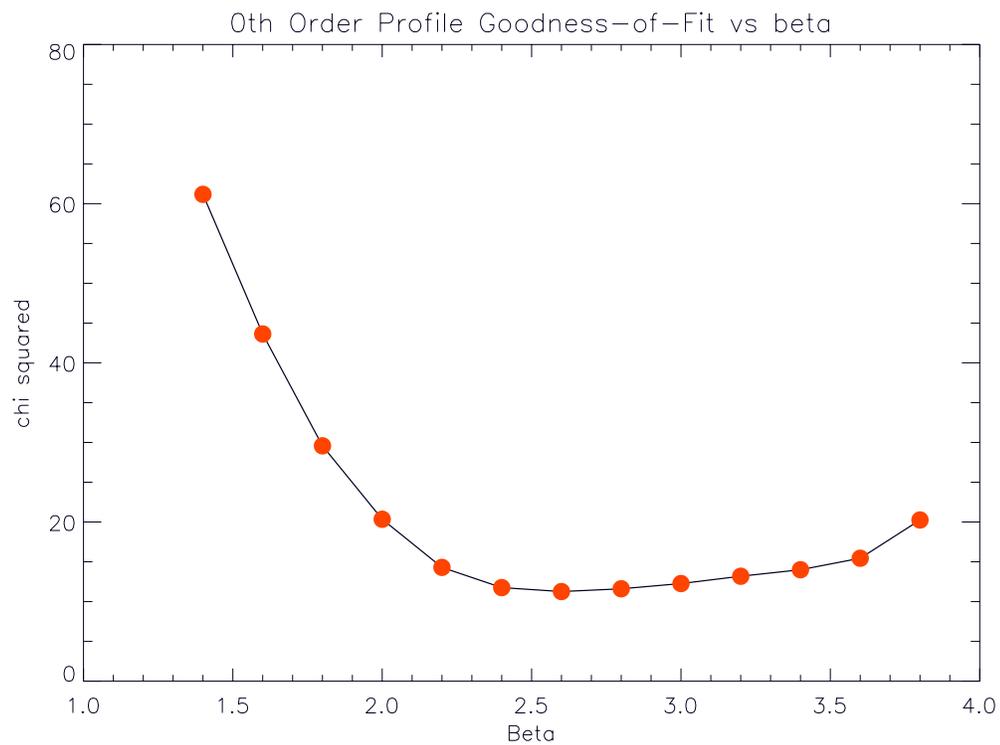
Figure 9.10: LETGS zeroth order profile goodness of fit vs. β, showing a best fit profile with an index of ~ 2.5 (see text).

spectral resolving power. For very large sources, the grating resolution may be no better than the intrinsic ACIS energy resolution.

The effect of increased source size on the apparent LETG spectral resolving power has been simulated using the *MARX* program, and results are shown in Figure 9.11. Currently, *MARX* tends to slightly overestimate resolving power, so the curves should be viewed as indicating trends rather than absolute values. Another illustration of the effect of source extent may be seen in Figure 9.30 (Section 9.4), which shows model spectra over a small wavelength range.

In each case, extended sources were modeled using a Beta model for the surface brightness profile. Beta models are often used to describe the distribution of emission in galaxies and clusters of galaxies, and have an identical form to the beta model used to describe the line profile above, except that the intensity dependence is radial:

$$I(r) = [1 + \left(\frac{r}{r_c}\right)^2]^{-\beta}$$

where I(r) is the surface brightness, and r is the radius, and r_c characterizes the source extent. β was set to a typical value of 0.75 for the simulations. r_c is very close to the radius of a uniform disk fit to a source and was varied in the simulation.

Off-Axis Sources

Similarly, for sources off axis, the increased point-spread function decreases the spectral resolving power. The effect on off-axis sources has been simulated with *MARX* and is shown in Figure 9.12.

As with extended sources, an ACIS pulse-height spectrum may, in extreme cases, provide energy resolution comparable to or better than the LETG for a source far off axis.

9.3.4   Grating Efficiency

Fine and Coarse Support Structure Diffraction

As explained in Section 9.1, the LETG has fine and coarse support structures which are periodic in nature, and have their own diffraction characteristics. The fine support structure disperses photons perpendicularly to the main spectrum, with about 1/26 the dispersion of the main grating. The coarse support is a triangular grid, and creates a very small hexagonal diffraction pattern which is generally only discernible in 0th order or for very bright lines. Examples of this secondary diffraction are visible in Figures 9.22, 9.23, and 9.26, all in Section 9.3.7.

The two support structures each diffract roughly 10% of the X-ray power, but the coarse-support diffraction pattern is so small that essentially all its photons are collected
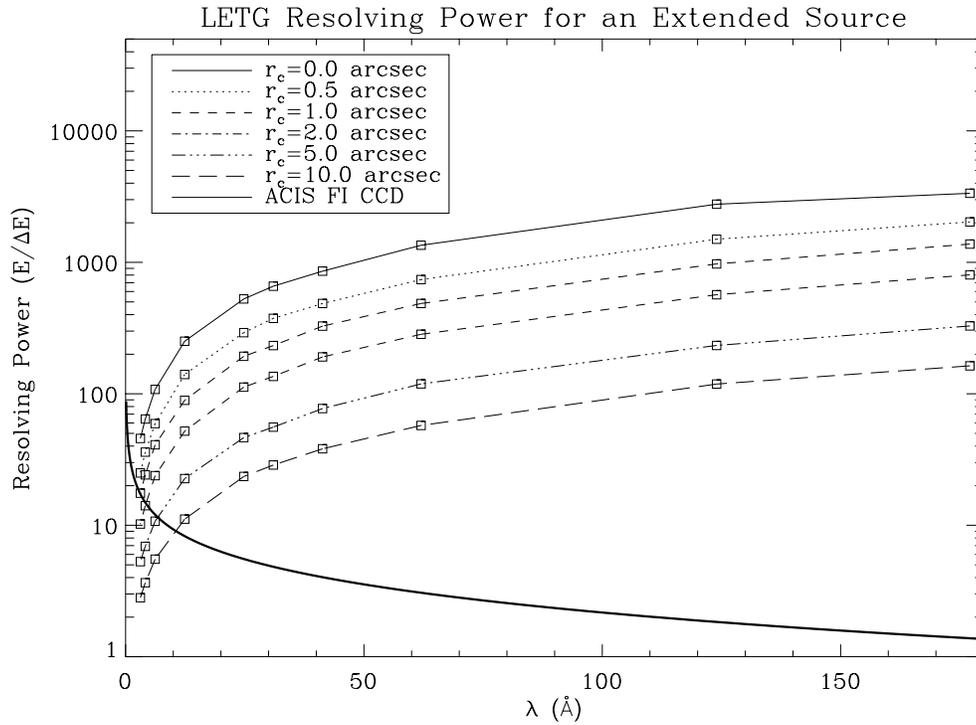
Figure 9.11: LETG spectral resolving power for extended sources. The predicted LETG re-solving power (E/ΔE) is shown versus wavelength for several source sizes. The *MARX* simulator has been used, and the source is represented by a β model as discussed in the text. (Note that *MARX* tends to slightly overestimate resolving power.) For compari-son, the spectral resolution for ACIS front illuminated CCD chips is shown (thick solid line). Note that the ACIS/FI curve does not include the effects of CTI, which progressivly degrades resolution away from the readout edge.
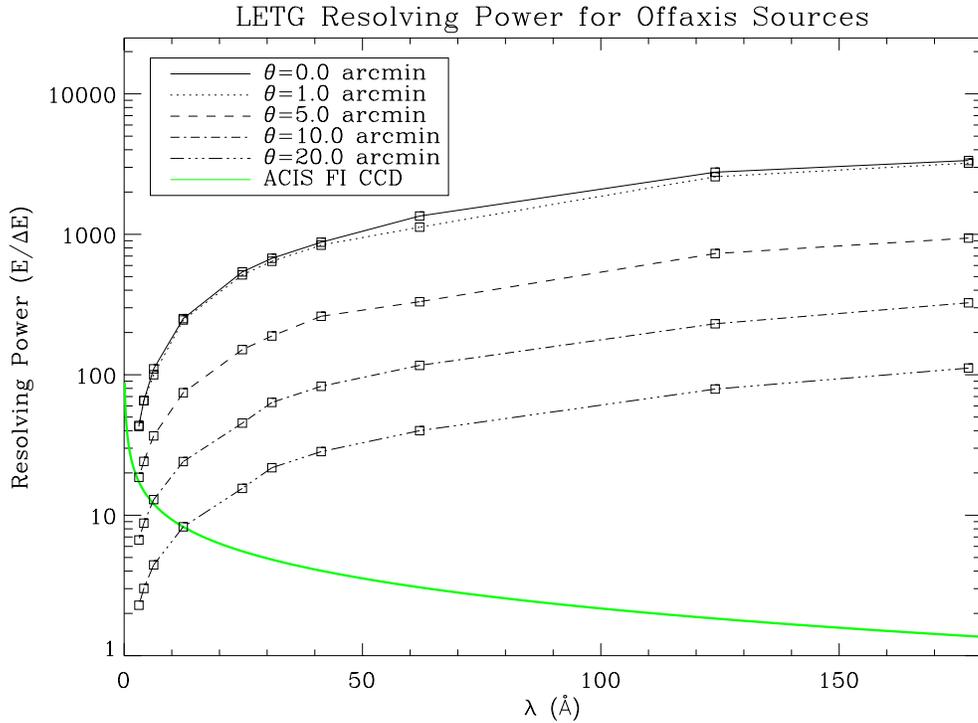
Figure 9.12: LETG spectral resolving power for off-axis sources. The predicted LETG resolving power (E/ΔE) is shown versus wavelength for various off-axis distances. The *MARX* simulator has been used, which somewhat overestimates the on-axis resolving power. For comparison, the spectral resolution for ACIS front-illuminated CCD chips is shown. Note that the ACIS/FI curve does not include the effects of CTI, which progressivly degrades resolution away from the readout edge.

along with the primary spectrum during spectral-region extraction in data analysis. A significant fraction of the fine-support diffraction pattern, however, may lie outside the spectral extraction region, resulting in a loss of several percent of the total X-ray intensity (see, e.g. Figure 9.22). The fractional *retention* of X-ray power in the source extraction region is referred to as the *spectral extraction efficiency* and is discussed further below.

Total Efficiencies

The zeroth, first, and selected higher-order grating efficiencies, based on a rhomboidal grating bar analytical model and verified by ground calibration, are shown in Figure 9.13. The efficiency for each order is defined as the diffracted flux with the grating assembly in place divided by the flux if the grating assembly were not in place. Plotted values are for the total diffraction efficiency (including photons diffracted by the coarse and fine support structures), with negative and positive orders summed. Even orders are generally weaker than odd orders up through roughly 6th order.

The wiggles near 80 Å, and the stronger features near 6 Å, arise from partial transparency of the gold grating material to X-ray photons. Note that there are no absorption-edge features from C, N, or O in the LETG efficiency as there are in the HETG, because the LETG does not use a polyimide support film.

9.3.5   Effective Area

The LETGS effective area for any diffraction order is equal to the product of the HRMA effective area, the net LETG efficiency for that order, and the overall detector efficiency (which varies slightly depending on exactly where the diffracted spectrum falls on the detector). All these quantities vary with photon wavelength.

Of these three contributors, the HRMA (see Chapter 4) is the best calibrated within the LETGS energy band. Next best is the LETG efficiency, based on both calibration data and theory. The major contributor to the effective area uncertainty lies in the efficiency of the HRC-S, especially at longer wavelengths (> 44 Å; < 0.28 keV). The HRMA+HRC-S effective area at those wavelengths could not be adequately calibrated on the ground. In-flight calibration (see Section 9.2.2), particularly of the net first order effective area, has provided the best and most extensive data, and the effective area is now believed to be accurate to a level of approximately 15 % or better across the entire bandpass. Higher order effective areas are straightforward to derive from grating efficiencies relative to first order. However, the uncertainty in the diffraction efficiency increases significantly with order number and is also large in even orders.
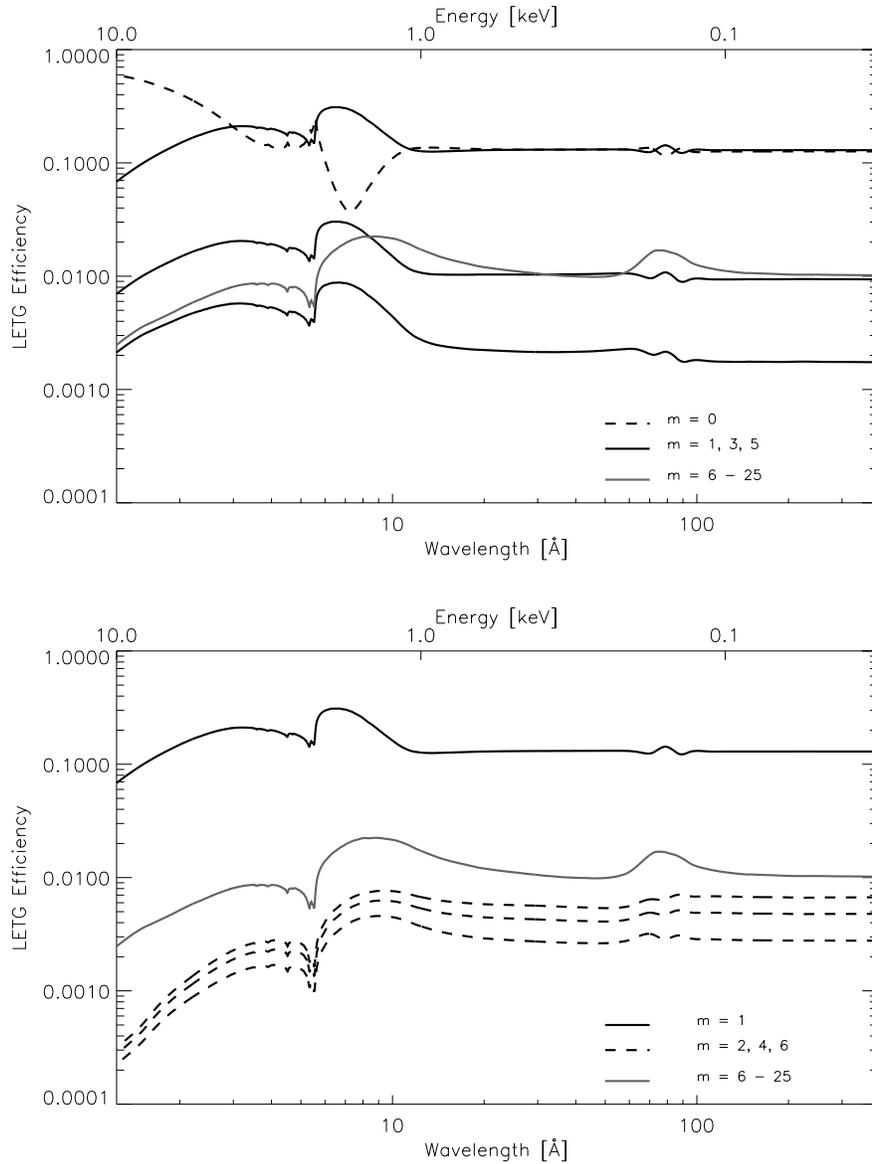
Figure 9.13: LETG grating efficiency. Summed positive and negative order efficiency is plotted versus wavelength. The top panel shows the zeroth and odd orders; bottom panel shows 1st and even orders. The summed efficiency of orders 6 through 25 is also included in both panels. Plotted values include all support structure diffraction. Features near 6 and 80 Å are due to the partial transparency of the gold grating material at these wavelengths.
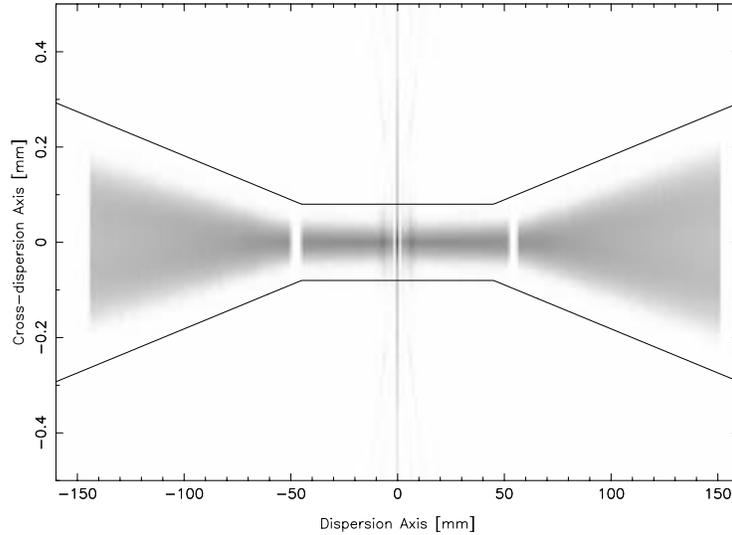
Figure 9.14: A MARX simulation of a flat spectrum illustrating the broadening of the LETG+HRC-S profile in the cross-dispersion direction, and showing the "bow-tie" spectral extraction window.

Instrument Spectral Features

In addition to fixed-position detector features (primarily detector segment gaps–see Section 9.3.2) there are instrumental spectral features which occur at fixed energies because of absorption edges in the materials comprising the HRMA, LETG, and HRC-S or ACIS-S. The edges are tabulated in Table 9.4 and can be seen in the effective area curves (such as Figure 9.17) as decreases or increases in effective area depending on whether the material is part of the mirror, the filter, or the detector. Every effort has been made to adequately calibrate *Chandra* over its entire energy range, but it should be understood that effective areas near absorption edges are extremely difficult to quantify with complete accuracy and uncertainties in these regions are inevitably higher.

Spectral Extraction Efficiency

In practice, it is impossible to "put back" photons which undergo secondary diffraction (from the coarse and fine support structures) in a real observation. Instead, one defines an extraction region for the observed spectrum and adjusts the derived spectral intensities to account for the fraction of total events that are contained within the extraction region.

The non-rectangular LETGS extraction region is shown in Figure 9.14. Its width varies with wavelength and has been optimized to match the astigmatic cross-dispersion that is a feature of Rowland-circle geometry, with the goal of including as much of the

Table 9.4: Instrumental Absorption Edges

Instrument	Element	Edge	Energy (keV)	Wavelength (Å)
HRC	Cs	L	5.714	2.170
HRC	Cs	L	5.359	2.313
HRC	I	L	5.188	2.390
HRC	Cs	L	5.012	2.474
HRC	I	L	4.852	2.555
HRC	I	L	4.557	2.721
LETG	Au	M	3.425	3.620
LETG	Au	M	3.148	3.938
HRMA	Ir	M	2.909	4.262
LETG	Au	M	2.743	4.520
HRMA	Ir	M	2.550	4.862
LETG	Au	M	2.291	5.412
LETG	Au	M	2.206	5.620
HRMA	Ir	M	2.156	5.750
HRMA	Ir	M	2.089	5.935
ACIS	Si	K	1.839	6.742
HRC, ACIS	Al	K	1.559	7.953
HRC	Cs	M	1.211	10.24
HRC	I	M	1.072	11.56
HRC	Cs	M	1.071	11.58
HRC	Cs	M	1.003	12.36
HRC	I	M	0.931	13.32
HRC	I	M	0.875	14.17
HRC	Cs	M	0.7405	16.74
HRC	Cs	M	0.7266	17.06
HRC	I	M	0.6308	19.65
HRC	I	M	0.6193	20.02
HRC,ACIS	O	K	0.532	23.30
HRMA	Ir	N	0.496	25.0
HRC	N	K	0.407	30.5
HRC,ACIS	C	K	0.284	43.6
HRC	Al	L	0.073	170
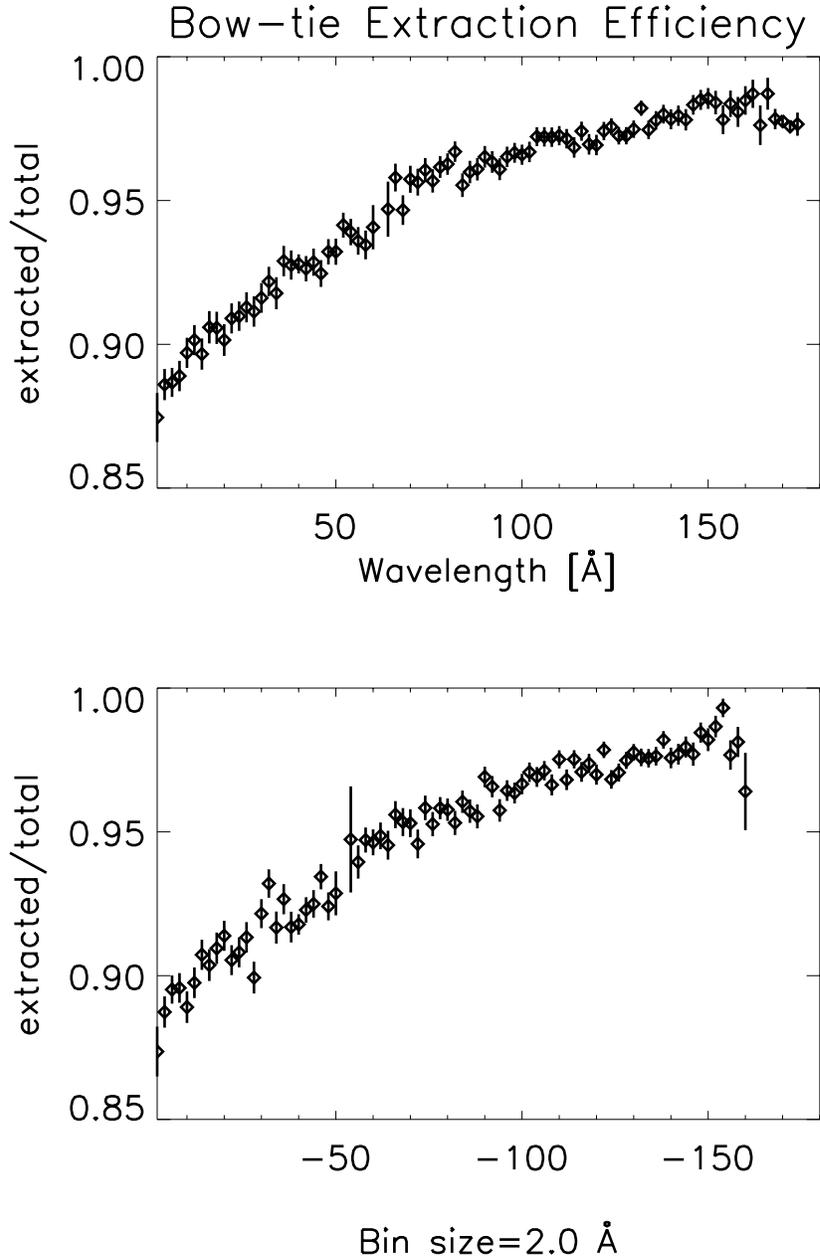
Figure 9.15: The *spectral extraction efficiency* for first order, representing the fraction of the power diffracted into the LETG 1st order that is enclosed within the default *CIAO* "bow-tie" spectral extraction window as a function of 1st order wavelength. The "missing" power is primarily due to diffraction of photons outside of the extraction region by the fine support structure. These extraction efficiencies were determined using *MARX* raytrace simulations. In-flight data, though noisier, have been found to agree with these efficiencies to a level of about 5 % or better. The uncertainty in the effective area calibration resulting from the extraction efficiency alone is therefore less than 1 %.

diffracted spectrum as possible while minimizing the included background. Extraction efficiency varies from $\sim 90\%$ near zero order to more than 95% at the longest wavelengths and is illustrated in Figure 9.15. Effective areas provided in this chapter and on the LETGS Observer Information web site (footnote 1) are based on this extraction region. *CIAO* v2.0 and higher enable adjustment of the bow-tie parameters by the user, but the user should be aware that such changes could change the effective extraction efficiency. The extraction efficiency for default parameters is included in CALDB versions 2.12 and higher, but *CIAO* is not yet capable of adjusting this efficiency according to the extraction region parameters.

Zeroth and First-Order Effective Areas

Although the HRC-S is the default detector for the LETG, other detector configurations are possible. Figures 9.16 (0th order) and 9.17 show effective areas for the LETG when using the HRC-S, HRC-S with LESF, or ACIS-S as the readout detector. Based upon these and other plots, the various tradeoffs as to the use of each detector are thoroughly discussed in Section 9.4.

Off-Axis and Extended Sources

Differences in the LETGS effective area for off-axis and significantly extended sources compared to the on-axis point source case is primarily determined by the HRMA vignetting function (see Chapter 4).

High-Order Diffraction Effective Areas

Although LETG (and HETG) has been designed to reduce complications from higher-order diffraction by suppressing even orders, many grating spectra will have overlapping diffraction orders. When ACIS-S is used as the detector, its intrinsic energy resolution can be used to separate orders. The situation is more complicated, however, with HRC-S, which has very little energy resolution. Detector options and various data analysis techniques are described in Section 9.4.

The relative contribution of higher-order photons with different detector configurations can be estimated by inspection of Figures 9.18, 9.19, and 9.20. As an example, say an observer plans to use the LETG/HRC-S configuration and wants to determine the intensity of a line at 45 Å, but knows that line may be blended with the 3rd order of a 15 Å line which has 10 times the emitted intensity of the 45 Å line. Looking at Figure 9.18, we read the 1st- and 3rd-order curves at $m\lambda = 45$ Å and see that the 3rd-order value is about one-tenth the 1st-order value. Multiplying by 10 (the ratio of the emitted intensities of the 15 and 45 Å lines), we compute that $\sim$50% of the feature at $m\lambda = 45$ Å will come
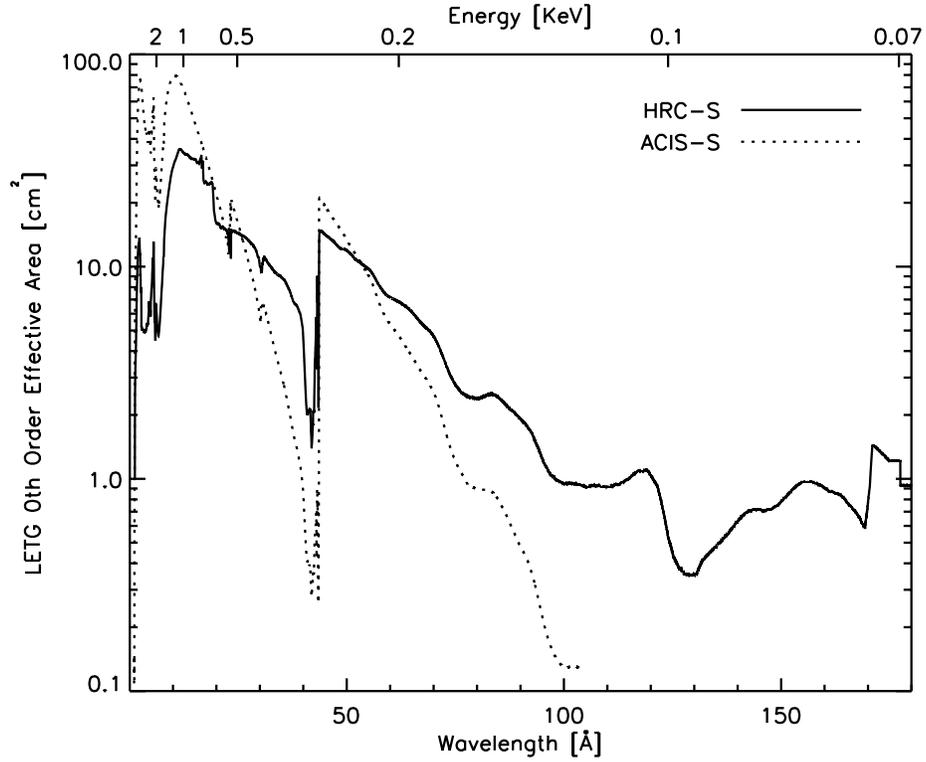
Figure 9.16: LETGS 0th-order effective area for an on-axis point source for the LETG with HRC-S and ACIS-S detectors. The 0th-order effective area for the HRC-S/LESF combination is the same as for the HRC-S. LETG+ACIS-S areas were computed using an effective area model that included the effects of contamination build-up extrapolated to the level expected in mid-May 2004.
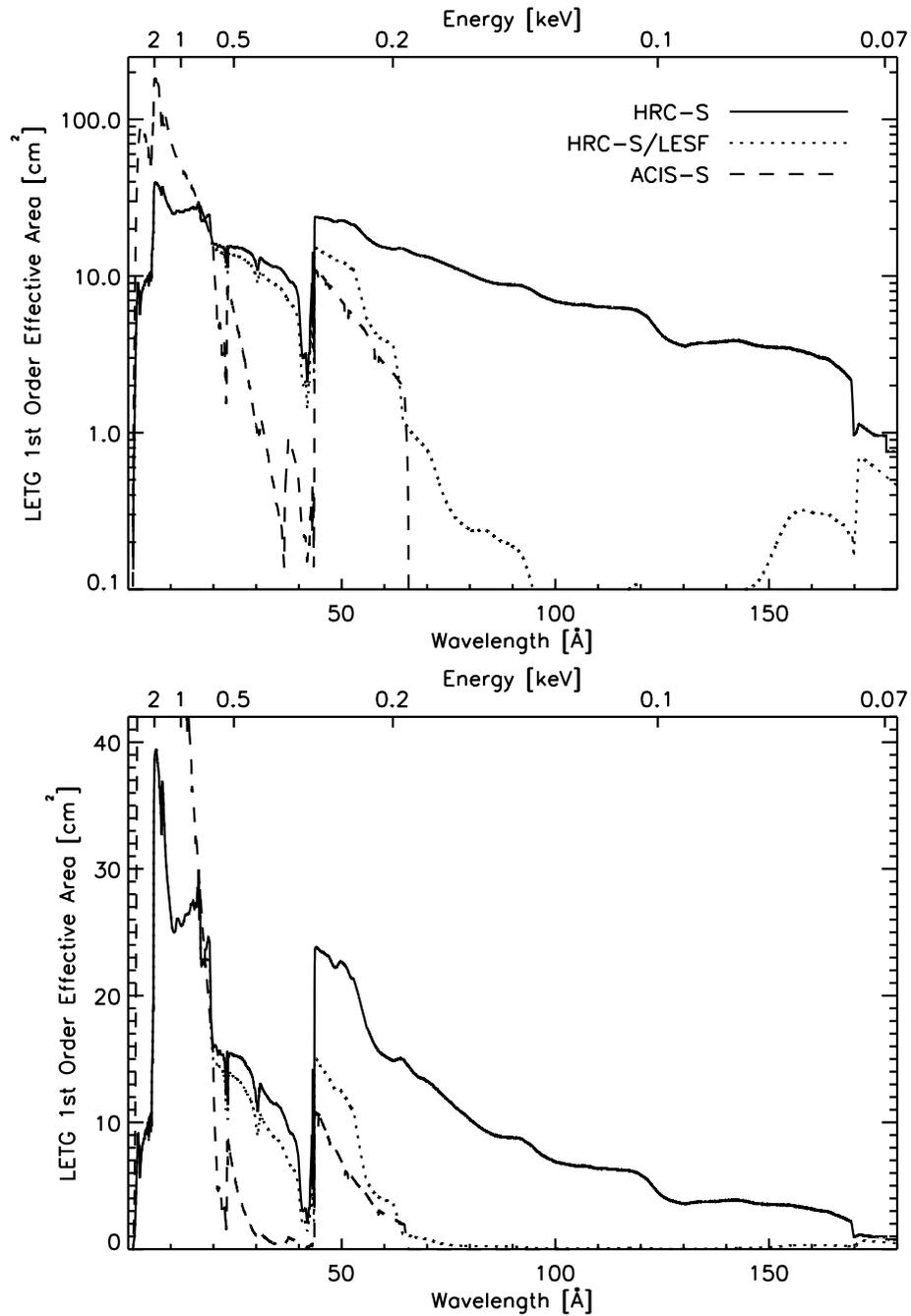
Figure 9.17: LETGS 1st-order effective area for an on-axis point source, with HRC-S, HRC-S LESF and ACIS-S detector configurations with log and linear scaling. Positive and negative orders summed. LETG+ACIS-S areas were computed using an effective area model that included the effects of contamination build-up extrapolated to the level expected in mid-May 2004. Note that the vertical scale of the linear plot has been truncated.
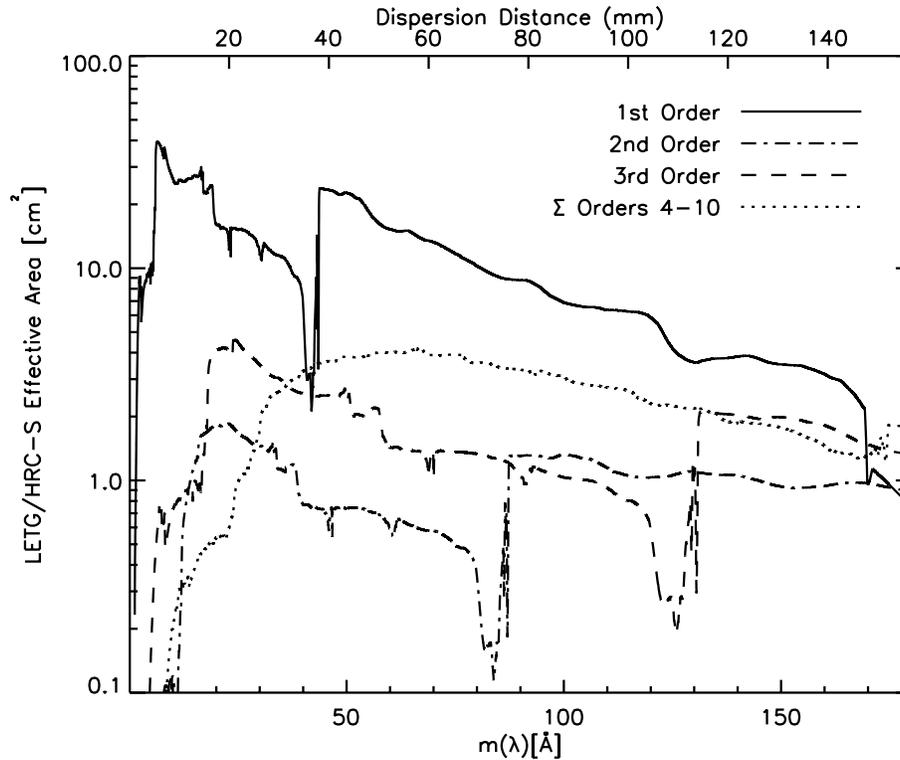
Figure 9.18: The combined HRMA/LETG/HRC-S effective area, illustrating the relative strengths of 1st and higher orders. Positive and negative orders are summed. In the label for the bottom axis, m is the order number. See the text for an example of how to determine the relative strength of overlapping lines from different orders.

from the 15 Å line. As discussed in Section 9.3.6 the 3rd-order contamination can be reduced somewhat by pulse height filtering, but the estimate above is a useful upper limit.

9.3.6 Background

The LETG is always used in conjunction with a focal-plane detector, so the LETG spectra will exhibit that detector's intrinsic, environmental, and cosmic background. The components of the background of the HRC are discussed in Chapter 7, section 7.8. The quiescent background rate over the full detector is roughly equal to the 184 counts/sec telemetry limit. Imposition of the HRC-S spectroscopy window reduces the rate to about 75 counts/sec, as discussed below.
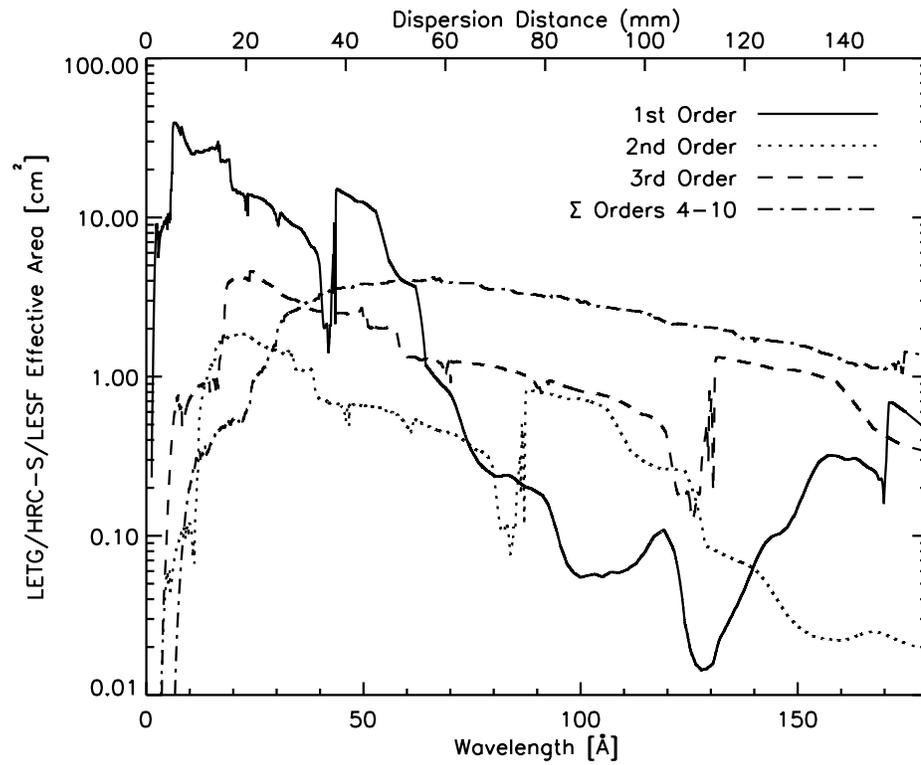
Figure 9.19: The combined HRMA/LETG/HRC-S/LESF effective areas for first and higher orders. Positive and negative orders are summed.
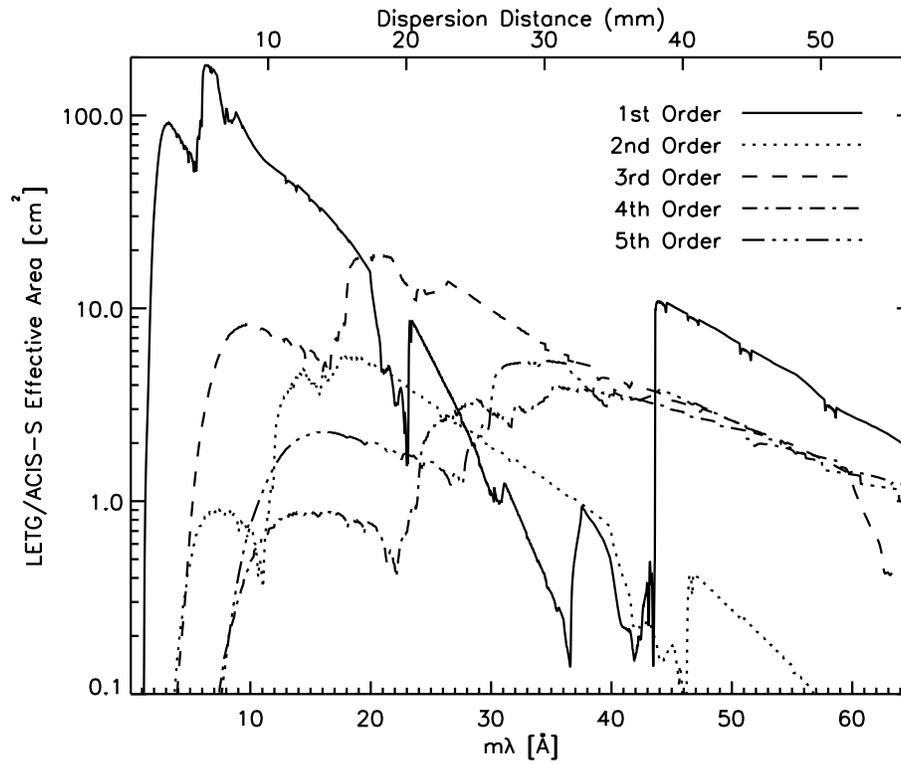
Figure 9.20: The combined HRMA/LETG/ACIS-S effective areas for first and higher orders. LETG+ACIS-S areas were computed using an effective area model that included the effects of contamination build-up extrapolated to the level expected in mid-May 2004. Positive and negative orders are summed.

Exposure Windows, Deadtime, and Timing Resolution

To avoid constant telemetry saturation, the HRC-S is operated in a default, windowed down "edge-blanking" configuration, in which data from only 6 of the 12 coarse taps in the center of the detector in the cross-dispersion direction are telemetered (see section 7.8.2 in Chapter 7). The edge-blanking creates an active detector area slightly less than 10 mm, or 3.4 arcmin, in the cross-dispersion direction. This window easily accommodates the (dithered) dispersed spectra of point sources; other windows may be specified for extended sources or other special cases. In the default configuration, the total quiescent background count rate for the HRC-S ranges from roughly 60 to 100 count/s. A typical value for planning purposes is 75 count/s.

As long as the total counting rate is below the 184 Hz telemetry limit, detector deadtime is negligible (and recorded in the secondary science "dtf" files—net exposure time is recorded in the image FITS file header). During background "flares" arising from an increased flux of solar wind particles, however, the background rate may rise above the 184-Hz telemetry limit. During these times detector deadtime may become significant. Current data processing algorithms correct for this deadtime with a typical accuracy of $\sim 10\%$ or better.

In general, the time resolution of an observation is approximately the average time between events. However, time resolution approaching 16μsec can be achieved with the HRC if the data rate is below telemetry saturation and the Imaging Mode is used (see Section 7.10.) This new mode utilizes only the central region of the HRC-S detector and provides a field of view of approximately $7' \times 30'$.

HRC-S Background Reduction via On-Ground Data Filtering

The quiescent background rate in the HRC-S is roughly 6×10^{-5} counts/s/arcsec^2, or 0.10 counts per pixel in 100,000 seconds. The area of a dispersed line in the LETGS spectrum is ~ 7 pixels in the dispersion direction (FWHM) by ~ 20 to 65 pixels in the cross-dispersion direction corresponding to roughly 15 to 45 background counts beneath the line in a 100,000 s exposure. However, the HRC-S pulse height distribution is narrow enough – with a sigma/mean of ~ 0.22 – that a large fraction of pulse-height space can be excluded from the data to further reduce the background, which has a relatively broad pulse-height distribution.

Since gain varies by more than a factor of two across the HRC-S, a gain map has been created which allows the calculation of position-independent pulse height (PI) values from PHA values as part of standard data processing. The relationship between photon wavelength and mean PI value has been determined from laboratory and flight data so that PI/wavelength filtering can be applied to LETGspectra to substantially reduce the background level using standard *CIAO* (version > 2.1) tools.

Roughly 60% of the background is removed in this way with a < 1% loss of (1st order) X rays, using a "light" PI filter. Observers can also apply "medium" and "heavy" PI filtering, as described on the LETGS Observer Information web page (footnote 1) and illustrated in Figure 9.21, where the successively lower curves correspond to the more stringent filtering. Those filters remove approximately 65% and 70% of the background, respectively, with around 2% and 5–15% X-ray losses. The heavy filter is not recommended for creating publishable spectra, but may be useful in isolating very low signal-to-noise spectral features. LETGS Effective Area curves are derived from data without PI filtering; the effect of light and medium filtering (<1% and 2%) is, however, essentially negligible.

Relevance for Higher Orders   The mean of the pulse-height distribution increases weakly with photon energy, such that a factor of two difference in energy corresponds to a shift in the mean of ∼12%, which is about one-half sigma. Therefore, the mean pulse height of fourth order will lie about one sigma away from the first order mean. The PI filters are a few to several sigma wide, however, so that only about 5% of 8th order is removed by the light filter. Order separation, even using the heavy filter, is therefore not of any practical use.

Relevance for Observation Planning   There are two backgrounds relevant for the LETG/HRC-S: the first is the unfiltered rate, which is roughly 75 ct/s during quiescence, but can rise during background 'flares' to cause telemetry saturation when the total (background plus sources) rate reaches 184 ct/s; the other is the filtered background rate, leading to ∼ 15-45 counts in a FWHM spectral bin per 100,000 s integration during quiescence, which may be used for estimating signal-to-noise (see also the discussion in section 9.5.1 and Figure 9.28 for the spectral dependence).

There is a third background rate which will be of interest when high time resolution (sub-msec) is required, which is the counting rate before any on-board screening is applied. See Section 7.10 for more information on the HRC-S Timing Mode.

ACIS-S Background

As with the HRC-S detector, background rates in ACIS are somewhat higher than expected, but lower than in the HRC. Pulse-height filtering applied during order separation further reduces the effective ACIS-S background to extremely low levels when used with gratings. The reader is directed to Chapter 6 for further discussion.

9.3.7   Sample Data

Figure 9.22 is a detector image of an 85 ksec LETGS observation of Capella (obsid 1248). The central 30 mm of the dispersion axis and the full extent of the telemetered cross-
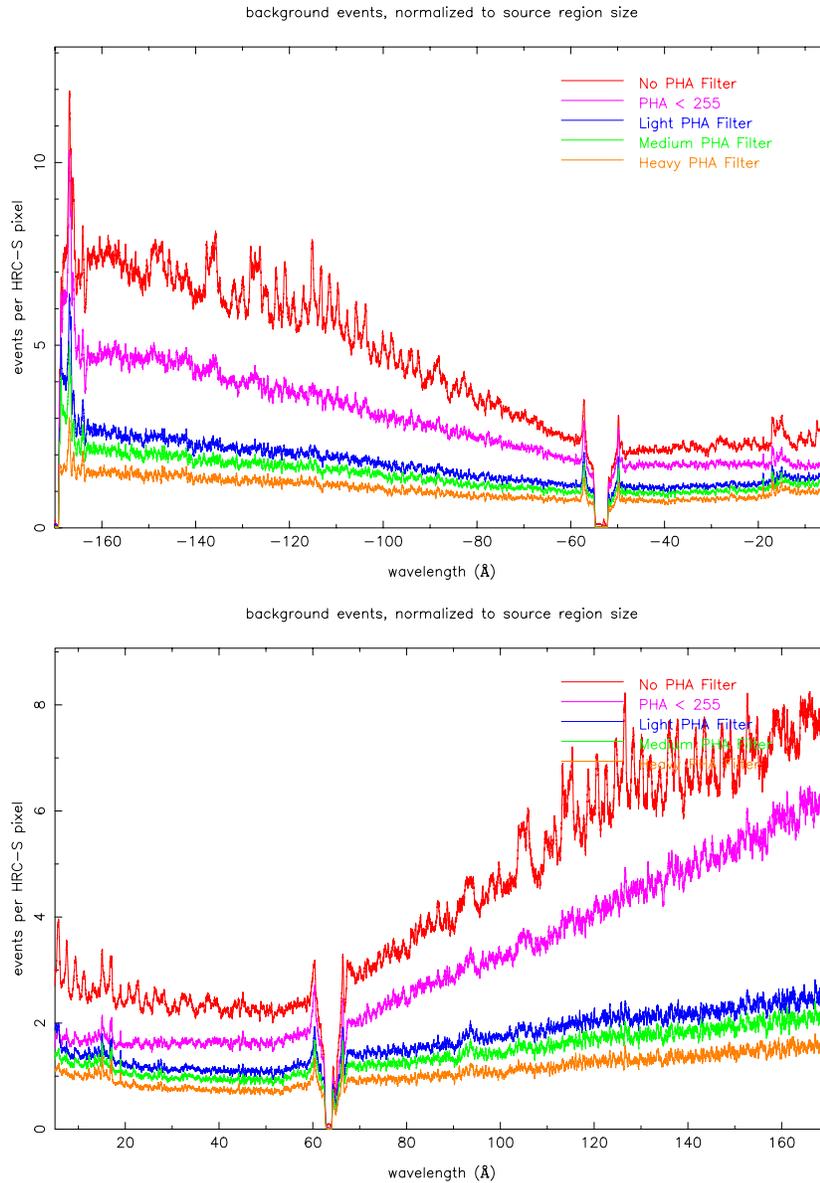
Figure 9.21: The LETG+HRC-S background from an observation of Capella. Spectra were derived from standard 'bowtie' background extraction region (see Figure 9.14). The curves from the top down correspond to: background spectrum with no PI filtering; minimal filtering (PHA=255 events removed) with 0% X-ray event loss; light filtering with 0.5% X-ray loss; 2% X-ray loss; and 5–15% X-ray loss. X-ray losses are for 1st order; losses will be slightly higher for higher orders, especially with heavier filtering. PI filtering is not applied at wavelengths shorter than 6 Å to avoid undesired effects on 0th order. The units of the y axis are total events/dispersion-pixel (summed in the cross dispersion direction), where one HRC pixel is 6.43 μm wide (0.0074 Å). The exposure time was 85 ks.
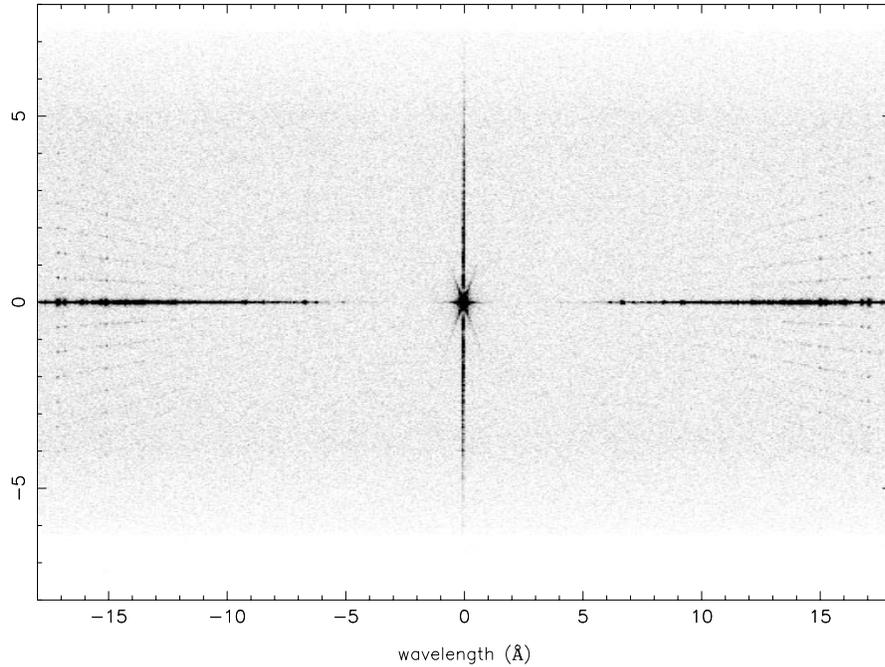
Figure 9.22: HRC-S detector image of LETGS observation of Capella. In order to illustrate the stretching of the cross-dispersion axis, both axes are in Å with 1.148 Å/mm; only the central 30 mm of the central plate is shown. The full extent of the telemetered six-tap cross-dispersion window is seen and measures 9.9 mm. The areas of reduced background at top and bottom are due to dither effects. Star-shaped coarse support structure diffraction is seen around zeroth order, and "cat's whiskers" fine support structure diffraction is seen above and below the primary dispersion axis, as well as in the vertical line through 0th order.

dispersion window (9.9 mm) is shown. The image is in angular grating coordinates (TG_D, TG_R), which have been converted to Å. The lines radiating from zeroth order above and below the primary dispersion axis are due to fine support structure diffraction. Star-shaped coarse support structure diffraction is seen around zeroth order. Figure 9.23 is a close-up of the bright Fe XVII, Fe XVIII, and O VIII lines between $\sim 15 - 17$ Å, in which many orders of fine support diffracted flux can be seen.

Figure 9.24 is an HRC-S image of a second Capella observation (obsid 1420, 30 ksec), showing positive order dispersion. The increasing cross-dispersion extent of lines at longer wavelengths is due to astigmatism in the HRMA/LETG system (see also Figure 9.14). The positive order HRC-S s plate gap is seen at ~ 63 Å. An extracted Capella spectrum (obsid 62435, 32 ksec), is shown in figure 9.25. Positive and negative order flux has been
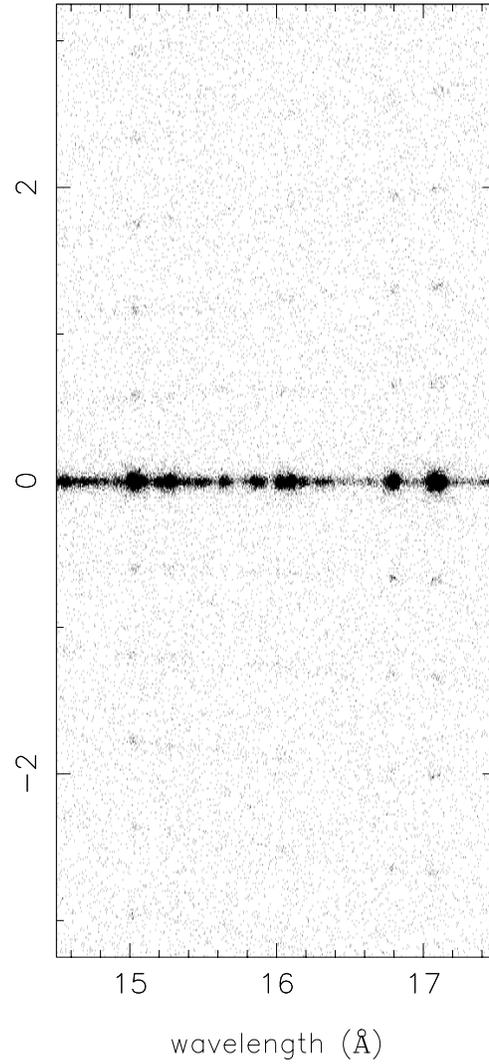
Figure 9.23: Detail of Figure 9.22, showing LETG/HRC-S image of bright lines in Capella. Both axes are in Å with 1.148 Å/mm. The Fe XVII lines at $\sim$ 15 and 17 Å are the brightest in the LETG Capella spectrum. Faint features above and below the primary spectrum are due to fine support structure diffraction.

summed.

Figure 9.26 is a zeroth-order image of summed Sirius AB observations (obsids 1421, 1452, 1459) with a total exposure time of 23 ksec. The star-shaped pattern is due to coarse support structure diffraction. Sirius A and B are separated by $\sim 4''$. The flux from Sirius A is due to the small but finite UV response of the detector.

9.4 Observation Planning

The purpose of this section is to provide further information directly related to planning LETGS observations and that is not explicitly presented in sections 9.1 and 9.3, and to reiterate the most relevant issues of instrument performance that should be considered when preparing an observing proposal.

9.4.1 HRC-S, ACIS-S and HRC-I Detector Choices

The best choice of detector will depend on the exact application; some considerations are listed below. For further details concerning the HRC and ACIS detectors, refer to chapters 7 and 6, respectively. We remind readers that contamination build-up on the ACIS detector has significantly reduced the effective area of the LETG+ACIS-S combination for wavelengths > 20 Å compared to that at launch.

HRC-S

- The HRC-S provides wavelength coverage from 1.2-175 Å (10-0.07 keV).

- The HRC-S provides the highest time resolution at $16\mu s$ *when the central plate only* is employed (note that photon time tag errors discovered on-orbit significantly degrade the effective time resolution of the HRC-I —see Section 7.10).

- The HRC-S can provide slightly better spatial (and thus spectral) resolution than ACIS for the LETG.

- HRC-S has essentially no intrinsic energy resolution and so overlapping spectral orders cannot be separated.

- The HRC-S QE is smaller than that of ACIS-S in the 1.2-20 Å (10-0.6 keV) range.

- The HRC-S background count rate is about 75 count s^{-1} in its windowed-down spectroscopic configuration during times of quiescence. However this can rise to exceed the HRC telemetry saturation limit of 184 count s^{-1} during background "flares". This saturation causes deadtime that can be corrected for to an accuracy of 5-10% at present. Background flares can also be filtered out using *CIAO* or other
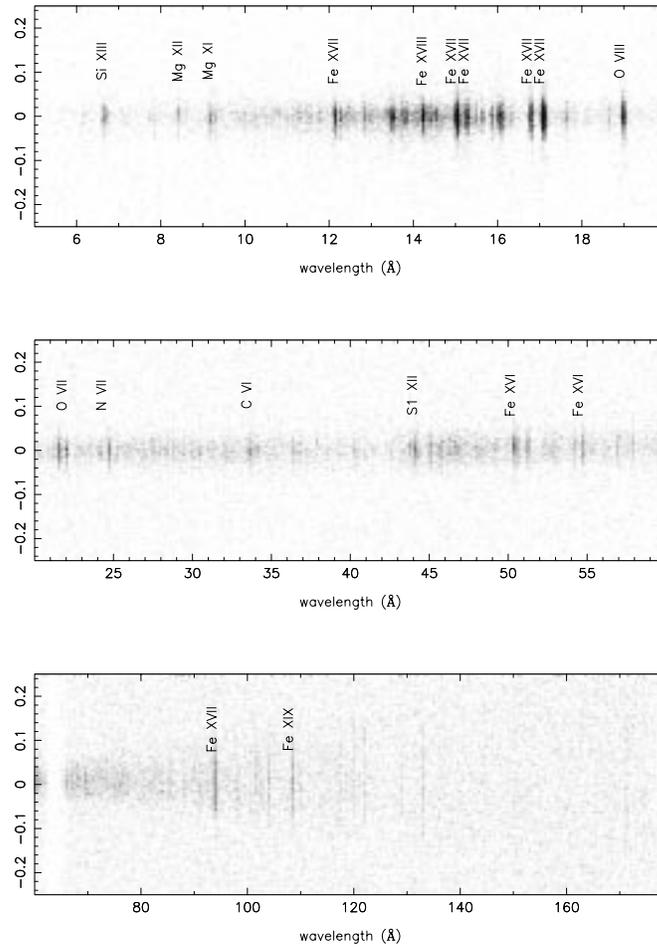
Figure 9.24: HRC-S detector image of a Capella observation, showing positive order dispersion. Both axes are in Å with 1.148 Å/mm. The increasing cross-dispersion extent of lines at longer wavelengths is due to astigmatism in the HRMA/LETG system. The positive-order HRC-S plate gap is at ∼ 63 Å.
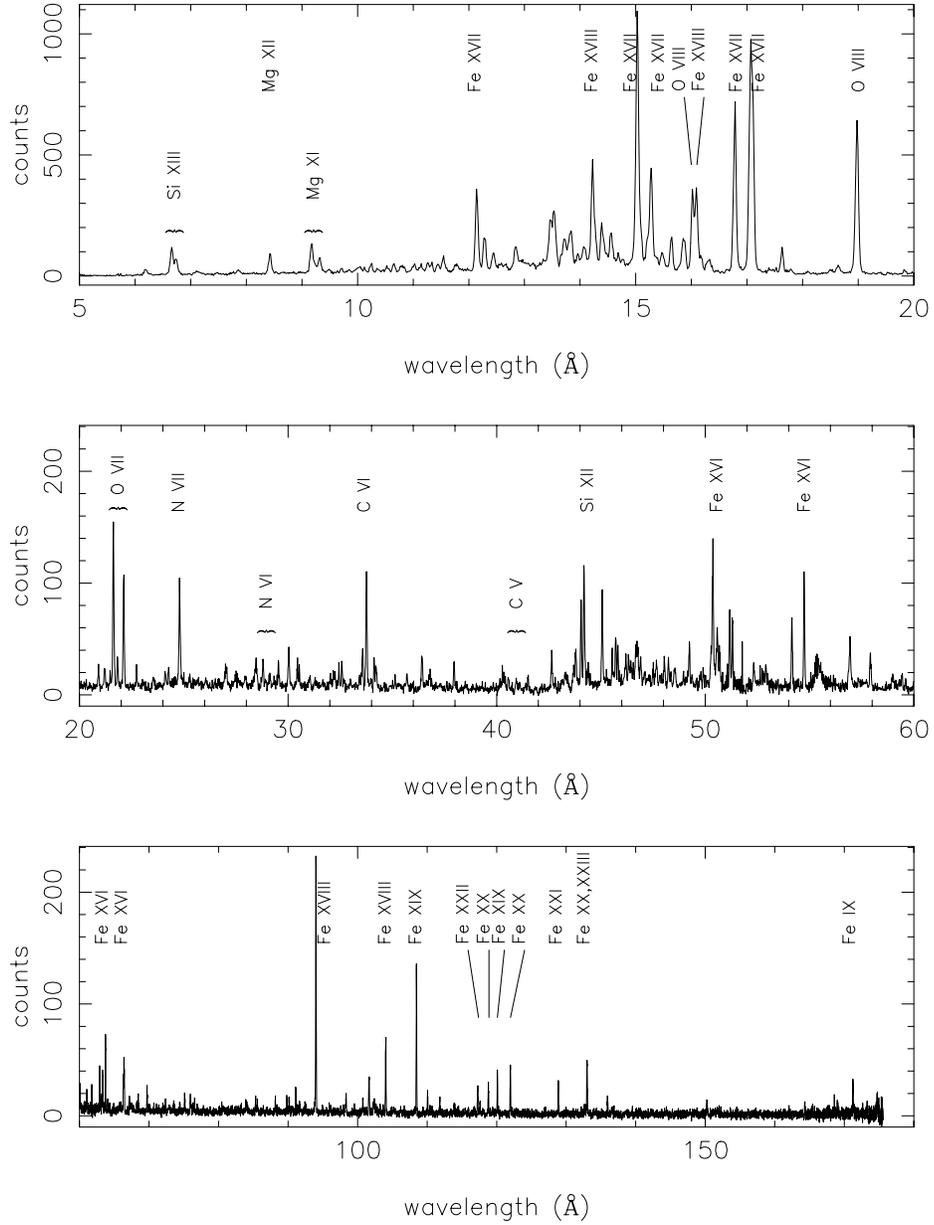
Figure 9.25: Extracted LETGS spectrum of Capella with some line identifications (from Brinkman et al. 2000, ApJ, 530, L111). Many of the lines visible between 40 and 60 Å are third order dispersion of the strong features seen in first order in panel 1.
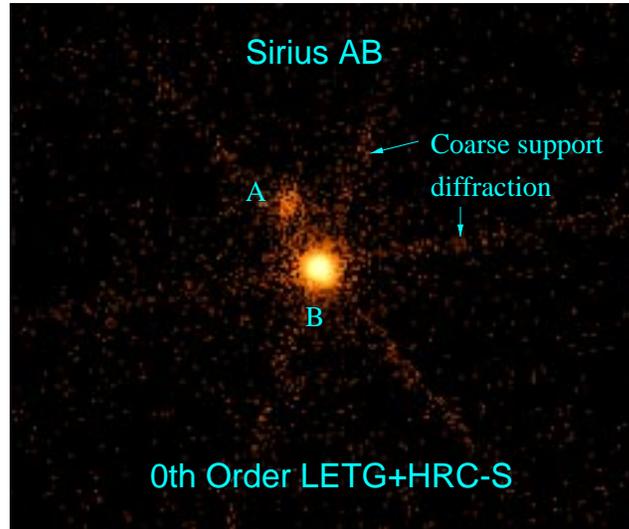
Figure 9.26: LETG/HRC-S zeroth order image of Sirius A and B. The two stars are separated by $\sim 4''$. Flux from Sirius A is due to the small but finite UV response of the detector. The star-shaped structure is due to coarse support diffraction.

software tools. These flares have been seen to affect 10-20% of some observations. Typical fractions are smaller than this; larger fractions are rare.

• The LESF filter region in principle can be used to obtain a higher-order spectrum relatively uncontaminated by first order for wavelengths above 75 Å ($E < 0.17$ keV; see Figure 9.17). This could be useful either for observing features in a high order for high spectral resolution that cannot be easily observed with the HETG/ACIS-S combination, or for providing a direct observation of higher order contamination in conjunction with an LETG+HRC-S observation in its nominal configuration. NB: this configuration has not yet been used in flight.

Summary   HRC-S is probably the best detector choice for spectroscopic observations in which one or more of the following observational goals apply:
—signal longward of 50 Å is of significant interest (see Figure 9.17));
—the highest time resolution is required;
—the highest spatial or spectral resolution *Chandra* can provide is required.

HRC-I

• The HRC-I provides wavelength coverage from 1.2-73 Å (10-0.17 keV).

- The raw HRC-I quiescent background event rate per unit area is lower than that of the HRC-S by about a factor of 8. After moderate filtering in both detectors, the ratio is about a factor of 4. HRC-I might therefore be a consideration if the source count rate is expected to be sufficiently high that HRC-S would be running close to saturation (note though the limitations on instrument count rates in the Chapter 7 in section 7.12).

- The HRC-I has similar imaging capabilities as HRC-S , though the UVIS is comprised of different thicknesses of polyimide and Al and consequently has different transmission characteristics. Most notably, the HRC-I has a lower sensitivity to longer wavelengths than HRC-S.

- The HRC-I timing resolution is limited owing to a hardware problem discovered on-orbit that can lead to erroneous time-tagging of photon events (see Section 7.10.)

- The details of the LETG+HRC-I effective area have been less well-studied in general than for the LETG+HRC-S combination.

- The HRC-I offers a broad detector in the cross-dispersion direction and this might be a consideration for observation of sources with extended components exceeding ~ 2 arcmin or so. Note, however, that the *Chandra* spectrographs are slitless, and the apparent spectral resolution is degraded according to source extension—see Figure 9.11.

- The HRC-I detector has certain count rate constraints discussed in Chapter 7 section 7.12. It may be that the 0th order image is to bright, or would extract significant amounts of charge. The HRC constraints need to be accounted for, and could require moving the 0th order off the nominal HRC-I aimpoint; this would result in a slightly reduced wavelength coverage by ~ 6 Å.

- The flat detector plates of the HRC-I depart from the Rowland geometry, hence degrading spectral resolution. A small focus offset can be used to optimize the focus of the dispersed spectrum.

Summary   HRC-I is possibly the best detector choice for sources in which signal longward of 73 Å (0.17 keV) is not of primary interest and accurate effective area knowledge for > 44 Å (< 0.28 keV) is not a strong concern, and in addition one or more of the following observational goals apply:
—HRC-S would be the detector of choice but the source is expected to have a count rate of more than an average of ~ 80 count s^{-1} and accurate photometry is required;
—very accurate light curves with the minimum of high background event filtering are required;

—high resolution timing is *not* required;
—a larger detector area in the cross-dispersion direction than is provided by the HRC-S is required.

ACIS-S

- Contamination build-up on the ACIS-S detector has significantly reduced the effective areas of the LETG+ACIS-S combination since launch (see Chapter 6 for details). ACIS-S provides an effective LETG 1st order wavelength limit of about 65 Å (0.19 keV) because longward of this the ACIS-S QE is essentially zero (see Figures 9.6 and 9.17).

- The intrinsic energy resolution of ACIS-S allows for discrimination between different and otherwise overlapping spectral orders. For dispersion distances of > 48 mm, the LETG+ACIS-S response is dominated by higher order throughput (Figure 9.17) and ACIS-S can therefore be useful for observing these higher spectral orders.

- Spectral resolution and line profile information are less well sampled due to the larger pixel size.

- ACIS-S allows several modes of operation (see Chapter 6) including continuous clocking (CC) if high time resolution is desired, or to avoid pileup.

- The full frame 3.2s exposure of ACIS-S in TE mode means that photon pileup can be a serious consideration, especially in 0th order. Proposers should also be aware that there is a potential for pileup in bright lines and continua and not assume that, because of dispersion, the flux is not sufficiently concentrated. At a count rate of about 0.05 photon/pixel/frame, up to a 50% loss of events due to pileup has been seen in the first order spectra obtained with the HETG/ACIS-S combination. Some of these events can be recovered by examining the higher order spectra but some events will have "migrated" out of the standard grade set, so the standard calibration curves no longer apply. Pileup can affect both the shape of the *PSF* and the apparent spectral energy distribution of your source. Pileup may be reduced by opting for a "sub-array" that reads out a smaller area of the detector for a decrease in the frame time (see also 9.4.2; see the ACIS chapter 6 for details concerning pileup, its effects, and how best to avoid it.)

- ACIS-S time resolution is lower than that of HRC and depends on the control mode adopted. In timed exposure (TE) mode the full frame exposure is 3.24s. This is reduced when using a subarray due to the shorter read-out time for the smaller detector region (again see Chapter 6 for details). The highest time resolution possible with ACIS-S (2.85 ms) is obtained in continuous clocking (CC) mode, but imaging

information in the cross-dispersion direction is lost and the background will be higher due to the implicit integration over the entire cross-dispersion column of the detector.

- The reduced energy resolution the FI chips suffer because of early on-orbit radiation damage increases with distance from the CCD readout. The LETG dispersion axis is parallel to the ACIS-S readout and the spectrum of a point source can be placed close to the readout such that the energy resolution is no longer a significant problem; a default SIM z offset of -8 mm is routinely applied to LETG+ACIS-S *point source* observations. If observations with extended sources are under consideration, or if for other reasons a SIM offset is undesirable, the resolution in the FI CCDs of the ACIS-S array might be a point to consider. From an LETG perspective, the effects of concern are a lowering of the CCD energy resolution that is needed for order sorting, grade migration that can make for difficult calibration of detector quantum efficiency, and at longer wavelengths (~ 50 Å) a loss of events that have pulse heights lower than that of the lower level discriminator—see Chapter 6 for a detailed discussion.

- The ACIS-S energy resolution enables removal of the vast majority of background events in LETG spectra; the effective ACIS-S background is consequently much lower than that of HRC-S or HRC-I.

Summary   ACIS-S is possibly the best detector choice for sources for which signal longward of 25 Å (0.5 keV) is not of any interest and one or more of the following observational goals apply:
—Particular spectral features of interest occur where the LETG+ACIS-S effective area is higher than that of LETG+HRC-S
—High time resolution beyond the 3.2 s exposure of TE mode (less if a subarray is used), or the 2.85 ms of CC mode (if applicable), is not important
—A low resolution 0th order spectrum from the S3 BI chip is of high scientific value, in addition to the dispersed LETG spectrum
—Order separation is important
—Pileup can either be avoided or mitigated or is not likely to be a problem.

9.4.2   Other Focal Plane Detector Considerations

Instrument Features and Gaps

Attention should be paid to the locations of instrument edge features and detector gaps to make sure that spectral features required to achieve science goals are not compromised by these. These features and gaps are listed for both HRMA+LETG+HRC-S and HRMA+LETG+ACIS-S combinations in Tables 9.3 and 9.4. Note that intrinsic instrumental features, such as edges, are not affected by dithering and offset pointing (see below),

but chip gaps in ACIS-S and HRC-S plate gaps, as well as the boundaries between "thick" and "thin" regions of Al that make the "T" shape of the HRC-S UVIS, are.

Dither

The standard LETG+HRC-S dither amplitude is 20 arcsec (40 arcsec peak-to-peak; 2 mm in the focal plane) and that of LETG+ACIS-S is 8 arcsec (16 arcsec peak-to-peak; 0.8 mm), in both axes. Spectral features in dispersed LETG spectra will experience the same dither pattern, and allowance for the size of the dither must be made when considering if spectral features of interest will encounter detector gaps.

In special cases, different dither amplitudes can be specified by the observer, though it must be kept in mind that detector safety constraints, such as accumulated dose/pore in the HRC (see 7.12), must not be violated.

SIM z Offsets

The SIM permits movement of the focal plane detectors in the spacecraft z direction (perpendicular to the LETG dispersion axis). This can be used to better position a source on ACIS-S or HRC detectors, for example to accommodate multiple sources, or to place a source over the HRC-S LESF filter region. The nominal aim point for the LESF requires a SIM z offset of +7 mm.

In the case of LETG+ACIS-S, a standard SIM z offset of -8 mm is applied to point source observations, *unless otherwise requested by the observer*, in order to place the source closer to the ACIS readout. In the case of extended sources, this offset might not be desirable as it could place part of the source off the detector. The effects of spacecraft dither should always be considered when choosing a SIM z offset.

Offset Pointing

Pointing off-axis in the observatory y axis can be used to change the wavelengths at which detector gaps occur, or to change the wavelength corresponding to the ends of the detectors. Examples of offset pointings are shown in Chapter 3. When choosing offsets, the approximate focal plane and dispersion relation scales of 20 arcsec/mm and 1.148 Å/mm are sufficiently accurate. As an example, by invoking a +2 arcmin offset pointing (see Chapter 3 for the convention), the long wavelength cut-off of the HRC-S can be extended in the + order from approximately 175 Å (0.0708 keV) for on-axis pointing to nearly 182 Å (0.0682 keV). This of course is obtained at the expense of a commensurate shortening of coverage in the − order.

Offset pointing leads to degradation of the *PSF*, and consequently the spectral resolution—see Figure 9.12. For offsets of order 2 arcmin or less this degradation is

negligible. For offsets of > 4 arcmin, spatial and spectral resolution will be considerably degraded.

In the case of the LETG+ACIS-Sconfiguration, certain offsets might be useful, eg, in order to place features of interest on (or off) backside illuminated chips for better low energy quantum efficiency. Table 9.3 and Figure 9.6 can be used to determine what offsets are required. Three useful offsets to consider for LETG+ACIS-S observations are the following:

$-0.33'$ *This is the default Y-offset value* and moves the 0th order of the target closer to the S4 chip by about 1 mm to avoid placing 0th order on one of the S3 node boundaries. The wavelength range for each chip using this setting is listed in Table 9.3.

$+1.5'$ This moves 0th order toward the S2 chip by about 4.5 mm and changes the S3 chip wavelength coverage to $-1.9 : +26.2$ Å. This offset is useful for keeping O K edge features on the S3 backside chip, but results in a very small degradation in the spectral resolution and might not be desireable if the very highest resolution possible with LETG+ACIS-S is required.

$+2.56'$ This moves 0th order by 8.6 Å, putting it on the edge of the S2 chip, so that half of 0th-order photons will be lost as they dither across the S2/S3 gap. The advantage is that the high-QE BI chips, S1 and S3, cover all wavelengths out to 56.9 Å, i.e., -56.9 to -28.7 Å for S1 and $+0.6$ to $+28.7$ Å for S3. Resolving power will be reduced by about 40%, however (see Figure 9.12).

HRC-S Windowing

As described in section 9.3, the HRC-S has a default spectroscopic "window" defined that limits the detector area from which events are telemetered to the ground. The window is a rectangle based on coarse position tap boundaries; the default rectangle is comprised of the central 6 taps in the cross-dispersion direction (corresponding to ~ 9.9 mm) and the whole detector length in the dispersion direction.

However, this window can be defined to suit special observational goals, such as if the source is extended and the width of the readout region must be increased (with increased risk of telemetry saturation during background flares). Another example is if there is an expected long wavelength cut-off in the source flux, perhaps due to an intervening ISM neutral H column density of $\geq 10^{19}$ cm^2, the rectangle could be reduced in size in the dispersion direction. Of course one would no longer be able to detect or use in analysis the higher orders that might fall outside the chosen window region.

When considering defining a special HRC-S window, it is reasonable to assume that the detector background is spatially uniform for the purposes of computing the total source + background count rate. The telemetry capacity of 184 count s^{-1} should be kept in mind to avoid telemetry saturation by using a window that is too big.

ACIS-S Modes

An LETG+ACIS-S observation needs to select a mode for the ACIS detector. The ACIS detector is very flexible but can also be complicated when deciding the best set-up. Prospective observers considering using ACIS-S for the focal plane detector are urged to read Chapter 6 carefully. The most common non-standard modes used for LETG+ACIS-S observations are those using sub-arrays, which can be a good way to both increase the time resolution and decrease pileup. Care must be taken when defining subarrays to make sure that the choice of SIM z plus any offset pointing in the z direction places the source comfortably inside the subarray. Modes with $\frac{1}{8}$ and $\frac{1}{4}$ sub-arrays are recommended for observers of point sources, or sources with relatively small extension, provided that a larger field in the cross-dispersion is not required for, eg, serendipitous sources.

$\frac{1}{8}$ The LETGspectral trace of a point source dithered using the normal ACIS pattern will fit inside a $\frac{1}{8}$ subarray with a 0.6s frametime. For a default LETG+ACIS-S SIM z of -8 mm, the subarray start row to place the source in the centre needs to be 113, so that the 128 rows of the subarray are ACIS-S rows 113-240.

$\frac{1}{4}$ For a $\frac{1}{4}$ subarray, a start row of 0 is appropriate for a SIM z of -8 mm.

For other values of SIM z, the appropriate start row can be computed using the ACIS-S pixel size of 24 micron to determine where the centre of the subarray in the z axis lies.

9.4.3   General Considerations

Complications from Other Sources

Field sources coincident with the target source dispersed spectrum should be avoided. This avoidance is most simply accomplished by imposing a roll angle constraint. Note that it is also desirable to retain a pristine region either side of the dispersed spectrum to enable an accurate estimation of the background within the spectral extraction window.

In some circumstances, photons dispersed by the LETG of bright sources outside of the direct field of view of the HRC or ACIS detectors might also give rise to significant signal on the detector.

Particular attention should be paid to optically-bright and UV-bright sources, even if these are some distance off-axis. The ACIS-S and HRC-S filters are much more transparent to optical and UV light than are those of HRC-I and ACIS-I (the HRC-S central "T" segment is closer in performance to that of HRC-I, but has completely different thicknesses of polyimide and Al layers). As an example, an observation of the bright A0 V star Vega ($V = 0.03$) in one of the outer HRC-S UVIS segments gave a count rate of about 475 count s^{-1}.

The energy resolution of the ACIS-S detector enables filtering out of all photons except those in a fairly narrow wavelength or energy range corresponding to the wavelength or energy of photons in a spectrum dispersed by the LETG. This means that contamination of the dispersed spectrum by, for example, the 0th order or dispersed spectrum of other sources *might* not be a significant problem.

However, a much better solution to problems of source contamination is, if it is possible within other observation constraints, to choose a roll angle (Chapter 3) that avoids the source contamination issue.

Roll Angle Considerations

Roll angle constraints can be specified to avoid contamination by off-axis sources, as described above, or to help separate the dispersed spectra of multiple sources in the cross-dispersion direction. The maximum separation between dispersed LETG spectra of two sources is obviously one that places the sources in a line perpendicular to the dispersion axis.

It is important to remember that roll angle constraints will also impose restrictions on the dates of target availability as discussed in Chapter 3. Exact restrictions depend on celestial position. Their impact can be examined using the observation visualizer tool.

High Order Throughput

It is expected that the majority of observations with the LETG will make use of the HRC-S as the readout detector because of its wavelength coverage and high quantum efficiency at long wavelengths. Since the HRC-S has very little energy resolution, the overlapping of spectral orders could be a significant issue and prospective observers should assess the degree to which their observation might be affected. The following list summarizes some of considerations:

Scientific Utility: Higher spectral orders provide higher spectral resolution than the first order spectrum by the approximate factor of the order number m. For observations in which features are expected to be seen in higher orders, this capability could be scientifically useful.

LESF: At the time of writing, the LESF, the thicker filters on the HRC-S, remains untested in flight, but could be useful for obtaining a spectrum containing mostly higher order flux.

Source Spectrum: For some sources higher orders will contain very little flux and will not be an issue. Typical examples are hot white dwarfs or relatively cool stellar

coronae $T \sim 10^6$ K. Sources whose spectra are fairly weak in the region where the effective area of the LETG+HRC-S is highest ($\sim$ 8-20 Å; 1.5-0.6 keV) compared to the spectrum at longer wavelengths are also going to be less affected by higher order throughput.

Estimates: Figure 9.18 can be used to estimate high order contamination. *PIMMS* can be used for gross estimates of higher order count rates; the *PIMMS* higher order calculation uses an effective area curve for orders $m > 1$ combined.

Instrumental Capabilities: Order separation is straightforward with ACIS-S. With HRC-S orders cannot be separated. Filtering methods based on the HRC-S event pulse height information enable some reduction of higher order events. Such techniques are limited by the width of the X-ray event pulse height distributions (section 9.3.6) and are of little use for removing 3rd order events, but can be of increasing use for successively higher order removal. Such filtering does greatly increase the uncertainty of the higher order contributions since at this time the exact fractions of higher order photons removed when using different filtering thresholds has not yet been determined. See 9.3.6 for further details.

Deconvolution and Forward Modeling: By folding a spectral model through an LETG -HRC-S instrument response that includes all significant higher orders (generally $\leq$ 10), the whole spectrum can be modeled at once. The capability to simultaneously specify the response matrices and effective areas (and extraction efficiencies) for multiple orders will be available within the *Sherpa* fitting engine of the next release of *CIAO* (v3.0). Combined response matrices including orders 1..6 are presently available under the LETG+HRC-S Effective Area page and may be used with current versions of *CIAO* and other spectral analysis software such as *XSPEC* and SPEX. While these response matrices are adequate for the analysis of continuum sources, note that they do not include the small-scale wavelength distortions discussed above, and hence care must be taken in analyzing line dominated spectra. An alternative approach is "bootstrap" modeling, where the analysis begins by only considering the shortest wavelengths. The approach assumes that contamination from the higher orders is minimal at the highest energies. The high energy data are used to deduce the higher order contribution at somewhat lower energies which is subtracted, and the process is repeated, working down in energy. The bootstrap approach is independent of an assumed source-model, but it may suffer from the amplification of noise in the case of weak sources and has mathematical problems in distributing photons into successively higher resolution orders. The latter renders the method better for continuum sources than for those dominated by spectral lines.
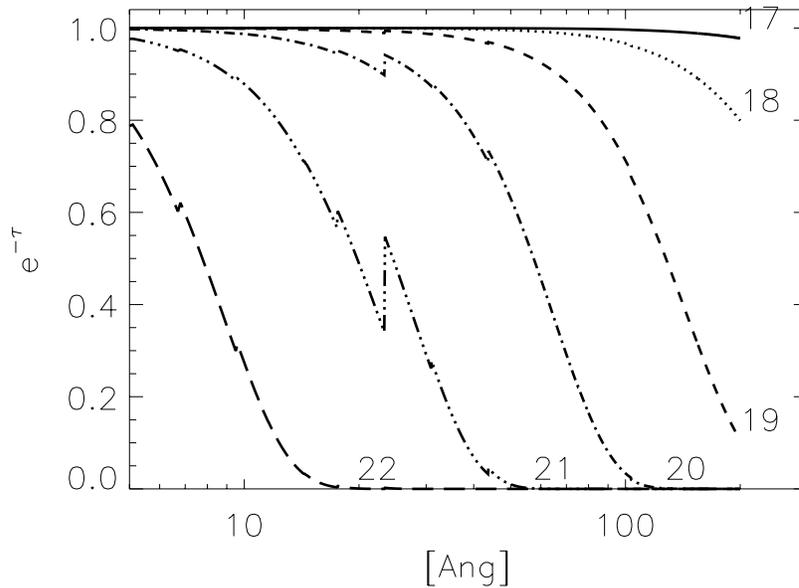
Figure 9.27: The ISM transmittance within the LETGS bandpass for different values of neutral hydrogen column density 10^{17}-10^{22} cm^2.

ISM Absorption

The long wavelength cutoff of the LETGS in tandem with the HRC-S detector of ∼175 Å (which can be extended with offset pointing as described above), extends well into the extreme ultraviolet (EUV). In this wavelength regime, even very nearby sources with relatively low ISM absorbing columns can be appreciably attenuated by H and He bound-free photoionizing transitions. Therefore observers should be aware that the effective long wavelength cutoff for anything but the most nearby sources (∼ 100 parsec or less) will probably be determined by ISM absorption. It is also important to remember that neutral and once-ionized He can dominate the ISM absorption cross-section in the 44-200 Å (0.28-0.062 keV) range, and consideration of the neutral H absorption alone is generally not sufficient. Shortward of the C edge near 44 Å (0.28 keV), metals become the dominant absorbers. For illustration, the ISM transmittance for a "typical" mixture of neutral and ionized H and He H:He:He$^+$ of 1:0.1:0.01 is illustrated in Figure 9.27 for the 5-200 Å range and for different values of the neutral hydrogen column.

Unfortunately, the tool for estimating the line-of-sight neutral H column density within the local galaxy that was located at the Center for EUV Astrophysics, University of

California, Berkeley is no longer available. It is hoped that this utility will be reinstated; information will be posted on the LETG webpage (footnote 2) when available.

The *CXC* web page has a tool COLDEN that provides the total *galactic* neutral hydrogen column for a given line-of-sight. This is described in Chapter 11. An IDL routine from the PINTofALE data analysis package for computing the ISM optical depth is available from http://hea-www.harvard.edu/PINTofALE/pro/ismtau.pro

9.5   Technical Feasibility

Another tool, *PIMMS* can be used for *rough planning purposes* and to predict 0th order pileup fractions in LETG+ACIS-S observations.

In all cases, proposers should be aware of possible limitations in the physical models and methods they are using. For example, older *XSPEC* versions might not include ISM absorption edges or spectral models at the high resolutions appropriate for *Chandra* grating observations. Available optically thin, collision-dominated plasma radiative loss models are also untested in detail at the line-by-line level, especially in the relatively unexplored spectral region 25-75 Å (0.5-0.17 keV). Some limitations in *MARX* modeling of LETG+HRC-S spectra are detailed below.

9.5.1   Simple Calculation of Exposure Times and Signal-to-Noise Ratio for Line and Continuum Sources

There is a discussion in chapter 8 (HETG), section 8.5.4, concerning the detection of an isolated emission line or absorption line. The discussion is based on a figure of merit which shows the dependence of signal-to-noise ratio on the combined effective area and resolution. The figure of merit graphs (Figures 8.32 and 8.31) include the LETG+HRC-S combination. The discussion in Chapter 8 is based on line equivalent width, which is appropriate for broadened lines and continuum features but which is more difficult to apply to simple modeled estimates of expected line fluxes. Additional formulae which are simple to apply are presented below. The units use Å rather than keV, Å being a much more natural unit of choice for dispersed spectra, and especially for the LETG range.

Emission Line Sources   The source signal S in a bin is the difference between the total counts and the background counts B. The estimated standard deviation of the source counts S in a spectral bin is given by Poisson statistics as:

$$\sigma_S = \sqrt{S + B} \tag{9.1}$$

Here we have made the important assumption that there is effectively no additional uncertainty in the estimation of the background B. Such an assumption may only be valid

if, for example, the detector region used to estimate the background within the spectrum extraction window is much larger than the window itself.

Spectrometer count rates for emission features are given by

$$s_l = A_{eff}(\lambda)\mathcal{F}_l(\lambda) \tag{9.2}$$

where s_l is the source count rate in the resolution element centered at λ, in counts/s, A_{eff} is the effective area in cm^2, and $\mathcal{F}_l$ is the source flux at the telescope aperture, in photons/cm^2/s. For A_{eff}, it is reasonable to use the total area obtained from the sum of $+$ and $-$ orders as illustrated in Figure 9.17. Raw source counts are estimated by multiplying this instrument count rate by an integration time.

Using equations 9.1 and 9.2, the signal-to-noise ratio for an integration time t is then

$$\frac{S}{\sigma_S} = \frac{s_l\sqrt{t}}{\sqrt{s_l + b}} \tag{9.3}$$

where b is the background count rate *within the spectrum extraction window* (i.e. "underneath" the spectrum) in the same resolution element centered at λ, in counts/s. Equation 9.3 provides the expected relation that is valid in the limit where the background count rate b is small compared with the source count rate s_l, that the signal-to-noise ratio scales with the square root of the exposure time.

The exposure time required to achieve a given signal-to-noise ratio is then provided by inversion of equation 9.3,

$$t = \left(\frac{S}{\sigma_S}\right)^2 \frac{s_l + b}{s_l^2}. \tag{9.4}$$

In order to make the exposure time estimate one needs to determine the background count rate, b. Since the spectrograph does not have infinite resolution, the flux from an otherwise narrow spectral line is spread over a typical line width, w_l. For LETG+HRC-S spectra, a good estimate for w_l is 0.07Å. This is somewhat larger than the FWHM value of 0.05Å listed in Table 9.1, but is more appropriate for calculations of signal-to-noise because it includes more of the line flux. For lines that are additionally broadened, simply use a value of w_l that covers the region under the feature of interest. The background rate b is then given by the quantity $b = w_l b'$, where b' is the background rate in units of count/Å/s. Background spectra for LETG+HRC-S from which one can readily estimate b are illustrated in Figure 9.28. Two scales are shown, one corresponding to b' and one corresponding to b where a width $w_l = 0.07$ Å was assumed. Note the y-axis units are per 10 ks. These curves correspond to both $+$ and $-$ orders added together and so are appropriate for use with the *LETG+HRC-S   total 1st order* effective area curves. These spectra are also available in ASCII format from the LETG Observer Information web page (footnote 2.)
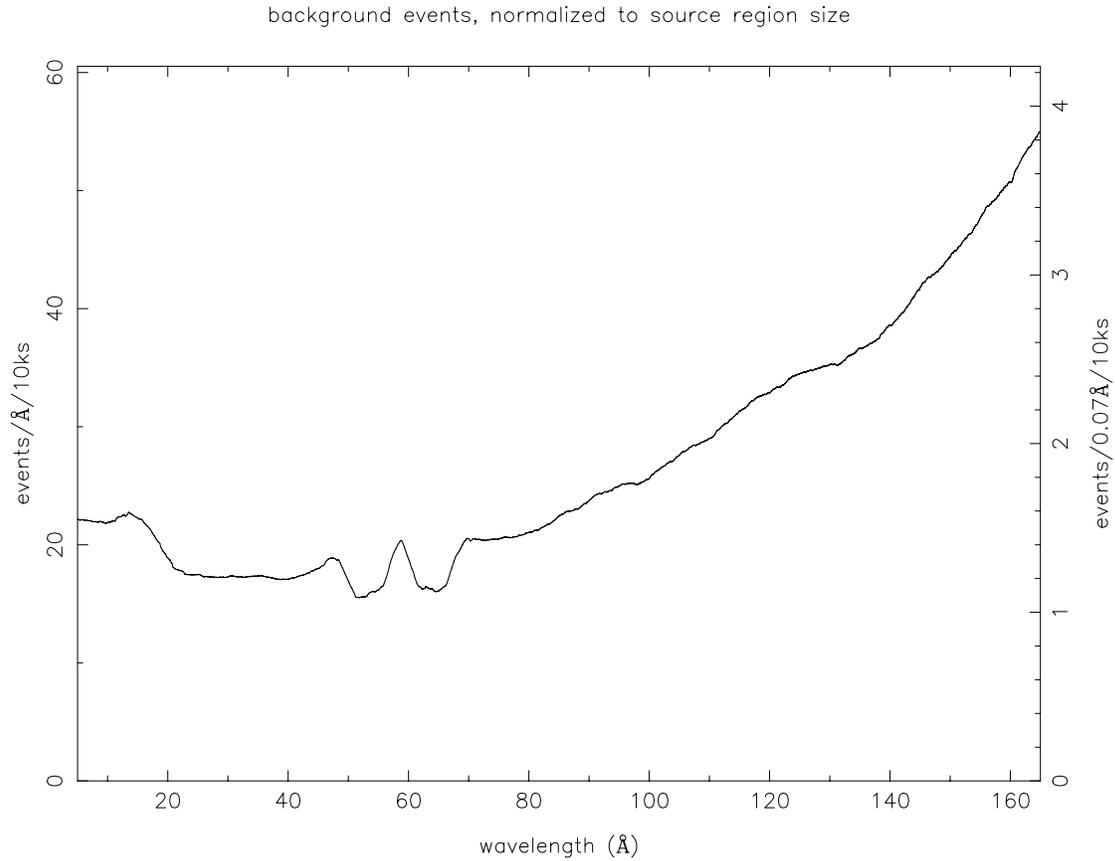
Figure 9.28: The LETG+HRC-S background count rate in the spectral extraction window as a function of wavelength for use in observation planning. Both + and - orders have been combined. These curves correspond to the "medium" (2% X-ray loss) PH filter described in the text. The left y axis is in units of counts/Å/10 ks, while that on the right is in units of counts/0.07 Å/10 ks; the latter corresponds to a typical line width over which most of the observed flux is distributed in the case of an intrinsically narrow spectral line compared to the instrument LRF.

Using the signal count rate s_l, provided by the product of source flux (at the telescope aperture) and effective area as stated in equation 9.2, we then obtain the two equations for the signal-to-noise ratio S/σ_S resulting from an exposure time t,

$$\frac{S}{\sigma_S} = \frac{\mathcal{F}_l A_{eff} t}{\sqrt{\mathcal{F}_l A_{eff} t + b' w_l t}} \tag{9.5}$$

and for the exposure time t required for a signal-to-noise ratio S/σ_S

$$t = \left(\frac{S}{\sigma_S}\right)^2 \frac{\mathcal{F}_l A_{eff} + b' w_l}{(\mathcal{F}_l A_{eff})^2}. \tag{9.6}$$

These simple equations, which include the effects of instrumental background, can also be easily applied to observations of lines on top of continua, as well as to situations in which features of interest lie on top of higher (or lower) spectral orders (HRC). In these cases, the continuum or higher order flux acts as an additional background term—the count rate/Å due to these additional terms is simply added to b'.

Continuum Sources Model fluxes for continuum sources can be expressed as flux densities in units of photons/cm^2/s/Å. To compute instrument count rates s_c from a continuum source spectrum, the A_{eff} function and spectrum must be partitioned with some bin size w, large enough to give adequate count rates. The product of the source spectrum with the A_{eff} function is then summed over some wavelength region of interest. Equation 9.2 becomes the sum:

$$s_c(\lambda) = \sum_{j=1}^{N} \mathcal{F}_c(\lambda_j) A_{eff}(\lambda_j) w \tag{9.7}$$

where $\mathcal{F}_c$ is the model source flux in photons/cm^2/s/Å, $A_{eff}(\lambda_j)$ is the effective area of the jth bin in cm^2. The region of interest spans bins 1 through N, and w is the bin width in Å. In using this formula for planning purposes, proposers must choose a spectral bin width that will demonstrate the viability of the program proposed. For fairly narrow spectral ranges in which A_{eff} is nearly constant, the sum over 1-N reduces to

$$s_c(\lambda) = \mathcal{F}_c(\lambda_j) A_{eff}(\lambda_j) N w \tag{9.8}$$

In this case one can of course simply chose a new bin size $w' = Nw$.

The difference between the continuum and the emission line case above lies in the units of $\mathcal{F}_c$, which is a flux density. The equations corresponding to the line source equations 9.5 and 9.6 are, for the signal-to-noise resulting from an exposure time t

$$\frac{S}{\sigma_S} = \frac{\mathcal{F}_c A_{eff} w t}{\sqrt{\mathcal{F}_c A_{eff} w t + b' w t}} \tag{9.9}$$

and for the exposure time t required for a signal-to-noise ratio S/σ_S

$$t = \left(\frac{S}{\sigma_S}\right)^2 \frac{\mathcal{F}_c A_{eff} w + b' w}{(\mathcal{F}_c A_{eff} w)^2}. \tag{9.10}$$

Note also in the above equations that the background b' is in units of counts/Å/s.

PIMMS **for Rough Planning Purposes**

PIMMS is described in Chapter 11. *PIMMS* is best suited to performing rough estimates of total or 0th order count rates, or estimating the fraction of 0th order events that would be piled up. Some degree of caution should accompany *PIMMS* calculations of detailed quantities such as count rates within narrow spectral bands using the Raymond-Smith model. For example, line positions and intensities in this model were only designed to represent total radiative loss and do not stand up to high resolution scrutiny. Calculations using powerlaw and featureless continua are not prone to such difficulties, but are susceptible to other *PIMMS* limitations. One particular limitation concerns the background model for HRC-S, which in *PIMMS* is currently (2002 Dec) assumed to be a single average number per spectral resolution element of 32 counts/100 ks. This approximation overestimates the background at higher energies, and underestimates the background at lower energies - see Figure 9.28.

MARX **Simulations**

The best tool available for the most accurate observation simulations is the *MARX* ray trace simulator. *MARX* is described further in Chapter 11; there is also a detailed user guide available. *MARX* allows one to simulate observations using any of the available *Chandra* instrument combinations. At the time of revision (Dec 2002), *MARX* has the following limitations for LETG+HRC-S observations:

- The HRC-S QE is known to be spatially non-uniform at the 10-15% level. The non-uniformity is characterized by a fairly steady gradient in QE from one side of each MCP to the other in the dispersion direction. The QE is more uniform in the cross-dispersion direction. This gradient in QE is not currently included in the *MARX* HRC-S model. Instead, this spatial variation is implicitly included in the QE in the dispersion coordinates of first order photons (ie the QE for first order is effectively correct, but could be in error by as much as 10-15 % for higher orders or for arbitrary imaging simulations).

- Instrument, sky and particle background is *not* directly included in *MARX* and needs to be simulated or otherwise accounted for by the user. Background can be simulated by approximating it as a flat field and adding this simulation to that of
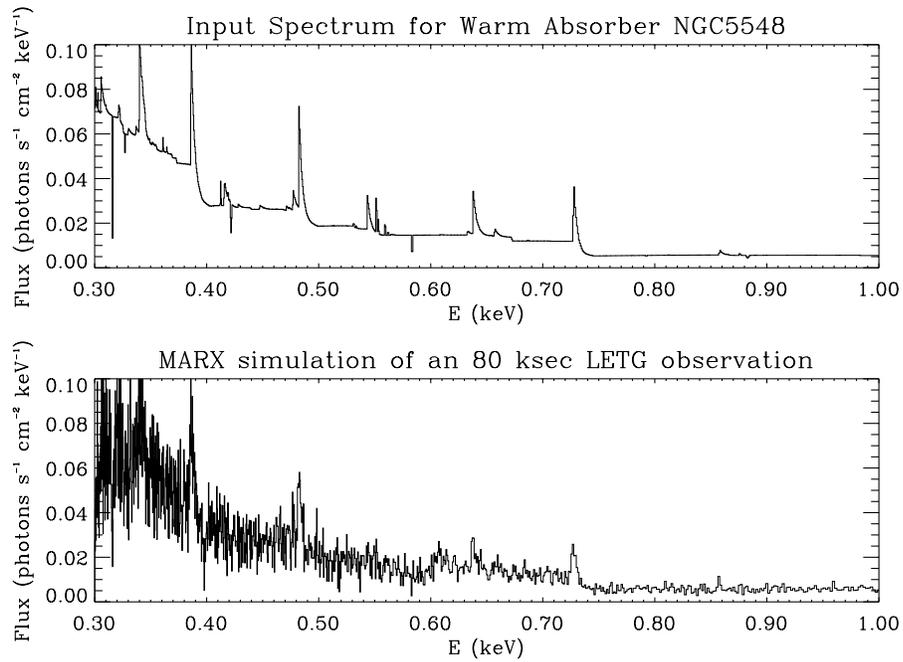
Figure 9.29: This figure shows the extracted first order spectrum for an 80 ksec observation of the AGN NGC5548. The input spectrum consists of a power–law plus a "warm" absorber (shown in the top panel). The simulated spectrum (bottom panel) has been corrected for the instrument response to give the flux from the source.

the source. Instructions for doing this will be included in *MARX* documentation. Ignoring background will affect HRC-S observation predictions the most. See section section 9.3.6) and Figure 9.28. One other way of simulating this for a point source is to obtain the empirical background spectra from the LETG Observer Information web page (footnote 2.) The background can then be simulated as a normal point source spectrum in *MARX* for the same exposure time as the actual source in order to obtain a realisation of the background count level. Note that the pulse height information simulated in *MARX* will not be correct. Further instructions for accounting for background will be posted on the LETGwebpage (footnote 2) and in the *MARX* documentation.
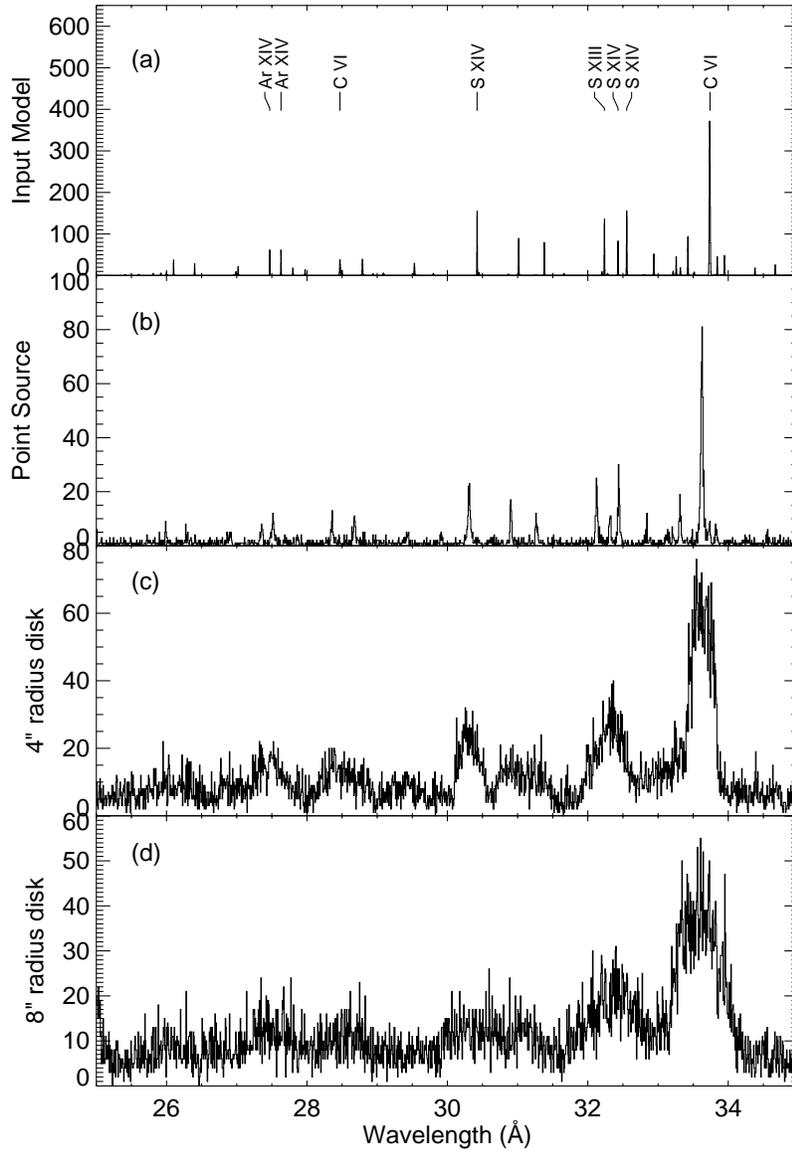
Figure 9.30: *MARX* simulation of spectra showing the effect of source extent. The panels show (a) computed input spectrum, (b) a *MARX* output of LETG spectrum of a point source, (c) the same as (b) except that the source is a disc of uniform brightness with radius of 4″, and (d) the same but with radius of 8″. See text for discussion.

9.6   References

Further LETGS information and calibration data can be found on the LETG Observer Information page [2] off the *CXC* website.[3] Newsletter articles summarizing calibration can be found in Issue 4 subassembly calibration[4], Issue 5 XRCF calibration[5], and Issue 6 calibration reports.[6]

Document history

- 02 Nov - updated by J.J. Drake, B. Wargelin, V. Kashyap and D. Pease

- 01 Dec - updated by B. Wargelin, M. Weisskopf.

- 01 Oct - updated by J.J. Drake, B. Wargelin, D. Pease, V. Kashyap and E. Raffauf

- 00 Nov - updated by J.J. Drake, B. Wargelin, D. Pease and P. Ratzlaff

- 00 Feb - revised and re-written by J.J. Drake, B. Wargelin and O. Johnson – some editing and cross-referencing by M. Weisskopf.

- 99 Dec - removal of LESF and HESF; D. Harris

- 99 Jun - updated by N. R. Evans

- 97 Aug - updated by N. Evans, J.J. Drake, J. Juda, D. Huenemoerder, M. Juda, M. Weisskopf, A. Tennant, P. Predehl, D. Swartz

- 97 May - updated by N. R. Evans, B. Wilkes, and J. Juda

- 94 Nov - updated using PDR material.

- 93 Jan - updated during visit to Utrecht; comments from A. Brinkman, R. Mewe, T. Gunsing, J. Heise, J. van Rooijen.

- 92 Nov - first draft

---

[2]http://cxc.harvard.edu/cal/Letg/
[3]http://cxc.harvard.edu/cal/
[4]http://cxc.harvard.edu/udocs/news_04/issue4aplatex.html
[5]http://cxc.harvard.edu/udocs/news_05/issue5latex.html
[6]http://cxc.harvard.edu/udocs/news_06/index.html

Part II

Policy, Planning, and Proposal Preparation

Chapter 10

Observing Policy

10.1 *Chandra* observing policy

10.1.1 Introduction and scope

This document establishes the observing policy for *Chandra*. This policy reviews and confirms the distribution of observing time amongst the Guaranteed Time Observers (GTOs) and General Observers (GOs), establishes guidelines for the resolution of conflicts between and within these groups, and sets guidelines for the distribution of observing time.

10.1.2 Applicable documents

Chandra Level-I Requirements and Policy

10.1.3 Distribution of data

Proprietary data

With certain exceptions, all data awarded either to GTOs or to GOs will be proprietary for one year (unless the observer specifies a shorter proprietary period), beginning when the data are made available to the observer. For fragmented "Long Duration" observations (see section 10.1.7), the one-year period for each target begins when 80% of the data have been made available to the observer.

Data from unanticipated Targets Of Opportunity (TOO) and other use of Director's Discretionary Time (see section 10.1.9) may be proprietary for limited periods – no more than three months – before they are placed into the public archive.

Calibration data scheduled and obtained by the *Chandra* X-ray Center (*CXC*) will not be proprietary and will be placed directly into the public archive. Data obtained during

slews from one target to another and from pointings made for operational reasons will also be placed directly into the public archive.

Data from Very Large Projects (*VLP*, Section 10.1.8) will not be proprietary.

Distribution of Observing Time

Distribution between GO and GTO Scientific observations commenced approximately 2 months after launch. X-ray data obtained during these first two months were considered calibration data and were placed directly into the public archive. Subsequent to this commissioning period, and exclusive of calibration time, the distribution of observing time between GTO and GO is as follows:

Months after launch	GO	GTO
3 - 4		100%
5 - 22	70%	30%
23 - end of mission	85%	15%

Distribution amongst GTO's As specified in the *Chandra* Level-I Policy and Requirements Document, the GTOs comprise the following, starting with Cycle 3 (after the IDSs had completed their observing programs): Four Instrument Principal Investigators (IPIs) for the *Chandra* Imaging Spectrometer (ACIS), for the High-Resolution Camera (HRC), for the Low-Energy Transmission Grating (LETG), and for the High-Energy Transmission Grating (HETG), and the Telescope Scientist (TS). Their observing time is based on a distribution of 4.0 "shares" as follows:

TS and LETG IPI	0.5 shares each	1.0 shares total
HETG, ACIS, and HRC IPIs	1.0 shares each	3.0 shares total

10.1.4 Target selection and phasing

Target selection will be phased with the *CXC* Call for Proposals (*CfP*). The cycle of target selection will begin with the GTOs specifying targets which over-subscribe the GTO time available. Any GTO-GTO conflict at this point shall be resolved by the GTOs. In the event that no resolution is achieved the GTOs shall write proposals in response to the *CfP*. After this, the GO proposals are received and GO-GTO conflicts are identified. In response, GTOs may either a) replace a conflicted target with an unconflicted backup target or b) write a proposal and let the peer review decide the conflict. Targets resulting from peer review of the responses to the *CfP* will be added to the unconflicted targets proscribed by the GTOs. This cycle of events will be repeated in this order for each *CfP*.

10.1.5   GTO Proposals

GTOs must thus submit proposals for observing time if there are also GO or GTO proposals for the same target/scientific goal. GTOs are guaranteed to receive their observing time in accordance with section 10.1.3, but can not reserve targets in advance of the *CfP*.

10.1.6   Conflict resolution

All conflicts (GO-GO, GO-GTO, or GTO-GTO) are decided as part of the peer review process with selection based on scientific merit.

10.1.7   Large Projects

Large Projects are those that are designated as such by the proposer and which require more than 300 ks observing time, whether long-duration observations of single targets or shorter duration observations of many targets. Large Projects are encouraged: for Cycle 5, 3 Ms of observing time will be allocated for Large Projects, subject to reasonable standards of scientific merit, as determined through peer review.

Large Projects shall be proposed to be completed within the time span covered by a *CfP* and cannot reserve targets beyond this. Those projects which are large owing to the observation of numerous objects (e.g., of a given class) should propose alternate targets (via a priority-ordered, slightly over-subscribed list), in the event of a conflict with an individual target of high scientific merit from another proposal during the same proposal cycle. The peer review shall either approve the individual observation from the other proposal and suggest (or select) alternate target(s) for the Large Project, or simply inform the Large Project proposers that one of their targets will be available in the public archive a year after the observation.

Since the science goals of Large Projects require large blocks of time, the topical panel which first reviews a Large Project is not allowed to suggest reductions in observing time (except in the above-mentioned case of multiple targets). Final selection is done by a merging panel which can recommend a reduction of observing time only in unusual cases. Proposers should be aware that Large Projects are more all-or-nothing propositions than are the regular proposals.

10.1.8   Very Large Projects

Very Large Projects are those that are designated as such by the proposer and which require 1Ms or more of observing time. Very Large Projects are encouraged, and up to 3 Ms of observing time have been set aside for this purpose in Cycle 5, subject to reasonable standards of scientific merit, as determined through peer review. Apart from the minimum amount of observing time and the restriction that data obtained under a

Very Large Project enters the public data archive immediately, the approach and selection procedures for Large Projects are applicable (Section 10.1.7)

10.1.9   Targets of Opportunity (TOOs)

There are two categories of Targets of Opportunity: Those that are proposed and selected through peer review; and those that simply occur and have been brought to the attention of the Director of the *CXC*, who may reschedule *Chandra* to obtain the appropriate observations in the best interest of the scientific community.

Pre-proposed TOOs

A proposed TOO may be reserved for a single proposal cycle. The proposer may propose to renew the opportunity in subsequent cycles.

Unanticipated TOOs

Data obtained from an unanticipated TOO is considered Director's Discretionary Time. These data may be kept proprietary for a period not to exceed three months.

10.1.10   GO time allocation

All GO time allocation will be subject to peer review.

10.1.11   GTO time allocation

All GTO targets with conflicts will be subject to peer review, consistent with the provisions of section 10.1.4.

10.1.12   Director's Discretionary Time (DDT)

For Cycle 5 700ks of observing time is reserved for (Director's Discretionary Time (DDT). This allocation includes unanticipated TOOs (10.1.9).

10.1.13   Time Critical Targets

The number of time-constrained targets accepted in any review will be limited to 20% of the total and constraints may not be imposed after the proposal has been reviewed.

10.2 Procedures concerning TOOs and DDT

The deep orbit of *Chandra* will permit relatively easy access to any TOO. The minimum planned response time to TOOs is ∼24 hours but operational experience may change this. The total number of TOOs performed are also limited by operational and man-power constraints.

Requests to either initiate a pre-approved TOO or to propose a new one are made to the *CXC* Director and it will be his decision to interrupt the timeline and conduct the observation. The investigator is required to submit an abbreviated version of the RPS form. The form, a Request for Observation (RfO), can be found at the *CXC* home page (http://cxc.harvard.edu) and submitted via the WWW.

The response to a TOO will be classified according to the time delay between trigger and observation. The faster the Chandra response, the more difficult, and the more limited the number of TOOs allowed. TOO followups (observations following a TOO within a few weeks) will also count as TOOs.

10.2.1 Pre-proposed TOOs

TOOs generated by a *CfP*-approved proposal are similar in spirit to the *IUE* or *RXTE* in that time is allocated to the proposal, but the time is unscheduled. To initiate the scheduling process, the investigator is required to specify in the RfO how the trigger condition has been met.

TOOs disrupt the timeline and it is possible that the TOO conflicts with a time-critical observation and/or with another TOO. In such situations, the *CXC* Director will determine priorities. Any disrupted preplanned observation will, however, be ultimately accomplished if feasible.

10.2.2 Unanticipated TOOs

A request for an unanticipated TOO observation is made directly to the *CXC* Director. Submission of an RfO is required. The procedure is as follows:

- The proposer must determine whether the target falls within the portion of the sky visible to *Chandra*. The *ObsVis* tool described in Chapter 11 can generate such information.

- The proposer must establish whether the target can be detected by *Chandra*. The tools described in Chapter 11 can be used for this purpose.

- The proposer must address the following questions:

– Why is the science from the observation important, and why not simply propose during the next *Chandra CfP*?

– Is there an impending, previously approved, *Chandra* observation, that can accomplish the objectives?

– How urgent is the TOO? Must the observation be done immediately?

– If relevant, what is the likelihood of additional transient behavior (i.e. does the phenomenon recur?) If reoccurrence is likely, what is the consequence if the target is not observed until the next occurrence?

– If data already exist in the archive, why is another observation with *Chandra* necessary?

– What is the proposed/suggested detector configuration?

If the proposed observation is accepted, a new timeline will be created as soon as possible. Some negotiation between the observer and the *CXC* may be necessary to achieve the optimum blend of response time and minimum impact on the rest of the schedule.

10.2.3   Director's Discretionary Time (DDT)

Requests for DDT must follow the same procedure as required for an unanticipated TOO. The procedure is described in section 10.2.2.

- The proposer may apply for a short period of time (≤ 3 months) during which the data is considered proprietary.

- A limited amount of funding is available to support DDT observations.

10.3   Criteria for Completeness and Data Quality

10.3.1   Completeness

Completeness refers to time on target or exposure time. Observations are scheduled based on the approved exposure time. Very occasionally, circumstances such as telemetry dropouts, scheduling efficiency, etc. may prevent the *CXC* from achieving this exposure time. The observation is considered complete if the achieved exposure is $\geq 80\%$ of the approved exposure time.

Observations ≤ 3 ks, will not be repeated, due to the associated high overhead and inefficiency. In this case, performing a single, best-efforts attempt to observe for the approved amount of time constitutes a completed observation.

10.3.2   Data quality due to high background

Data can be lost (or overwhelmed) because of occasional episodes of very high background. If the principle target was a point source and the background is ≥ 10 times nominal for $\geq 50\%$ of the observation, the target may be observed again for a period of time equal to the amount of time lost due to the high-background. If the target is extended, and the background increase is ≥ 5 times nominal for $\geq 50\%$ of the observation, then another observation may be scheduled to replace the amount of time lost due to the high-background. We realize that application of these limits are somewhat arbitrary. The intent is to only schedule additional observations if the scientific objectives were not achieved due to the high background. If "cosmic weather" causes only some deterioration in data quality, the observation is considered complete.

Although the *CXC* monitors space weather, there is no real time contact with the Observatory. Ultimately, it is the observer's responsibility to determine if the data require another observation according to the criteria above. An application for an additional amount of time on target should be made to the *CXC* Director. Providing a plot of the background counting rate vs. time and a short table with the integrated time at different background levels is required.

10.3.3   Data quality - telemetry saturation due to x-ray sources

Telemetry saturation produced by the target and/or other sources in the field of view are the responsibility of the observer. The unique case of a previously unknown transient appearing in the field of view will be handled case-by-case.

Chapter 11

Resources for Proposers and Proposal Submission

The *CXC* has extensive on-line resources for *Chandra* proposers and a suite of software tools for common proposal-related tasks. All proposal-related material can be found at http://cxc.harvard.edu/proposer.

11.1 On-line Resources

11.1.1 The Call for Proposals

The main reference document for writing *Chandra* proposals is the Chandra Call for Proposals. The *CfP* contains instructions for proposal preparation and submission, and the deadline for proposal submission. The *CfP* is available from the *CXC* website http://cxc.harvard.edu/proposer/CfP.

Hardcopy is available upon request to the *CXC* HelpDesk.

11.1.2 The HelpDesk Form

We are using commercial Helpdesk software to track your requests and problems. Click on "log into the *CXC* HelpDesk" and the HelpDesk login box will appear. Enter a user name (we suggest first and middle initial followed by last name, but any unique string will be okay) and press enter/return to log in. No password is required. Once you have logged in you can send a query (or "ticket") by clicking on the "Submit Ticket" in the left hand frame. New users are advised to enter their name, email address and phone number (this only needs to be done once.) HelpDesk also allows you to search previous tickets that are not private. More detailed information is given on the HelpDesk interface. Users can also email the *CXC* HelpDesk :

cxchelp@head-cfa.harvard.edu

.

Finally, in the last few days before and after the proposal deadline we activate a dedicated email address for problems with proposal submission. This should be used for proposal submission purposes only, and is not active for most of the year. This dedicated email address helps the *CDO* to deal more efficiently with the very large volume of correspondence we receive around the proposal deadline. Dates for which the address is switched on will be posted on the proposer page. The proposal help email address is:

prophelp@head-cfa.harvard.edu

.

Proposal queries submitted via the HelpDesk interface and cxchelp email alias will always be answered.

11.1.3   Searching the *Chandra* Archives and Downloading data

ChaSeR (Search and Retrieval from the Chandra Data Archive) allows a user to check what observations have been made of an object, what the status of the observations is (observed, publicly released, etc.), and ultimately to select data products and retrieve them. The web version of *ChaSeR* can be accessed at http://cda.harvard.edu:9011/chaser/mainEntry.jsp.

There is also a downloadable version of *ChaSeR* which has somewhat more sophisticated search capabilities than the web version. *ChaSeR* is available from the Chandra Data Archive http://cxc.harvard.edu/cda/.

Chaser also includes a precession tool and provides quick access to images. *ChaSeR* is extensively documented on the archive pages of the Chandra website. In particular there are detailed instructions for installations on many systems, and a useful FAQ page. The user is referred to these sources for installation instructions as well as usage tips, updates, and more complete documentation.

The Target Pages (http://cxc.harvard.edu/targets/) can also be used to search the Chandra Data Archive (but not to download archival data). Detailed target lists can be found at http://cxc.harvard.edu/target_lists/index.html.

Another tool of interest is the processing status tool that provides detailed and comprehensive information about the processing of each ObsId. The processing status tool can be accessed via the Target Search Pages (click on the ObsID on the search results page). It can also be accessed from http://cxc.harvard.edu/soft/op/op_pst.html.

11.1.4   Instrument Information

Information on *Chandra* instruments and calibration can be found in this Guide, and via the "Instruments and Calibration" link on the *CXC* webpage. Significant updates and changes will be posted in the Announcements Box on the *CXC* webpage.

11.1.5 Instrument Response Functions

Instrument response functions (RMFs and ARFs) for simulating spectra within *Sherpa* and *XSPEC* can be found on the proposer page and the Calibration Database (CALDB) page. These responses should be used for proposal preparation only; they should NOT be used for data analysis!

11.2 Proposal Preparation Software

The *CXC* provides several software tools to aid in proposal preparation.

11.2.1 *dates*, *colden*, *precess*, *PIMMS* and *ObsVis*

These tools perform the following functions:

- *precess* is an interactive astronomical coordinate conversion program. It allows not only precession of equatorial coordinates but conversion between equatorial, ecliptic, galactic and supergalactic coordinates.

- *colden* is an interactive program to evaluate the neutral hydrogen column density at a given direction on the sky. *colden* accesses two databases: the Bell survey (Stark et al 1992 ApJS 79. 77) and the Dickey & Lockman 1990 (ARA&A, 28, p.215) compilation of Bell and other surveys for all-sky coverage.

- *dates* is an interactive calendar and time conversion tool.

- *ObsVis* is a tool to aid observation planning allowing inspection of instrument fields-of-view (FOVs), observatory roll angle and target visibility. It will display the instrument field of view on a Digital Sky Survey or user-loaded image and mark the locations of sources from various X-ray catalogs.

- *PIMMS* (*P*ortable *I*nteractive *M*ulti-*M*ission *S*imulator) was developed at NASA-GSFC by Dr. K. Mukai[1]. It allows the user to convert between source fluxes and count rates for different missions. *PIMMS* also uses simple spectral models (blackbody, bremsstrahlung, power, Raymond-Smith) in calculating count rates or fluxes.

All of these tools have web interfaces linked into the Proposer pages. They also have command-line (non-web) versions which have additional features. For example, command line versions of *precess*, *colden*, *dates* and *PIMMS* allow for a list of input parameters in a text file. The web version of *ObsVis* will give target visibility and nominal roll angle as a

---

[1]We thank Koji for making some changes to the code for *Chandra*.

function of time, but the command-line version is required to show instrument "footprints" on a Digital Sky Survey image.

The command-line versions of these tools are distributed with *CIAO*. *Chandra* users with *CIAO* installed can run these routines in the same way as all other *CIAO* tools. Standard *CIAO* helpfiles are available. It is not necessary to have have *CIAO* installed to run the proposal tools. Proposers without *CIAO* who need the command-line tools can download them from the proposer page.

11.2.2   Software Helpfiles and Proposal Threads

Helpfiles for proposal-related software (see Section 11.2) and proposal "Threads" are available from the *CXC* proposer site. These are new to Cycle 5, and replace Chapters 11-13 of the Cycle 4 *Proposers' Observatory Guide*. Helpfiles are available over the web as HTML files, in PDF format and as part of the *CIAO* "ahelp" system. Proposal Threads are modeled on *CIAO* threads and give step-by-step examples of how to perform feasibility calculations, fill in RPS forms and submit a proposal. They are intended primarily (but not exclusively) for less experienced *Chandra* users.

11.2.3   *MARX*

MARX is a suite of programs created by the *MIT/CXC* group and designed to enable the user to simulate the on-orbit performance of the *Chandra* X-ray Observatory. *MARX* provides a detailed ray-trace simulation of how *Chandra* responds to a variety of astrophysical sources and can generate standard FITS events files and images as output. It contains detailed models for the HRMA mirror system on board *Chandra* as well as the HETG and LETG gratings and all focal plane detectors. The most recent version of *MARX* is V3.01. More detailed information, including the source code and documentation, is available from the *MIT MARX* Web Page. *MARX* should be used to demonstrate the feasibility of challenging observations, for example resolving multiple or overlapping sources with unique spectra, HETG observations of extremely bright objects, or grating observations of extended sources.

11.2.4   *CIAO*

CIAO is an extensive suite of tools designed for *Chandra* data reduction. Although not designed specifically for proposal preparation, *CIAO* can be used to analyze simulated *Chandra* data (e.g. from *MARX*) and create simulated spectra. Full details can be found at http://cxc.harvard.edu/ciao/. *Sherpa* is an interactive spatial/spectral fitting package which forms part of *CIAO*. It can also be used for simple simulations of *Chandra* spectra.

11.2.5 *XSPEC*

XSPEC is the spectral analysis portion of the Xanadu X-ray data analysis package, developed and maintained at NASA-GSFC. *XSPEC* can be obtained from http://heasarc.gsfc.nasa.gov/docs/xanadu/xspec/index.html.

The spectral simulation portion of *XSPEC* can also be run on-line. *WEBSPEC* can be accessed from http://heasarc.gsfc.nasa.gov/webspec/webspec.html.

11.3 Proposal Submission

Electronic submission of proposals via the Remote Proposal Submission (RPS) system is required. RPS was first developed at the HEASARC, in the Laboratory for High Energy Astrophysics at NASA-GSFC. It was adapted for use with *Chandra* by the *CXC*. Paper copies of the proposal will only be accepted from individuals without access to the Internet. Those individuals should notify the *CXC* via HelpDesk well before the proposal deadline.

A proposal submitted via RPS consists of two parts; forms with essential information such as Principle Investigator and target and instrument information, and the science justification. The science justification is a postscript file prepared by the proposer using the word-processing facilities of her/his choice. A LaTeX template is available which formats text to specifications given in the *CfP*. In addition, the Principle Investigator must provide a list of *Chandra* programs she/he has been involved with. Full details of proposal requirements can be found in the *CfP*.

The science justification is uploaded to the RPS server at the end of the proposal submission process once the forms have been submitted. The RPS forms (consisting of a Cover Page, General Form and Target Forms) are usually filled out on-line. *Chandra* RPS can be accessed via http://cxc.harvard.edu/cgi-bin/RPS/Chandra/RPS.pl.

Proposals can also be submitted via the RPS email server. This is sometimes preferable for a large number of targets. Instructions to use the e-mail server may be obtained by sending a blank e-mail message to:

<center>`rps@head-cfa.harvard.edu`.</center>

The web version of RPS has extensive on-line help. In addition, there is a "proposal submission" thread which gives step-by-step instructions on filling in the RPS forms and submitting a proposal.

11.3.1 Help After Submitting: When You've Discovered A Mistake

If the mistake is discovered before the deadline, please go through the submit process as if you had not submitted before, and send notice to *CDO* via HelpDesk (or the prophelp

email address) that you have re-submitted. Once a proposal arrives, it is scanned to see if it may duplicate a previously-received proposal. Proposals that appear to be duplicates are then flagged for the attention of a member of the *CDO*. The proposal with the most recent date and time is accepted as the "final" proposal.

It is possible to correct minor errors in forms after the proposal deadline, especially if the item is critical to the success of the potential observation (e.g. incorrect coordinates). Please inform the *CDO* as soon as possible after the mistake is discovered.

Late changes in the Science Justification are not allowed. However, some typographical or numerical errors can be misleading, and corrections of such can be sent to the *CDO* in a letter of explanation. If appropriate, this letter will be included in material sent to the Peer Review. Note that a long list of corrections to a careless submission cannot be accepted since this would be *de facto* a late-proposal submission.

Part III

Appendices

Appendix A

Contact Information

A.1 Contact Information

The Proposal Review is organized for NASA by the *CXC* Directors Office (*CDO*) under the direction of Dr. Fred Seward (Assistant Director). Questions should be submitted to the *CDO* via our HelpDesk (http://cxc.harvard.edu/helpdesk/) (preferable) or by email: (cxchelp@cfa.harvard.edu). We strongly recommend the use of this HelpDesk as opposed to contacting individual staff members as it is routinely monitored and so not affected by the schedules of individuals.

A.2 *CDO* Staff

- Dr. Harvey Tanabaum, Director
- Dr. Fred Seward
- Dr. Belinda Wilkes
- Dr. Andrea Prestwich
- Dr. Nancy Evans
- Ms. Tara Gokas
- Ms. Mihoko Yukita
- Ms. Kathleen Manning

Appendix B

Acronym List

This list is a superset of acronyms and abbreviations used in this document.

ACA Aspect Camera Assembly

ACACAL ACA Calibration Data

ACIS Advanced CCD Imaging Spectrometer

ACIS-I ACIS Imaging array

ACIS-S ACIS Spectroscopic array

ADC Analog-Digital Conversion

ADU Analog to Digital Unit

AGASC AXAF Guide and Aspect Star Catalog

AO Announcement of Opportunity

ARF Ancillary Response Function

ARM Alignment Reference Mirror

ASC AXAF Science Center

ASCA also known as Asuka, Astro-D - Japanese X-ray satellite

ASCDS ASC Data Analysis System

ASCII American National Standard Code for Information Exchange

ASVT Avionics and Software Validation and Test (facility)

ASPQUAL Aspect Solution Quality Indicators

AXAF Advanced X-Ray Astrophysics Facility

BI Back-illuminated

CAP Command Action Procedure (used to communicate with spacecraft)

CC Continous Clocking

CCD Charge Coupled Device

CCDM Communication, Command, and Data Management

CDR Central Data Recorder (also Critical Design Review)

CfP Call for Proposals

CGCD Crossed Grid Charge Detector

CoI Co-Investigator

COLDEN Calculate Neutral Hydrogen Column Density

CR Cosmic Ray

CSS Coarse Sun Sensor

CTE Charge Transfer Efficiency

CTI Charge Transfer Inefficiency

CXC Chandra X-ray Center

CXCDS Chandra X-ray Center Data Systems

CXO Chandra X-ray Observatory

DBE Double Bit Error

DDT Director's Discretionary Time

Dec Declination

DO Director's Office

DOT Detailed Operations Timeline

DSN Deep Space Network

DSS Digital Sky Survey

EA Effecive Area

E/PO Education and Public Outreach

EC Ecliptic Coordinates

EDT Eastern Daylight Time

EPHIN Electron Proton Helium Instrument

ESA Earth Sensor Assembly

FCM Flux Contamination Monitor

FEF FITS Embedded Function (used to generate RMF fordetectors)

FI Focal Plane Instrumentation (Front-Illuminated)

FITS Flexible Image Transport System

FLA Fiducial Light Assemblies

FOT Flight Operations Team

FOV Field of View

FPSI Focal Plane Scientific Instruments

FPX Focal Plane X

FPY Focal Plane Y

FSS Fine Sun Sensor

FTA Fiducial Transfer Assembly

FTS Fiducial Transfer System

FUV Far-UV

FWHM Full Width Half Maximum

GESS Grating Element Support Structure

GMST Greenwich Mean Sidereal Time

GMT Greenwich Mean Time

GO General Observer

GSFC Goddard Space Flight Center

GST Greenwich Sidereal Time

GTO Guaranteed Time Observer

GUI Graphical User Interface

HDOS Hughes-Danbury Optical System

HEASARC High Energy Astrophysics Science Archive Research Center

HEG High Energy Grating

HESF High Energy Suppression Filter

HESS HETG Support Structure

HETG High Energy Transmission Grating

HETGS HETG Spectrometer

HPD Half Power Diameter

HQ Headquarters

HRC High Resolution Camera

HRI High Resolution Imager

HRMA High Resolution Mirror Assembly

HST Hubble Space Telescope

IAU International Astronomical Union

ICD Interface Control Document

IDR Intermediate Data Record

IDS Interdisciplinary Scientist

IPI Instrument Principal Investigator

IPS Integral Propulsion System

IRAF Image Reduction and Analysis Facility

IRU Inertial Reference Unit

ISIS Interactive Spectral Interpretation System

IUE International Ultraviolet Explorer

IUS Inertial Upper Stage

JD Julian Day

JPL Jet Propulsion Laboratory

KSC Kennedy Spaceflight Center

LESF Low-energy Suppression Filer

LETG Low Energy Transmission Grating

LETGS LETG Spectrometer

LGA Low Gain Antenna

LRF Line Response Function

LSF Line Spread Function

MARX Model of AXAF Response to X-rays

MCP Micro Channel Plate

MEG Medium Energy Grating

MIT Massachusetts Institute of Technology

MJD Modified Julian Date

MSFC Marshall Space Flight Center

MTA Monitoring and Trends Analysis

MUPS Momentum Unloading Proplusion System

NASA National Aeronautics and Space Administration

NASCOM NASA Communication system

NDC NRT Data Capture

NISN NASA Integrated Services Network

NMM Normal Maneuver Mode

NOAO National Optical Astronomy Observatory

NPM Normal Pointing Mode

NRA NASA Research Announcement

NRAO National Radio Astronomy Observatory

NRT Near-Real Time (telemetry data)

OAC Orbital Activation and Checkout

OBA Optical Bench Assembly

OBC On-Board Computer

OBSCAT Observing Catalog

OBSVIS Observation Visualizer

OCC Operations Control Center

OFLS Off-line System

ONLS On-line System

OS Operating System

PCAD Pointing Control and Attitude Determination

PDR Preliminary Design Review

PH Pulse Height

PHA Pulse Height Amplifier (or Amplitude)

PI Principal Investigator

PIMMS Portable Interactive MultiMission Software

PSF Point Spread Function

PSPC Position Sensitive Proportional Counter

QE Quantum Efficiency

RA Right Ascension

RCS Reaction Control System

RCTU Remote Command and Telemetry Unit

RfO Requests for Observations

RMF Redistribution Matrix Function

ROSAT Roentgen Satellite

RPS Remote Proposal Submission

RRC Retroreflector Collimator

RWA Reaction Wheel Assembly

SAO Smithsonian Astrophysical Observatory

SI Science Instrument

SIM Scientific Instrument Module

SMF Software Maintence Facility

SNR Supernova Remnant

SOHO Solar and Heliospheric Observatory

SOP Standard Operating Procedure

SOT Science Operations Team

SSR Solid-State Recorder

STScI Space Telescope Science Institute

TAI International Atomic Time

TBD To Be Determined

TBR To Be Reviewed

TE Timed Exposure

TIM Technical Interchange Meeting

TOO Target of Opportunity

TS Telescope System, or Telescope Scientist

UT Universal Time

UTC Universal Time Coordinated

UV Ultraviolet

UVIS UV Ion Shield

VCDU Virtual Channel Data Unit

VETA Validation Engineering Test Article
(mirror)

WGACAT White-Giommi-Angelini   Catalog
(ROSAT)

WWW World-Wide Web

XMM X-ray Multi-Mirror Mission

XRCF X-ray Calibration Facility

XSPEC X-ray Spectral fitting package

XTE X-ray Timing Explorer

XUV Extreme Ultraviolet